Vítor Manuel Pereira

Disorder and Localization Effects in Correlated Electronic Systems

Departamento de Física
Faculdade de Ciências da Universidade do Porto
October 2006

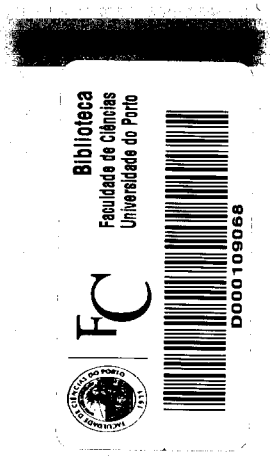

Vítor Manuel Pereira

Disorder and Localization Effects in Correlated Electronic Systems

Departamento de Física
Faculdade de Ciências da Universidade do Porto
October 2006

MC

Vítor Manuel Pereira

Disorder and Localization Effects in Correlated Electronic Systems

Tese submetida à Faculdade de Ciências da Universidade do Porto
para obtenção do grau de Doutor em Física

Departamento de Física
Faculdade de Ciências da Universidade do Porto
October 2006

AMV

Acknowledgements

I am most indebted to many people who, knowingly or not, have helped me throughout these doctoral years. It all starts with the privilege of working with my supervisor for the doctoral program at FCUP, professor João M. B. Lopes dos Santos, my mentor since the graduation years, and with whom there is always so much to learn, investigate and discuss (be the subject condensed matter theory or pretty much anything else). It is, and I am shure will always be, a pleasure to do physics with you.

When my PhD program had barely started, I came to meet professor Antonio H. Castro Neto, my supervisor at Boston University (BU). Staying in Boston under his attention was perhaps my most important experience as a training physicist. For many reasons, that include the quality of the scientific research and scientific debate at BU, my supervisor's expertise as a leading condensed matter theorist, but mostly from my personal contact with prof. Castro Neto's disturbingly unbreakable good spirits and optimism, which only seem to grow with the difficulties at hand, and readily spread among its collaborators.

At several stages, I benefited from discussing my ongoing work with other people. Among them, and for their precious insights, comments or suggestions, I would like to mention Leo Degiorgi (ETH), Paco Guinea (ICMM, Madrid), Nuno Peres (Universidade do Minho), Yuri G. Pogorelov (FCUP), Eduardo Castro (FCUP), Eduardo Novais (Duke University), Marcello Silva Neto (University of Utrecht), Peter Littlewood (Cambridge University) and Anders Sandvik (Boston University).

I acknowledge Boston University and its Department of Physics, for all the institutional and practical support during my four half-year stays at BU, including the access to the scientific computing facilities. Likewise, I recognize the support of the Department of Physics at FCUP, especially for their invitation to a teaching assistant position during the last year, and Centro de Física do Porto, for all financial, office and computational support.

I thank my family, Tânia's and my friends; I thank B. J. Teitleman for always insisting upon showing me the other side of things; my fellow students and post-doctoral researchers both at BU (especially the *Brazilian contingent* who helped me settle during the first weeks); and my fellow graduate students in Porto (mathematicians included, of course). Thanks to Miguel for the tips and suggestions about everything, especially on how to use OpenMP to get your code scheduled at 200% CPU. I would also like to mention Anton Kozlov, and David Sheridan, who is an amazing source of american culture, and did his best at coaching me how to strike a good hard liner.

My PhD activities, including the travelling expenses between Porto and Boston, would not have been possible without the doctoral grant from Fundação para a Ciência e a Tecnologia, under the reference SFRH/BD/4655/2001, and to which I am most grateful indeed.

Last, but foremost, as always, I mention you, Tânia. In particular because...

Abstract

This thesis is about electrons in disordered structures, and electrons correlated with other degrees of freedom. In particular, the discussions and results in the ensuing chapters pertain to two main categories that can be summarily synthesized as electrons interacting with localized magnetic moments – as in the DEM – and electrons in disordered two dimensional carbon.

Double Exchange Model (DEM). With regard to the DEM, we discuss in detail the region of validity of the DE limit for magnetic systems described by a Kondo lattice Hamiltonian, putting in perspective the two opposed limits $J \to \infty$ and $J \to 0$, and concluding that the former appears as the best approximation in the intermediate coupling regime. For DE systems with low densities of electronic carriers, the effects of Anderson localization are found here to be of paramount relevance. In that context we provide the first mapping of the mobility edge, E_C, as a function of the local spin magnetization in this system, and show that such magnetization dependent E_C has profound consequences to the magneto-transport response, including CMR effects, strongly enhanced electrical conductivities in the ferromagnetic phase, or blue-shifts of the plasma edge in the optical reflectivity.

The stability of free magnetic polarons in the pure low density DEM is addressed both phenomenologically and numerically. It is found that, at low densities, the PM-FM transition is mediated by a polaronic phase, which has the effect of considerably reducing the Curie temperatures, T_C, with respect to the mean-field estimates. At the same time, we analyze the related problem of phase separation in this same low density regime. We demonstrate that the phase separation instability characteristic of this model is strongly suppressed when electrostatic and localization corrections are included in the free energy, and establish a connection between the resulting ground state and the non-interacting polaronic phase.

Magnetic Hexaborides. A microscopic theory for rare-earth ferromagnetic hexaborides, of the type $Eu_{1-x}Ca_xB_6$, is proposed on the basis of the DE Hamiltonian. In these compounds, the reduced carrier concentrations place the Fermi level near the mobility edge, introduced in the spectral density by the disordered spin background. We show that some of their puzzling experimental signatures, such as the Hall effect, magnetoresistance, frequency dependent conductivity, and dc resistivity can be quantitatively described and coherently understood within the model. The region of magnetic polaron stability detected through Raman scattering experiments is also well reproduced, and we make specific predictions as to the behavior of the Curie temperature as a function of the plasma frequency, proposing a phase diagram for the doped family. We also discuss how recent transport and magneto-optical measurements confirm our Double Exchange (DE)-based picture and reproduce our originally proposed phase diagram.

Anderson Localization. We present evidence regarding the relevance of the local environment statistics in the phenomenon of Anderson localization. It is shown that the fluctuations in the inverse participation ratio, or in the local density of states, exhibit critical behavior, and provide strong evidence supporting the LDOS as an order parameter for the Anderson transition.

Graphene. Our incursion onto the subject of two dimensional carbon, reveals the consequences of different types of disorder for the electronic structure of graphene. We underline, in particular, the case of vacancies, which are shown to induce the emergence of localized modes at the Fermi energy, with a huge concomitant enhancement of the density of states. The relevance of these results in the explanation of the magnetism detected in disordered graphite is addressed.

Resumo

A presente tese é dedicada ao estudo de electrões em estruturas desordenadas, e electrões correlacionados com outros graus de liberdade. Em particular, as discussões e resultados apresentados nos capítulos seguintes poderão organizar-se segundo duas categorias principais, nomeadamente electrões interagindo com momentos magnéticos locais – tal como no MDT – e electrões no carbono bidimensional com desordem.

Modelo de Dupla Troca (MDT). Relativamente ao MDT, o regime de validade do limite de dupla troca é discutido em detalhe no âmbito de sistemas descritos pela rede de Kondo, colocando-se em perspectiva os limites $J \to \infty$ e $J \to 0$, e concluindo-se acerca da melhor aplicabilidade do primeiro nos casos de acoplamento intermédio. Para sistemas de DT com uma densidade baixa de portadores, mostra-se que os efeitos associados à localização de Anderson são de máxima relevância. Nesse contexto, é apresentada a primeira trajectória do limiar de mobilidade, E_C, como função da magnetização local para este problema, mostrando-se ainda que a existência de um limiar de mobilidade dependente da magnetização tem profundas consequências na resposta eléctrica e magnética do sistema, incluindo o aparecimento de efeitos de magnetorresistência colossal, condutividades dramaticamente amplificadas na fase ferromagnética, ou desvios para o azul na frequência de plasma.

A estabilidade de polarões magnéticos no MDT a baixa densidade é estudada fenomenológica e numericamente. Decorre dos resultados que, a baixas densidades, a transição PM-FM é mediada por uma fase polarónica, donde decorre um abaixamento considerável das temperaturas de Curie, T_C, relativamente às estimativas típicas de campo médio. Ao mesmo tempo, é abordada a questão da separação de fases no MDT. Demonstra-se que a instabilidade subjacente à separação de fases é fortemente suprimida através da inclusão de contribuições electrostáticas e de localização na energia livre, evidenciando-se ainda as similaridades entre o estado fundamental daí resultante e a fase polarónica.

Hexaboretos magnéticos. No âmbito dos hexaboretos de európio do tipo $Eu_{1-x}Ca_xB_6$, é proposto um modelo microscópico alicerçado no MDT. Nestes compostos, a reduzida densidade electrónica implica a significativa proximidade entre o nível de Fermi e o limiar de mobilidade induzido pela desordem magnética. Mostra-se aqui que as intrigantes características experimentais destes hexaboretos, como sejam o efeito Hall, a magnetorresistência, a condutividade óptica ou a resistividade, podem ser descritas e entendidas de modo coerente com base nesse modelo. A região de estabilidade polarónica registada em medidas Raman é igualmente bem reproduzida pelo correspondente diagrama de fases do MDT, sendo ainda proposto o diagrama de fases para os hexaboretos dopados. Finalmente, discute-se como este modelo e o diagrama de fases proposto vêm a ser corroborados por resultados experimentais subsequentes.

Localização. Entre os nossos resultados, são avançadas provas relativas à importância das propriedades locais no processo de localização de Anderson. Mostra-se que tanto a fracção de orbitais que contribuem para um dado autoestado, como a densidade local de estados, exibem flutuações com comportamento crítico, dando força a uma interpretação da densidade local de estados como possível parâmetro de ordem na transição de Anderson.

Grafeno. A incursão no tópico do carbono bidimensional revela algumas das consequências que diferentes modelos de desordem trazem para a estrutura electrónica do grafeno. É destacado, em particular, o caso de lacunas, das quais resultam estados localizados no nível de Fermi, ao mesmo tempo que fazem surgir um pico significativo na densidade de estados em E_F. O significado destes resultados para a compreensão do magnetismo detectado em amostras de grafite é discutido no final.

Résumé

Le sujet de cette thèse est les électrons en structures désordonnées, et les électrons corrélées avec d'autres degrés de liberté. En particulier, les discussions et les résultats dans les chapitres suivants concernent deux catégories principales qui peuvent être sommairement synthétisées comme des électrons en interaction avec des moments magnétiques localisés – comme dans le MDE – et des électrons dans le carbone bidimensionnel désordonné.

Modèle du Double Échange (MDE). En qui concerne le MDE, on discute en détail la région de validité du limite de DE pour des systèmes magnétiques décrits par un Hamiltonien de Kondo, et on compare les deux limites opposées, $J \to \infty$ et $J \to 0$, en concluant que le premier apparaît comme une meilleure approximation dans le régime d'accouplement intermédiaire. Pour des systèmes avec de faibles densités des électrons, les effets de localisation d'Anderson ont une importance primordiale. Dans ce contexte on fournisse la dépendance du bord de mobilité, E_C, en fonction de la magnétisation du système, et nous prouvons qu'une telle dépendance a des conséquences profondes sur la réponse magnétique et électrique, comme par exemple, des effets de CMR, des conductivités fortement augmentées dans la phase ferromagnétique, ou le décalage vers le bleu de la fréquence de plasma dans la réflectivité optique.

La stabilité des polarons magnétiques dans le MDE est adressée phénoménologique et numériquement. On constate que, pour des faibles densités, la transition PM-FM est interpolée par une phase polaronique qui a l'effet d'une considérable réduction des températures de Curie, T_C, vis-a-vis les valeurs obtenus en champ moyen. En même temps, on étude le problème de la séparation et coexistence des phases dans ce même régime de faible densité. On démontre que l'instabilité vers la séparation des phases caractéristique de ce modèle est fortement supprimée sur l'effet des contributions électrostatiques et de localisation dans l'énergie libre, et on établisse une liaison entre l'état fondamental résultant et la phase polaronique.

Hexaborures magnétiques. On propose une théorie microscopique pour les Hexaborures ferromagnétiques, du type $Eu_{1-x}Ca_xB_6$, basée sur le Hamiltonien de DE. Dans ces substances, pour vue de la faible concentration d'électrons, le niveau de Fermi et le bord de mobilité se trouvent très proches. On montre que la majorité de leur signatures expérimentales, comme l'effet de Hall, la magnetorésistance colossale, la conductivité optique, et la résistivité peuvent être quantitativement décrites et entendus dune façon cohérente avec ce modèle. La région de stabilité des polarons magnétiques détectée par Raman est également reproduite, et nous faisons des prévisions spécifiques en ce qui concerne le comportement relatif entre la température de Curie et la fréquence de plasma, proposant le diagramme de phase pour la famille dopée. On discute également les récentes expériences magnéto-optiques que confirment notre scénario théorique basé dans le MDE, et reproduisent le diagramme de phase.

Localisation d'Anderson. On présente des évidences concernant la pertinence de l'environnement local dans le phénomène de la localisation d'Anderson. On montre que les fluctuations dans le rapport inverse de participation, ou dans la densité locale d'états ont un comportement critique, et fournissent évidence soutenant la densité locale d'états comme paramètre d'ordre pour la transition d'Anderson.

Graphène. Notre incursion dans le sujet du carbone bidimensionnel montre les conséquences que différents modeles de désordre peuvent avoir dans la structure électronique de graphène. Nous accentuons, en particulier, le cas de lacunes, qui donnent lieu a l'émergence des modes localisés à l'énergie de Fermi, au même temps qu'une énorme résonance apparaît dans la densité d'états. La pertinence de ces résultats pour une explication du magnétisme détecté en graphite désordonné est adressée.

Contents

List of Figures

List of Acronyms

AFM	Antiferromagnetic or Antiferromagnetism
ARPES	Angle-Resolved Photoemission Spectroscopy
BMP	Bound Magnetic Polaron
BZ	Brillouin Zone
CF	Continued Fraction
CMR	Colossal Magnetoresistance
CaB_6	Calcium hexaboride
CPA	Coherent Potential Approximation
DEM	Double Exchange Model
DE	Double Exchange
DFT	Density Functional Theory
dHvA	de Haas–van Alphen
DMS	Diluted Magnetic Semiconductors
DOS	Density of States
EuB_6	Europium hexaboride
$Eu_{1-x}Ca_xB_6$	Calcium-doped Europium hexaboride
FIR	Far Infra-Red
FMP	Free Magnetic Polaron
FM	Ferromagnetic or Ferromagnetism
GF	Green Function
HTA	Hybrid Thermodynamic Approach
HTSC	High Temperature Superconductivity

HOPG	Highly Oriented Pyrolytic Graphite
IPR	Inverse Participation Ratio
IPM	Independent Polaron Model
IR	Infra-Red
KLM	Kondo Lattice Model
LDA	Local Density Approximation
LDOS	Local Density of States
MC	Monte Carlo
MFM	Magnetic Force Microscopy
MI	Metal-Insulator
MOSFET	Metal-Oxide-Semiconductor Field Effect Transistor
MR	Magnetoresistance
PBC	Periodic Boundary Conditions
PM	Paramagnetic or Paramagnetism
PS	Phase Separation
QHE	Quantum Hall Effect
RE	Rare-Earth
RKKY	Ruderman-Kittel-Kasuya-Yosida
RPA	Random Phase Approximation
STM	Scanning Tunneling Microscopy
SW	Spectral Weight
SdH	Shubnikov de Hass
TDOS	Typical Density of States
VCA	Virtual Crystal Approximation
WDA	Weighted Density Approximation
WS	Wigner-Seitz
XRES	X-Ray Emission Spectroscopy

"Those who have taken upon them to lay down the law of nature as a thing already searched out and understood, whether they have spoken in simple assurance or professional affectation, have therein done philosophy and the sciences great injury. For as they have been successful in inducing belief, so they have been effective in quenching and stopping inquiry; and have done more harm by spoiling and putting an end to other men's efforts than good by their own."

— **Francis Bacon**, Novum Organum [Bacon, 1620].

1. Introduction

"God could cause us considerable embarrassment by revealing all the secrets of nature to us: we should not know what to do for sheer apathy and boredom"

— J. W. von Goethe.

1.1. Context

The fields of correlated and disordered electronic systems have been the most active areas of research in condensed matter theory in the last decades. This derives mainly from the unexpected and intriguing behaviour that can be extracted when correlations and/or disorder are added to electronic models. The distinctive trait of these problems is the fact that traditional perturbative methods tend to fail in properly describing the many-body ground state of those systems. In addition, there is the non-irrelevant motivation that correlations and disorder are the driving mechanisms of many exciting and promising phenomena such as High Temperature Superconductivity (HTSC), Kondo physics, Colossal Magnetoresistance (CMR) or spin transport.

In the recent years a large fraction of theoretical and experimental effort in solid state physics has been oriented towards the understanding and optimization of very large changes occurring in the electric resistivity under the application of small magnetic fields. This magnetoresistive effect occurs traditionally in specially tailored thin film heterostructures, or in ferromagnetic metallic oxides like mixed-valence manganites[1] [Pu et al., 1995]. In fact, it was in the context of manganites, one of the richest topics in condensed matter [Dagotto, 2003], that the Double Exchange Model (DEM) and its variants acquired its notorious relevance.

The DEM is one of our subjects, but in a slightly different context. Large magnetoresistance effects are known to occur in Eu-based hexaborides [Paschen et al., 2000]. As a consequence — and following a series of experiments which unveiled intriguing connections between their magnetic, transport and optical properties — the series of compounds $R_{1-x}A_xB_6$, where A is an alkaline-earth metal such as Ca or Sr, and R a rare-earth magnetic ion, has recently attracted considerable interest. EuB_6 is a ferromagnetic metal, with many intriguing properties like its very small carrier density, which increases upon decreasing the temperature, or an electrical resistivity that drops precipitously below T_C. The theoretical understanding of these and other effects in EuB_6 has been characterized by controversies surrounding their underlying microscopic origins.

[1] Although its origin and magnitude is quite different in these two classes of materials.

One of our central objectives with this thesis, is to state our case whereby the DE mechanism, combined with a reduced carrier density and the inevitable Anderson localization effects, provides a coherent framework for the interpretation of most experimental measurements pertaining to these hexaborides. As it turns out, the extremely low density regime of the DEM has remained much unexplored, mainly because all attentions were upon the opposite limit, suitable for the manganites. This work tries to fill some of those gaps and clarify others.

As our work in those matters unfolded, exciting, unconventional and unforeseeable physics started to emerge from studies of graphene, made possible by recent developments in the techniques for growth and control of materials at the atomic scale. Graphene is one of the allotropic forms of carbon, consisting of a two dimensional sheet of carbon atoms with sp^2 hybridization arranged in a honeycomb lattice, and constitutes the building block of most Carbon-based materials, including graphite, nanotubes, fullerenes, etc. Presumed until recently to be unstable on account of instabilities towards the formation of curved structures, single planes of graphene have now been successfully prepared and characterized by independent experimental groups [Novoselov et al., 2005a,b; Zhang et al., 2005].

Magneto-transport measurements indicate that the low energy charge and spin excitations in these systems are Dirac fermions (electrons with a linear dispersion), a consequence of the peculiar structure of the honeycomb lattice. This means that the concept of effective mass, which controls much of the physical properties of ordinary metals and semiconductors, doesn't hold and leads to an unusual electrodynamics. As an example, Dirac fermions are known to exhibit anomalous properties, like suppression of screening, in the presence of disorder and interactions [DiVincenzo and Mele, 1984; González et al., 1996]. In addition, the high mobility of graphene samples allowed the identification of anomalous features in the Shubikov de-Haas oscillations and the integer Quantum Hall Effect (QHE), the latter displaying an anomalous (half-integer) quantization rule for the conductance [Novoselov et al., 2005a; Zhang et al., 2005].

The role of disorder is crucial. It was always observed that when graphite or fullerenes are bombarded with high energy protons, ferromagnetic behavior is measured [Esquinazi et al., 2003]. The potential technological implications of these findings in micro and nano devices for spintronics, optics, and quantum computing are clear. Ferromagnetism in Carbon based structures above room temperature, clearly challenges the traditional paradigm of localized magnetism based on d and f orbitals, and remains to be explained. Graphene also confronts the current wisdom on localization and transport in 2D since graphene and graphite-based devices exhibit an unexpected universal minimum metallic conductivity, have very high mobilities and display ballistic transport over micrometer distance scales [Novoselov et al., 2005a]. The wealth of results, formalism and predictions tailored for the usual metallic Fermi liquid paradigm, is, to a great extent, not directly applicable to graphene. Therefore many of the concepts upon which our physical intuition regarding electronic systems is founded, require a revision for this new scenario.

1.2. Organization of the Thesis

The thesis begins with a review of the recursive method, a powerful, versatile and efficient method to extract relevant physical information like spectral densities, the spectrum itself and response functions

from (mostly, but not restricted to) single-particle Hamiltonians. This chapter was designed much like a general review and overview, including some historical notes on the method and condensed matter theory as well. It is completely self-contained and serves mainly for the author's own reference and sorting of ideas, but can also be a useful starting point for a student or whoever feels interested in the matter.

The core matter of the thesis lies within chapter 4, wherein our studies regarding the double exchange model at low densities are expounded. Before that, an excursion into the phenomenology of the Eu-based hexaborides is needed, and so the third chapter is dedicated to a brief coverage of the experimental knowledge about those compounds. Chapter 4 is the longest and densest, as it includes the discussions about Anderson localization, and the double exchange model for magnetic hexaborides.

Chapter 5 is devoted to the physics of magnetic polarons and the phase separation instability in the double exchange model, and the last chapter describes some of our results in the context of disorder and localization effects for electrons in graphene.

Throughout the text, several ancillary details of direct relevance to our argumentation have been transferred to the appendices at the end of each chapter.

1.3. Original Content and External Material

This thesis contains around 80 figures, the vast majority of which is divided into further subfigures. With the exception of chapter 3, dedicated to the experimental signatures of Eu-based hexaborides, all these figures exhibit results obtained by the author, including all the demonstrative plots presented in the chapter about the recursive method. Moreover, all the numerical algorithms used for the core computations, have been coded by the author from blank files. The only exception where recourse was made to external routines is for the full diagonalization of matrices, where `LAPACK`, or `LAPACK`-derived routines were used.

2. The Recursive Method

> *"(...) in a large system, such as all solid state physics, one is always overwhelmed by too much information, in principle an infinite amount. The trouble with computers is that they give too many numbers, whereas physically one wants some combined quantity such as a magnetic moment."*
>
> — **V. Heine**, The Recursion Method and its Applications [Heine, 1980, pp. 3]

2.1. Introduction

2.1.1. When k-space will not do

The most immediate, and certainly self-evident, property of a disordered system is the absence of symmetry, wherefrom its classification arises. Of particular relevance in the context of solid-state theory is the lack of the periodicity that characterizes crystals. The enormous developments in solid state physics during the most of the XX^{th} century hinge, one may say, upon a central cornerstone: Bloch's theorem and the concept of electronic band. A wealth of important theoretical tools, theorems and results have been developed within a theoretical framework that assumes translational invariance of the target systems. This is true to the extent that solid state physics is developed in classical textbooks around perfect lattices in perfect crystals.

Absence of such ideal regularity is, nonetheless, an insurmountable reality of the solid state, that starts with the ideal crystal being thermodynamically unstable towards the presence of defects[1]. Next come the real crystals where all classes of defects, grain boundaries and impurities are intrinsic to the growth process. Of course these are still the *"clean"* cases, where the overall regularity is scarcely broken, and always at scales considerably larger than the interatomic distances. For such cases, Bloch's theorem is still a central and decisive player, side by side with the tools of perturbative approaches. For them, disorder is frequently seen as an unsought property from the materials scientist perspective, or as a technical hindrance for the theoretical approaches.

Then, there is the broad class of the so-called disordered systems. For the purpose of our discussion, these are the cases in which absence of periodicity is a feature, rather than a nuisance. Here k-space methods often become unwieldy, as the plane wave basis might be just as good as anything else. That disorder is a feature means simply that the system's properties and behavior are such that, had disorder been absent, they would be something completely different. To this class of materials belong many of the systems at the forefront of today's research in condensed matter (amorphous solids, alloys, glasses,

[1] At any non-zero temperature.

diluted ferromagnetic metals, some nanostructured materials, etc.). Of course, absence of periodicity is not an exclusive consequence of disorder or vice-versa. Full translational invariance makes little sense in problems involving surfaces (surface states, adatoms, the Density of States (DOS) at the surface of some metal, etc), interfaces, quantum dots and certain mesoscopic systems.

The message is then that, such examples beg that absence of periodicity in the electronic environment be accounted for from the beginning, as opposed to starting from a Bloch-like view, trying to make physics fit the mathematics of perfect periodicity.

2.1.2. Local electronic structure

The above cited examples are not the only ones in which one might consider abandoning k-space. In many situations, the attention is upon the local electronic environment, and it is of interest to develop a theory or approach closer to the physics we want to describe. This might occur because in a system only the first few atomic shells neighboring some atom are of relevance in describing its physics (like in many transition metal compounds [Haydock, 1980]; or because one is really focusing on the local electronic structure, as when addressing the intriguing features revealed by surface scanning techniques as Scanning Tunneling Microscopy (STM), Magnetic Force Microscopy (MFM) or even Angle-Resolved Photoemission Spectroscopy (ARPES).

The development of the recursive approach is closely connected with the problem of local electronic structure. The ideas behind this technique germinated during the early 1970's in the context of studies involving random and ordered alloys, moment formation and studies regarding metal surfaces[2]. The basic concepts were strongly inspired by Friedel: he introduced the Local Density of States (LDOS) in electronic structure calculations, replacing wave functions [Friedel, 1954], and realized that the LDOS exhibits an independence upon boundary conditions known as *invariance property*[3] [4] [Friedel, 1954; Heine, 1980].

The local point of view, besides allowing us to follow the historical path of the developments in the recursive technique, is of great avail in providing us with a notation and language most appropriate for the discussions that will follow. Recursion is useful in any problem (physical or not) regarding spectral properties of operators that, when defined on a countable basis, are relatively sparse, and anything that can be formulated as a linear eigenvalue problem will do. But, when presented with recourse to atomic orbitals, neighboring atomic shells, one-dimensional chains, and tight-binding models, the method acquires a very intuitive physical meaning, rather appropriate for the overall context of this work.

The recursive method is tailored for the calculation of LDOS. Physically the LDOS describes the effect of the rest of the solid on a given region: it *measures* the amplitude of each eigenstate within some energy E on a particular atom or bond. In terms of the eigenstates $\psi_n(r)$ and eigenenergies E_n of a given

[2] Heine [1980, Chap. VI] gives a very personal and interesting account of the relevant historical circumstances.

[3] This insensitivity to distant changes in the system, besides being of obvious relevance in studying local properties, contrasts with the unpredictably erratic behavior of the eigenstates under the same kind of perturbation.

[4] The concept of nearsightedness of the electronic system introduced by Kohn [1996] in the context of DFT is very closely related to this (see also cond-mat/0506687 for a more recent discussion).

Hamiltonian it is simply the DOS *projected* upon a given orbital:

$$n_r(E) = \sum_n |\psi_n(r)|^2 \delta(E - E_n)\,, \tag{2.1}$$

where $\psi_n(r) \equiv \langle r|\psi_n\rangle$ and r is a general coordinate representing a given orbital[5]. The fact that, as we will see below, $n_r(E)$ can be expressed in terms of a Green Function, permits a powerful generalization of the physical quantities that can be addressed, much beyond what (2.1) would seem to imply[6]. This, added to the fact that in solid-state theory much of what we need is presentable through some appropriate Green Function (GF), is a first hint of the broad capabilities of this tool.

2.1.3. Why Recur?

Quantum mechanical problems are traditionally formulated in terms of the Schrödinger equation and its solution [Fetter and Walecka, 1971]. In solid-state physics this entreats the calculation of a quantity of eigenstates and eigenvalues of the order of 10^{23} which, well, most of the time are rather useless, not to speak about the numerical difficulties in obtaining them in the first place! Solving for the greenian, being totally equivalent to the solution of Schrödinger equation, allows for a much more interesting approach. This happens because *small parts* of the GF can be computed independently of the unwanted remainder and, therefore, for the set of problems that can be cast as a few matrix elements of some greenian operator, recursion is arguably the best procedure, as it yields a convergent sequence of bounded approximants for those matrix elements.

Recursive algorithms, at use since at least Euclid of Alexandria, are highly advantageous for numerical tasks: they are easy to implement, of fast execution and generally economical in storage. A recursion scheme is almost a *machine ready* formulation of a problem. To this we add elegance of representation: the recursive method was the first to produce and make use of a Continued Fraction (CF) representation of the local GF [Kelly, 1980].

Tight-binding Hamiltonians, to which we devote our attention, are strikingly sparse in their matrix representation. Thus, it comes as no surprise the feeling of uneasiness one might encounter if having to apply generic diagonalization schemes to store, handle and diagonalize a matrix that has $\sim 100\,\%$ of zeros. More seriously, generic diagonalization routines put hard limits upon the treatable sizes of the model systems. In the recursion method the sparseness is key because repeated matrix-vector operations are the elementary operations. The spirit is to calculate nothing more than what is exactly needed to address the spectral problem. Such laconism is possible through the tailoring of an optimized basis of states, generated iteratively by the recursive procedure, and particularly fit for the calculation of *local* quantities like the LDOS in (2.1). How this can be achieved so efficiently constitutes the subject of the coming paragraphs.

In the sections that shall ensue, *all* the numerical examples, demonstrations and tests have been implemented by the author, all the plots in the figures resulting from these calculations.

[5] In most cases used along this work it coincides with the Wannier orbital of an atom at position r.

[6] Here *local* is an example of the use of the language of electronic structure to describe a *projected* spectral density.

2.2. The Chain Model and the Tridiagonalization Scheme

2.2.1. Transformation to a chain

The power of the recursive method resides in that calculating matrix elements of the greenian can be converted in a highly efficient iterative procedure through its representation in terms of a CF. In section 2.3 it will become obvious that such economy requires a tridiagonal — or Jacobi — representation of the Hamiltonian. Again, standard tridiagonalization algorithms like the Givens or Householder reduction [Press et al., 1992] turn out to be rather demanding for the solid-state applications of our interest, as far as storage and time resources are concerned. Let us then expose one of the most efficient ways to achieve the Jacobi form of an hermitian operator.

We consider discrete basis sets (usually infinite), that generate the Hilbert space, $\mathbb{H}$, of the problem, and will refer frequently to the *local* basis $\{\phi_0(r), \phi_1(r), \ldots, \phi_n(r), \ldots\}$ which, for convenience, we take as orthogonal and normalized[7]. They provide a definition for the matrix elements, H_{mn}, of $\boldsymbol{H}$:

$$\boldsymbol{H} = \sum_{mn} H_{mn} |\phi_m\rangle\langle\phi_n| \,. \tag{2.2}$$

The task is, hence, to construct a new basis $\{u_0, u_1, \ldots, u_n, \ldots\}$ in which $\boldsymbol{H}$ has the tridiagonal representation

$$\boldsymbol{H} = \begin{pmatrix} a_0 & b_1 & 0 & 0 & 0 & \ldots \\ b_1 & a_1 & b_2 & 0 & 0 & \ldots \\ 0 & b_2 & a_2 & b_3 & 0 & \ldots \\ \ldots & \ldots & \ldots & \ldots & \ldots & \ddots \end{pmatrix} . \tag{2.3}$$

We call such basis the *tridiagonal basis*. This form determines that only neighboring states in the tridiagonal basis are connected through the Hamiltonian:

$$\boldsymbol{H}\,|u_n\rangle = a_n|u_n\rangle + b_n|u_{n-1}\rangle + b_{n+1}|u_{n+1}\rangle \,. \tag{2.4}$$

This is the familiar situation encountered in one-dimensional chains with nearest neighbor hopping. Interestingly, it means that, since an hermitian operator can always be brought to tridiagonal form, every quantum-mechanical problem has some *effective chain model* representation. The sole information being $\boldsymbol{H}$, the determination of the unknown a_n, b_n, u_n proceeds iteratively as follows:

1. An *arbitrary*[8], normalized, state $|u_0\rangle$ is chosen as starter. This state determines trivially the value of a_0:

$$a_0 = \langle u_0 \,|\boldsymbol{H}\,|\, u_0\rangle \;; \tag{2.5}$$

2. In the next step we apply $\boldsymbol{H}$ to generate a new state, from which we remove the projection onto $|u_0\rangle$. This state, defined by $|\tilde{u}_1\rangle \equiv \boldsymbol{H}\,|u_0\rangle - a_0|u_0\rangle$, is by construction orthogonal to $|u_0\rangle$. Its

[7] This saves the introduction of an overlap matrix and causes no loss of generality, as the extension to non-orthogonal basis is straightforward [Haydock, 1980].

[8] Most of the times there are physical reasons which determine a specific choice as will be shown below.

norm and normalized counterpart are denoted by b_1 and $|u_1\rangle$:

$$|b_1|^2 = \langle \tilde{u}_1 | \tilde{u}_1 \rangle \tag{2.6a}$$

$$|u_1\rangle = b_1^{-1} |\tilde{u}_1\rangle \,. \tag{2.6b}$$

At this stage we have produced two matrix elements, a_0 and b_1, and a new basis vector, u_1.

3. The third and following iterations are completely analogous, and we give their general form. The a_n are always the diagonal elements, $\langle u_n \,|\boldsymbol{H}\,|\, u_n\rangle$, calculated with the vectors from the previous step. Having calculated the set of orthonormal states $\{u_0, \cdots, u_n\}$, the next one is obtained calculating $\boldsymbol{H}\,|u_n\rangle$, after which its components of u_n and u_{n-1} are projected out:

$$|\tilde{u}_{n+1}\rangle \equiv \boldsymbol{H}\,|u_n\rangle - a_n |u_n\rangle - b_n |u_{n-1}\rangle \tag{2.7a}$$

$$|b_{n+1}|^2 = \langle \tilde{u}_{n+1} | \tilde{u}_{n+1} \rangle \tag{2.7b}$$

$$|u_{n+1}\rangle = b_{n+1}^{-1} |\tilde{u}_{n+1}\rangle \,. \tag{2.7c}$$

The orthonormality condition only fixes $|b_n|^2$, an arbitrariness that we use to choose the b_n as positive reals, as is already implicit in (2.6) and (2.7).

Having said this, we can condense the complete recursion scheme with regard to a starting vector $|u_0\rangle$ as a tree-term recurrence with an initial condition:

$$b_0 |u_{-1}\rangle = 0 \,, \tag{2.8a}$$

$$b_{n+1} |u_{n+1}\rangle = \boldsymbol{H}\,|u_n\rangle - a_n |u_n\rangle - b_n |u_{n-1}\rangle \,. \tag{2.8b}$$

By construction, each $|u_n\rangle$ is orthogonal to its two predecessors. It remains to show that it is in fact orthogonal to *all* the preceding vectors[9]. The reader can convince itself easily of this by noting that any extra orthogonalizing terms on the r.h.s of (2.8b) will have a zero coefficient.

As the algorithm unfolds, the prescription (2.8) generates a new basis element and a pair of tridiagonal coefficients with each step. Aside from the orthogonalizing operation, each step involves only repeated multiplications of the previously calculated u_n by $\boldsymbol{H}$, which is a very fast operation for sparse matrices and tight-binding Hamiltonians. To this, we add the enormous advantage that a three-term recurrence in a carefully organized numerical implementation permits the calculation of $\{a_n, b_n\}$ keeping only two vectors in back-storage. These two features allow us to work with Hilbert spaces of much higher dimension than would be possible otherwise, an attractive feature for typical condensed matter problems. Regardless of the fact that we are building an orthonormal basis, we are not guaranteed to generate a tridiagonal basis that spans the whole original Hilbert space. This peculiarity is due to the fact that we had to choose a given u_0 upon which $\boldsymbol{H}$ is repeatedly applied, and, therefore, only states that belong to the invariant subspace generated by u_0 will appear in the chain. This is particularly important when $\boldsymbol{H}$

[9]For that we can take any $m < n-1$. We know that $\langle u_m | \tilde{u}_{n-1}\rangle = \langle u_m | \boldsymbol{H}\,|u_n\rangle = \left(\boldsymbol{H}\,|u_m\rangle\right)^\dagger |u_n\rangle$, and that, from (2.8b), the highest index state generated by $\boldsymbol{H}\,|u_m\rangle$ is $|u_{m+1}\rangle$. Therefore the last equality is zero since we assumed $m+1 < n$.

exhibits some symmetry: if u_0 is chosen belonging to an invariant subspace generated by a symmetry operation, the chain states will remain in that subspace. This determines whether the chain terminates before $N = \dim(\mathbb{H})$ iterations or not. If a state of zero norm is encountered, implying that $b_N = 0$, the recursion relation is interrupted and the chain terminates: the set of linearly independent states, $\mathcal{S} = \{u_n\}$, such that $H|u_n\rangle \in \mathcal{S}$ has been exhausted.

Let us now introduce some physical content in these general arguments. That the outcome of the recursion scheme depends on the choice for the initial state, means that, whereas $\boldsymbol{H}$ defines the model in a physical problem, u_0 poses the specific question. Take, for instance, the Heisenberg model that couples neighboring spins via an exchange energy. The total spin along the quantization axis, S_z, is a conserved quantity reflecting the underlying global rotational invariance of the problem. We can study the spectral properties of this model by focusing only upon a subspace of given S_z at a time, on which we apply the recursive approach [10].

Another important physical example for our purposes, is the case of non-interacting, tight-binding, electronic problems on a lattice, modeled by an Hamiltonian in the second quantized form:

$$\mathcal{H} = \sum_{i,\delta} t_{i,\delta}\, c_i^\dagger c_{i+\delta}\,, \tag{2.9}$$

where $c_i^\dagger$ is the operator that creates an electron at the local Wannier orbital $\phi_i(r) \equiv \phi(r - R_i)$, and $t_{i,\delta}$ the nearest-neighbor hopping (taken as constant below, for simplicity of discussion). Any quantum state of a single electron in this N-orbital system is of the form

$$|\Psi\rangle = \sum_{i=1}^{N} a_i\, |\phi_i\rangle\,. \tag{2.10}$$

Suppose we apply our recursive scheme to (2.9), choosing for initial state a single local orbital, ϕ_0. The starter for the tridiagonal basis is $u_0 \equiv \phi_0$ and, from (2.8), the next vector, u_1, will be a state with amplitude limited to the neighboring sites from the original orbital; the second will extend to the next nearest neighbors, and so on, in such a manner that the nth chain state spreads until the nth *"shell"* around the original orbital. This is clearly seen in Fig. 2.1, where the real space representation of selected chain states is shown. Three aspects are worth mentioning in this figure: (*i*) the amplitude distributes itself most significantly farther and farther from the central site (the starting orbital) as the index n of u_n increases; (*ii*) all the states exhibit the full point symmetry of the lattice about the origin, reflecting the fact that the starting vector is localized on a single site having an s-wave symmetry (it is also remarkable that in 2.1d the details of the lattice start to vanish and one can appreciate a coarse-grained s-wave symmetry); (*iii*) despite (*i*), states higher in the the chain still exhibit residual amplitudes at almost all inner shells whose purpose is to ensure orthogonality of the basis. For comparison and better appreciation of these remarks, we present in Fig. 2.2 the corresponding plots for an initial state of different symmetry, namely the state $u_0 \propto \phi_{(1,0)} - \phi_{(0,1)} + \phi_{(-1,0)} - \phi_{(0,-1)}$, for which the similarities and differences are self-evident.

We have thus come to the point where we know a numerically efficient procedure to obtain a tridiagonal representation of our Hamiltonian. In the way we learned that states obtained at higher recursion

[10] This turns out to be the only manageable way to perform exact diagonalization calculations on such problems.

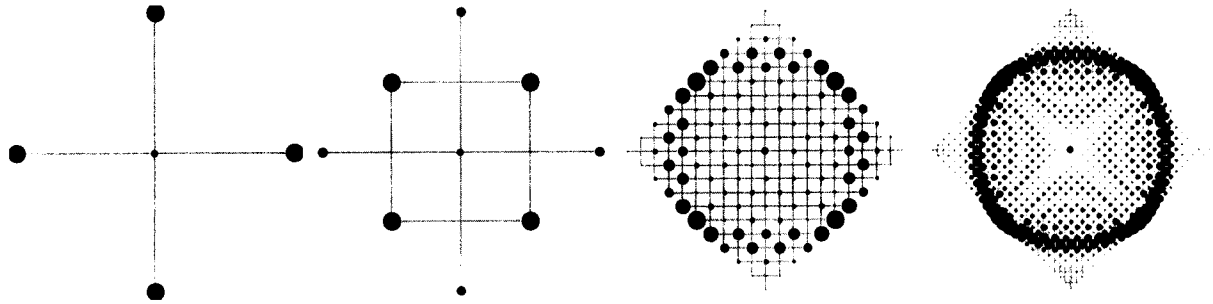

(a) State u_1 *(b) State u_2* *(c) State u_{10}* *(d) State u_{25}*

FIGURE 2.1 .: *Selected chain states for the tight-binding model* (2.9) *in 2D. The starting orbital occupies the central position (black). Each circle has a radius proportional to the amplitude of the state on that lattice site, and a color that identifies its sign: red for negative and blue for positive amplitudes.*

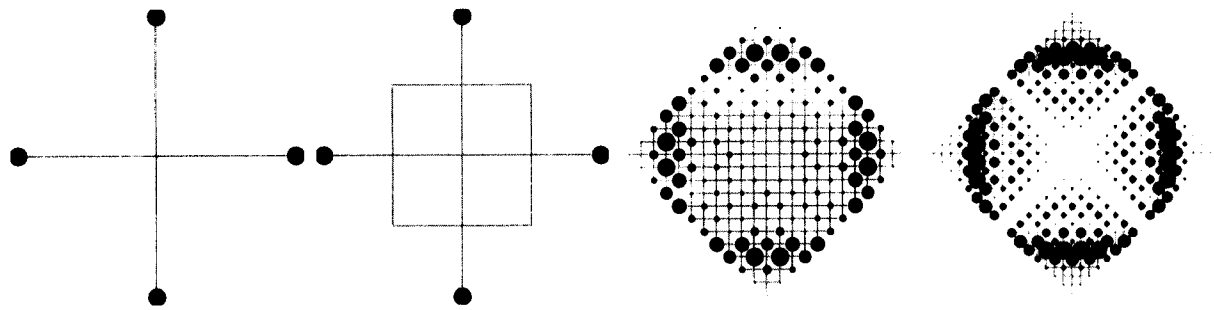

(a) State u_0 *(b) State u_1* *(c) State u_{10}* *(d) State u_{15}*

FIGURE 2.2 .: *An analogous plot to the one in Fig. 2.1, this time for a starting vector with p-symmetry* $u_0 \propto \phi_{(1,0)} - \phi_{(0,1)} + \phi_{(-1,0)} - \phi_{(0,-1)}$ *as described in the text. (d)*

steps have lesser and lesser weight on the local environment around u_0. Incidentally, the examples above demonstrate the usefulness of borrowing the language of local electronic structure in discussing this general technique.

2.2.2. Exact diagonalization and orthogonal polynomials

Although a pure analytical approach based on the recursion scheme can suit some specific problems, its numerical implementation and most real life situations require a finite-dimensional Hamiltonian matrix. We now consider that a finite chain of length N has been constructed and the tridiagonal form of the Hamiltonian

$$\begin{pmatrix} a_0 & b_1 & 0 & \dots & 0 & 0 \\ b_1 & a_1 & b_2 & \dots & 0 & 0 \\ 0 & b_2 & a_2 & \dots & 0 & 0 \\ \vdots & \vdots & \vdots & \ddots & \vdots & \vdots \\ 0 & 0 & 0 & \dots & a_{N-2} & b_{N-1} \\ 0 & 0 & 0 & \dots & b_{N-1} & a_{N-1} \end{pmatrix} \tag{2.11}$$

has been hence attained. We assume additionally, that such finite chain is the result of a truncation in the recursive procedure[11], thereby being an incomplete representation of the original Hamiltonian. Since all knowledge about a system is contained in its eigenstates and eigenvalues, the first thing one can do with the information at hand in (2.11) is to calculate those quantities. Diagonalization of a Jacobi matrix is a reasonably fast numerical procedure and (2.11) lends itself very suitable to direct application of standard numerical diagonalization routines. Although this is what suffices for practical purposes we will explore some important consequences of the Jacobi form. The secular equation in the tridiagonal basis reads

$$\boldsymbol{H}\,|\psi_\alpha\rangle \equiv \sum_n P_n(E_\alpha)\,\boldsymbol{H}\,|u_n\rangle = E_\alpha \sum_n P_n(E_\alpha)\,\boldsymbol{H}\,|u_n\rangle\,, \tag{2.12}$$

where $P_n(E)$ is the amplitude of the eigenstate belonging to the eigenvalue E on the chain state u_n. The eigenvalues, E, are the zeros of $\det(\mathbb{1}E - \boldsymbol{H})$, which is rather easy to calculate from (2.11). For that, let $\Delta_n(E)$ represent the principal leading minor [12] of order n of $\mathbb{1}E - \boldsymbol{H}$, and, in particular, $\Delta_N(E) = \det(\mathbb{1}E - \boldsymbol{H})$. Developing the determinant along the last line, we have

$$\Delta_N(E) = (E - a_{N-1})\Delta_{N-1}(E) - b_{N-1}^2\Delta_{N-2}(E)\,. \tag{2.13}$$

Given that all $\Delta_n(E)$ are determinants of tridiagonal matrices, the above relation is valid for any order principal leading minors, which results in a definition in terms of a recurrence relation with initial

[11] The other possibility is, naturally that $\mathbb{H}$ was originally finite and small enough that machine limitations would not call the practical need for such truncation.

[12] The k^{th} order principal leading minor of a $n \times n$ matrix $\boldsymbol{A}$ is the determinant of the first k rows and columns of $\boldsymbol{A}$.

conditions cast as

$$\Delta_0(E) = 1, \quad \Delta_{-1}(E) = 0 \tag{2.14a}$$

$$\Delta_n(E) = (E - a_{n-1})\Delta_{n-1}(E) - b_{n-1}^2\Delta_{n-2}(E)\,. \tag{2.14b}$$

The initial conditions guarantee that $\Delta_n(E)$ is a polynomial of order n in E and that the zeros of $\Delta_N(E)$ are the eigenvalues of (2.11). As to the eigenstates, if (2.8) is applied to the r.h.s of (2.12), one readily obtains another three-term recurrence relation for the P_n's (cfr. (2.8)):

$$b_{n+1}P_{n+1}(E) = (E - a_n)P_n(E) - b_nP_{n-1}(E)\,. \tag{2.15}$$

Eq. (2.15) is a second-order difference equation and, as such, needs two initial conditions. If we do not impose a normalization of the eigenstates, the $P_n(E)$ are undefined up to a constant factor, allowing us to choose a particularly adequate initial condition:

$$P_{-1}(E) = 0\,, \quad P_0(E) = 1\,, \tag{2.16}$$

in order to make $P_n(E)$ a real polynomial of order n in E. Not only that, but the $\{P_n(E)\}$ turn out to be a family of orthogonal polynomials[13]. To appreciate how this comes about, it suffices to expand the definition of orthogonality of the chain states, $\langle u_m|u_n\rangle = \delta_{mn}$, using the resolution of the identity for the vector space defined by $\{u_n\}$. Recalling that the eigenstates in (2.12) are not normalized we have:

$$\hat{1} = \sum_\alpha |\psi_\alpha\rangle \frac{1}{|\mathcal{N}_\alpha|^2} \langle\psi_\alpha|\,, \tag{2.17}$$

where the normalization is just

$$\mathcal{N}_\alpha = \left[\sum_n P_n(E_\alpha)^2\right]^{1/2}. \tag{2.18}$$

With the help of (2.16) a simpler expression for the eigenstates' normalization is $\mathcal{N}_\alpha^{-1} = \langle u_0|\psi_\alpha\rangle$, and therefore

$$\langle u_m|u_n\rangle = \sum_\alpha \langle u_m|\psi_\alpha\rangle \left|\langle u_0|\psi_\alpha\rangle\right|^2 \langle\psi_\alpha|u_n\rangle = \sum_\alpha \left|\langle u_0|\psi_\alpha\rangle\right|^2 P_m(E_\alpha)P_n(E_\alpha) \tag{2.19}$$

$$= \sum_\alpha \left|\langle u_0|\psi_\alpha\rangle\right|^2 \int P_m(E)P_n(E)\delta(E - E_\alpha)dE\,. \tag{2.20}$$

Resorting to the earlier definition of local density of states in (2.1), this can be cast simply as

$$\delta_{mn} = \int P_m(E)P_n(E)n_0(E)dE\ : \tag{2.21}$$

[13]Because (2.15) is of second order, there is another, linearly independent, solution, $\{Q_n(E)\}$, resulting from the choice $Q_0(E) = 0$, $Q_1(E) = 1$. This is the so-called irregular solution [Haydock, 1980, §11], and, with due differences, shares all the properties of $\{P_n(E)\}$.

the statement that $\{P_n(E)\}$ are, indeed, a family of orthogonal polynomials under a weight function, n_0, that coincides with the LDOS on the starting orbital. This conclusion allows, at once, the enumeration of rather important properties of the spectrum of (2.11).

First, is easily shown by inspection that the determinants $\Delta_n(E)$ are related to these polynomials via

$$\Delta_n(E) = P_n(E) \prod_i^n b_i \,, \tag{2.22}$$

with the consequence that the eigenvalues of (2.11) are also the zeros of $P_N(E)$[14]. Now, a general characteristic of orthogonal polynomials is the Sturm property of the zeros of successive $P_n(E)$'s: i.e., the zeros of $P_n(E)$ interlace the ones of $P_{n+1}(E)$[15], the same applying directly to the eigenvalues of our tridiagonal matrix[16]. For practical applications this Sturm property can be useful in the numerical calculation of the zeros of $P_N(E)$ (the eigenvalues), although in most cases one is better resorting to standard and optimized diagonalization routines applied to (2.11).

Second, an immediate consequence of the Sturm property is the absence of degeneracy in the eigenvalues (Appendix 2.A). Degenerate eigenvalues are always a consequence of some underlying symmetry – physical or merely abstract – in the Hamiltonian, and its absence in the tridiagonal representation indicates that the chain model is a somewhat symmetry-purged representation of the original problem. So, even for a problem with small $N = \dim(\mathbb{H})$ where one could easily obtain the N chain states, the chain would terminate after some fraction of N steps, every time the original problem is degenerate. This was already unveiled in page 12, where it was stated that the chain model contains only one symmetry – the symmetry of u_0. This is one of the trade-offs of the recursive technique for tridiagonalization: it is fast, economical and numerically stable, but we are always bound to our choice for u_0 — a particular realization of that old prosaic aphorism that guarantees the non-existence of such thing as a free lunch.

Third, and important to the extent of justifying the title of the present subsection, the extremal eigenvalues of the chain model (2.11) converge uniformly (and rapidly) to the eigenvalues of the original problem, provided care has been taken in handling the subtleties just mentioned with an appropriate choice of the starting state, u_0. This is again a trivial consequence of the Sturm property of the zeros of $\Delta_n(E)$, and the fact that the spectrum is bound in almost all problems of interest.

This last point is the essence of the Lanczos approach and what lies behind the designation *"exact diagonalization"* in the context of solid state problems. Many times the knowledge of the ground state and a few low-lying excited states suffices for a broad understanding of a physical system, but, just as often, the problem is unmanageable for a full diagonalization. The field of strongly correlated electronic systems has been rather prolific on that regard, with Hilbert spaces rising exponentially with the system size. For them, the local or short-range character of the interactions has meant that this so-called *"exact*

[14] This can be interpreted in terms of boundary conditions as follows: because the chain of size N terminates at the orbital u_{N-1}, the amplitude of any eigenstate on the hypothetical u_N (i.e. $P_N(E_\alpha)$) can only be zero.

[15] This is quite familiar in the context of quantum mechanics where the wavefunctions of successively excited states have interlaced zeros (seek no further than, for instance, the solutions for the 1D infinite square well problem), a simple consequence of the stationary Schrödinger equation reducing to a Sturm-Liouville differential problem.

[16] That is indeed a property one expects for *any* hermitian tridiagonal matrix, as hinted by the generality of the above developments.

diagonalization" scheme has been very fruitful in the obtention of exact ground states[17] for important models. The basic procedure for an *"exact diagonalization"* calculation is rapidly outlined as:

1. Choose some adequate u_0 in the Hilbert space of interest of the target problem (usually a random state to overcome the symmetry related problems above).

2. Use the recursive method to build an effective chain of size N, and monitor the values of its ground state as N increases.

3. Wait until the ground state of the chain has converged (which usually happens for incredibly less iterations than $\dim(\mathbb{H})$[18]) and terminate the chain. Transform the ground state of the converged/truncated chain back to the original basis and there you have the ground state of the original problem.

At first sight, the last step is easier said than done. The attraction of the recursive method, and what guarantees its usability in the above mentioned cases, lies on the economy that comes from the need to retain only the complete representation of two chain states during the recursion, which keeps storage requirements at $\mathcal{O}(N)$ as opposed to $\mathcal{O}(2^N)$, as is typically the case for $S = 1/2$ systems. Assume that the chain truncation occurs at the N^{th} state, and that the original vector space has $M = \dim(\mathbb{H})$. If the ground state, $|\Psi_0\rangle$, is wanted in the original basis $\{\phi_1, \phi_2, \ldots, \phi_M\}$, then a change of basis is required:

$$|\Psi_0\rangle = \sum_{n=0}^{N} g_n |u_n\rangle = \sum_{m=1}^{M} \gamma_m |\phi_m\rangle \,, \tag{2.23a}$$

$$\text{with} \quad \gamma_m = \sum_{n=0}^{N} \langle \phi_m | u_n \rangle \, g_n \,. \tag{2.23b}$$

The last result obviously requires the knowledge of *all* the chain states! Fortunately, it doesn't require them all at once. So, the only way to obtain the γ_m's is to rebuild the chain model[19], bookkeeping $\langle \phi_m | u_n \rangle$ at every step so that, in the end, all γ_m's are obtained. Compared to the sole calculation of the ground state energy, the execution time clearly doubles when we want to know the ground state proper, introducing another trade-off.

This method was used by the author to obtain the spin stiffness and spin correlations of the *XXZ* Heisenberg model with $S = 1/2$, and to investigate the scaling properties of this and other ground state properties [Gu, **VITOR M. PEREIRA**, and Peres, 2002]. It is widely used in current problems, either in the form presented here, or in one of its variations that, among others, include optimized algorithms, or extensions for finite temperature calculations [Aichhorn et al., 2003; Jaklic and Prelovsek, 1994].

[17] Or, more accurately, extremal eigenvalues and eigenstates with a controlled convergence.
[18] More on this will come in sec. 2.5.2.
[19] Using the same starter, u_0, naturally.

2.3. Local Density of States and Green Functions

The first attempts to calculate LDOS are attributed to Cryot-Lackmann [Kelly, 1980] who introduced [Cyrot-Lackmann, 1967, 1968, 1969] a method based on the calculation of the moments of the LDOS,

$$\mu_r^{(n)} \equiv \int E^n n_r(E) dE = \langle r | \boldsymbol{H}^n | r \rangle \tag{2.24a}$$

$$= \sum_{r_1, r_2, \ldots, r_{n-1}} \langle r | \boldsymbol{H} | r_1 \rangle \langle r_1 | \boldsymbol{H} | r_2 \rangle \ldots \langle r_{n-1} | \boldsymbol{H} | r \rangle \ . \tag{2.24b}$$

which involved the analytical calculation of as many moments as possible by, essentially, counting the returning paths to the target local orbital. Although the calculation of the first few is a feasible analytical task, for the higher order moments, the work quickly becomes daunting and numerical approaches are needed. Sadly enough, the problem of extracting the LDOS numerically from a finite set of moments is rather troublesome insofar as the absolute values of $\mu_r^{(n)}$ grow very rapidly, and, besides, a finite set of moments does not determine univocally a given LDOS. Amidst such difficulties the recursive technique emerged as a much more controlled and efficient way to get $n_r(E)$ from the corresponding local GF.

2.3.1. Green Functions

Given that the subject of Green Functions (GFs) in solid-state problems is extensively documented [Mahan] we limit our prose to a brief presentation of the quantities of relevance for our applications of this method, mainly for establishing the notation.

The Greenian or resolvent operator, $\boldsymbol{G}(E)$, associated with the Hamiltonian $\boldsymbol{H}$ is an alternative to the Schrödinger equation method of tackling a quantum mechanical problem. It is defined formally as

$$\boldsymbol{G}(E) = \frac{1}{E - \boldsymbol{H}} = \sum_\alpha |\psi_\alpha\rangle \frac{1}{E - E_\alpha} \langle \psi_\alpha | \,, \tag{2.25}$$

where the last equality results from a simple spectral decomposition. Of special interest for us are the matrix elements of the Greenian defined, as usual, through

$$G_{r,r'}(E) = \langle r | \boldsymbol{G}(E) | r' \rangle \ , \tag{2.26}$$

and, in particular, the diagonal matrix elements, that we designate generally by Green functions:

$$G_r(E) = \langle r | \boldsymbol{G}(E) | r \rangle = \sum_\alpha |\langle r | \psi_\alpha \rangle|^2 \frac{1}{E - E_\alpha} \,. \tag{2.27}$$

Dynamical properties are readily obtained from the so-called retarded Green functions which, in the energy representation used above, are obtained from $G_r(E)$ by adding a small imaginary part to the argument E[20]. From now on, we will be using the retarded counterpart of (2.25). Having established this, we drop the qualifier *retarded* and use $G_r(E)$ without the explicit imaginary part, always having in mind that it actually stands for $G_r^R(E)$ and the limit is implied.

[20] More precisely, the retarded GF is related to the GF through $G_r^R(E) = \lim_{\eta \to 0} G_r(E + i\eta)$.

The representation in (2.27) is very useful in that we readily conclude that the only singularities of $G_r(E)$ are simple poles at the (real) eigenvalues of $\boldsymbol{H}$. Since the residues at those poles are necessarily positive, the imaginary part of the retarded GF is positive whenever its complex argument E lies in the lower half of the complex plane. Given that the converse follows from hermiticity, one concludes that the zeros of $G_r(E)$ are also real and interspersed with the eigenvalues E_α [21].

The total DOS is related to the trace of $\boldsymbol{G}(E)$, and a simple application of the Cauchy identity allows one to present the LDOS as

$$n_r(E) = -\frac{1}{\pi} \lim_{\eta \to 0} \mathrm{Im}\left[G_r(E + i\eta)\right] . \tag{2.28}$$

The analytical properties enumerated above guarantee that n_0 is defined positive.

2.3.2. Continued Fraction Representation

Obtaining the local GF, $G_0(E)$, is straightforward in the tridiagonal basis. Recalling the definitions (2.25) and (2.26) for the GFs, using the orthogonal, tridiagonal basis generated by u_0, $\{u_0, u_1, \ldots, u_N\}$, and knowing that the representation of $\boldsymbol{H}$ in this basis is what was shown in (2.11), what is needed is but the first diagonal element of

$$\begin{pmatrix} E-a_0 & -b_1 & 0 & \ldots & 0 & 0 \\ -b_1 & E-a_1 & -b_2 & \ldots & 0 & 0 \\ 0 & -b_2 & E-a_2 & \ldots & 0 & 0 \\ \vdots & \vdots & \vdots & \ddots & \vdots & \vdots \\ 0 & 0 & 0 & \ldots & E-a_{N-2} & E-b_{N-1} \\ 0 & 0 & 0 & \ldots & -b_{N-1} & E-a_{N-1} \end{pmatrix}^{-1} . \tag{2.29}$$

It is useful to introduce the quantities $D_n(E)$, defined as the determinants of the submatrix obtained from $\mathbb{1}E - \boldsymbol{H}$ by removing its first n lines and columns [22]. $G_0(E)$ will simply be the first cofactor of the quantity between braces divided by its determinant. As we already know from Sec. 2.2.2, determinants of tridiagonal matrices have a peculiar recursive structure that arises here again. Namely,

$$G_0(E) = \frac{D_1(E)}{D_0(E)} = \frac{1}{E - a_0 - b_1^2 \dfrac{D_2(E)}{D_1(E)}} , \tag{2.30}$$

[21] A function with such analytical properties is called a Herglotz function.

[22] Notice that this is the opposite of the definition of the principal leading minors, $\Delta_n(E)$, introduced before. (See footnote 12 on page 14).

and is obvious that this structure will repeat itself in $D_2(E)/D_1(E)$ and subsequent quotients of the type $D_{k+1}(E)/D_k(E)$, resulting in the Continued Fraction expansion for $G_0(E)$:

$$G_0(E) = \cfrac{1}{E - a_0 - b_1^2 \cfrac{1}{E - a_1 - b_2^2 \cfrac{1}{\ddots \quad b_{N-1}^2 \cfrac{1}{E - a_{N-1}}}}} . \tag{2.31}$$

By analogy with eq. (2.30), we can define the quantities[23] $G_k(E) = D_{k+1}(E)/D_k(E)$, whereupon their recursive character is immediately exposed:

$$G_n(E) = \frac{1}{E - a_n - b_{n+1}^2 G_{n+1}(E)} , \tag{2.32a}$$

$$G_{N-1} = \frac{1}{E - a_{N-1}} . \tag{2.32b}$$

The single most important fact about this CF expansion is the fact that its coefficients are the same as the ones appearing in the tridiagonal representation of $\boldsymbol{H}$ (2.11), and in the recursion relations for the orthogonal polynomials $P_n(E)$ that define the eigenstates of the chain (2.15). Although we have been using N-sized chains, the case of interest in condensed matter problems is, usually, the infinite target solid, in which case, the CF expansion above extends indefinitely. In any way, those cases require in general the truncation of the chain at some point, and (2.31) above represents just an approximation to $G_0(E)$. For those cases, it is more appropriate to refer to the expansion in (2.31) as $G_0^{(N)}(E)$, which stands for the N^{th} order approximation to $G_0(E)$.

The relation between $G_0^{(N)}(E)$ and the orthogonal family of polynomials is more profound than this mere sharing of coefficients. In fact, it can be shown that this truncated approximation corresponds precisely to the Padé approximant $[N-1/N]$ to $G_0(E)$, which turns out to be simply

$$G_0^{(N)}(E) = \frac{Q_N(E)}{b_1 P_N(E)} , \tag{2.33}$$

where P_n and Q_n are the orthogonal polynomials introduced above (see Appendix 2.B). When compared to the CF expansion (2.31), this form is very transparent in what concerns the analytic structure of $G_0^{(N)}(E)$, namely, that all its poles are at the eigenstates of the chain and interlace its zeros:

$$G_0^{(N)}(E) = \frac{Q_N(E)}{b_1 P_N'(E)} \sum_\alpha \frac{1}{E - E_\alpha} . \tag{2.34}$$

Incidentally, since this corresponds to the LDOS

$$n_0^{(N)}(E) = \sum_\alpha \frac{Q_N(E_\alpha)}{b_1 P_N'(E_\alpha)} \delta(E - E_\alpha) \equiv \sum_\alpha w_\alpha \, \delta(E - E_\alpha) , \tag{2.35}$$

[23] These are, essentially, the local GFs for the sub-chains constructed from the original one by removing the first k states.

and since it was shown in one of the Appendices that $\forall\alpha : P_N(E_\alpha) = 0 \Rightarrow Q_N(E_\alpha) \neq 0$ one concludes, via (2.27), that all eigenstates of the chain have some finite weight on the initial state.

Another physically important property to retain from $G_O^{(N)}(E)$ brings us back to the question of the moments of the LDOS (2.24). One of the solutions that tries to avoid the problems raised at the opening of the current section in calculations involving moments relies upon the use of polynomial moments, instead of the actual $\mu_0^{(0)}$. The polynomial moments are defined as

$$\lambda_n = \int T_n(E) n_0(E) dE \,, \tag{2.36}$$

where $\{T_n(E)\}$ is a set of orthogonal polynomials under some known weight function. These do not grow as uncontrollably as $\mu_0^{(n)}$, and are efficient provided that their weight function has the same essential singularities as $n_0(E)$ [Haydock, 1980]. For example, the so-called *kernel polynomial method*[24] introduced by Silver *et al.* [Parker et al., 1996; Silver and Röder, 1997; Silver et al., 1996; Weisse et al., 2005] uses Chebyshev polynomials for $T_n(E)$. We can see here that the optimal polynomials for such procedure are precisely the $P_n(E)$ obtained from the chain model and, in this sense, an optimization of the polynomial moments method degenerates into the recursive scheme. Not only this but, the more important point we want to underline regarding the moments of the LDOS is that the convergent $G_0^{(N)}$ contains an information equivalent to the calculation of $2N$ moments[25]

Having said this we still face a problem. The inevitable truncation of the chain model in practical applications implies that our approximation for the LDOS is a sum of Dirac δ functions. This is nothing new, inasmuch as, strictly, it is the DOS of a finite system. The problem with that is that we want $G_0^{(N)}$ to be an approximation to the GF, $G_0(E)$, of a macroscopic system. In particular our approximation should retain the analytical features of $G_0(E)$, with special emphasis on the branch cut in $\mathrm{Im}\big(G_0(E)\big)$ responsible for the overall *smoothness* of the DOS characteristic of macroscopic systems. We, therefore, need some extra processing of the CF expansion.

2.3.3. Processing the Continued fraction

> *"Strictly, the LDOS for any finite cluster is a mess of spikes and one must not complain if that is what the calculations give. "*
>
> — **V. Heine**, The Recursion Method and its Applications [Heine, 1980, pp. 77].

What guarantee do we have that our approximation $G_0^{(N)}$ gets better as we increase the chain size, N ? At first one might be tempted to invoke the algebraic properties of the CF expansions of real numbers [Beskin, 1987] and conclude that, since $G_0^{(N)}$ is just a convergent, it should approximate monotonically some limiting value. Things are more elaborated when dealing with meromorphic functions. Haydock

[24] The kernel polynomial method is perhaps the closest competitor to the recursive technique in the calculation of projected spectral properties [Weisse et al., 2005].

[25] The mathematical justification is discussed at the end of Appendix 2.B. See also [Haydock et al., 1975, §3].

$$
\begin{aligned}
&|u_0\rangle = |\phi_0\rangle && \\
&|\tilde{u}_1\rangle = t|\phi_{-1}\rangle + t|\phi_1\rangle && \\
&|u_1\rangle = \big(|\phi_{-1}\rangle + |\phi_1\rangle\big)/\sqrt{2} && a_0 = \epsilon, \quad b_1 = \sqrt{2}t \\
&|u_2\rangle = \big(|\phi_{-2}\rangle + |\phi_2\rangle\big)/\sqrt{2} && a_1 = \epsilon, \quad b_2 = t \\
&|u_3\rangle = \big(|\phi_{-3}\rangle + |\phi_3\rangle\big)/\sqrt{2} && a_2 = \epsilon, \quad b_3 = t \\
&\cdots && \cdots \\
&|u_n\rangle = \big(|\phi_{-n}\rangle + |\phi_n\rangle\big)/\sqrt{2} && a_{n-1} = \epsilon, \quad b_n = t
\end{aligned}
$$

FIGURE 2.3 .: *Transformation to a chain applied to the 1D tight-binding model. The $|\phi_n\rangle$ represent the local Wannier orbitals at site n.*

showed that, for complex E, the recursion scheme gives a monotonically convergent sequence of approximations for the projected resolvent, in the case the $\{a_n, b_n\}$ can be computed exactly [Haydock, 1980; Haydock and Te, 1994]. When exact arithmetic is beyond reach (in a computer implementation) he showed that errors introduced in the computation of the states/coefficients decrease exponentially with their chain index [Haydock and Te, 1994]. This what we expect physically because $G_0(E)$, or $n_0(E)$, are local quantities and we know since Fig. 2.1 that the amplitude of u_n is concentrated within shells farther and farther away from u_0 as n increases.

2.3.3.1. The Square Root Terminator

For definiteness, we now turn to an example that can be treated exactly with the recursive technique: the infinite length tight-binding model (2.9) in 1D, with constant hopping t. At each site of the 1D lattice there is a local orbital ϕ_n, with $n \in \mathbb{Z}$, and a local energy, ϵ. We will calculate the LDOS on a single orbital, ϕ_0, chosen for convenience. Application of the recursive prescription of (2.8b), results in the parameters cast in Fig. 2.3. Apart from the first iteration, the $\{a_n, b_n\}$ settle immediately, allowing us to write (2.32) as

$$
G_0(E) = \frac{1}{E - \epsilon - 2t^2 g(E)}, \qquad g(E) = \frac{1}{E - \epsilon - t^2 g(E)}, \tag{2.37}
$$

with the converged part (independent of n) represented as $g(E)$. A general property of the recursive transformation, evidenced here in a somewhat extreme way, is that the b_n are of the order of the average hopping multiplied by the average number of neighbors. Therefore we should not expect the convergence of the approximants $G_0^{(N)}(E)$ to arise from the divergence or weakening in the magnitude of the tridiagonal coefficients. It is rather the contrary. The exact convergence in Fig. 2.3 comes as a great convenience providing a mean to solve the infinite continued fraction for its infinite convergent. In fact,

$$
g_0(E) = \frac{1}{2t^2}\left\{E - \epsilon - \sqrt{(E-\epsilon)^2 - 4t^2}\right\}, \tag{2.38}
$$

and we obtain immediately, via (2.28):

$$n_0(E) = \begin{cases} \frac{1}{\pi} \frac{1}{\sqrt{(E-\epsilon-2t)(E-\epsilon+2t)}} & , -2t < E-\epsilon < 2t \\ 0 & , \text{otherwise,} \end{cases} \tag{2.39}$$

for the exact LDOS at ϕ_0 which, because the system is translationally invariant, coincides with the exact DOS for this problem[26]. This last point is completely general and shows that the calculation of the LDOS yields at once the total DOS in *ordered* problems. As the reader familiar with the classical orthogonal polynomials might have already suspected from the recursion coefficients in Fig. 2.3, the chain transformation of this problem corresponds to the solution of the recursion relations for the Chebyshev polynomials of the first kind, $T_n(E)$ [Arfken, 1970, Chap. 13], a statement readily confirmed by the weight function $n_0(E)$ in (2.39) with $t = 1/2$ and $\epsilon = 0$.

This example is of high relevance in that it exemplifies one of the ways in which the CF expansion can be processed (in this case solved exactly). Indeed, the common situation for a broad class of problems is that the $\{a_n, b_n\}$ tend to converge for asymptotic values — say a_∞ and b_∞ — if $n_0(E)$ has a connected support, that is, if there are no band gaps. Such circumstance, implies that, in (2.32) the CF can be terminated not with G_{N-1} but, instead, by effectively replacing G_N by g_0 above and, again, the chain can be solved exactly. The asymptotic $g_0(E)$, with ϵ replaced by a_∞ and t by b_∞, goes by the name of *square root terminator* for the Continued Fraction, a terminology that reflects the fact that $g_0(E)$ is appended at some iteration of the CF, thus allowing the practical termination of the CF. This type of procedure was the one originally introduced by Haydock *et al.* [Haydock et al., 1972], not only because the *"experimental"* knowledge at the time supported the stated asymptotic behavior of $\{a_n, b_n\}$, but mostly because the terminator $g_0(E)$ readily solves the problem of the analytical structure of the GF. In particular it introduces the branch cut in the real energy axis needed to obtain a smooth DOS characteristic of macroscopic systems. In practical terms, the DOS obtained with a square root terminator corresponds to a semi-circular DOS (the imaginary part of g_0), upon which the extra, non-converged, $\{a_n, b_n\}$ add the structure needed to reproduce the LDOS of the system. The role of the terminator is, roughly speaking, to define the center of the band (a_∞) and its bandwidth ($4b_\infty$), the profile of $n_0(E)$ being contained in the local information carried by the tridiagonal coefficients.

A working example of these aspects is presented in Fig. 2.4 for a tight-binding Hamiltonian in a 3D square lattice. This is a non-trivial example[27] but the figure leaves no doubt as to the convergence of the coefficients b_n, and to the fact that just a few iterations suffice to delineate the distinctive features of the DOS, which then becomes indistinguishable from the actual result within a couple dozen steps. In particular, the van Hove singularities are reproduced exactly at the band edges, and with remarkable accuracy at $|E| = 2$. The accuracy at the band edges derives from the choice of the square root terminator, which carries its square root singularity to the final LDOS, thus rendering it generally adequate for DOS calculations in 3D systems. Another, more subtle, aspect regarding the numerical DOS plotted in Fig. 2.4

[26] A subtle detail deserves a comment. Eq. 2.38 is quadratic in $g(E)$ and a selection of the solution was made in 2.39. The choice is determined by the fact that, being itself a GF, $g(E)$ needs to have the correct analytical properties mentioned in (sec. 2.3.1), which are satisfied by only one of the solutions.

[27] In the sense that, contrary to the case in Fig. 2.3, the analytical calculation of the $\{a_n, b_n\}$ soon becomes impossible.

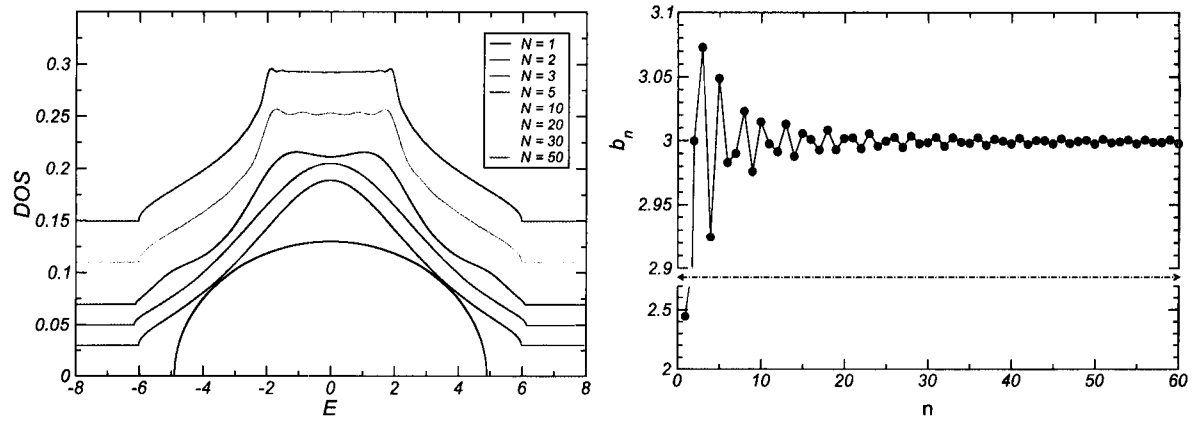

FIGURE 2.4 .: *Numerical results for the 3D tight-binding example discussed in the text ($t = 1$). (a) The LDOS calculated by appending a square root terminator after N iterations (for clarity of the presentation, the vertical axis was shifted for $N > 1$). (b) The corresponding chain coefficients b_n (notice that the vertical axis was truncated for clarity).*

is the fact that the van Hove singularities are well reproduced without noticeable Gibbs oscillations. This differs from what would be obtained via standard polynomial approximations[28], and the reason lies in that the recursion method provides the optimal orthogonal family for polynomial interpolations, as aforementioned at the end of sec. 2.3.2. Finally, the 2D case is also provided in Fig. 2.5 for comparison.

2.3.3.2. Delta Function Broadening

Going back to the problem of having a truncated chain, an alternate way to obviate the difficulties that the form in eq. (2.35) presents is to *broaden* the set of δ functions. This is achieved with the introduction of a finite, but small, imaginary part for the energy E in the expression for the GF (2.34), akin to the introduction, *by hand*, of a finite lifetime for the eigenstates. In practice this means that an approximation for the GF is obtained from the truncated form in (2.32) by replacing $E+i\,\Gamma$ for E. As a result, eq. (2.35) is transformed to a sum of Lorentzians of half-width 2Γ, thereby lending some degree of smoothness to the resulting DOS.

An explicit demonstration of this expedient at work is presented in Fig. 2.6 for the 3D tight-binding on the square lattice. The trade-offs involved in this smoothing procedure are obvious. A finite chain of size N has an average energy resolution, of which a rough estimation is $\Delta E \sim w/N$, where w is the bandwidth of the target system. Applying this estimate to the example in the figure built with $N = 80$ chain states, we get $w/N = 12/80 \sim 0.15$. Accordingly, it doesn't come as a surprise that the DOS obtained with a broadening $\Gamma = 0.1$ (and smaller) appears too spiky, particularly at the band center[29]. With $\Gamma = 0.5$, on the other hand, the resulting approximation for the DOS appears clearly *over-smoothed*, missing essentially all the relevant features. By construction, sharply defined band edges and van Hove

[28]For example, in the *kernel polynomial method* that relies on a Chebyshev expansion of the Dirac-δ function, Gibbs oscillations at singularities are a known pathology that has to be handled by the introduction of seemingly arbitrary damping factors to smooth this effect [Silver et al., 1996].

[29]Remember that the eigenstates of the finite chain tend to be more dense at the extremal energies, a consequence of the Sturm property of the zeros of $P_n(E)$ (Appendix 2.A)

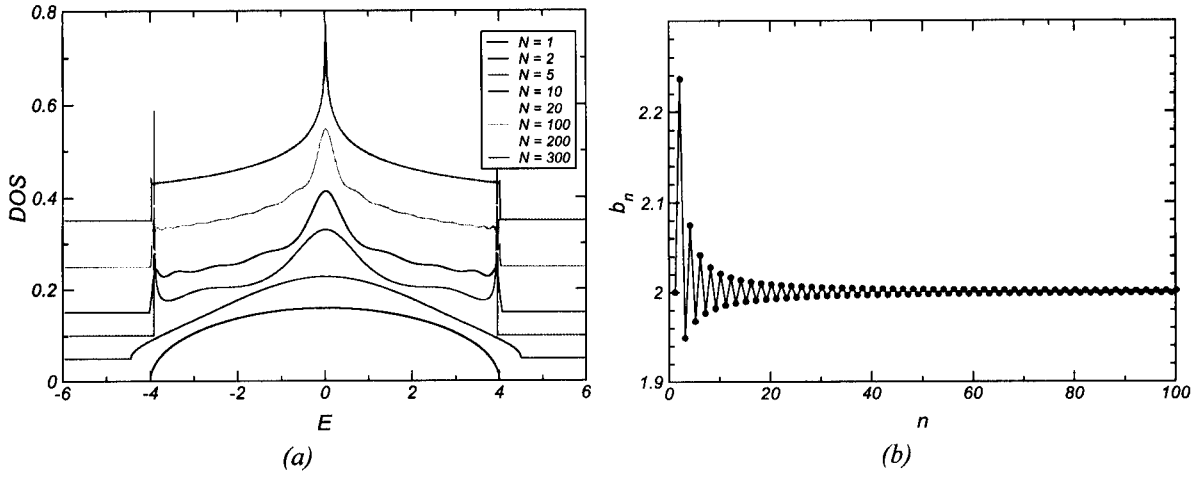

FIGURE 2.5.: *Numerical results for the 2D counterpart of the tight-binding example presented in Fig. 2.4 ($t = 1$). (a) The LDOS calculated by appending a square root terminator after N iterations (for clarity of the presentation, the vertical axis was shifted for $N > 1$). (b) The corresponding b_n coefficients.*

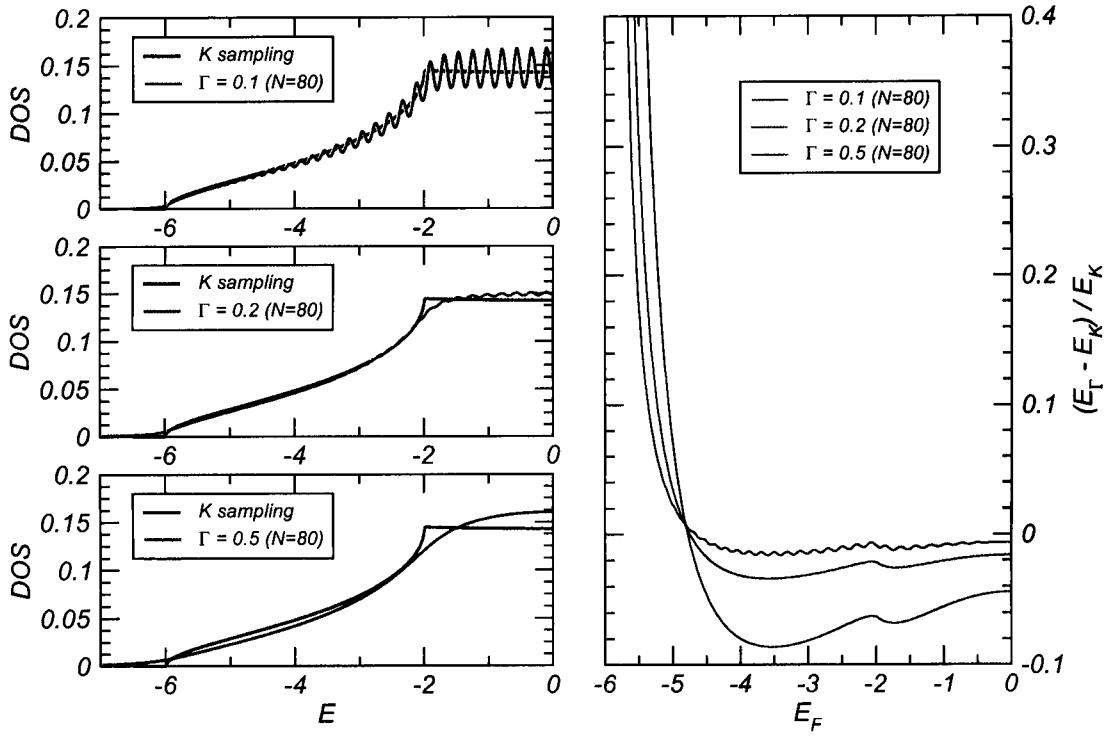

FIGURE 2.6.: *(left) The DOS for the 3D tight-binding on the square lattice obtained for different broadening widths, Γ, of a chain truncated at $N = 80$ ($t = 1$). For comparison, each panel also displays the DOS obtained from a sampling of the k-space with 2000^3 reciprocal space cells. (right) The relative difference of energies calculated with broadening and with k-space sampling.*

singularities are beyond reach, as is the reproduction of any features with characteristic energies smaller than $\sim \Gamma$. This arises from the limit that the chain length imposes on the resolution of the broadened DOS, with the consequence that higher resolutions imply higher chains. It is remarkable, though, that integrated quantities, out of which most physics arises, are much more controlled, in the sense illustrated by the right panel of Fig. 2.6. The energy

$$E(E_F) \equiv \int_{-\infty}^{E_F} n(E) E dE \tag{2.40}$$

is evaluated for the different broadenings and is then relatively compared with the, for all purposes, exact result obtained from a sampling on the k-space. If $\Gamma = 0.1$ the relative error is within $\sim 1\%$ for the most part of the band, and is clear that, despite the spikier structure of the DOS, the smaller the Γ, the better the approximation to the exact result. We will come back later to the question of integrated quantities and their convergence.

For the cases where the square root terminator becomes unwieldy, this broadening scheme is the easiest approach to extract an overall profile of the DOS, and other physical quantities depending on it. But care is always advised in the conclusions drawn.

2.3.3.3. Integrated Quantities and Re-differentiation

That different methods for processing the continued fraction are being presented here somehow reflects the circumstance that the LDOS (or GF) obtained from the finite approximants to the CF is not a stable convergent quantity for real energies. The convergence of the approximants $G_0^{(N)}(E)$, alluded before for complex E, fails if E rests on the real axis [Haydock, 1980; Haydock and Te, 1994]. Nothing unexpected, though. Just have present what happens to the LDOS when one goes from a chain of size N to a chain of size $N+1$: all the eigenvalues are displaced (always the Sturm property) introducing infinite changes in the LDOS at those energies, or, equivalently, on the GF near its poles. As generally happens with quantities expressed in terms of Dirac δ functions, their definition begs the definition of some associated integrated quantity. In solid-state problems the DOS is not habitually an aim *per se*, but rather a mean to achieve some physically measurable property, defined as

$$F = \int n_0(E) f(E) dE\,, \tag{2.41}$$

of which the total energy is an example corresponding to $f(E) = E$. It turns out that F above is a stable convergent quantity, provided that $f(E)$ is a *well behaved* function [Haydock, 1980; Nex, 1978].

There are two distinct situations regarding the expression above: the integral can be over the whole support of $n_0(E)$, or it can be within a defined interval. The first case is almost trivially understood by inserting eq. (2.35) in the last one:

$$F = \int n_0(E) f(E) dE = \sum_{\alpha=1}^{N} w_\alpha f(E_\alpha)\,. \tag{2.42}$$

This corresponds to a general Gaussian quadrature formula whose weights are obtained from the or-

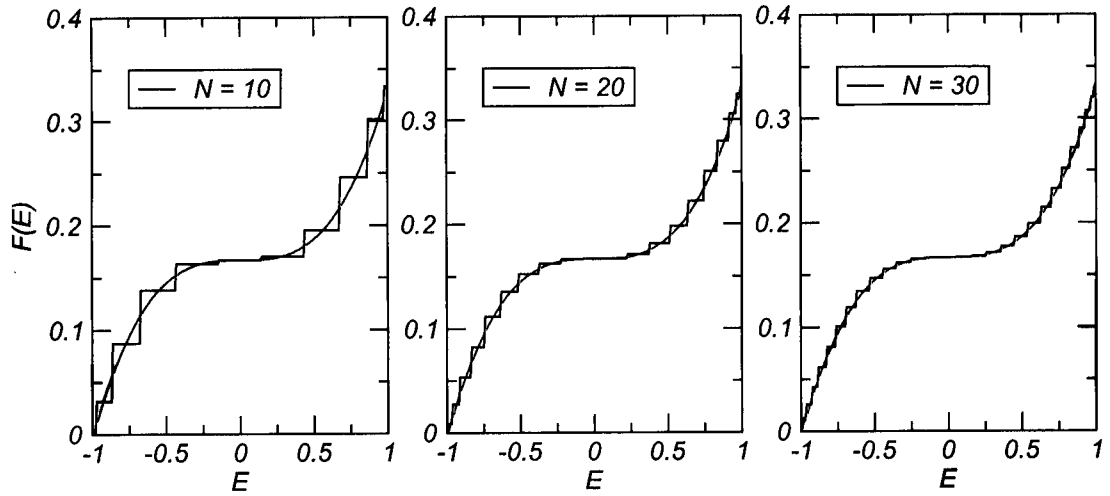

FIGURE 2.7 .: *An example of the crude approximation to* $F(E) = \int^E \epsilon^2 n_0(\epsilon) d\epsilon$ *via the naïve quadrature discussed in the text, for* $n_0(\epsilon) = \frac{1}{2}\Theta(\epsilon + 1)\Theta(1 - \epsilon)$. *the continuous (red) line denotes the exact result for* $F(E)$. *Several chain lengths,* N, *were used for comparison.*

thogonal family $P_n(E)$, just as in Legendre's or other classical Gaussian quadrature scheme[30]. The convergence of F then follows as in the classical quadrature problem, and all known properties of the Gaussian quadrature remain valid.

The case of indefinite integrals of the form

$$F(E_F) = \int_{-\infty}^{E_F} n_0(E) f(E) dE \tag{2.43}$$

is more interesting, not so straightforward, and deserves more attention. A crude estimate of $F(E_F)$ could be obtained from (2.42) restricting the terms of the sum that satisfy $E_\alpha < E_F$. This would yield a very crude approximation indeed, for $F(E)$ would exhibit a square step structure, with plateaux between the E_α, as depicted in Fig. 2.7. The solution, adapted from the classical moments problem to the language of the recursive technique by Nex [1978], hinges upon a very smart trick. The step-like structure that $F(E)$ would acquire from that naive generalization of the quadrature to an indefinite integral is a simple consequence of the fact that, in (2.42) the nodes are fixed, whereas E_F can be anything. How useful would it be if one could have a node that moves along the upper limit E_F? Here is how to achieve that. A given chain characterized by $\{a_0, \ldots, a_{N-1}\}$ and $\{b_1, \ldots, b_N\}$ determines a set of fixed nodes. An extra node is forced to lie at E_F, and, since an extra node implies a longer chain, a fictitious state, a_N^*, is added to the chain (that now has $N + 1$ states). From the recursion relations for $P_{N+1}(E)$ (2.15), a node at E_F is present if one requires

$$a_N^* = E_F - b_N P_{N-1}(E_F)/P_N(E_F)\,. \tag{2.44}$$

Therefore the result is a $N + 1$-sized chain whose associated spectrum, following from $P_{N+1}^*(E) = 0$,

[30]This is a Gaussian quadrature in the strict sense. Since Jacobi and Christoffel, it is known that the optimal abscissas for the N-point Gaussian quadrature formula are precisely the roots of the orthogonal polynomial for the same interval and weighting function: i.e., the eigenstates, roots of $P_N(E)$, orthogonal under $n_0(E)$.

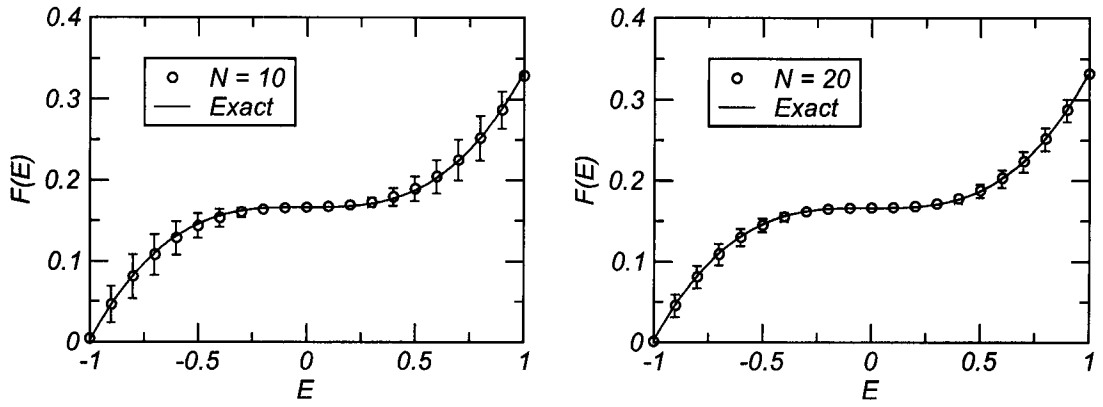

FIGURE 2.8 .: *An example of the proper quadrature applied to* $F(E) = \int^E \epsilon^2 n_0(\epsilon) d\epsilon$, *with* $n_0(\epsilon) = \frac{1}{2}\Theta(\epsilon + 1)\Theta(1 - \epsilon)$. *Two chain lengths,* $N = 10$ *and* $N = 20$, *were used. The continuous (red) line denotes the exact result and the circles, with respective error bars, represent the results of quadrature. Notice how* $N = 10$ *is sufficient to render the quadrature quite indistinguishable from the exact result. Notice also that the error bars differ approximately by half between the two cases.*

determines the nodes for a Gaussian quadrature to (2.43). The associated weights are obtained from the new chain exactly in the same way as the ones in (2.42). Eq. (2.42) can now be applied, discarding again the terms with $E_\alpha > E_F$, and the dubious status[31] of the node at E_F will be used to define precise upper and lower bounds for $F(E_F)$ [Nex, 1978]:

$$F_-(E_F) = \sum_{E_\alpha < E_F} w_\alpha^* f(E_\alpha) \tag{2.45a}$$

$$F_+(E_F) = \sum_{E_\alpha < E_F} w_\alpha^* f(E_\alpha) + w_F^* f(E_F)\,, \tag{2.45b}$$

the approximate result being defined as the average of the above bounds:

$$F(E_F) = \sum_{E_\alpha < E_F} w_\alpha^* f(E_\alpha) + \frac{1}{2} w_F^* f(E_F)\,. \tag{2.46}$$

Fig. 2.8 shows the result of this procedure applied to the same example used in Fig. 2.7. The first virtue of this result is the appearance of a majorant and minorant for the approximated $F(E_F)$, allowing the introduction of error bars in the resulting curve. The second virtue is the very good approximation attained with a reduced number of chain states. In fact, despite the error bars, the points in Fig. 2.8 rest on top of the exact curve even for $N = 10$, a situation verified in general whenever $f(E)$ is a smooth function. Another example, perhaps physically more meaningful, is the one shown in Fig. 2.9, where the integrated DOS, $\left(N_0(E) = \int^E n_0(\epsilon) d\epsilon\right)$, is presented. This last particular choice is deliberate. The third virtue of the quadrature formula (2.46) is the smoothness of the resulting $F(E_F)$, in opposition with the situation in Fig. 2.7. This is rather convenient as one can calculate the integrated DOS using quadrature and re-differentiate the result to obtain the DOS proper. As a matter of fact, in those cases where one does not know anything a priory about the band under analysis, other than the chain coeffi-

[31] This is related with the fact that the last term retained in the quadrature sum is $\int^{E_F} w_F f(E)\delta(E - E_F) dE$.

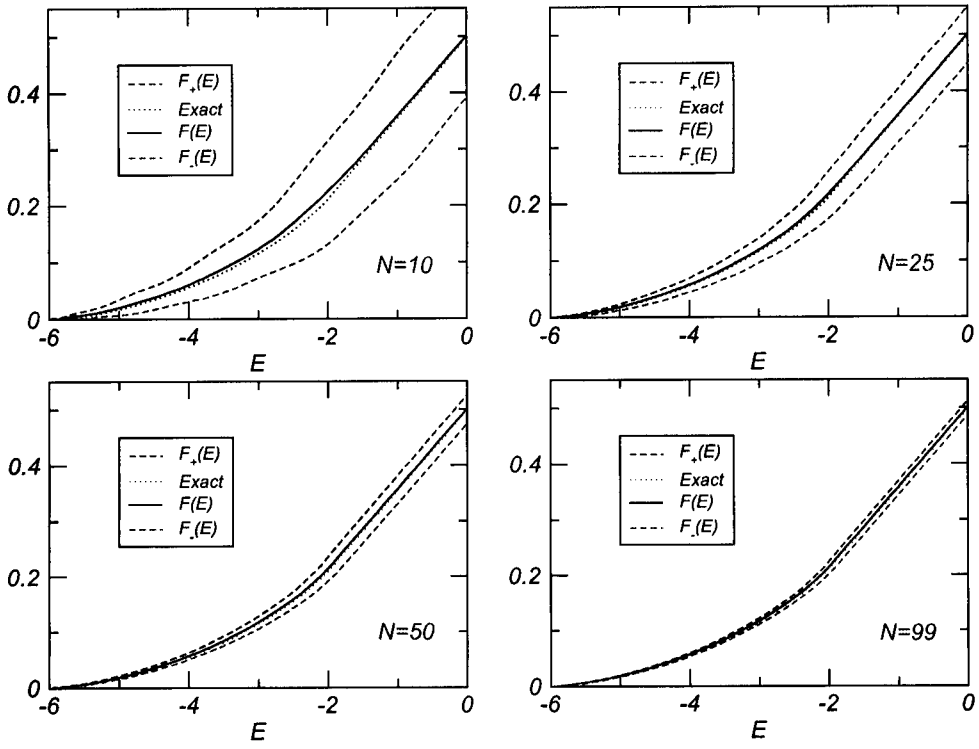

FIGURE 2.9.: *The integrated DOS* $\left(F(E) \equiv N_0(E) = \int^E n_0(\epsilon)d\epsilon\right)$ *for the tight-binding model on a 3D square lattice, at different chain lengths, N, obtained by quadrature. The shadowed region is limited by the upper and lower bounds* $F_{\pm}(E)$ *defined in* (2.45). *The (red/dotted) curve labeled* exact *was obtained from a sampling in K-space. Notice how it cannot be distinguished from the approximate* $F(E)$ *for* $N = 25$ *and above.*

cients $\{a_n, b_n\}$ it generates, this re-differentiation method is certainly the most adequate. Returning to our ubiquitous example, the data in Fig. 2.9 concerning $N_0(E)$ can be differentiated yielding the curve shown in 2.10a. Notice how the exact result is remarkably reproduced, despite the additional numerical differentiation operation, and using no information other than the $\{a_n, b_n\}$. The sole exceptions are the immediate vicinity of the singularities, which, even so, are accounted for within the error bars obtained by differentiation of the $F_{\pm}(E)$. The power of this approach for the estimation of DOS is better appreciated when the band is gapped. One such case is depicted in 2.10b for a DOS exhibiting two regions of abrupt gaps [32]. A self-evidence that would qualify as a fourth virtue of the quadrature approach regards the fact that, in those cases where the DOS is not a goal, its calculation is naturally bypassed in the calculation of integrated quantities.

Amongst the three techniques presented here for the extraction of the DOS from the finite approximants $G_0^{(N)}(E)$ the last two, δ function broadening and quadrature, are the ones that do not assume anything about the DOS, thereby having a broad scope of application. The square-root termination is specific of bands with connected support. The concept of terminator has a very precise physical meaning. A terminator is nothing but the Green Function associated with a semi-infinite tight-binding chain for which we know the exact behavior of the coefficients $\{a_n, b_n\}$ *ad infinitum*, and for which we can

[32]The exact expression for the DOS in 2.10b is, apart from a normalization factor, $\cos(\pi x/6)\left[\Theta(3-x)\Theta(-2+x) + \Theta(1-x)\Theta(x) + \Theta(3+x)\Theta(-1+x)\right]$. In this case we did not start from a given model Hamiltonian, but departed instead from this expression for the DOS, for which the $\{a_n, b_n\}$ coefficients were constructed using the polynomials orthogonal under it. Then we applied the quadrature and differentiated to obtain Fig. 2.10b.

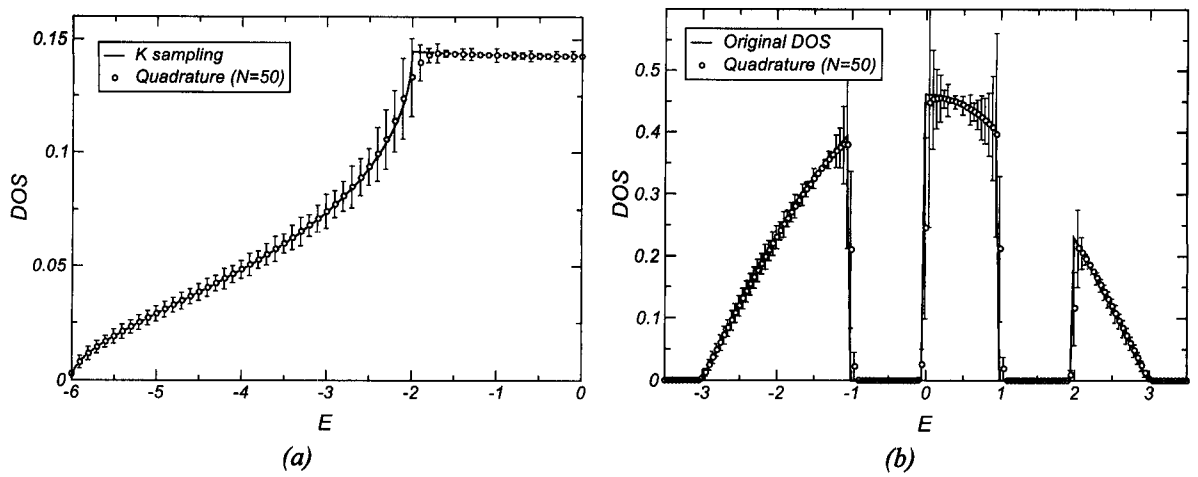

FIGURE 2.10 .: *(a) The DOS for the tight-binding model on a 3D cubic lattice obtained by differentiation of $N_0(E)$ in Fig. 2.9. (b) The same procedure applied to an arbitrary band with two gaps[32]. Notice that, in both cases, although the error bars are relatively high, the expected value for the DOS (the circles) is barely distinguishable from the exact one throughout most of the domain.*

solve the infinite CF expansion in some closed form. Hence, appending a terminator to the chain model representation of a physical problem corresponds to reducing the infinite system to a local region of interest plus an infinite, exactly solvable, system, with a matching boundary condition, as illustrated schematically in Fig. 2.11. The matching is essential as, otherwise, it would correspond to the introduction of an artificial potential at the boundary and strong scattering occurs. The manifestation of this is the appearance of strong spikes interspersing the resulting DOS. This is one of the reasons that render the square root terminator discussed above rather useless in systems with gaps. Possible generalizations for those cases are to be addressed next.

2.4. Gapped and Disordered Systems

2.4.1. Singularities and Asymptotic Behavior of the Continued Fraction

The complete set of tridiagonal coefficients, defining an alternative representation for a given Hamiltonian, encodes all the information about it. The tailoring of the tridiagonal basis in such a way that the

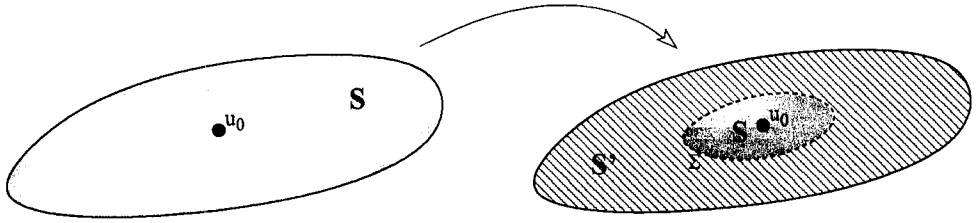

FIGURE 2.11 .: *Schematic representation of the physical meaning of a terminator for the CF in the recursive method. In the calculation of the projected DOS, or local GF, on u_0 using a terminator one retains a locally relevant portion of the system of interest, $\mathbf{S}$, and connects a solvable chain that matches the original one at the boundary Σ.*

probability density for successive u_n gets distributed farther and farther away from the starting state has the consequence that, at least for ordered systems, the $\{a_n, b_n\}$ reach some asymptotic regime. The cases discussed above are representative of the simplest of such regimes: a damped oscillation converging towards limiting values $\{a_\infty, b_\infty\}$. In reality, the asymptotic regime conceals a richness much beyond this.

First, the damped oscillations reflect the presence of internal singularities in $n_0(E)$. The period of oscillation is related to the position of the singularities within the band, while the decaying rate to its strength [Gaspard and Cyrot-Lackmann, 1973; Hodges, 1977; Luchini and Nex, 1987]. This is important because, on one hand, for the cases where the band structure is totally unknown, one can identify the type of singularities just from the observation of the asymptotic regime, and, on the other, knowledge of an analytic form for the asymptotic behavior allows the construction of much more appropriate terminators. This has been pursued by Magnus [1984] who, studying classical orthogonal polynomials associated with singular weight functions, was able to systematize some analytical expressions for the asymptotic of $\{a_n, b_n\}$ for several types of singularities. This raises the possibility, at least in principle, of constructing chain models asymptotically equivalent to the physical system of interest, but with a precisely known structure of coefficients that would allow the computation of specifically tailored terminators. The proposal of a *general terminator* for the recursion method [Haydock and Nex, 1985] follows closely along these same lines.

Second, as was early realized [Gaspard and Cyrot-Lackmann, 1973], this convergence only applies to single connected band structures. Multiband systems are characterized by coefficients oscillating endlessly in a somewhat predictable way [Turchi et al., 1982]. For them, internal van Hove singularities have a secondary role, being overshadowed by the influence of the relative position and spectral weight of the multiple bands in determining the profile of $\{a_n, b_n\}$.

2.4.2. Band Gaps and the asymptotic problem

Consider a LDOS, $n_0(E)$, consisting of two symmetric square steps, separated by a sizeable gap, as shown in the lower panels of Fig. 2.12. Building the orthogonal family $\{P_n(E)\}$ associated with it allows us to obtain the recursive coefficients show in Fig. 2.12a,b. As expected, b_n oscillates perpetually between two limiting values, which poses an immediate problem for the square root termination: which of the two limiting values should one consider in the terminator? Since in the simple square root termination (sec. 2.3.3.1) b_∞ determines the bandwidth, one should choose the largest asymptotic value. But the result is terrible, as Fig. 2.12c documents, with the resulting DOS ending *contaminated* by strong spikes[33]. This example is a very particular case of the periodicity imposed on the coefficients by the band gaps, happening only for a symmetric, single gap, band. A periodic behavior of the coefficients in general determines that, having reached the asymptotic regime after, say, N chain states, the CF expansion

[33] If the terminator is applied after the N-th iteration there will be always N spikes centered at the zeros of $P_N(E)$. These spikes are therefore just the δ's expected from a truncated $G_0^{(N)}(E)$, broadened by the imaginary part of the terminator. This is completely general, independent of the shape and position of the bands.

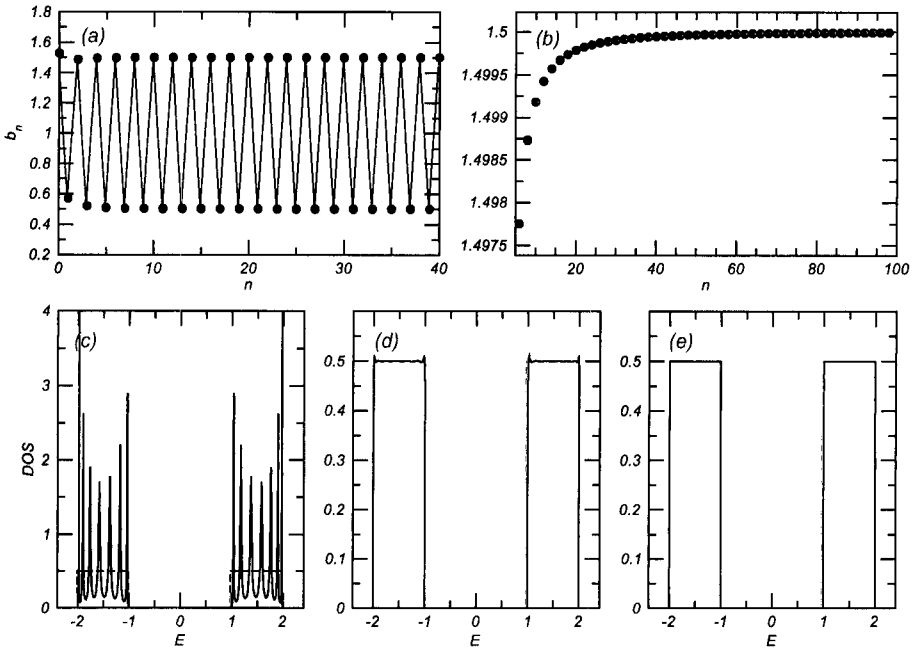

FIGURE 2.12 .: *Recursive coefficients associated with a band consisting of two symmetric square steps (the dashed/red curves in the lower of panels). (a) The coefficients b_n exhibit an oscillating behavior, converging towards two well separated values. (b) A detail of the convergence of b_n to the upper limit. (c) The square root terminator applied after 15 iterations. Notice the 14 spikes[33] in the DOS obtained with this terminator, and how it completely fails to reproduce the shape of the exact DOS. This should be compared with the results from the periodic terminator* (2.49) *using 15 (d) and 51 (e) iterations.*

(2.32) acquires the form

$$G_0(E) = \cfrac{1}{E - a_0 - b_1^2 \cfrac{1}{E - a_1 - b_2^2 \cfrac{1}{\ddots \quad b_{N-1}^2 \cfrac{1}{E - a_{N-1} - b_N^2 t_m^N(E)}}}}, \tag{2.47}$$

where $t_m(E)$ is the periodic *tail* of the CF, and m is the period ($a_{n+m} = a_n$):

$$t_m^N(E) = \cfrac{1}{E - a_N - b_{N+1}^2 \cfrac{1}{E - a_{N+1} - b_{N+2}^2 \cfrac{1}{\ddots \quad b_{N-1}^2 \cfrac{1}{E - a_{N+m-1} - b_{N+m}^2 t_m^N(E)}}}}. \tag{2.48}$$

This is nothing but the generalization of (2.37) and, $t_m^N(E)$ in itself qualifies as the CF expansion of a finite chain of size m. Everything we know applies here as well, in particular, $t_m^N(E)$ can be cast in the form of eq. (2.33) with the corresponding polynomials $\{\mathcal{P}_n, \mathcal{Q}_n\}$ being determined by the periodic $\{a_{N+i}, b_{N+i}\}$, and permitting to obtain a closed form for the terminator. $t_m^N(E)$ will satisfy a quadratic

equation of the type $t(E)^2 + B(E)t(E) + C(E) = 0$, with coefficients that involve combinations of $\{\mathcal{P}_n, \mathcal{Q}_n\}$[34]. The solution for $t_m^N(E)$ is therefore a more generalized square root terminator. For the symmetric case illustrated in Fig. 2.12, it's straightforward to obtain the terminator used in Figs. 2.12(d,e)

$$t_2^N(E) = -\frac{2(E - a_{N+1})}{W - X + \sqrt{(W+X)^2 - 4Xb_{N+1}^2}}, \text{with} \tag{2.49a}$$

$$W = (b_{N+1} + b_{N+2})(b_{N+1} - b_{N+2}), \quad X = (E - a_N)(E - a_{N+1}), \tag{2.49b}$$

as well as the, notoriously symmetric, band edges E_i:

$$E_i = \frac{a_N + a_{N+1}}{2} \pm \frac{1}{2}\left\{(a_N - a_{N+1})^2 + 4(b_{N+1} \pm b_{N+2})^2\right\}^{\frac{1}{2}}. \tag{2.50}$$

The identification of the periodicities in the unsymmetrical gap and multiple gap cases is not as easy. The $\{a_n, b_n\}$ in Fig. 2.13a are self evident with respect to this difficulty. Moreover, it is not guaranteed that the periodicity is commensurate with the chain as the expression in (2.48) implies. The periodicity in those cases is better appreciated in the *phase space* representation (a_n, b_n^2) suggested by Turchi et al. [1982] and shown in Fig. 2.13b. It is possible also to attain closed expressions for the general gap [Haydock and Nex, 1984; Turchi et al., 1982] but, as it would certainly lead to a rather lengthy section, we refrain to elaborate further on that, and limit ourselves to presenting the form of the terminator for the general single gap [Haydock and Nex, 1984]:

$$t^N(E) = \frac{1}{2b_N^2} \frac{(E - A)^2 + A^2 - B + 2b_N^2 - \sqrt{X(E)}}{E - 2A + a_{N-1}}, \tag{2.51}$$

with A and B related to the band edges through, $4A = \sum E_i$ and $4B = \sum E_i^2$, and $X(E) = \prod_{i=1}^4 (E - E_i)$. This has been applied to the unsymmetrical band in Fig. 2.13(c,d), allowing the successful reconstruction of the DOS. Notice that such favorable outcome means that the terminator represents an infinite chain that matches the finite set of calculated $\{a_n, b_n\}$ and exhibits the same periodic behavior. This is rather remarkable, judging from the seemingly non-periodic aspect of Fig. 2.13(a).

2.4.3. Stochastic Recursive Method

So far our emphasis has been almost exclusively restricted to the calculations leading to the LDOS. This is a special type of spectral density. Thermodynamic properties of physical systems, such as its energy, or chemical potential, require the knowledge of the full spectral density:

$$n(E) = \frac{1}{N} \sum_{\alpha} \delta(E - E_\alpha), \tag{2.52}$$

[34]To see this write (2.48) in the form $\mathcal{Q}_m(E)/b_{N+1}\mathcal{P}_m(E)$, as if b_{N+m} were zero. Then use (2.15) to expand $\mathcal{P}_m(E)$, $\mathcal{Q}_m(E)$ and replace $a_{N+m+1} + t_m^N(E)$ for a_{N+m+1} in those expressions.

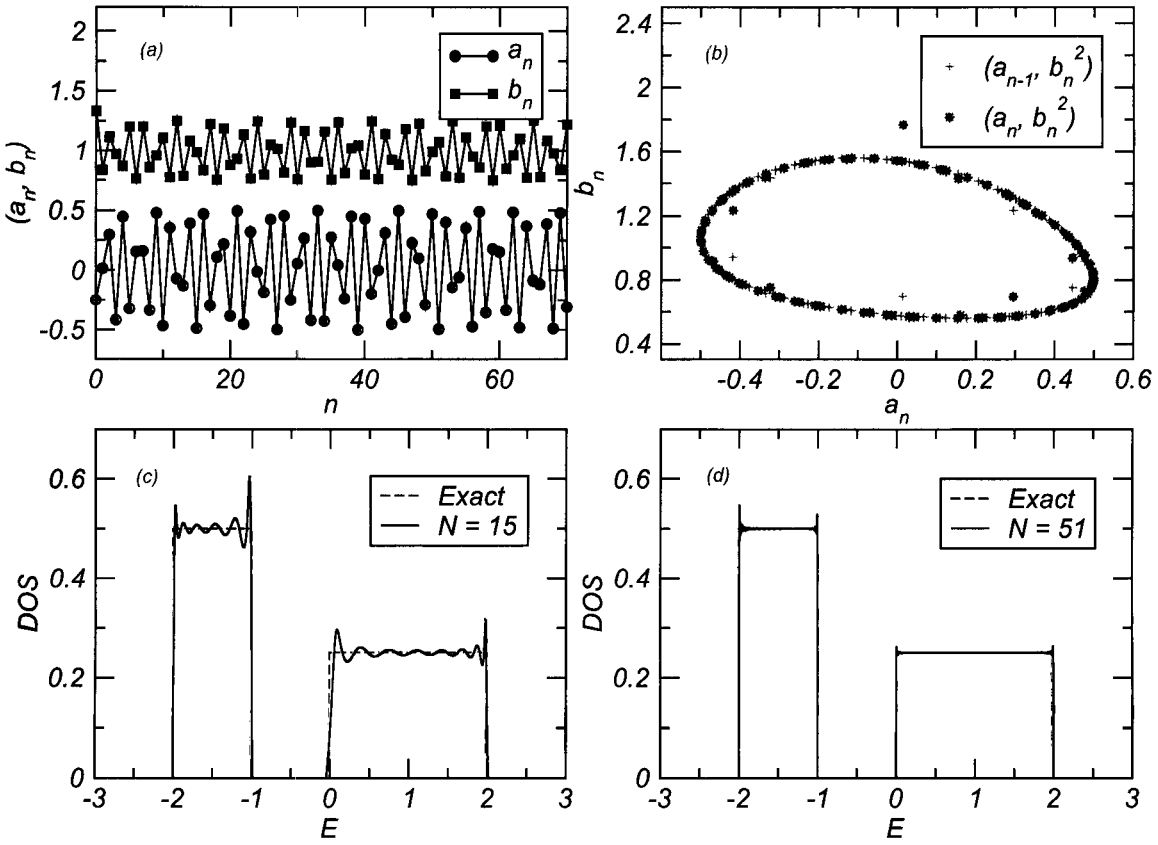

FIGURE 2.13 .: *Recursive method applied to the general gapped band shown in the lower panels. (a) The* $\{a_n, b_n\}$ *coefficients. (b) The phase space representation* (a_n, b_n^2) *and* (a_{n-1}, b_n^2). *In (c) and (d) the terminator in eq. 2.51 is used to append the CF expansion of chains with* $N = 15$ *and* $N = 51$, *respectively.*

which involves the sum over all the eigenstates E_α. Clearly, from completeness of the Hilbert space, the DOS and LDOS are related via

$$n(E) = \frac{1}{N} \sum_r n_r(E) \,. \tag{2.53}$$

In ordered systems (like all the examples presented up to this point), translational invariance dictates that the DOS is effectively the LDOS, or, at most, a sum over a restricted number of orbitals if the unit cell of the model accommodates several orbitals. In the absence of this symmetry, the LDOS is just what it is — a spectral density projected onto a single state in the Hilbert space of the problem, usually a local orbital in the real space. Using the relation above to arrive at the DOS amounts to going back and diagonalize it exactly. Fortunately, we can obtain 2.52 from the identity

$$\langle n_\varphi(E) \rangle = n(E) \,, \tag{2.54}$$

where $\langle n_\varphi(E) \rangle$ is the average of the LDOS projected onto some random state[35], φ, spanning the full Hilbert space, $\mathbb{H}$, of the problem (see Appendix 2.D for details regarding the identity above)[36]. Having φ spread over $\mathbb{H}$ requires something we didn't contemplate so far, that being the need for a finite system.

[35]This means that $|\varphi\rangle = \sum_r^N \varphi_r |r\rangle$, and the φ_r are randomly distributed as discussed in Appendix 2.D.

[36]Total randomness of the state φ is crucial because, otherwise, one might be in fact calculating just another projected DOS on some subspace of $\mathbb{H}$.

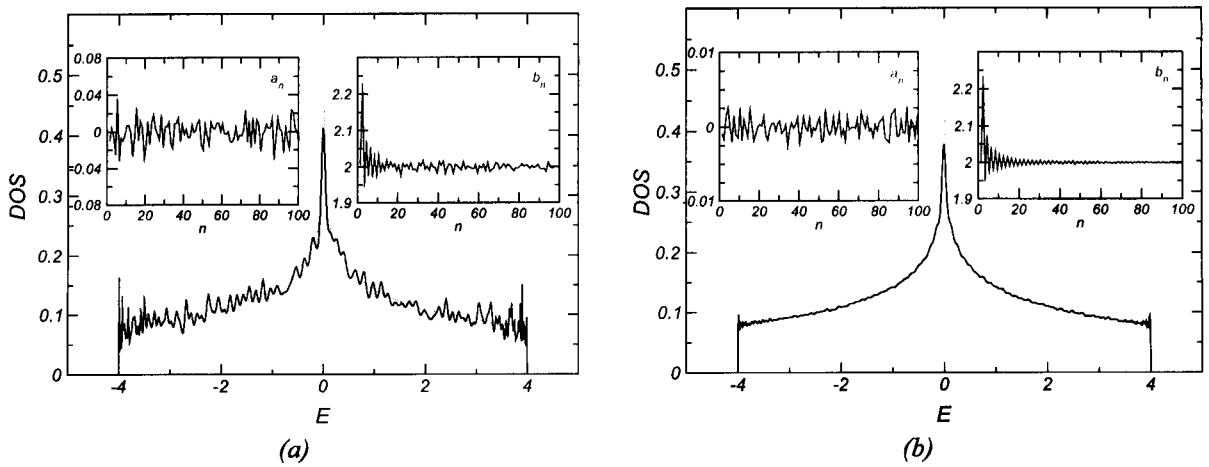

FIGURE 2.14 .: *DOS for the 2D tight-binding model on the square lattice. The main panels show the LDOS calculated with a random state u_0 on a lattice with 200×200 sites (a) and 2000×2000 sites (b). 100 chain states and PBC were used. The dashed line is the DOS obtained from a K-space sampling. The insets show the corresponding coefficients a_n and b_n (cfr. with Fig. 2.5). No averages have been performed.*

Up to this point our system was, for all purposes, infinite in the sense that there were no boundaries and the chain states u_n could spread further and further as in Figs. 2.1 and 2.2[37]. Using $\varphi = u_0$ leads to a chain model of a finite system and this should reflect itself through finite size effects of some sort. Fig. 2.14 shows what happens when the LDOS for the ordered 2D tight-binding model is calculated with different system sizes. If we compare the chain model in 2.14a with its *infinite* counterpart of Fig. 2.5, the salient difference is the behavior of the b_n. It ts no longer a uniform, damped oscillating function, and its behavior leads to a noisy LDOS in the end, as shown. Things improve considerably for a large system as in Fig. 2.14b. This last panel also reflects the self-averaging property of the DOS: the calculation of the LDOS using a random u_0 in a very large system almost dispenses the averaging process of eq. 2.54.

In a disordered electronic problem one is frequently facing the need for calculating configurational averages. If the disordered model is parametrized by a set of variables $\{\varepsilon_i\}$ having some joint probability distribution, $\mathcal{P}(\{\varepsilon_i\})$, then we can define the configuration averaged DOS as

$$\overline{n}(E) = \sum_{\alpha} \int \cdots \int \delta\Big(E - E_\alpha\big(\{\varepsilon_i\}\big)\Big) \mathcal{P}(\{\varepsilon_i\})\, \mathcal{D}\{\varepsilon_i\}\,. \tag{2.55}$$

To apply the recursive method, the most expedite way[38] is resorting to 2.54 so that our starting orbital samples the entire system uniformly and, in practice, two averaging procedures are performed: one over the random starting vectors, φ, and one over configurations of disorder :

$$\overline{n}(E) = \overline{\langle n_\varphi(E)\rangle}\,. \tag{2.56}$$

[37] A machine representation of the *entire* system/Hilbert space was clearly not needed, the ones for neighboring u_n being enough.

[38] There is an alternate and very elegant proposal by Mookerjee [1973] for configurational averages of the type 2.55. It is based upon the fact that the positive definiteness of a probability distribution $p(\varepsilon_i)$ can itself be viewed as the LDOS for some chain model in a given Hilbert space. The proposed method consists in finding that chain (the reverse recursive problem) and the calculation of a given average, $\overline{A}$, follows from the Greenian associated with a specially crafted hyper-Hamiltonian in the expanded Hilbert space.

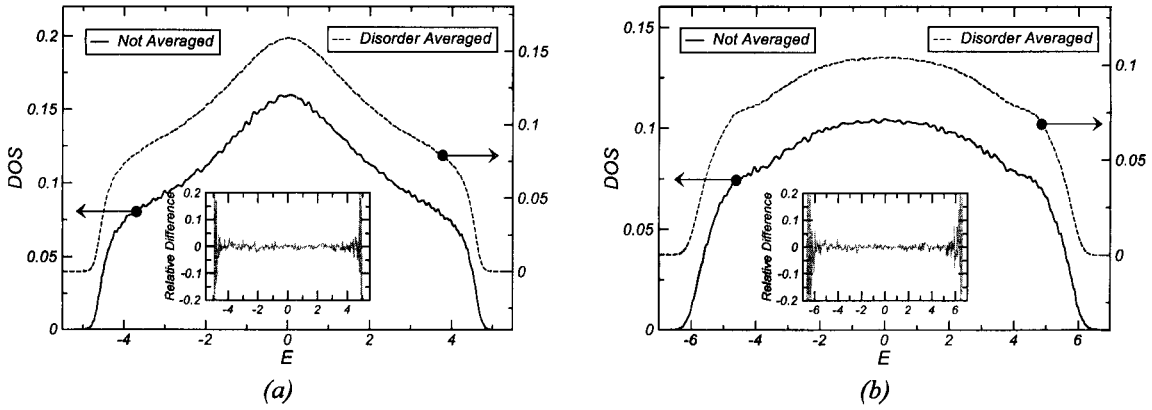

FIGURE 2.15 .: *DOS of the 2D Anderson model, obtained averaging over disorder configurations on a* 2000×2000 *lattice, for disorder strengths* $W = 4$ *(a), and* $W = 8$ *(b). 100 chain states were used. Each panel exhibits the DOS for a single configuration (left axis), and averaged over 10 configurations (right axis). The insets show the relative difference* $(n_\varphi - \overline{n}_\varphi)/\overline{n}_\varphi$.

A frequent example of such kind of system is the Anderson model, whose Hamiltonian reads

$$\mathcal{H} = \sum_i \varepsilon_i \, c_i^\dagger c_i - \sum_{i,\delta} t_{i,\delta} \, c_i^\dagger c_{i+\delta} \,, \tag{2.57}$$

with ε_i a random variable uniformly distributed in the interval $[-W/2, W/2]$. The strength of disorder is quantified by the width, W, of the site energies' distribution. In Fig. 2.15 the DOS for the 2D Anderson model has been calculated as prescribed above, and one sees that the DOS obtained from a single disorder configuration is already a good approximation to $\overline{n}(E)$, the relative error being well below 5% for most of the band. Also significant is the fact that the Lifshitz tails in the DOS appear well defined even for a single configuration, without averaging.

The conclusion follows that this stochastic approach permits the fast calculation of the DOS for systems with sizes much beyond the capacity of exact spectral methods. The self-averaging property of the DOS and a random, uniform, starting orbital allows for rather accurate results with a relatively small number of averages.

2.5. Numerical Caveats

We reserved this space for a few brief remarks regarding some aspects that, having been omitted in the preceding sections, might have raised legitimate questions from the reader, and, hence, beg to be clarified.

2.5.1. Versatility from a smart choice of the starting state

From what was presented so far regarding the recursive method, one is now in the position to know that the choice of the starting state, u_0, determines the questions one might ask. The basic question is the proper LDOS, that is, the DOS projected onto a single local orbital. But the formalism is completely general and any state in the Hilbert space of the problem is an equally suited candidate for u_0. Of course,

some especially tailored states are more useful than others in addressing typical questions for solid-state problems. One such question is the single particle spectral function, $A(k,\omega)$, defined as

$$A(k,\omega) = \sum_{\alpha} |\langle 0\,|c_k|\,\psi_\alpha\rangle|^2\,\delta(\omega - E_\alpha + E_0)\,. \tag{2.58}$$

Clearly, this is just the DOS projected onto a plane wave state because we have simply $c_k^\dagger|0\rangle = |k\rangle$. Instead of enumerating other particular cases (like absorption rates, etc.), we present a generalization of the formulation that broadens the scope of direct applicability of the method.

Given an arbitrary quantum mechanical operator $\boldsymbol{A}$ defined in the Hilbert space of some Hamiltonian $\boldsymbol{H}$ whose ground state is $|\Psi_0\rangle$, we define the zero temperature autocorrelator:

$$S_A(t) = \left\langle \Psi_0 \left| \boldsymbol{A}^\dagger(t)\boldsymbol{A} \right| \Psi_0 \right\rangle\,, \tag{2.59}$$

and its Fourier transform, that we call *spectral function* associated with $\boldsymbol{A}$:

$$S_A(\omega) = \int_{-\infty}^{+\infty} S_A(t)\, e^{i\omega t}\, dt\,. \tag{2.60}$$

It is straightforward to show that (2.60) can be written using a Lehmann representation as

$$S_A(\omega) = 2\pi \sum_m \langle\Psi_0|\boldsymbol{A}^\dagger|m\rangle\,\langle m\,|\boldsymbol{A}|\,\Psi_0\rangle\,\delta(E_0 - E_m + \omega)\,, \tag{2.61}$$

in order to emphasize our familiar form. $S_A(\omega)$ can be obtained via recursion method, but now two steps are needed. First we need to calculate the exact ground state, $|\Psi_0\rangle$, of the problem by performing a Lanczos diagonalization. Having obtained $|\Psi_0\rangle$, a normal recursion procedure yields $S_A(\omega)$ if the starting vector is chosen as

$$u_0 = \frac{\boldsymbol{A}|\Psi_0\rangle}{||\boldsymbol{A}|\Psi_0\rangle||}\,. \tag{2.62}$$

That this is true follows from the fact that, apart from a normalization factor, $S_A(\omega)$ is simply a projected DOS. Since most measurable properties in solid-state problems can be expressed in terms of correlators of the form (2.59), this demonstrates how useful and versatile the method is. One needs only to tailor the starting vector, u_0 according to the question we intend to address.

2.5.2. On the chain model

The discussion of the recursive method and the transformation to a chain has been restricted to Hermitian operators (the Hamiltonian) and orthogonal (Wannier) orbitals. This choice is motivated solely by the simplicity of the discussions, formulas and expressions that are obtained for those cases, and is by no means a restriction of the method. The generalization to non-hermitian and non-orthogonal basis sets is straightforward as discussed in [Haydock, 1980; Haydock and Kelly, 1975].

The recursive steps in eq. 2.8b for the transformation to a chain imply that, within exact arithmetics, all chain states are strictly orthogonal. The numerical computation will always introduce roundoff errors

that lead to an accumulated loss of orthogonality. Remarkably, the stability in the construction of the chain (and in particular, the calculation of the $\{a_n, b_n\}$) requires just the linear Independence of the u_n. Therefore, in most cases one doesn't need to venture into re-orthogonalization schemes that would spoil the economy of the recursive technique [Haydock, 1980, Sec. 7]. Nonetheless loss of orthogonality has serious consequences for exact diagonalization calculations, one of them being the appearance of the so-called *"ghost"* eigenvalues: spurious states that cannot be mapped to the eigenvalues of the original $\boldsymbol{H}$. For example, a frequent situation is that some eigenvalues of the finite chain appear with multiplicities higher than one.

Still in the context of exact diagonalization (Lanczos), the convergence of the chain eigenvalues to the real eigenvalues of the problem occurs later and later for successively excited state energies. Adding the mentioned problems with loss of orthogonality to this, when an eigenstate at some arbitrary energy is needed, it is sometimes advisable to perform a suitable transformation of the original Hamiltonian so that the new extremal eigenenergies lie in the desired energy range, improving convergence. In fact, the convergence of the Lanczos method is closely related to the convergence of the simpler power method[39] or the inverse iteration methods, [Press et al., 1992] which depends strongly on the level spacing between the target/extremal eigenvalue and the immediate neighboring eigenvalues. Therefore, even the convergence to the ground state depends on the particular spectrum of the problem at hand[40].

As to the execution time efficiency, the sole fundamental fact to be retained is that, in the transformation to the chain, execution time is essentially determined by the algorithm chosen to calculate $H|u_n\rangle$. Thus, in order to improve on the CPU time effort, the attention should be on the method used for the implementation of this key operation.

2.5.3. On the calculation of the LDOS

An important practical detail when using square root terminators to terminate the CF expansion and obtain the LDOS is that, many times, the asymptotic value of b_n is hard to define[41]. Since a good asymptotic value is needed to avoid a spiky DOS, when that happens, an overestimate for b_∞ is preferred and the reason is simple. An overestimated b_∞ will lead to an effective bandwidth larger than the bandwidth of the target system. However, since the LDOS drops very rapidly to zero at energies out of the band of the target system[42], the LDOS calculated with the overestimated b_∞ will be effectively zero beyond the real band edges. This can be used to detect the actual band edges and extract a better estimate for the asymptotic b_n.

Another caveat is that, although a random u_0 should be allright as a *general purpose* starting vector for the chain, in ordered systems one is better off starting with a localized state. The reason is efficiency: with a localized state, the vector-vector and vector-matrix operations involve operations with a considerable number of zeros, when compared with the random u_0. At the machine level, handling zeros is much

[39] The Lanczos tridiagonalization procedure can be seen as a Gram-Schmidt orthogonalization procedure on the Krylov space $\{u_0, \boldsymbol{H}\, u_0, \boldsymbol{H}^2 u_0, \ldots, \boldsymbol{H}^N u_0\}$ generated in the power method. Since the eigenvalues of the Lanczos matrices are the eigenvalues of $\boldsymbol{H}$ projected onto these Krylov spaces, the convergence to the extremal eigenvalues is quite natural.

[40] Exact results for majorants can be obtained, as mentioned *en passant* by Haydock and Te [1994, Sec. II.A].

[41] Disordered systems are typical examples.

[42] To see this happening look, for instance, to what happens in the gapped region of Fig. 2.12c when the simple square-root terminator is tentatively applied to a gapped DOS.

faster than floating point reals and the execution time is substantially reduced[43].

Contrary to what happens when using polynomial moments for the estimation of the DOS, the recursive method doesn't provide us with an intrinsic energy resolution associated with the number of chain states used in the computations. An average resolution of the method can be defined as

$$\Delta E = w/N \tag{2.63}$$

where w is the bandwidth of the problem, and N the number of chain states used. The motivation of this definition is purely heuristic and says that, since the chain model has necessarily N distinct eigenvalues spread between E_0 and $E_0 + w$, we define ΔE to be the *average* level spacing. This was somehow explored in Sec. 2.3.3.2 and can be inferred from Fig. 2.6.

Finally, if for some reason one is limited to a small sized cluster which should mimic an infinite system, then boundary conditions can be important. In particular, for open boundary conditions a highly symmetric cluster shape is discouraged because the interference effects are strongest in such case. More efficient alternatives are a rough boundary or periodic boundary conditions. In any case, the recursion steps should not go past some empirical threshold that balances the trade-off between the need for as many chain states as possible, and the unwanted features related to the finite size of the cluster [Haydock, 1980; Heine, 1980]

[43] Other advantage is that one doesn't get finite-size structure in the DOS nor does one need to average over u_0 as in sec. 2.4.3.

Appendices for this chapter

Appendix 2.A On the Sturm property of the leading minors

Definition Let A be a tridiagonal symmetric matrix as in (2.11), with $b_i \neq 0$, $\forall i \leq N$, and $\Delta_n(E)$ its principal leading minor[12] of order n, obeying the recurrence relations (2.14):

$$\Delta_0(E) = 1, \quad \Delta_{-1}(E) = 0 \tag{2.64a}$$

$$\Delta_n(E) = (E - a_{n-1})\Delta_{n-1}(E) - b_{n-1}^2\Delta_{n-2}(E)\,, \tag{2.64b}$$

Lemma 2.1. *The zeros of successive determinants $\Delta_n(E)$ are never coincident.*

Proof For *reductio ad absurdum* purposes assume that it was otherwise for, say, E_k. Then $\Delta_n(E_k) = \Delta_{n-1}(E_k) = 0$ and we would have immediately $\Delta_{n-2}(E_k) = 0$. The recursion relation above (2.64) would then propagate this result leading to the impossibility of having $\Delta_0(E) = 0$.

Theorem 2.2. *For all n, the principal leading minor $\Delta_n(E)$ of a symmetric tridiagonal matrix has its zeros interlaced with the ones of $\Delta_{n-1}(E)$.*

Proof To prove the theorem we resort to induction. Fig. 2.16 is provided for guidance in the arguments to follow.

The result is readily proven for $n = 1$ and $n = 2$. Assume then its validity for all $p < n$, meaning that the zeros of $\Delta_{n-2}(E)$ interpolate the ones of $\Delta_{n-1}(E)$. Let $E_1 < E_2 < \cdots < E_{n-1}$, be the zeros of $\Delta_{n-1}(E)$. For every E_k, $\Delta_{n-2}(E_k)$ and $\Delta_n(E_k)$ have opposite signs by virtue of (2.64). But, given that $\Delta_{n-2}(E)$ has exactly one zero between adjacent E_k's (induction hypothesis), it changes sign once in that interval and likewise for $\Delta_n(E)$. Therefore, $\Delta_n(E)$ has $n-2$ zeros that interpolate the E_k's. Now, for the remainder 2 zeros notice that, for n even, because $\lim_{E\to\pm\infty}\Delta_{n-2}(E) = \lim_{E\to\pm\infty}\Delta_n(E) = +\infty$, then $\Delta_{n-2}(E_1) > 0$ and $\Delta_{n-2}(E_{n-1}) > 0$, which implies that $\Delta_n(E_1) < 0$ and $\Delta_n(E_{n-1}) < 0$. For odd n just invert all the signs. Together with the lemma above, this guarantees the existence of two additional zeros of Δ_n: one below E_1 and one above E_{n-1}. All zeros of Δ_n are thereby interlaced with the zeros of Δ_{n-1}, which, by induction, proves the theorem. □

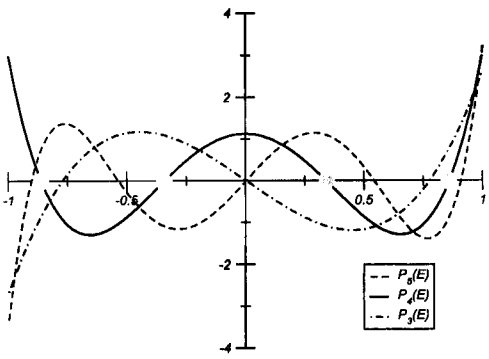

FIGURE 2.16 .: *Three successive orthogonal polynomials associated with a flat LDOS in the domain $[-1, 1]$. They are proportional to the respective $\Delta_n(E)$, via eq. (2.22). The circles in the horizontal axis mark the zeros, E_k, of $P_4(E)$ (or $\Delta_4(E)$).*

Corollary 2.3. *Δ_n has n distinct roots.*

Appendix 2.B The truncated CF and Padé approximants

Let us revisit the expression (2.30) that gives $G_0(E)$ as the quotient of two determinants:

$$G_0(E) = \frac{D_1(E)}{D_0(E)}\,. \tag{2.65}$$

$D_0(E)$ is the determinant of the matrix $\mathbb{1}E - \boldsymbol{H}$ corresponding to the entire chain and, therefore, coincides with $\Delta_N(E)$ introduced in (2.13) and (2.14). For the full chain we could define the family of polynomials $P_n(E)$, orthogonal under the LDOS on the state u_0, and saw in (2.22) that $\Delta_N(E) = b_1 b_2 \ldots b_N P_N(E) = D_0(E)$.

$D_1(E)$, being the first cofactor, is the determinant of $\mathbb{1}E - \boldsymbol{H}$ with its first line and column removed. Clearly, this corresponds to the same chain with the state u_0 suppressed. Therefore, we can construct a new family of orthogonal polynomials, $Q_n(E)$, for this chain and conclude, in a totally analogous way, that $D_1(E) = b_2 b_3 \ldots b_N Q_N(E)$. This yields at once

$$G_0^{(N)}(E) = \frac{Q_N(E)}{b_1 P_N(E)}\,. \tag{2.66}$$

Both P_n and Q_n are a very peculiar set. They obey the same recursion relation (2.15) and are nothing but two linearly independent solutions for this second order difference equations (as already hinted in footnote 13, page 15). Their differences stem from the initial conditions $P_{-1} = Q_0 = 0$ and $P_0 = Q_1 = 1$, which conditions also determine that $Q_n(E)$ is of degree $n-1$, and that its zeros never coincide with the ones of $P_n(E)$ [Haydock, 1980].

Now notice that $G_0^{(N)}(E)$ is also what, in the language of continued fractions [Baker, 1975; Beskin, 1987], is called the N^{th} convergent to $G_0(E)$. That $G_0^{(N)}(E)$ corresponds to the $[N-1/N]$ Padé approximant to $G_0(E)$ follows directly from the normalization $P_0(E) = 1$ and from a general theorem relating the sequence of approximants to a Continued Fraction with sequences of Padé approximants [See Baker, 1975, Chap. 4].

Finally, we terminate this digression through Padé approximants by noting a result with physical significance. It can be shown very generally [see Baker, 1975, Chap. 7] that the denominators of the sequence of $[N-1/N]$ Padé approximants to a particular power series

$$A(x) = \sum a_j x^j \tag{2.67}$$

for successive values of N are orthogonal to each other under a specific weight function, $w(E)$ that satisfies

$$a_n = \int E^n w(E) dE\,. \tag{2.68}$$

From the above discussion, and from (2.66), we already know that the denominators are the $P_N(E)$, and

know further under which weight function they constitute an orthogonal family: the LDOS

$$n_0(E) = \sum_\alpha |\langle u_0|\psi_\alpha\rangle|^2 \, \delta(E - E_\alpha) \tag{2.69}$$

Therefore, since the Padé approximant $[N-1/N]$ reproduces the first $2N$ coefficients of (2.67) (i.e.: the a_n are explicitly contained within the coefficients of the Padé approximant) this means that, it reproduces the first $2N$ moments of the LDOS as well. Stated plainly, $G_0^{(N)}$ contains all the information to reproduce the first $2N$ moments of the LDOS.

Appendix 2.C The CF expansion and Dyson's equation

Here we provide a different perspective on the CF expansion of the local Green Function (GF). We first recall that if the Hamiltonian can be written as

$$\boldsymbol{H} = \boldsymbol{H}_0 + \boldsymbol{V} \tag{2.70}$$

then, using the definition in eq. (2.25) for the greenian, we have

$$\boldsymbol{G} = \frac{1}{E - \boldsymbol{H}_0 - \boldsymbol{V}} = \frac{1}{(\boldsymbol{G}^0)^{-1} - \boldsymbol{V}} = \boldsymbol{G}^0 \frac{1}{1 - \boldsymbol{V}\boldsymbol{G}^0} , \tag{2.71}$$

which, is readily expanded into the infinite series

$$\boldsymbol{G} = \boldsymbol{G}^0 + \boldsymbol{G}^0\boldsymbol{V}\boldsymbol{G}^0 + \boldsymbol{G}^0\boldsymbol{V}\boldsymbol{G}^0\boldsymbol{V}\boldsymbol{G}^0 + \ldots . \tag{2.72}$$

This expansion can be condensed in the recursive form known as Dyson's equation:

$$\boldsymbol{G} = \boldsymbol{G}^0 + \boldsymbol{G}^0\boldsymbol{V}\boldsymbol{G} . \tag{2.73}$$

When we want to calculate the LDOS, we are interested in a particular matrix element of the greenian, namely $G_0(E) \equiv \langle u_0 \, |\boldsymbol{G}(E)| \, u_0\rangle$. In the tridiagonal basis defined by $|u_0\rangle$ (2.8) the Hamiltonian reads

$$\boldsymbol{H} = \sum_n a_n c_n^\dagger c_n + \sum_n b_n c_{n+1}^\dagger c_n + \text{h.c.} , \tag{2.74}$$

where the $\{a_n, b_n\}$ are just the associated tridiagonal coefficients (2.3). The best way to calculate $G_0(E)$ is to use a diagrammatic representation of Dyson's expansion for the local GF $G_0(E)$ as in Fig. 2.C. Such representation is useful because it clearly shows that the calculation of $G_0(E)$ amounts to finding all possible paths that depart and terminate at the starting orbital. In particular, $G_1(E)$ in Fig. 2.17b includes all paths that depart and arrive at orbital u_1 without ever passing by u_0[44]. From the

[44] $G_1(E)$ is, thus, equivalent to the local GF for a chain that starts with the orbital u_1, instead of u_0.

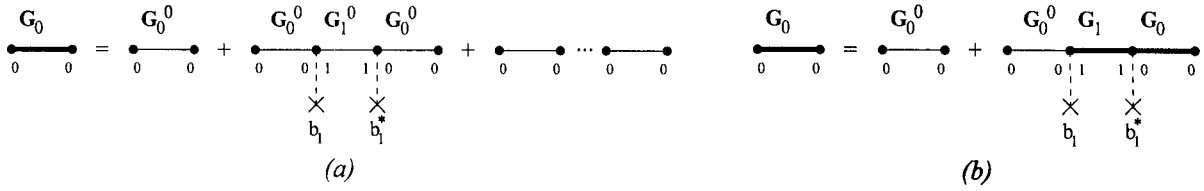

FIGURE 2.17 .: *Diagrammatic expansion for the calculation of $G_0(E)$ based on Dyson's expansion of eq.2.73.*

diagrammatic expansion it is transparent that

$$G_0(E) = G_0^0(E) + b_1^2\, G_0^0(E) G_1(E) G_0(E)\,, \tag{2.75a}$$

$$\cdots$$

$$G_n(E) = G_n^0(E) + b_{n+1}^2\, G_n^0(E) G_{n+1}(E) G_n(E)\,, \tag{2.75b}$$

where $G_n^0(E)$ is just $(E - a_n)^{-1}$. We can now solve (2.75a) for $G_0(E)$ obtaining

$$G_0(E) = \frac{1}{E - a_0 - b_1^2 G_1(E)}\,, \tag{2.76a}$$

$$G_n(E) = \frac{1}{E - a_n - b_{n+1}^2 G_{n+1}(E)}\,. \tag{2.76b}$$

Notice that this generates a continued fraction expansion for $G_0(E)$ just as we expect. In fact, eqs. (2.76) correspond exactly to the ones obtained before using an explicit expansion of the determinants in (2.30-2.32).

Appendix 2.D DOS from the average LDOS

Let us use the definition

$$n(E) = \frac{1}{N} \sum_{\alpha}^{N} \delta(E - E_\alpha) \tag{2.77}$$

for the exact, *total*, DOS, and

$$n_\varphi(E) = \sum_{\alpha}^{N} |\langle \varphi | \psi_\alpha \rangle|^2\, \delta(E - E_\alpha)\,, \tag{2.78}$$

for the DOS projected on the state φ. If we expand this state in the local basis as $|\varphi\rangle = \sum_r \varphi_r |r\rangle$, then the expression above can be cast as

$$n_\varphi(E) = \sum_{\alpha} \delta(E - E_\alpha) \sum_{r,r'} \langle \psi_\alpha | r \rangle \langle r' | \psi_\alpha \rangle\, \varphi_r \varphi_{r'}\,. \tag{2.79}$$

Without loss of generality, we restrict ourselves to the cases where the matrix representation of the Hamiltonian in the local basis has only real entries, and, hence, we can consider that the φ_r are all real,

apart from an unphysical global phase. Now if the φ_r are random variables subject to the sole constraint $\sum_r \varphi_r^2 = 1$, the average of the LDOS will be

$$\langle n_\varphi(E)\rangle = \sum_\alpha \delta(E - E_\alpha) \sum_{r,r'} \langle \psi_\alpha | r\rangle \langle r' | \psi_\alpha\rangle \langle \varphi_r \varphi_{r'}\rangle \ , \tag{2.80}$$

with,

$$\langle \varphi_r \varphi_{r'}\rangle = \frac{1}{\mathcal{N}} \int_{-\infty}^{\infty} \cdots \int_{-\infty}^{\infty} \delta\Big(1 - \sum_i \varphi_i^2\Big)\, \varphi_r \varphi_{r'} \prod_{i=1}^{N} d\varphi_i \,, \tag{2.81}$$

$\mathcal{N}$ being a normalizing factor[45]. The integral above, well familiar in the context of problems in statistical mechanics, equals

$$\frac{1}{2} \frac{\pi^{N/2}}{\Gamma\big(\frac{N}{2}+1\big)} \delta_{r,r'} \,. \tag{2.82}$$

Combining this with the result for the norm, $\mathcal{N} = \frac{\pi^{N/2}}{\Gamma(N/2)}$, the exact and intuitive result

$$\langle \varphi_r \varphi_{r'}\rangle = \frac{1}{N} \delta_{r,r'} \tag{2.83}$$

is readily obtained. The consequence of this result is that the average of the LDOS can now be written as

$$\langle n_\varphi(E)\rangle = \frac{1}{N} \sum_\alpha \delta(E - E_\alpha) = n(E) \,. \tag{2.84}$$

[45] Of course, the *spherical* normalization constraint on the variables φ_i means they can take values only in the interval $[-1, 1]$. The presence of the δ function permits the safe extension of the integration limits to infinity.

3. EuB6: Background and Significance

"The men of experiment are like the ant, they only collect and use; the reasoners resemble spiders, who make cobwebs out of their own substance. But the bee takes the middle course: it gathers its material from the flowers of the garden and field, but transforms and digests it by a power of its own. Not unlike this is the true business of philosophy (science); for it neither relies solely or chiefly on the powers of the mind, nor does it take the matter which it gathers from natural history and mechanical experiments and lay up in the memory whole, as it finds it, but lays it up in the understanding altered and disgested. Therefore, from a closer and purer league between these two faculties, the experimental and the rational (such as has never been made), much may be hoped."

— **Francis Bacon**, Novum Organum [Bacon, 1620, XCV].

3.1. Crystal Structure

Almost all stable Rare-Earth (RE) borides belong to the class of clathrates[1] [Etourneau and Hagenmuller, 1985]. In the hexaborides, the boron atoms are arranged in a tridimensional skeleton of interconnected B_6 octahedra, the interstices of which are occupied by the RE (Fig. 3.1). The rare-earth ion is weakly bound, undergoing large excursions from its equilibrium position. The boron framework, on the other hand, is kept through strong covalent bonds, accounting for the hardness of hexaborides, with high melting points and low coefficients of thermal expansion [Mandrus et al., 2001]. EuB_6 has the full cubic symmetry, belonging to the P_{m3m} (O_h^1) space group, with a lattice parameter of 4.185Å (as determined by high-resolution, synchrotron X-ray diffraction [Blomberg et al., 1995; Fisk et al., 1979; Süllow et al., 1998]). Within this space group the Eu ions are located at the $m3m$ (0,0,0) corners while a B_6 octahedron is at the body-centered position. The shortest B-B bonds connect the B_6 octahedra through the cell faces, as in Fig. 3.1.

Despite the high cohesion of the B skeleton, the presence of Boron defects seems ubiquitous, perhaps due to the sample preparation techniques [Blomberg et al., 1995]. In particular, Monnier and Delley [2001] showed by first-principles calculations that a B_6 vacancy is energetically more favorable than 6 individual, separated, B vacancies, thus being the likeliest type of defect in the bulk.

For the specific case of EuB_6, the presence of a robust Ferromagnetic or Ferromagnetism (FM) phase would imply a symmetry lowering either to orthorhombic or tetragonal, since long range or-

[1] Clathrates are inclusion compounds in which a guest species (an atom, ion or molecule) occupies the inside of a cage formed by the host species or by a rigidly bonded lattice of host species [McNaught and Wilkinson, 2005].

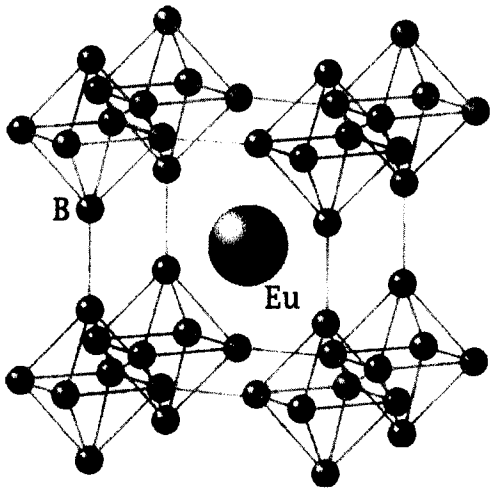

(a)

Parameter	Value
a	4.1849 Å
d_{inter}	1.6964 Å
d_{intra}	1.7596 Å
$d_{\text{Eu-B}}$	3.0783 Å
$\nu_{\text{u.cell}}$	7.330×10^{-23} cm^3

(b)

FIGURE 3.1 .: *(a) Representation of the real-space crystal structure of* EuB_6. *(b) Relevant lattice distances [Blomberg et al., 1995].*

der FM is forbidden by group-theoretical arguments within the P_{m3m} space group [Rado and Suhl, 1965]. The FM transition is not accompanied by any detectable, long-range, structural change as seen in X-ray scattering [Henggeler et al., 1998; Süllow et al., 1998], or in magneto-acoustic experiments [Zherlitsyn et al., 2001], and thus the global cubic symmetry is preserved inside the FM phase. Nonetheless, other experiments did find evidence for very small *local* reductions of symmetry [Gavilano et al., 1998; Martinho et al., 2005].

3.2. Theoretical Electronic Structure

In and of itself, Boron is a rather remarkable atomic species from the chemical point of view [Pauling, 1931]. For example, the valence of boron ions in many metal borides cannot be described by an usual oxidation state, especially for MB_6. Early theoretical studies established that, for the B framework, there are 7 internal bonding molecular orbitals requiring seven pairs of electrons, and 6 external orbitals connecting adjacent B_6 octahedra. To saturate these 10 (covalent) bonding orbitals per B_6, an electron transfer of 2 electrons from the metallic atom is needed [Lipscomb, 1954; Lipscomb and Britton, 1960]. In view of this, the metallic or semiconducting character would depend whether the RE is di- or trivalent in the hexaboride. While this simple electron counting argument seems to apply in the case of trivalent hexaborides[2], in EuB_6, the metallic ion clearly adopts a divalent configuration[3], whence a semiconducting behavior should emerge.

The nature of the electronic structure of MB_6 has been for a long time a rather unsettled matter[4]. The debate hinges around the X point in the Brillouin Zone (BZ): the crucial point. Pioneering calculations predict EuB_6 to be a polar semiconductor [Yamazaki, 1956], but self-consistent bandstructure calcula-

[2]Say, LaB_6 or YbB_6.

[3]Mössbauer and isomer-shift spectroscopy clearly confirm the presence of divalent Eu only in the hexaborides [Blomberg et al., 1995; Clack et al.; Fisk et al., 1979; Geballe et al., 1968; Li et al., 2000].

[4]And, in my opinion, still is as far as theoretical Density Functional Theory (DFT) approaches are considered.

tions reveal that divalent hexaborides should be semimetals instead [Hasegawa and Yanase, 1979]. This was confirmed via Local Density Approximation (LDA) by [Massidda et al., 1996] and a view of EuB_6 as a semimetal with a tiny valence-conduction band overlap at the X point in the BZ lingered for some time. However, bandstructure calculations are well known to give highly distinct, and even contradictory, results when applied to this class of materials[5]: depending on the approximations and implementations of DFT used, the result of LDA calculations for the same compound can be rather different both at the qualitative and quantitative level. Calculations going beyond LDA use the so-called GW approximation for the self-energy and still exhibit notable disparities: at times a gap of $\sim 0.8\,\text{eV}$ [Tromp et al., 2001], or a smaller one of $\sim 0.3\,\text{eV}$ [Kino et al., 2002] appears, (both for CaB_6); at others, an increased overlap is found [Kino et al., 2002; Rodriguez et al., 2000]. The most recent band structure calculations reveal a gap of $0.8\,\text{eV}$, within a Weighted Density Approximation (WDA) approximation [Wu et al., 2004]. Such uneven conclusions are clearly seen in the plots of Fig. 3.2 that summarizes those results.

There are two issues that, somehow, justify this unsettled state of affairs. First, it is recognized by the authors that slight differences in the implementation can yield such discrepancies[6]. Second, and of special relevance for our discussion, is the frequent extrapolation of results obtained for nonmagnetic hexaborides to the case of EuB_6, which is clearly different due to the presence of the f orbitals that require careful account of Coulomb interactions within DFT [Kunes and Pickett, 2004].

From this disparity, one can certainly say that, the available methods and results for band structure calculations are not reliable nor definitive sources in characterizing the band structure near the X point in the BZ. The question remains: is stoichiometric EuB_6 a semiconductor or a semimetal? Nevertheless, they all agree to other important aspects, like the bandstructure in the remainder of the BZ, the various lattice parameters obtained from total energy minimization, or the *atomic orbital* character of the bands: the s, p, d orbitals of the RE do not contribute for the valence band, which is made up from the bonding combination of the $2p$ orbitals of B. Additionally, the bottom of the conduction band has a strong $5d$(Eu) nature, with the highest charge density found in the interstitial regions between neighboring RE ions [Kino et al., 2002; Massidda et al., 1996].

3.3. Experimental Electronic Structure

For some time it was believed that the four frequencies observed in de Haas–van Alphen (dHvA) and Shubnikov de Hass (SdH) experiments were associated with a Fermi surface consisting of an electron and a hole pocket at the X point, and hence consistent with a semimetallic nature of EuB_6 [Aronson et al., 1999].

Notwithstanding, among the probes that, on the experimental front, can glimpse the underlying electronic structure, ARPES and X-Ray Emission Spectroscopy (XRES) are, arguably, the most reliable sources at our hands in this matter[7]. All such experiments, performed on EuB_6, and other non-magnetic

[5] This has maculated results since Hasegawa and Yanase. See further discussions in Tromp et al. [2001] or Wu et al. [2004].

[6] These slight differences, which would not lead to such catastrophic differences in more *conventional compounds*, can be a slightly different value used for the volume of the unit cell [Hasegawa and Yanase, 1979; Massidda et al., 1996], a different approximation for the pseudopotentials, whether f electrons are accounted for or not, etc. [Kino et al., 2002; Wu et al., 2004]

[7] Anticipating perhaps the critique of ARPES being a surface probe, we underline that, there is overwhelming evidence that the

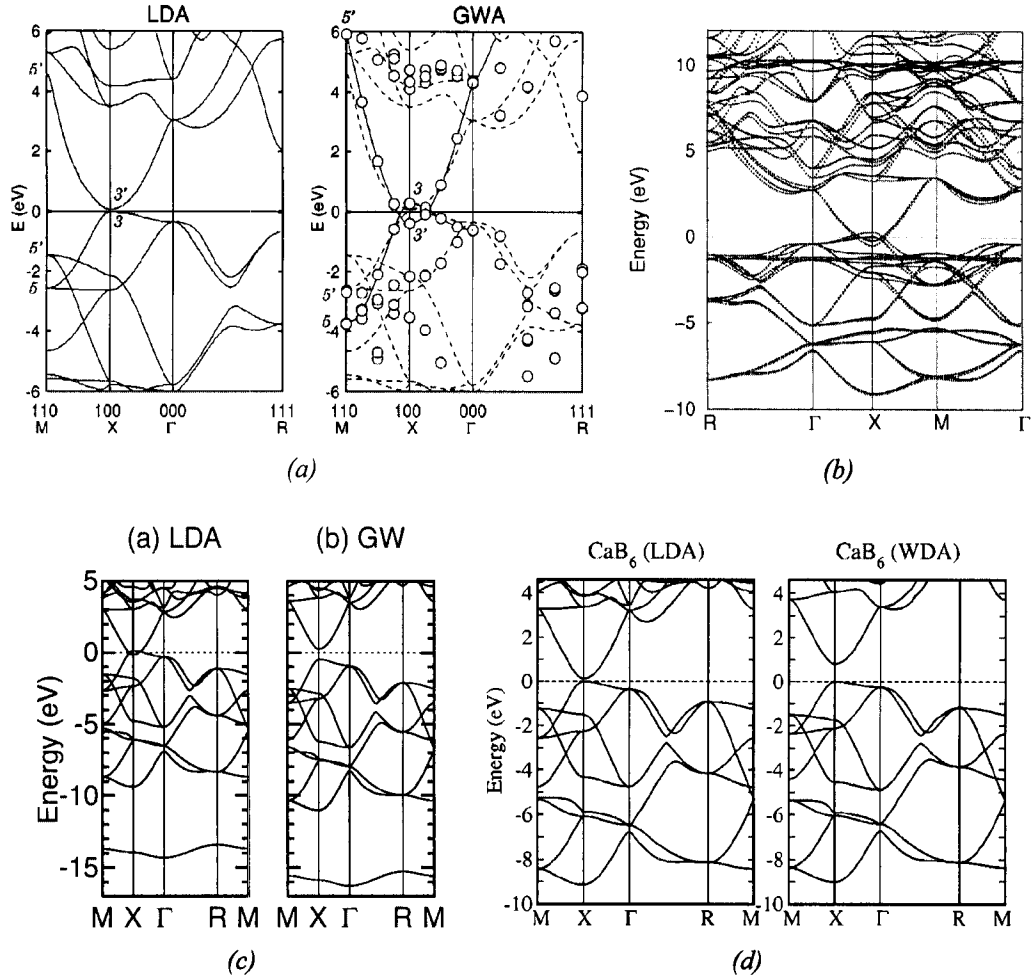

FIGURE 3.2 .: *(a) Bandstructure calculated for CaB_6 within LDA and LDA+GW, featuring, respectively, a tiny gap and an overlap, as calculated by Kino et al. [2002]. (b) LDA+U for EuB_6, featuring a band overlap and slight spin-splitting of the bands, after Kunes and Pickett [2004]. (c) LDA and LDA+GW for CaB_6, featuring a small overlap and a significant gap, respectively [Tromp et al., 2001]. (d) LDA and LDA+WDA, featuring, respectively, a tiny gap and sizeable gap, obtained by Wu et al. [2004]. Notice that, apart from the vicinity of the X point near the Fermi level, the remainder of the band structure is accurately reproduced among all existing results.*

hexaborides clearly show the presence of a sizeable gap of $\sim$ 1 eV [Denlinger et al., 2002; Souma et al., 2003]. An example is shown in Fig. 3.3. In particular, EuB_6 exhibits an ellipsoidal, pocket-like, Fermi surface, with a Fermi energy lying at the bottom of the conduction band (Fig. 3.3b). This is further supported by electronic tunneling experiments that unveil a gap of this same order of magnitude, and by the optical absorption threshold in CaB_6 [Rhyee et al., 2003b]. Adding to this, the behavior of the low-temperature thermoelectric power hints at a clear separation between conduction and valence bands [Giannò et al., 2002].

It is thus evident that overwhelming evidence for a gap between the conduction and valence bands in the hexaborides comes from these experiments probing more or less directly the excitation spectrum.

results thus obtained reflect indeed the bulk behavior: the measured band dispersions match well with that of the bulk, band bendings are absent, and the size of the Fermi surface estimated from ARPES agrees with the Hall resistivity measurements of the carrier densities.

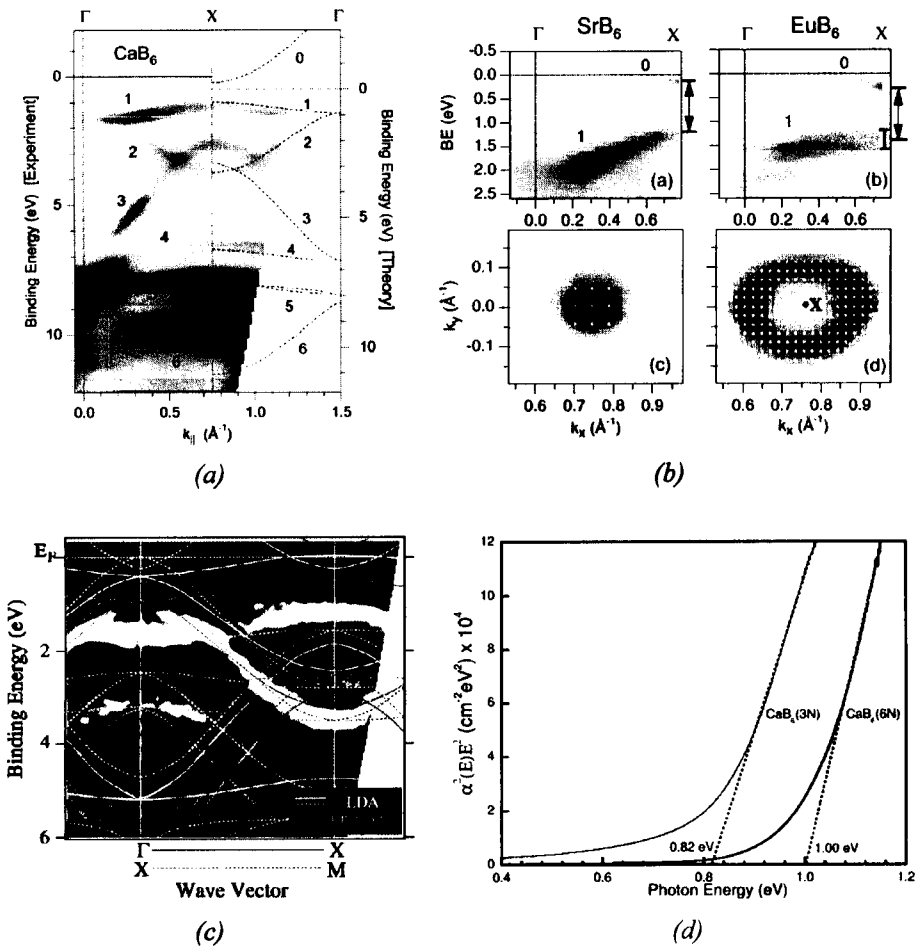

FIGURE 3.3 .: *(a) Band structure along Γ-X in the BZ as observed in ARPES for CaB_6, compared with the LDA+GW calculations [Denlinger et al., 2002]. (b) Band structure near the X point for SrB_6 and EuB_6 (top) and a snapshot of the Fermi surface (bottom) revealing the electron pockets [Denlinger et al., 2002]. (c) The same as in (a), measured by Souma et al. [2003]. (d) Infrared absorption for 2 samples of CaB_6, after Rhyee et al. [2003b].*

As to the dHvA and SdH results cited above, the dozens of Tesla required to observe the quantum oscillations allow for the re-interpretation of the carrier pockets as the result of a spin-split conduction band [Denlinger et al., 2002]. In fact, other authors measuring dHvA and SdH oscillations, even though obtaining results consistent with the latter, find clear evidence for full spin splitting of at least some pockets due to the high magnetic fields [Goodrich et al., 1998].

In summary, the electronic structure of divalent hexaborides is well reproduced using current implementations of DFT and LDA except for the vicinity of the Fermi level in the neighborhood of the crucial X point in the BZ. Here, theoretical calculations reveal themselves highly unreliable. This hindrance is solved by precise experimental probes that agree as to the presence of a gap of $\sim$ 1 eV between conduction and valence bands. In the case of EuB_6 it is found that the Fermi level lies at the very bottom of the conduction band.

3.4. Magnetism

EuB_6 outstands among divalent hexaborides for its robust ferromagnetism, due to the half-filled $4f^7$ shell of Eu^{2+}[8]. The $^8S_{7/2}$ state adopted by the ion, implies an effective Curie-Weiss magnetic moment[9] of $\mu_{eff} = 7.94\,\mu_B$, a value confirmed by several susceptibility and magnetization measurements, which also reveal that the long range magnetic order is established below $T_C \simeq 15\,K$ [Fisk et al., 1979; Geballe et al., 1968; Henggeler et al., 1998; Süllow et al., 1998; Wigger et al., 2004].

With regards to the bulk properties as a magnet, EuB_6 turns out to be a remarkably soft ferromagnet: there is no detectable hysteresis in the $M(H)$ curves (Fig. 3.4a), and remanent magnetization or coercive fields are well below the accuracy of the SQUIDs typically used [Goodrich et al., 1998; Süllow et al., 1998]. The magnetic response is generally isotropic but, under applied fields, Süllow et al. [1998] finds an interesting anisotropic behavior emerging below T_C : the system exhibits some magnetic anisotropy with an easy axis varying in direction with T and H (Fig. 3.4d). Connected with this, the FM transition occurs through 2 magnetic transitions at $T_{C1} = 15.3$ K and $T_{C2} = 12.7$ K, the latter being associated with a spin reorientation caused by the varying easy axis. At any rate, these anisotropies are rather small, to such an extent that, at zero field, the magnetic ground states are presumably degenerate, implying in turn the absence of FM domains.

No doubt is left as to the bulk character of the FM transition from the specific heat dependence on the temperature (Fig. 3.4f) [Fisk et al., 1979; Geballe et al., 1968; Süllow et al., 1998]. In addition, specific heat undoubtedly corroborates the origin of the magnetic moment stemming from the $4f$ shell, because of the *release* of $R\log(8)$ of entropy between $T = 0$ and $T > T_C$ (see inset in Fig. 3.4f). The magnetization curves $M(T, H)$ are generally well described by a Brillouin model[10] with $J = 7/2$ [Goodrich et al., 1998; Süllow et al., 1998; Wigger et al., 2004], and near the critical point the order parameter exhibits a power law scaling in T, H very close to what is expected for a Heisenberg ferromagnet [Süllow et al., 2000]. Finally, the pressure dependence of T_C (Fig. 3.4c) clearly reveals the enhancement of bulk ferromagnetism.

3.5. Transport

The interesting and unconventional nature of EuB_6 is best apprehended when analyzing the intricate correlations between electronic and magnetic degrees of freedom. Since the beginning, EuB_6 has revealed itself as an extremely good metal [Fisk et al., 1979; Guy et al., 1980], with residual resistivities ($T \to 0$) of the order of $\sim 10\mu\Omega$.cm, or less [Aronson et al., 1999; Süllow et al., 1998]. This observations clearly challenged the earlier theories for the electronic structure of divalent hexaborides and are responsible for the interest developed around this material in the beginning (70's-80's). A distinctive feature occurs in the behavior of $\rho(T)$ as the temperature is lowered past T_C . As seen in Fig. 3.5b, the onset of FM order signaled by the sharp increase in the magnetic susceptibility is accompanied by a precipitous drop of

[8] This should imply a strongly localized magnetism. Also remarkable is that EuB_6 is one of the few metallic ferromagnets that keep an apparent O_h^1 symmetry (sec. 3.1).

[9] This is defined as $\mu_{eff}^2 = \mu_B^2\, g^2 J(J+1)$, g being the Landé giromagnetic factor.

[10] A notable exception are the results inferred for the magnetic moment from neutron diffraction, which unveil a rather sluggish onset of the magnetic order close to T_C [Henggeler et al., 1998].

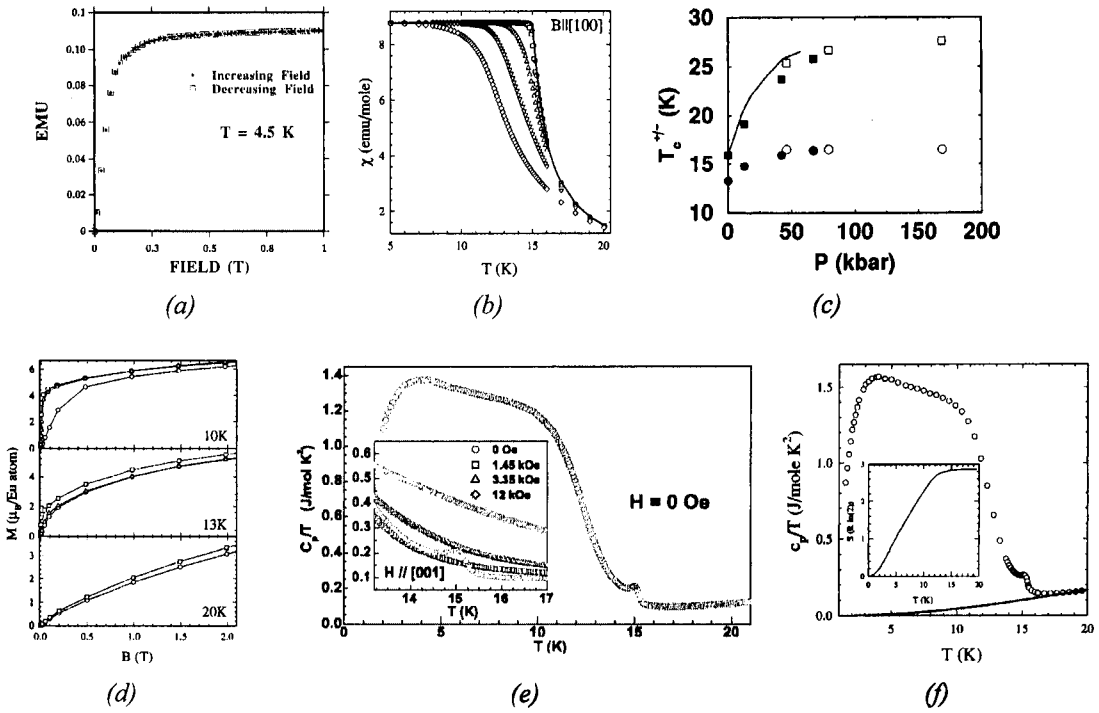

FIGURE 3.4 .: *Magnetic behavior of* EuB_6. *(a) Magnetization curves displaying no hysteresis [Goodrich et al., 1998]. (b) Typical behavior of the magnetic susceptibility (H=0.005, 0.01, 0.02, 0.05, 0.1 and 0.2 T). (c) Pressure dependence of* T_C *[Cooley et al., 1997]. (d) Slight magnetic anisotropy below* T_C *for* $B\|[100](\bigcirc)$, $B\|[110](\triangle)$ *and* $B\|[111](\square)$. *(e) Specific heat and detail of its field dependence near* T_C *[Urbano et al., 2004]. (f) Specific heat,* $c_p(H = 0)$, *and entropy (inset). All data from Süllow et al. [1998], except in (a), (c) and (e).*

the electrical resistivity. Such steep plunging is best appreciated in the normal T-scale of Fig. 3.5a, in which the drop in $\rho(T)$ almost resembles a superconducting transition in a dirty superconductor. Another point of notice is that, this enormous variation is preceded by a cusp-shaped upturn in $\rho(T)$ that develops slightly above T_C , and can be very accurately used to determine the Curie temperature by pure electrical means, as documented in Fig. 3.5c. Such cusp features are typical evidence for spin fluctuations interfering with transport [Fisher and Langer, 1968]. This hint is confirmed by the CMR response of EuB_6 under external magnetic fields, which can be as high as 100% in the vicinity of T_C [Paschen et al., 2000; Süllow et al., 1998] (Figs. 3.5e and 3.5f are quite explicit on this regard).

So far, these magneto-transport properties are reminiscent from the behavior observed in the heavily studied CMR manganites [Salamon and Jaime, 2001], albeit with smaller T_C 's. In fact, the realization that EuB_6 was a CMR material with a much simpler structure than the manganites, fueled the renewed interest and a series of important experiments during the last couple of years.

But some surprises exist down the road. Despite being a good metal, EuB_6 has a very small carrier density. More precisely, carrier densities estimated from Hall effect measurements amount to as little as $\sim 10^{19}\text{cm}^{-3}$, or ~ 0.001 carriers per unit cell [Fisk et al., 1979; Paschen et al., 2000; Rhyee et al., 2003a]. This is consistent with the small electron pockets that define the electronic bandstructure of EuB_6 in the vicinity of the Fermi energy, as resolved by ARPES. Notwithstanding, this material can

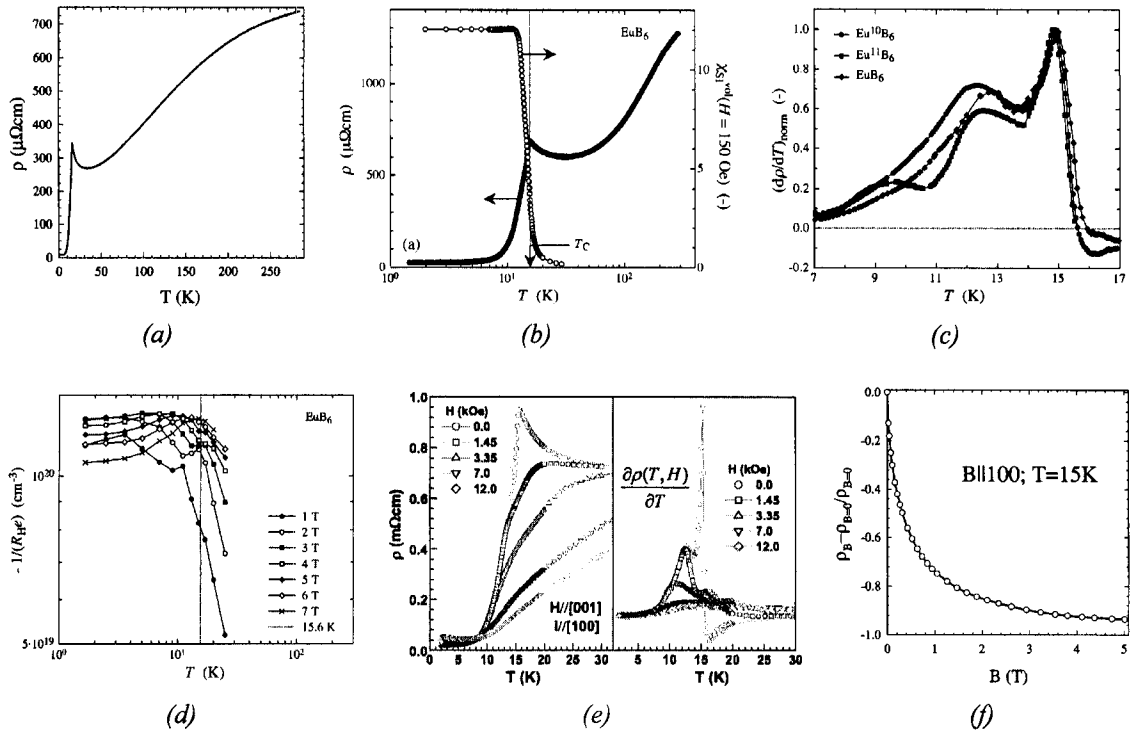

FIGURE 3.5 .: *Some magneto-transport properties of* EuB_6. *(a) Temperature dependence of* $\rho(T)$ *[Süllow et al., 1998]. (b)* $\rho(T)$ *and* $\chi(T)$ *display a clear correlation. (c) Low-temperature behavior of* $\partial\rho(T)/\partial T$. *(d) The Hall coefficient under different applied magnetic fields. (e) Magnetic field effect upon* $\rho(T)$ *and its derivative [Urbano et al., 2004]. (f) Magnetoresistance [Süllow et al., 1998]. Other data from [Paschen et al., 2000].*

attain residual resistivity ratios[11] of the order of 50-100 [Süllow et al., 1998, Table I], and consequent variations in electronic Hall mobility of one order of magnitude, exhibiting $|\mu_H|$ as high as $2000\text{cm}^2/\text{V}$ at $T = 1.5$ K [Paschen et al., 2000].

Most intriguing has been the reproducible variation of the effective carrier density, n_e with temperature. As soon as the FM order sets in at T_C , n_e is significantly enhanced with decreasing temperatures, and can vary by a factor of 3 between $T > T_C$ and $T \simeq 0$ K, as in Paschen et al. [2000]. Conversely, the same response is seemingly obtained with the application of an external magnetic field (Fig. 3.5d), and such situation is not related with the anomalous Hall effect characteristic of some FM metals [Pugh and Rostoker, 1953]. This implies that the localized spins influence the transport at a deeper level — much beyond scattering effects — that implies some sort of influence in the electronic structure.

Finally, specific heat, electrical resistivity and thermal conductivity measurements support the idea advanced earlier that the Boron skeleton and rare-earth ion are relatively independent in structural terms. This influences the phonon spectrum of the system and brings some peculiarities. In particular, the phonon spectrum can be explained in terms of a model that combines a typical Debye solid with an Einstein, dispersionless, mode [Mandrus et al., 2001]. The first is ascribed to the Boron cage for which a Debye temperature $\Theta_D = 1160$ K is obtained [Mandrus et al., 2001], thus reflecting the expected rigidity of the covalent structure. In, opposition, the dispersionless mode ascribed to the *independent* Eu ion lies

[11] $\rho(T \simeq 300\text{K})/\rho(T \simeq 0))$.

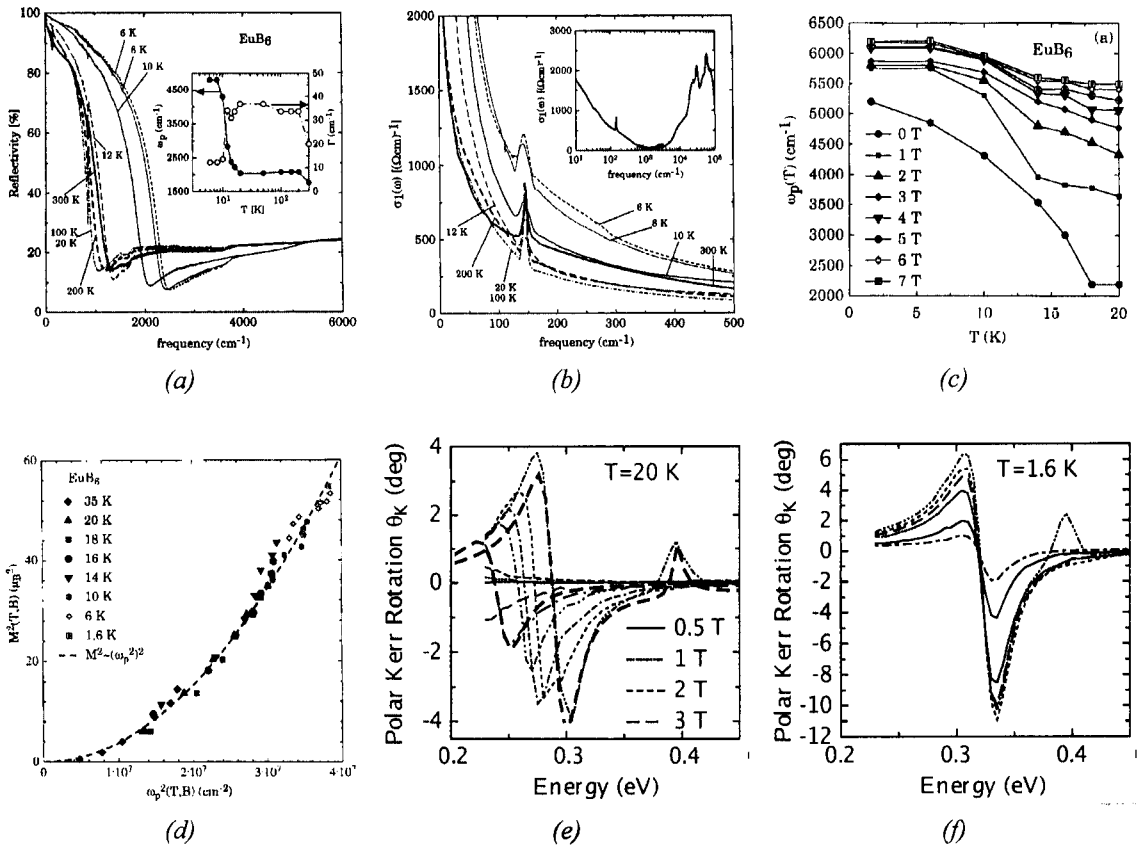

FIGURE 3.6.: *Magneto-optical response of* EuB_6. *(a) Reflectivity spectra for* EuB_6 *in the IR region. Inset shows* ω_p *and the metallic scattering rate,* Γ *[Degiorgi et al., 1997]. (b) Optical conductivity in the FIR. Inset shows the complete* $\sigma_1(\omega)$ *at 300 K [*ibidem*]. (c) Temperature and field dependence of* ω_p *[Broderick et al., 2002b]. (d) Scaling of* ω_p *with the magnetization [*ibidem*]. (e) Low energy polar Kerr rotation spectra above* T_C *, showing a blue-shift with increasing magnetic fields, after Broderick et al. [2003]. (f) The same as in (e), but far below* T_C *, and showing no shift in the resonance energy.*

only at $\Theta_E = 150$–$200\,\mathrm{K}$ [Vonlanthen et al., 2000; Wigger et al., 2004].

3.6. Optical Response

Optical reflectivity experiments performed in EuB_6 confirm the last mentioned phonon energy scales, that reflect themselves in the appearance of an optical mode near 145 cm^{-1} and another dispersive mode around 850 cm^{-1} [Degiorgi et al., 1997][12]. However, the most remarkable feature in the reflectivity signal is the giant blue-shift of the unscreened plasma edge, ω_p, simply under a temperature variation, never before seen [Broderick et al., 2003; Degiorgi et al., 1997].

At $T > T_C$, the reflectivity spectrum displays a typical metallic behavior, with a very well defined plasma threshold in the Far Infra-Red (FIR), at about 2200 cm^{-1}, as shown in Fig. 3.6a. As a consequence, its Kramers-Kronig transform, the optical conductivity, exhibits a consistent Drude-like shape in the FIR, as documented in Fig. 3.6b. With the establishment of the long-range magnetic order, the plasma edge increases markedly in such a way that ω_p varies by a factor of almost 3 between T_C and

[12] A brief conversion reminder: $1\ cm^{-1} \simeq 1.44\ K \simeq 1.24 \times 10^{-4}$ eV.

$T \ll T_C$ [Broderick et al., 2002b; Degiorgi et al., 1997]. Underlying this giant effect is a considerable transfer of spectral weight from the high energy components to the FIR region. The effect occurs irrespective of whether the temperature is lowered below T_C , or an external magnetic field is applied to the sample: for instance, at $T \simeq 1$ K there is no prominent shift up to $H = 10$ T [Broderick et al., 2002a]. This is summarized by the curves ω_p (T,H) in Fig. 3.6c, and is best appreciated through the remarkable scaling of ω_p with the magnetization shown in Fig. 3.6d. These experimental values of ω_p are obtained from fittings of the data to a Drude-Lorentz model[13], that describe quite accurately the reflectivity spectra at all temperatures and magnetic fields studied.

Another optical experiment especially suited to probe the response of the electronic system to the local magnetic environment, is the magneto-optical Kerr effect. EuB_6 is exceptional here too, with maximum values of the Kerr rotations lying among the very largest values ever observed [Broderick et al., 2002a]. A resonance occurs near 0.3 eV, and its blue-shift with H clearly reveals its association with the plasma edge (Figs. 3.6e,3.6f)[14]. This is strong evidence for an interplay between the free electron components (the conduction band electrons) and the localized electron components (the f electrons), in the sense that such interplay is known to cause a strong resonance in the Kerr angle at frequencies coinciding with the plasma edge [Feil and Haas, 1986], and has been observed in other f-electron systems [Salghetti-Drioli et al., 1999].

From a macroscopic and qualitative point of view, these features in the absorption spectra amount to a temperature (or field) induced variation of the *color* of this material, an interesting behavior in itself as color changes in solids usually happen through doping or structural transitions[15] .

At last, we come to Raman spectroscopy. It turns out that, in the FIR spectral region, and in a relatively narrow temperature window $T_C < T < T_m$, the diffusive response characteristic of a collision-dominated electronic scattering is replaced by a broad gaussian peak developing around 50–100 cm, as shown in Fig. 3.7a. The fact that this feature is strongly polarization dependent[16], and that the peak position evolves with T or H as plotted in Fig. 3.7b, is claimed to be strong evidence for the presence of magnetic polarons in this temperature range [Heiman et al., 1983; Peterson et al., 1985]. It therefore means that the PM-FM transition is mediated by the presence of a polaronic phase, and that these polarons are involved in precipitating the transition into the long-range ordered magnetic phase.

3.7. Doping EuB6

Due to the structural organization of the atoms inside the hexaborides' unit cell, the rare earth ion can be substituted relatively easily. Of interest to us is the substitution of Ca for some of the Eu atoms, defining the family of Calcium-doped Europium hexaboride ($Eu_{1-x}Ca_xB_6$).

Calcium hexaboride (CaB_6) — the extreme opposite to EuB_6 within this family — has been in the spotlight for some time following some experimental reports claiming its association with a new kind

[13] Which models incorporate a Drude (metallic) component and 4 or 5 Lorentz oscillator components associated with interband processes [Broderick et al., 2002b].

[14] For reference, 0.3 eV equates to approximately 2400 cm^{-1}.

[15] The blackbody *glowing* is obviously excluded from this discussion. Furthermore, besides EuB_6, only the pnictide TbN is known to display this temperature induced blue-shift [Wachter et al., 1998].

[16] It occurs only for selected configurations of the relative polarizations of the incident and scattered beams.

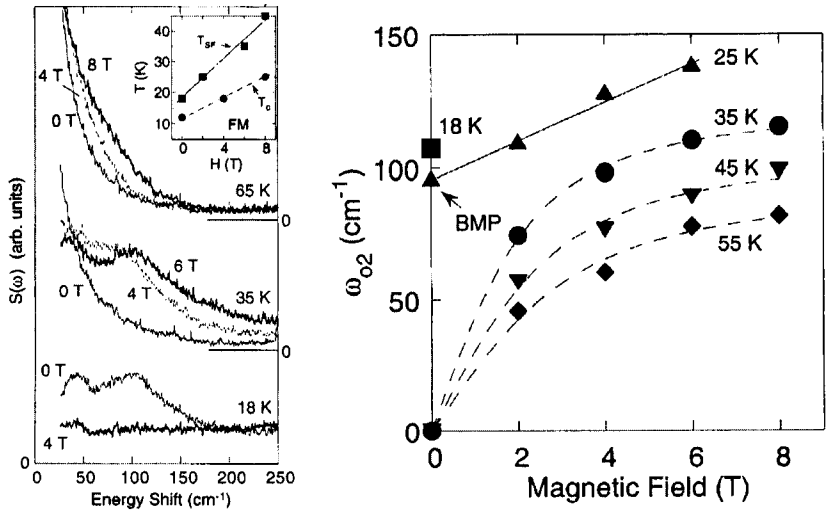

FIGURE 3.7.: *Raman scattering of* EuB_6 *in the FIR spectral region. (a) Field and temperature dependence of the Raman spectrum near and above* T_C *. The inset shows the temperature window of stability for this feature in the spectrum, as function of H [Nyhus et al., 1997]. (b) Variation in the position of the broad peak with H [*ibidem*].*

of, high-T_C , *exotic* magnetism [Young et al., 1999]. Nonetheless, since such conclusions have been proven to stem from a deficient experimental interpretation, they will not be addressed here, beyond the discussion included in Appendix 3.A.

The first thing one notices as EuB_6 is doped is a frailer ferromagnetism, with lower values of T_C consistently obtained the higher the doping strength, x (Fig. 3.8a), and terminating in CaB_6 exhibiting no FM at all. Concurrently, the massive drop in $\rho(T)$ below T_C characteristic of the compound at $x = 0$, is weakened and the distinctive metallic character evolves into a bad metal behavior at low/intermediate dopings (Fig. 3.8b). Despite this, the system still exhibits quite a CMR at $x = 0.2$ as shown in Fig. 3.8d. As x is increased from zero, the doped compounds start to display higher residual resistivities (Fig. 3.8b) and at the extreme doping limit, the resistivity ends up in a typical semiconducting behavior for CaB_6 (Fig. 3.8c). Hence the system clearly undergoes a Metal-Insulator (MI) transition induced by the doping level.

It is most interesting to observe how the transport correlates with the magnetization of the samples. One of the intriguing features is the fact that, for $x = 0.4$, the Hall coefficient R_H scales with the magnetization in a way that is at odds with the behavior found at $x = 0$. R_H is depicted in Fig. 3.8e: there is a range of magnetizations where this quantity remains basically unchanged, until some threshold is attained, above which $|R_H|$ is suddenly reduced (or, conversely, n_e increased)[17]. Also intriguing is the exponential dependence of the resistivity on the magnetization, as in Fig. 3.8f, and the exponential scaling of ω_p with M for $Eu_{0.6}Ca_{0.4}B_6$: there is a clear an significant distinction between this and the linear scaling observed in pure Europium hexaboride (Fig. 3.6d), that correlates with the fact that $\rho(T)$ seems to indicate that the $x = 0.4$ compound is arguably on or quite near the insulating side of the MI transition.

[17]Unlike what happens at $x = 0$, where the carrier density is immediately increased as soon as the magnetization is non-zero (Fig. 3.5c).

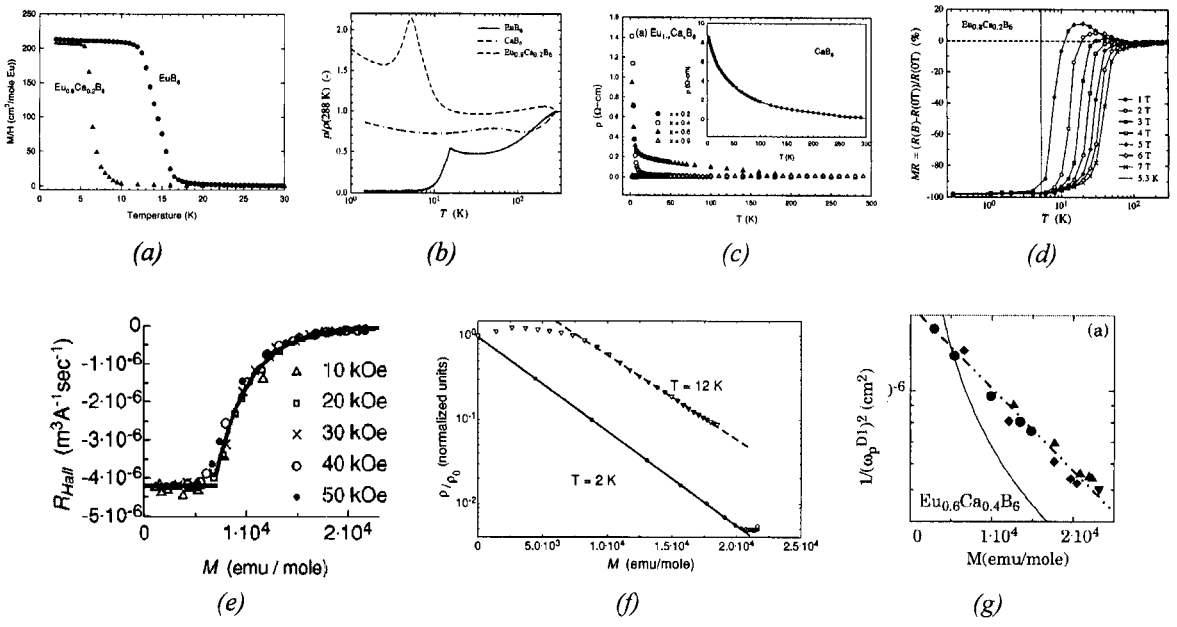

FIGURE 3.8.: *Some effects of doping in the magneto-transport properties of* $Eu_{1-x}Ca_xB_6$. *(a) $M(T)/T$ for x=0 and x=0.2, showing the smaller T_C of the latter [Rhyee et al., 2003c]. (b) Comparison of the normalized resistivity, $\rho(T)/\rho(288K)$, for x=0, 0.2 and 1 [Paschen et al., 2000]. (c) $\rho(T)$ for x=0.2, 0.4, 0.6, 0.9 and 1 (inset), where the evolution into the semiconducting behavior is clearly visible [Rhyee et al., 2003a]. (d) Magnetoresistance for x=0.2 at several external magnetic fields [Paschen et al., 2000]. (e) Scaling of the Hall coefficient, R_H, with M, for x=0.4 [Wigger et al., 2002b]. (f) Exponential dependence of the resistivity on the magnetization for x=0.4 [*ibidem*]. (g) Scaling of the unscreened plasma frequency with M for x=0.4 [Perucchi et al., 2003].*

A last point on the measured properties of Eu-based hexaborides is due to be addressed. Perhaps the reader became curious after examining Fig. 3.8, and comparing the data in panels 3.8b and 3.8c for $\rho(T)$ of CaB_6. Although the former uses a log scale in the horizontal axis, it is clear that this sample shows an overall featureless resistivity, whereas panel 3.8c displays a clear semiconducting-like $\rho(T)$. This example serves to illustrate an important point: the measured properties of Eu-based hexaborides are sample-dependent [Cooley et al., 1997; Denlinger et al., 2002; Süllow et al., 2000]. This is not so surprising as the origin of carriers lies in the presence of structural defects which beget a chemical potential at the bottom of the conduction band and a very small carrier concentration. This sensitivity to the sample preparation technique manifests itself both in EuB_6 and understandably more so in $Eu_{1-x}Ca_xB_6$. Therefore, there is no guarantee, in principle, that differently prepared/treated samples will exhibit exactly the same quantitative behavior for a given nominal composition[18] .

[18] Just as an example, the experimental signature for the two magnetic transitions described above for EuB_6 is seen only in the purest samples (characterized by the lowest $\rho(T=0)$), the same happening with the tiny anisotropy in the magnetism.

Appendices for this chapter

Appendix 3.A A word on the magnetism of CaB6

In 1999, Young et al. [1999] presented experimental evidence for ferromagnetism with $T_C \simeq 600$ K in a low density electron gas with densities of the order of 10^{19} cm^{-3}. Such unexpected magnetism appeared in samples of slightly doped CaB_6, namely $Ca_{1-x}La_xB_6$ and $Ca_{1-x}Th_xB_6$, but the effect was limited to an extremely narrow compositional range ($0.005 < x < 0.015$). In fact, this was the first experimental report of a FM ground state in a 3D diluted electron gas, and it was so apparently remarkable that David Ceperley himself commented on the same issue of Nature [Ceperley, 1999] that the reported effect might well be the blueprint for a polarized Wigner solid, a long standing theoretical prediction for the ground state of an extremely diluted electron gas [Jones and Ceperley, 1996; Zong et al., 2002].

As expected, a series of studies in CaB_6 ensued, trying to pinpoint the cause for such high-T_C magnetism. On the theoretical side, besides the polarized Wigner solid hypothesis, excitonic effects [Murakami et al., 2002] and defect states [Monnier and Delley, 2001] have been invoked. Interest in this compound raised, and it certainly influenced the amount of work done in EuB_6.

To my best knowledge of the literature, however, the magnetism seen in this compound has an extrinsic origin. In particular, Fe and Ni contaminants are the likeliest culprits. Despite the fact that initial experiments seemingly had control over the amount of magnetic impurities in the samples, a reasonable amount of literature concluded otherwise. All experiments that include a careful chemical characterization of the samples found that, although as-grown samples exhibit roughly the same magnetic behavior, the strength of the magnetic moment and the magnetic phase itself either disappears or is almost completely reduced upon surface treatment. These magnetic impurities are imprinted in the samples though electrochemical effects during the mixing phase [Bennett et al., 2004; Mori and Otani, 2003; Otani and Mori, 2002], and by contamination from the crucibles used in sample preparation [Matsubayashi et al., 2002, 2003; Taniguchi et al., 2002].

For this reason, CaB_6 is considered here as a diamagnet.

4. The DEM and Magnetic Hexaborides

"The theoretical oriented scientist cannot be envied, because nature, i.e. the experiment, is a relentless and not very friendly judge of his work. In the best case scenario it only says "maybe" to a theory, but never "yes" and in most cases "no". If an experiment agrees with theory it means "perhaps" for the latter. If it does not agree it means "no". Almost any theory will experience a "no" at one point in time — most theories very soon after they have been developed."

— **Albert Einstein**, Theoretische Bemerkungen zur Supraleitung der Metalle [Einstein, 1922].

4.1. The Basic Premises

The development of the microscopic model that is to be described in a moment, draws support from a series of factors revealed by the wealth of measurements presented in the last section. So, now I summarize my understanding of the essential experimental results in a way suitable for theoretical consideration in the following premises.

1. EuB_6 is a good metal characterized by a very small carrier density which, at $T \gg T_C$ is of the order of 10^{-3} electrons per unit cell. For definiteness, I take the reference values $n_e(T \gg T_C) \simeq 0.003$ and $n_e(T \ll T_C) \simeq 0.009$, as reported by Paschen et al. [2000].

2. The magnetism of EuB_6 arises entirely from the half-filled $4f$ shell of Eu^{2+} in the state $^8S_{7/2}$. This implies localized magnetism stemming from magnetic moments of magnitude $S = 7/2$. Within this formulation these electrons do not itinerate at all. We designate the resulting magnetic moment by *local spin*, and use the term *magnetization of the system* when alluding to long range ordered phases of these spins.

3. The electronic properties are to a great extent determined by the electronic structure near the Fermi level, E_F. The conduction and valence bands of EuB_6 are separated by a gap of the order of 1 eV, as per the discussion in section 3.3. This fundamental gap lies at the X point in the BZ, and the close proximity of E_F to the bottom of the conduction band dictates a pocket-like structure for the Fermi surface. Given that the interest will be almost completely in a temperature range of the order, or below, T_C, the electronic states in the valence band are disregarded.

4. The conduction electrons arise from the presence of defects in the structural arrangement of the

boron framework. These defects generate a surplus of electrons that occupy states in the conduction band.

5. Given the scalings of several magneto-transport properties, it is assumed that the influence of external magnetic fields is happening only through its effect on the magnetization of the localized spins. This excludes orbital effects, which is a generally valid assumption for moderate magnetic fields, like the ones used in most experiments.

6. The conduction band electrons interact with the local spins only through the Hund's coupling between the electron's spin and the local moments'.

7. Given the isovalency of Ca and Eu in the hexaborides, the Eu→Ca substitution in $Eu_{1-x}Ca_xB_6$ does not change significantly the number of carriers in first approximation. Therefore, from the point of view of our microscopic mechanism, this substitution has the simple effect of diluting the cubic lattice of localized spins, and of suppressing the number of lattice sites among which the conduction electrons can itinerate.

Our discussion starts with the case of EuB_6. The Hamiltonian describing conduction electrons hopping in a tridimensional cubic lattice, and coupled to local spins at each lattice site is

$$\mathcal{H}_{KLM} = \sum_{\langle i,j\rangle,\sigma} t_{i,j}\, c^{\dagger}_{i,\sigma} c_{j,\sigma} + \text{h.c.} + J_H \sum_{i,\alpha,\beta} \vec{S}_i \cdot \vec{\tau}_{\alpha,\beta}\, c^{\dagger}_{i,\alpha} c_{i,\beta} \tag{4.1}$$

usually known as $s-f$ or Kondo Lattice Model (KLM) Hamiltonian [Doniach, 1977], and is one of the canonical models in strongly correlated electronic systems. It applies generally to many materials that get their magnetic properties from a system of localized magnetic moments coupled indirectly via an interband exchange coupling to itinerant electrons. In this expression, $t_{i,j} \equiv t$ is the hopping integral between neighboring lattice sites, $c^{\dagger}_{i,\sigma}(c_{i,\sigma})$ are the second-quantized fermionic creation (annihilation) operators at latice site i, $\vec{S}_i$ represents the local magnetic moment of magnitude $S = 7/2$, J_H the exchange coupling of the latter to the itinerating electrons, and $\vec{\tau} = (\tau_1, \tau_2, \tau_3)$ is the vector of Pauli matrices. The sum in the first term is over all pairs of nearest neighboring sites $\langle i, j\rangle$.

Since $S = 7/2$ is a rather high spin, the local spin operator is replaced by the classical vector $\vec{S}_i$, parametrized with spherical angles as $\vec{S}_i = S\big(\sin(\theta_i)\cos(\varphi_i), \sin(\theta_i)\sin(\varphi_i), \cos(\theta_i)\big)$. This transforms the second term in (4.1) into a generalized potential term for the electrons, which will be a disordered potential above T_C , where all $\vec{S}_i$ are uncorrelated. Furthermore, the magnetic and electronic time scales are well apart in such a way that the magnetic background provided by the $\vec{S}_i$ is essentially quenched. This means that the typical time between spin fluctuations is much longer than the time for the electronic subsystem to reach its ground state[1].

4.1.1. Estimation of Parameters

The KLM requires a total of 3 parameters, namely t, J_H and the electronic density, n_e, that should be matched with the experimentally accessible values for EuB_6. The electronic density comes directly from

[1] In other words, the electronic problem can be diagonalized for static configurations of the local spins (adiabaticity).

the Hall effect measurements and, as said above, is taken as $n_e(T \gg T_C\ ) \simeq 0.003$ and $n_e(T \ll T_C\ ) \simeq 0.009$.

The hopping parameter, t, can be estimated both from electronic structure calculations and from effective electronic masses accessed through transport and optical experiments. Since both tend to present the results in terms of the effective mass, m^*, we extract the value of t by means of the relation $t \simeq \hbar^2/2m^*a^2$, that arises within a low-wavelength expansion of the simple cubic, tight-binding, dispersion relation. Using several sources that relate both m^* [Aronson et al., 1999; Kunes and Pickett, 2004; Massidda et al., 1996; Wigger et al., 2004] and t [Kunes and Pickett, 2004; Lin and Andrew.J.Millis, 2004; Massidda et al., 1996], one can see that t should lie somewhere in the interval

$$t \sim 0.5 - 1\,\text{eV}. \tag{4.2}$$

In our model t will be taken as a free fitting parameter. Consequently, for the model to be meaningful in the context of EuB_6 the results should lie within the above range.

As for J_H it is generally agreed in the literature [Kunes and Pickett, 2004; Lin and Andrew.J.Millis, 2004; Wigger et al., 2004] that, for divalent Eu:

$$J_H \sim 0.15 - 0.20\,\text{eV}, \quad \text{which yields} \quad J_H S \sim 0.52 - 0.70\text{eV}. \tag{4.3}$$

Therefore, t and J_H are of the same order of magnitude. Since the carrier density of our target system is so small, we anticipate that our KLM will in fact reduce effectively to the DE limit of the former. The DE limit of eq. (4.1) corresponds to the effective Hamiltonian (zeroth order in t/J_H) that is usually derived from the KLM in the strongly interacting limit $J_H \gg t$. This might certainly qualify as a bold assumption insofar as (4.3) and (4.2) do not yield such limit. The crucial point, however, is that the electron density is very small, thus placing the Fermi level too close to the bottom of the band. As we show below, this configures another limit for the application of the DEM, in which case the parameter J_H is removed from the problem[2], and the reasonable parameter space reduces to the relations in (4.2) and the possible values of n_e. The procedure to connect our model with the theory will be to pin the value of n_e to the densities found experimentally in the Paramagnetic or Paramagnetism (PM) phase. By doing this there remains only a single parameter – t – that is to be fitted and the result compared to (4.2).

4.2. The Double Exchange Model at Low Density

4.2.1. The DE Hamiltonian

All the subsequent discussions behoove the description of how the DEM emerges as the effective Hamiltonian of eq. (4.1). In (4.1) the quantization axes for the electron's spin have been chosen globally, say the Oz direction (the same for all classical spins $\vec{S}_i$, Fig. 4.1). Since we are interested in the limit $J_H \gg t$, this is not the best choice as the interacting term is nondiagonal in this representation, and it better be to simplify the projection of the high energy states within perturbation theory. Therefore, one needs to

[2]It is important to know that J_H has the value reported above, though.

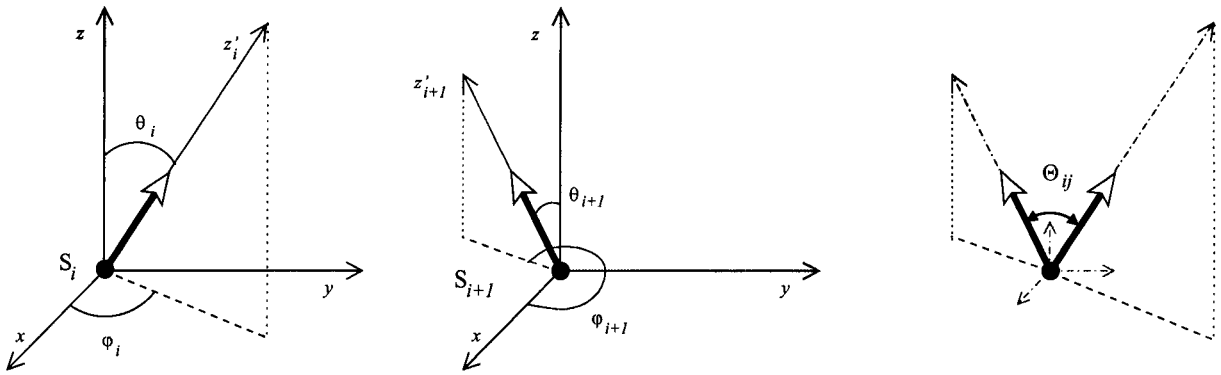

FIGURE 4.1 .: *Schematic representation of the quantization axes. The global quantization axis is Oz, and one defines local quantization axes, Oz_i' that correspond to the orthogonal coordinate system obtained from $Oxyz$ by a space rotation (θ_i, ϕ_i), thereby yielding a Oz_i' axis parallel to the direction of the (classical) local spin $\vec{S}_i$. The right-most depiction exemplifies the definition of the relative tridimensional angle, Θ_{ij}.*

diagonalize the second term of (4.1), which is accomplished by making the quantization axis to coincide with the direction of $\vec{S}_i$ at each site (a rotation by (θ_i, φ_i), see Fig. 4.1).

In order to simplify the notation we rewrite eq. (4.1) using a spinor notation for the second quantized fermion operators:

$$\mathcal{H}_{KLM} = \sum_{i,j} t_{i,j}\ \Psi_i^\dagger \tau_0 \Psi_j + \text{h.c.} + J \sum_i \Psi_i^\dagger \left(\vec{n}_i \cdot \vec{\tau}\right)\ \Psi_i\,, \tag{4.4}$$

where

$$J = J_H S\,, \quad \vec{S}_i = S\,\vec{n}_i\,, \quad \Psi_i \equiv \begin{pmatrix} c_{i,\uparrow} \\ c_{i,\downarrow} \end{pmatrix}\,, \quad \Psi_i^\dagger \equiv \begin{pmatrix} c_{i,\uparrow}^\dagger & c_{i,\downarrow}^\dagger \end{pmatrix}\,, \quad \tau_0 = \begin{pmatrix} 1 & 0 \\ 0 & 1 \end{pmatrix}\,, \tag{4.5}$$

the last one (τ_0) reflecting the fact that the kinetic term is diagonal in spin space in the eigenbasis of τ_3. We now introduce the $SU(2)$ matrices U_i, that define the unitary transformation in the Hilbert space of the single particle problem $(h \otimes s)^3$:

$$\boldsymbol{U} = \left(\bigoplus_{i=1}^{N} U_i \right)\,. \tag{4.6}$$

and that allows us to write (4.4) as:

$$\mathcal{H}_{KLM} = \sum_{i,j} t_{i,j}\ \Psi_i^\dagger U_i^\dagger U_i \tau_0 U_j^\dagger U_j \Psi_j + \text{h.c.} + J \sum_i \Psi_i^\dagger U_i^\dagger U_i \left(\vec{n}_i \cdot \vec{\tau}\right)\ U_i^\dagger U_i \Psi_i\,. \tag{4.7}$$

The goal, of course, is to find the U_i that diagonalize $\vec{S}_i \cdot \vec{\tau}$:

$$\tau_3 = U_i \left(\vec{n}_i \cdot \vec{\tau}\right)\ U_i^\dagger\,. \tag{4.8}$$

Fortunately we know from elementary quantum mechanics that, upon performing a rotation that brings Oz into the direction of $\vec{n}$, the eigenstates of τ_3, $\{|\uparrow\rangle, |\downarrow\rangle\}$, are transformed into the eigenstates of

[3] h is the Hilbert space defined on the basis of local Wannier orbitals $\{|\phi_i\rangle\}$ and s the Hilbert space defined by $\{|\uparrow\rangle, |\downarrow\rangle\}$.

$\vec{n}_i \cdot \vec{\tau}$, $\{|+\rangle, |-\rangle\}$. Therefore, if $\hat{\mathcal{R}}(\varphi, \theta)$ is the operator corresponding to such rotation and $R(\varphi, \theta)$ its representation in the basis $\{|\uparrow\rangle, |\downarrow\rangle\}$, we have:

$$R(\varphi_i, \theta_i) = U_i^{\dagger} . \tag{4.9}$$

Therefore, using the gauge $\chi = -\varphi$ for the Euler angles, one sees that

$$R(\varphi_i, \theta_i) = \begin{pmatrix} \cos\left(\frac{\theta_i}{2}\right) & -\sin\left(\frac{\theta_i}{2}\right) e^{-i\varphi_i} \\ \sin\left(\frac{\theta_i}{2}\right) e^{i\varphi_i} & \cos\left(\frac{\theta_i}{2}\right) \end{pmatrix} \Rightarrow U_i = \begin{pmatrix} \cos\left(\frac{\theta_i}{2}\right) & \sin\left(\frac{\theta_i}{2}\right) e^{-i\varphi_i} \\ -\sin\left(\frac{\theta_i}{2}\right) e^{i\varphi_i} & \cos\left(\frac{\theta_i}{2}\right) \end{pmatrix} , \tag{4.10}$$

and the Hamiltonian (4.7) can be written as

$$\mathcal{H}_{KLM} = \sum_{i,j} \tilde{\Psi}_i^{\dagger} \Big(\mathcal{T}_{ij} + \mathcal{J}_{ij} \Big) \tilde{\Psi}_j , \tag{4.11}$$

where

$$\mathcal{J}_{ij} = J \, \tau_3 \, \delta_{ij} , \quad \mathcal{T}_{ij} \equiv t_{ij} U_i U_j^{\dagger} = t_{ij} \begin{pmatrix} a_{ij} & b_{ij} \\ -b_{ij}^{*} & a_{ij}^{*} \end{pmatrix} , \quad \tilde{\Psi}_i = U_i \, \Psi_i \equiv \begin{pmatrix} c_{i,\Uparrow} \\ c_{i,\Downarrow} \end{pmatrix} \tag{4.12}$$

with new fermionic operators $c_{i,\Updownarrow}(c_{i,\Updownarrow}^{\dagger})$ that destroy (create) electrons at a site $\boldsymbol{r}_i$ with spin parallel or anti-parallel to the local moment therein. The hopping coefficients in this basis are explicitly:

$$a_{ij} = a_{ji}^{*} \qquad a_{ij} = \cos\left(\frac{\theta_i}{2}\right) \cos\left(\frac{\theta_j}{2}\right) + \sin\left(\frac{\theta_i}{2}\right) \sin\left(\frac{\theta_j}{2}\right) e^{i(\varphi_j - \varphi_i)} \tag{4.13a}$$

$$b_{ij} = -b_{ji} \qquad b_{ij} = \sin\left(\frac{\theta_i}{2}\right) \cos\left(\frac{\theta_j}{2}\right) e^{-i\varphi_i} + \sin\left(\frac{\theta_j}{2}\right) \cos\left(\frac{\theta_j}{2}\right) e^{-i\varphi_j} . \tag{4.13b}$$

Notice that, in this local quantization basis, the off-diagonal part of $\mathcal{H}_{KLM}$ has been transferred completely to the kinetic term, both in real and spin space. It is useful to realize that the diagonal and off-diagonal hopping elements have moduli

$$|a_{ij}| = \sqrt{\frac{1 + \vec{n}_i . \vec{n}_j}{2}} = \cos\left(\frac{\Theta_{ij}}{2}\right) \tag{4.14a}$$

$$|b_{ij}| = \sqrt{\frac{1 - \vec{n}_i . \vec{n}_j}{2}} = \sin\left(\frac{\Theta_{ij}}{2}\right) , \tag{4.14b}$$

the angle Θ_{ij} being the angle between the neighboring local spins, as illustrated in Fig. 4.1. The form (4.11) is perfect for the separation of the energy scales in the limit $J \gg t$. Such energies correspond to the eigenvalues of the (diagonal) second term in (4.11). For that we use the projection technique by means of which a unitary transformation is applied to $\mathcal{H}_{KLM}$

$$\hat{H}' = e^{\hat{S}} \, \hat{H} \, e^{-\hat{S}} , \tag{4.15}$$

and $\hat{S}$ should be chosen so as to integrate out the transitions between the eigenstates of $\mathcal{J}_{ij}$ in first order

in t/J. A suitable choice turns out to be (see Appendix 4.B for details)

$$S = \sum_{i,j} \tilde{\Psi}_i^\dagger s_{ij} \tilde{\Psi}_j \,, \quad \text{with} \quad s_{ij} = \frac{t_{ij}}{2J} \begin{pmatrix} 0 & b_{ij} \\ b_{ij}^* & 0 \end{pmatrix} , \tag{4.16}$$

that has precisely the intended effect upon the off-diagonal terms, yielding an effective Hamiltonian that reads

$$\mathcal{H}'_{KLM} \equiv e^S \hat{\mathcal{H}}_{KLM} e^{-S} = \sum_{i,j} \tilde{\Psi}_i^\dagger \; h'_{ij} \tilde{\Psi}_j \,, \tag{4.17}$$

where

$$h'_{ij} = J\delta_{ij} \begin{pmatrix} 1 & 0 \\ 0 & -1 \end{pmatrix} + t_{ij} \begin{pmatrix} a_{ij} & 0 \\ 0 & a_{ij}^* \end{pmatrix} + \mathcal{O}\left(\frac{t^2}{J}\right) . \tag{4.18}$$

When the high energy states are projected out in the strong coupling regime, the so-called Double Exchange effective Hamiltonian obtains:

$$\mathcal{H}_{DE} = \sum_{ij} t_{ij} a_{ij} d_i^\dagger d_j \,. \tag{4.19}$$

In this expression we took $J < 0$ for definiteness and dropped the constants. The operator $d_i \equiv c_{i\Uparrow}$ corresponds to an effective spinless electron[4] .

The DEM Hamiltonian looks extremely simple in that it corresponds to a tight binding problem for spinless electrons, but the simplicity is only superficial per force of the factor a_{ij} that encompasses the information about the local spin background. It is obvious at once that the electronic problem described by (4.19) is intrinsically disordered at any non-zero temperature on account of the existence of disordered spin configurations.

4.2.2. The DE Regime

It is worth to underline that the condition $J \gg t$ is essential for eq. (4.19) to be a strict effective Hamiltonian in the low energy subspace. Now it is shown that the DE approximation is still a valid one even if $J \sim t$ provided the carrier density is small. Recalling what as been estimated for J_H and t in § 4.1.1, I will concentrate on the case $J \equiv J_H S \sim t$.

The distinctive feature of the DE limit is that the electron always keeps its spin parallel to the local moment's at every visited site. Stated formally, this means that the local spin polarization per electron

$$m = \frac{1}{N_e} \sum_{i=1}^{N} \left\langle c_{i\Uparrow}^\dagger c_{i\Uparrow} - c_{i\Downarrow}^\dagger c_{i\Downarrow} \right\rangle_{GS} \tag{4.20}$$

is equal to unity for electron densities satisfying $n_e \leq 1$. Moreover, in the strict DEM limit ($J \gg t$), m, by construction, is unity for any configuration of the local spins, which is the same as saying, for any magnetization of the system. This is strikingly different from what happens in the opposite (Ruderman-

[4] It appears here spinless because it is the dynamic variable of an electron that hops between neighboring sites keeping its spin always parallel to the local moment directions. So, in actuality, it works as if there was no spin degree of freedom for these quasiparticles.

Kittel-Kasuya-Yosida (RKKY)) limit of the interaction strength: to lowest order of perturbation theory in J/t, the local spin polarization (4.20) is identically zero[5] . Therefore the local spin polarization is a good quantity to ascertain how close we are to the DE limit for arbitrary t/J, and that is what is studied below.

Let us start with the complete KLM Hamiltonian in the form (4.11), where we have a basis defined with local quantization axes. In order to proceed analytically in obtaining some estimates, we *restore the translational symmetry by hand* imposing a virtual crystal type of approximation (VCA) that amounts to replacing the hopping parameters a_{ij} and b_{ij} in (4.12) as follows:

$$a_{ij} \rightarrow |a_{ij}| \rightarrow a \equiv \cos\left(\frac{\Theta}{2}\right), \quad b_{ij} \rightarrow |b_{ij}| \rightarrow b \equiv \sin\left(\frac{\Theta}{2}\right). \tag{4.21}$$

Therefore the complex phases are ignored and a uniform tilting angle, Θ, is considered. With these simplifications, the KLM Hamiltonian is straightforwardly diagonalized in real space through a simple Fourier transform, yielding:

$$\mathcal{H}_{KLM} = \sum_k \tilde{\Psi}_k^\dagger \, h_k \tilde{\Psi}_k \,, \text{with} \quad h_k = \begin{pmatrix} \epsilon_a(k) + J & \epsilon_b(k) \\ \epsilon_b(k) & \epsilon_a(k) - J \end{pmatrix} \text{and} \quad \epsilon_x(k) = -2xt \sum_{\mu=1}^{3} \cos(k_\mu) \,. \tag{4.22}$$

In this result it is interesting to see that the hybridization between the two bands is dispersive and is not perturbative with respect to the $\epsilon_a(k)$ bands[6] . In addition, the hybridization is extremal at the center and boundaries of the BZ, being zero only at the k-space surface corresponding to $\frac{1}{4}$ filling. Working out the diagonalization in the spin sector, one gets the two bands:

$$E_\pm(k) = \epsilon_a(k) \pm \sqrt{J^2 + \epsilon_b(k)^2} \,, \tag{4.23}$$

and, as discussed in detail in Appendix 4.C, the expression for the local polarization (4.20) within this VCA:

$$m = -\,\text{sign}(J) \frac{1}{N_e} \sum_{k<k_F} \left(1 + \frac{\epsilon_b(k)^2}{J^2}\right)^{-\frac{1}{2}} . \tag{4.24}$$

In the limit of extremely low carrier density, the local polarization reads:

$$m \simeq -\,\text{sign}(J) \left[1 + \left(\frac{6tb}{J}\right)^2\right]^{-1/2} . \tag{4.25}$$

For definiteness, consider the PM phase, in which case $b = 2/3$[7] , and the local polarization at low

[5] This is readily seen writing (4.20) in the basis with global spin quantization axis where $m \propto \sum_i \cos(\theta_i) \langle c_{i,\uparrow}^\dagger c_{i,\uparrow} - c_{i,\downarrow}^\dagger c_{i,\downarrow} \rangle$. This is identically zero to zeroth order or in a PM regime. Notice how different this is from the *global* spin polarization.

[6] I.e., the hybridization between the two bands is essentially of the same order as the dispersion of the bands themselves.

[7] Consult Appendix 4.D for details.

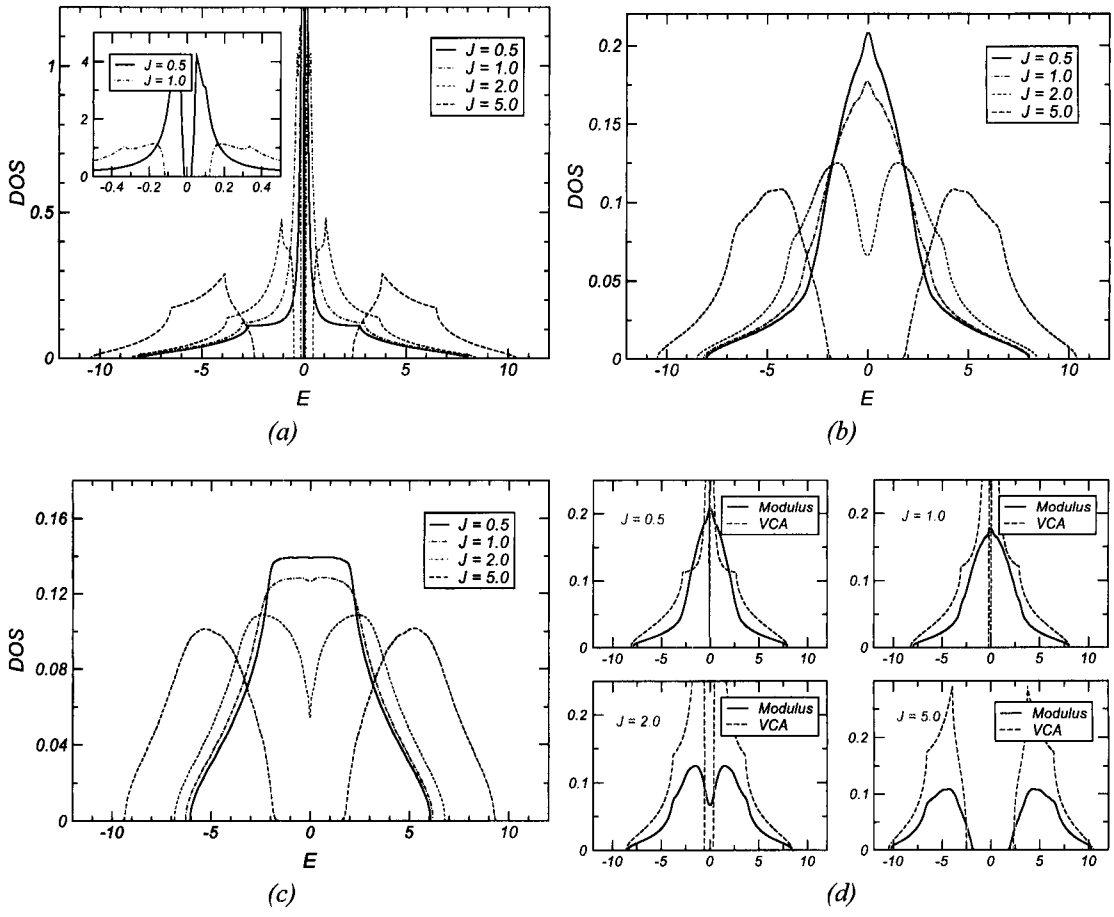

FIGURE 4.2 .: *DOS for the KLM in the PM phase ($M = 0$) within several approximations. (a) DOS associated with the spectrum of the VCA expressed in eq.* (4.23) *for $b = 2/3$. The inset is a magnification of the low energy range to highlight the features at smaller J. (b) DOS associated with the full KLM Hamiltonian* (4.11) *when the complex phases of a_{ij} and b_{ij} are ignored. The result is averaged over 100 configurations of local spin disorder. (c) Exact DOS for the full KLM Hamiltonian, averaged over 100 configurations of local spin disorder. (d) Case by case comparison between the results of (a) and (b).*

densities will have values like

$$m(n_e \ll 1) = \begin{cases} 0.243 & \text{if} \quad J = -t \\ 0.447 & \text{if} \quad J = -2t \\ 0.781 & \text{if} \quad J = -5t \end{cases} . \tag{4.26}$$

Well, it turns out that these results reveal nothing particularly interesting. But one should not neglect the approximations involved in the Virtual Crystal Approximation (VCA). In particular, we neglected the complex phases which is an uncontrolled assumption because the coherence factors are simply dropped *ad-hoc*. For example, the spectrum (4.23) is gapped no matter the strength of J, which is clearly wrong. In fact, the effects of the approximations assumed above can be observed in a rather illustrative way in the plots of Fig. 4.2 obtained with the recursive method. Panel 4.2a shows the DOS coming out of the VCA spectrum (4.23). Since within the VCA the full symmetry of the underlying lattice is maintained, one observes the expected sharp van Hove singularities and the gap mentioned above. Now, if we had

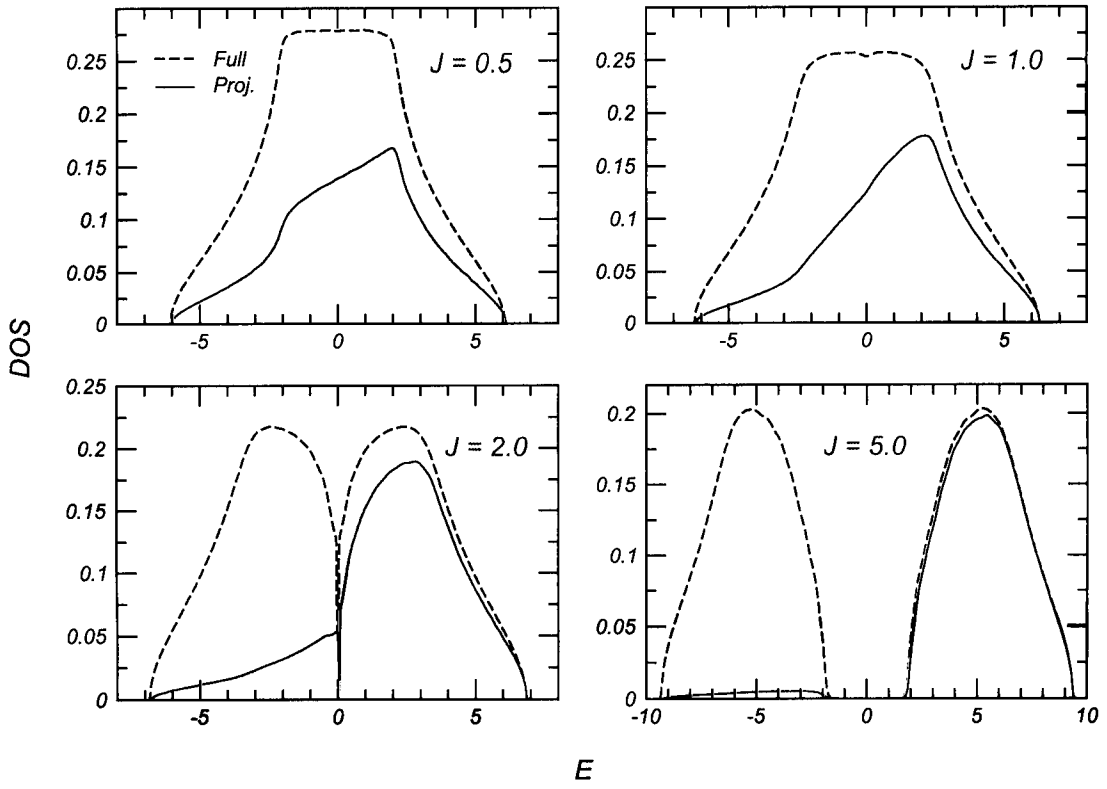

FIGURE 4.3 .: *Examples of projected DOS, $\rho_{\downarrow}(E)$, calculated via recursive method for the full KLM (solid lines), in comparison with the total DOS (dashed lines). Each panel pertains to a different coupling J. All results averaged over several instances of magnetic disorder ($M = 0$).*

not undergone the VCA and had restrained ourselves to the first simplification in (4.21) $\left((a_{ij}, b_{ij}) \rightarrow (|a_{ij}|, |b_{ij}|)\right)$, we would have obtained a disordered problem, whose DOS in the PM phase is presented in 4.2b. The magnetic disorder clearly smoothens the van Hove critical points while preserving the bandwidth. But, most importantly, the gap opens only above some threshold coupling. Panel 4.2d shows an explicit comparison between the two approximations. Panel 4.2c displays the exact DOS for the KLM. No approximations are involved other than averaging over configurations of magnetic disorder. The errors introduced by the different approximations are obvious from comparison with the exact DOS, namely, the overestimate of bandwidths, and the features small coupling J.

Figure 4.2c is the exact, disorder averaged DOS for the KLM, and the local polarization (4.20) can be calculated numerically just as well. The procedure is as follows. The zero temperature ground state of the electron system will be some Fermi sea wavefunction, which we designate $|FS\rangle$:

$$|FS\rangle = \prod_{m=1}^{N_e} c_m^{\dagger}|0\rangle \quad \text{, with eigenstates } \{E_m\}: \quad E_1 < E_2 < \cdots < E_{N_e} \tag{4.27}$$

Naturally, if we choose some arbitrary basis $\{\alpha\}$ the expectation value of $c_\alpha^{\dagger} c_\alpha$ is related to the eigenbasis projections through

$$\left\langle FS \left| c_\alpha^{\dagger} c_\alpha \right| FS \right\rangle = \sum_{m=1}^{N_e} |\langle \alpha | m \rangle|^2 \,, \tag{4.28}$$

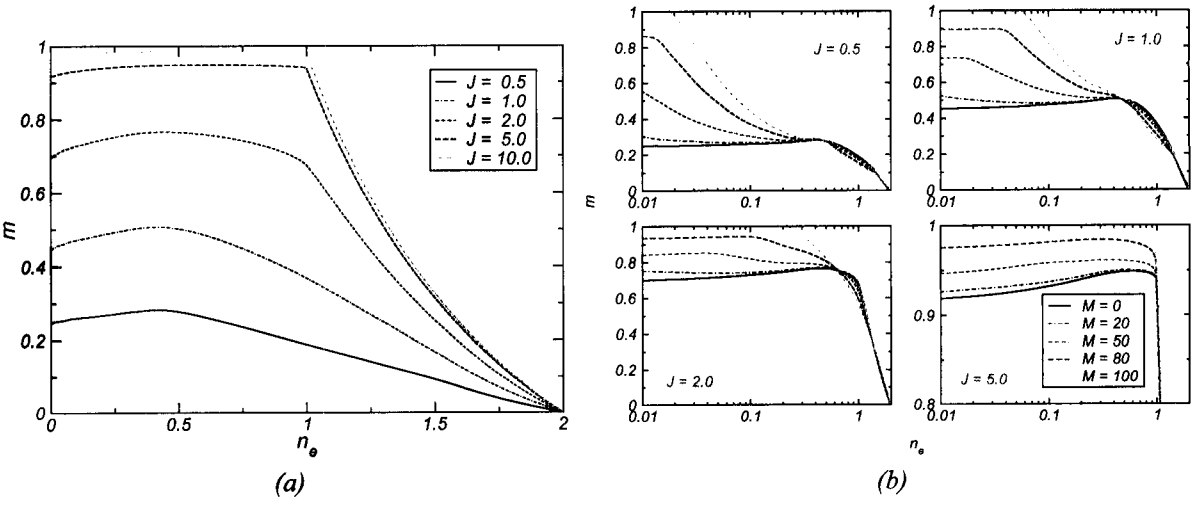

FIGURE 4.4 .: *Local polarization per electron as a function of n_e in for the KLM. (a) The local polarization in the PM phase for different couplings J/t. (b) The local polarization at different couplings and magnetizations (logarithmic scale in the horizontal axes).*

and this is true, in particular, for the local quantization basis, making it possible to write (4.20) relative to the eigenstates:

$$m = \frac{N}{N_e}\frac{1}{N}\sum_i \sum_{m=1}^{Ne} \left[|\langle i, \Uparrow | m\rangle|^2 - |\langle i, \Downarrow | m\rangle|^2 \right]$$
$$= \frac{N}{N_e}\int_{-\infty}^{E_F} [\rho_{\Uparrow}(E) - \rho_{\Downarrow}(E)] \ . \tag{4.29}$$

In the last expression we introduced the locally polarized LDOS, defined as:

$$\rho_{\Updownarrow}(E) = \frac{1}{N}\sum_{i=1}^{N} \rho_{i,\Updownarrow}(E) \quad \text{and} \tag{4.30}$$

$$\rho_{i,\Updownarrow}(E) = \sum_m |\langle i, \Updownarrow | m\rangle|^2 \, \delta(E - E_m) \tag{4.31}$$

The last expression is simply a projected DOS, and since Chapter 2 that we are familiar with the procedures to handle projected DOS for any type of quantum system. In particular we know (Appendix 2.D) that, within the philosophy of the recursive method, (4.30) can be readily obtained from an average over random choices of starting vectors projected onto a single local spin subspace (either $|\Uparrow\rangle$ or $|\Downarrow\rangle$)[8]. Examples of these projected DOS thus calculated are shown in Fig. 4.2.2. These projected DOS and the global DOS allow the direct calculation of m, which has been calculated for the exact KLM with the outcome shown in Fig. 4.4. There are several interesting aspects regarding the results in this figure. Let us look first at panel (a), calculated for the PM phase (random local spin orientations). First, it clearly evinces that, in the case where $J = t$, the local polarization per electron is roughly ~ 0.5 for small

[8]This means that we can simply choose a normalized starting vector of the type $|u_0\rangle = \sum_{i=1}^{N} a_i^0 |i, \Uparrow\rangle$ and calculate the LDOS projected onto this state (averaging over a set of random $\{a_i^0\}$) to obtain $\rho_{\Uparrow}(E)$.

densities, meaning that 75% of the states are parallel to the local spins. Now a 75% polarization is a considerable polarization and thus one can argue that the system is leaning rather significantly towards the DE limit[9]. The situation improves significantly as J is increased, just as expected. In second place, we notice that this state of affairs persists over a rather broad range of densities, wherefrom one can tentatively infer that the DE limit describes more successfully the KLM for $J/t \sim 1$ than the RKKY limit does. The third point has to do with the maximum of $m(n_e)$ occurring at some density in the vicinity of $1/4$ filling. To comprehend that we invoke the analytical calculation developed above, and the resulting dispersion (4.23) in particular. As mentioned above, the hybridization is maximal at the bottom of the band, and zero precisely at $1/4$ filling. Although with due caution in view of the consequences of the approximations involved, this provides a qualitative explanation for the behavior of the curves $m(n_e)$.

Of course that a criterion based on the magnitude of local polarization is only valid in the PM phase, where we know that such quantity vanishes in the RKKY limit. Within RKKY, as soon as the local spins start to be polarized (i.e., as soon as $M > 0$) the global polarization per electron will be unity in the limit $n_e \to 0$. Since

$$m = \frac{1}{N_e} \sum_i \cos(\theta_i) \langle c^\dagger_{i,\uparrow} c_{i,\uparrow} - c^\dagger_{i,\downarrow} c_{i,\downarrow} \rangle \,, \tag{4.32}$$

we can expect, for the sake of the argument, local and global polarizations to be related on average by $m \simeq M m_{global}$, in the RKKY limit. Consequently, if the RKKY were to hold, m would be expected to saturate at M. In panel (b) one observes that as the magnetization of the system is increased, the local polarization increases accordingly, and is maximum at the lowest densities. The important note, however, is that the *saturation* of m as $n_e \to 0$ occurs not at M but at higher values. In particular, already for $J = 1$ the saturation value of m is always closer to unity (the DE limit) than M (the RKKY limit), as is clearly shown in that panel.

Therefore, the lowest densities are closer and closer to the DE limit even for moderate couplings. From this we argue that the physics of the KLM at moderate dopings, $J \gtrsim t$ can be captured to a great extent by the DE effective Hamiltonian. From here onwards, and unless explicitly mentioned otherwise, the discussion is based on such Hamiltonian, in the form written in (4.19).

4.3. Magnetic Disorder in the DEM

Due to the assumption of classical localized spins, the DEM (and, naturally, its ascendant the KLM) is intrinsically disordered. A glimpse of that was already seen in the former paragraphs where the need to *average over several realizations of disorder* arose. We recall that

$$\mathcal{H}_{DE} = \sum_{ij} t_{ij} a_{ij} d^\dagger_i d_j \quad , \quad a_{ij} = \cos\left(\frac{\Theta_{ij}}{2}\right) e^{i\Phi_{ij}} \,, \tag{4.33}$$

[9]It is important to notice that in the extreme RKKY limit the local polarization is effectively zero. Thus we are comparing 0.75 with zero.

where the relative complex phase has the value

$$\Phi_{ij} = -\operatorname{arccot}\left[\cot(\varphi_i - \varphi_j) + \cot\left(\frac{\theta_i}{2}\right)\cot\left(\frac{\theta_j}{2}\right)\csc(\varphi_i - \varphi_j)\right]. \tag{4.34}$$

This places the DEM among one of the conventional models of disorder for electronic systems [Kramer and MacKinno 1993]: non-diagonal disorder. The essence of this lies in that we assume static configurations of the $\{\vec{S}_i\}$ which, through the spin dependent hopping, provides a random background among which the electrons itinerate. This is an approximation of quenched magnetic disorder, and assumes the separation of the characteristic relaxation times of the electronic and local spin subsystems.

From (4.33) two important aspects regarding the nature of the disorder in this system emerge. The first one is that the complex Berry phase in a_{ij} works as if a random magnetic flux crosses each closed path within the lattice, and, in this sense it is a mixture of a random hopping and random flux models. Secondly, the disorder is quite weak indeed. Although off-diagonal disorder is generally weaker in comparison with diagonal disorder, the DEM provides one of the weakest cases. This can be seen analyzing the probability distribution for the absolute value of the hopping $|a_{ij}|$:

$$\mathcal{P}(a \equiv |a_{ij}|) = \int \frac{d\Omega_i}{4\pi}\int \frac{d\Omega_j}{4\pi}\,\delta\left(a - \sqrt{\frac{1+\cos(\Theta_{ij})}{2}}\right) = 2a,\ (0 < a < 1)\,. \tag{4.35}$$

$\mathcal{P}(a)$ is linear and drops to zero as a approaches zero, which is clearly weaker than, say, an uniform distribution with the same width. This qualification based solely upon the probability distributions and their statistical consequences[10] , is naturally inconclusive as to the physical consequences. For that one needs to address the nature of the states, namely which and how many states are localized. But before delving onto such matters, it is appropriate to introduce our approach to the thermodynamics of the DEM.

4.3.1. Hybrid Thermodynamic Approach

The DE Hamiltonian (4.33) represents a system of classical spins that do not interact directly via a conventional exchange term. Their interaction comes indirectly from the fact that certain configurations of the local spins will minimize the energy of the electron gas. At absolute zero temperature, it is more or less evident that the ground state corresponds to ferromagnetism for any density of electrons [Tsunetsugu et al., 1997]. For other than this specific case, thermodynamics comes into play. Of course, all relevant quantities follow from the partition function

$$\Xi = \int \mathcal{D}\vec{S}_i\ \mathrm{Tr}\Big[\exp\big(-\beta(\mathcal{H}(\vec{S}_i) - \mu N)\big)\Big]\,. \tag{4.36}$$

The integral spans all local spins, $\vec{S}_i$, and the trace is over the electronic degrees of freedom, for which N is the number operator. The electrons can be easily traced out in this grand canonical ensemble yielding

[10] For instance, the average fluctuations associated with them.

an (exact) effective spin Hamiltonian that reads

$$\Xi = \int \mathcal{D}\vec{S}_i \exp\left(-\beta H_{eff}(\vec{S}_i)\right), \quad \beta H_{eff} = -\sum_n \log\left[1+\exp\left(-\beta(E_n(\vec{S}_i)-\mu)\right)\right], \tag{4.37}$$

$E_n(\vec{S}_i)$ being the eigenenergies of the one-electron Hamiltonian. Here, however, lies the origin of the difficulties that this system poses to analytical and numerical approaches. The latter are rather notorious, for one might think that once the effective spin Hamiltonian is written down, the energy of spin configurations can be calculated and the problem can be tackled with usual Monte Carlo (MC) techniques. That is indeed so formally. Unfortunately, the effective Hamiltonian — that is, the energy associated with a given spin configuration — requires the knowledge of the electronic eigenstates associated with such configuration. In other terms, the MC methodology would imply the full re-diagonalization of the electronic problem at every tentative update of the local spin configuration[11] . This is clearly prohibitive, imposing an upper limit of $\sim 6^3$ on the sizes of the systems that can be thus studied [Calderón and Brey, 1998; Dagotto, 2003], and such sizes are meaningless as far as localization studies are concerned.

Our approach to this problem tries to circumvent these issues through a compromise in which the electronic problem is solved exactly and the spin subsystem treated within mean-field[12]. It hinges upon the fact that, writing H_{eff} in terms of the total electronic DOS

$$\beta H_{eff} = -\int_{-\infty}^{\infty} \rho(E,\vec{S}_i)\log\left[1+\exp\left(-\beta(E-\mu)\right)\right]dE, \tag{4.38}$$

the dependence on the spin configuration is completely transferred to the DOS. Since the treatment of the exact effective Hamiltonian is out of reach, we resort to the Bogoliubov-Gibbs inequality for the canonical free energy[13] :

$$\mathcal{F} \equiv -T\log(\Xi) \leq \langle H_{eff}\rangle_t - T\mathcal{S}_t . \tag{4.39}$$

Here $\langle ...\rangle_t$ means the averages are calculated with a *trial* statistical operator — other than the canonical Maxwell distribution — and $\mathcal{S}_t$ is the associated entropy. Since our system is expected to exhibit either ferro or paramagnetism, the simplest suitable choice is the one generated by the uniform mean-field Hamiltonian

$$\mathcal{H}_t = -h\sum_i^N \vec{S}_i{}^z , \tag{4.40}$$

where h is a variational parameter used to minimize the inequality (4.39). Since all averages are now done with regard to this $\mathcal{H}_t$, we have:

$$\mathcal{M} \equiv \left\langle \vec{S}_i \right\rangle_t = \int \mathcal{D}\vec{S}_i \exp(-\beta\mathcal{H}_t)\vec{S}_i = \left(\coth(\beta h) - \frac{1}{\beta h}\right)\vec{u}_z \equiv \mathcal{L}(\beta h)\,\vec{u}_z , \tag{4.41}$$

[11] This is a serious difficulty because the electronic spectrum, as a whole, reflects global properties of the system and therefore is rather sensitive even to minor changes in the underlying spin configuration.

[12] The principles behind this approach have also been presented by Alonso et al. [2001b].

[13] Units where $k_B = 1$, and thus $T = 1/\beta$.

($\mathcal{L}(x)$ is the familiar Langevin function),

$$-T\mathcal{S}_t = \log\left[\frac{\sinh(h)}{h}\right] - h\mathcal{M}\,, \tag{4.42}$$

and

$$\beta\,\langle H_{eff}\rangle_t = -\int_{-\infty}^{\infty} \left\langle \rho(E,\vec{S}_i)\right\rangle_t \log\Big[1+\exp\big(-\beta(E-\mu)\big)\Big]dE\,. \tag{4.43}$$

Therefore, the trouble in calculating the equilibrium free energy now boils down to the computation of $\left\langle \rho(E,\vec{S}_i)\right\rangle_t$. We know that the recursive method can be used to obtain the exact $\rho(E,\vec{S}_i)$ for a given configuration $\{\vec{S}_i\}$. It is then a matter of straightforward statistics to obtain the averaged DOS. Hence, the electronic problem is still treated exactly for every configuration of local spins. These configurations are generated with the probability distribution $\sim \exp(-\beta h \sum_i \vec{S}_i{}^z)$ and, since βh and $\mathcal{M}$ are univocally related through (4.41), we simplify the notation and write

$$\left\langle \rho(E,\vec{S}_i)\right\rangle_t \equiv \rho(E,\mathcal{M}) \tag{4.44}$$

whenever we refer to the *DOS averaged over configurations of disorder compatible with an average magnetization* $\mathcal{M}$.

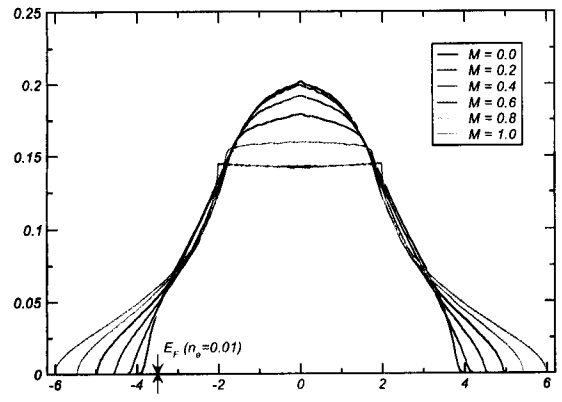

FIGURE 4.5 .: *DOS for the DEM at different magnetizations, as defined in eq.* (4.44). *The arrows signal the position of* $E_F(\mathcal{M}=0)$ *for an electron concentration of* $n_e = 0.01$ *(*$N = 100^3$ *sites, PBCs,* 10×5 *averages).*

We also recall that when $E_F \gg T$, the logarithm in eq. (4.43) can be replaced by $\Theta(\mu - E)$ meaning that the thermal excitations of the electronic subsystem can be neglected to a great extent. According to our discussion in sec. 4.1, $t \sim 1$ eV in EuB_6, whereas $T_C \simeq 15K$. This suggests a "zero-temperature" description of the electronic system, the thermal/entropic effects being assigned entirely to the spin subsystem[14] .

The essential ingredient is the ability to calculate $\rho(E,\mathcal{M})$ accurately, yet in a time and memory effective manner, provided by the recursive method. It is worth reminding the reader that, according to the details of the recursive technique expounded in chapter 2, the calculation of $\rho(E,\vec{S}_i)$ (that is, for a given configuration) encompasses in itself an average over stochastic starting orbitals. This would require a double averaging procedure[15] to extract $\rho(E,\mathcal{M})$. In view of the self-averaging nature of the DOS, it turns out that this averages can be combined in one single averaging process, changing the spin configuration at every new starting vector. Fig. 4.5 shows some examples of this central quantity obtained at different magnetizations. Each of those curves — all averages included — can be obtained in essentially the same time it takes to fully

[14]Clearly this is true as far as thermal excitations of the electronic states across the Fermi level are concerned. The electron system will indirectly *feel* the effects of temperature through the dependence of the DOS on $\mathcal{M}$ and, consequently, on T.

[15]Over starting wavefunctions for a static configuration $\{\vec{S}_i\}$, repeated several times for different $\{\vec{S}_i\}$, generated stochastically.

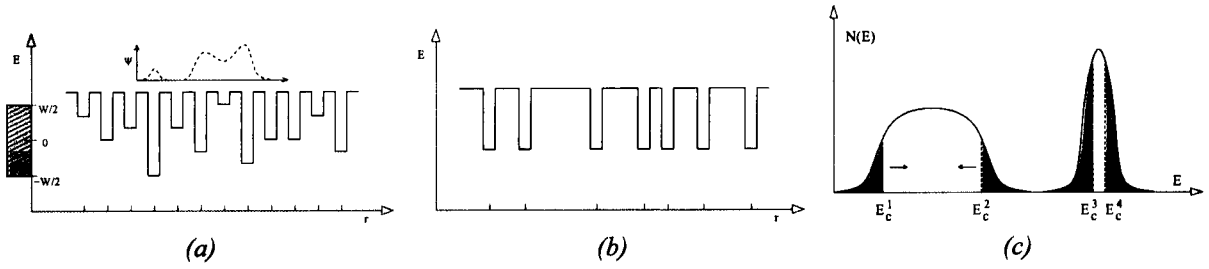

FIGURE 4.6 .: *Schematic depiction of a putative random potential for Anderson's model of diagonal disorder (a), and for a non-diagonal situation, similar to the DEM (b). On the top of (a) we sketch two putative localized wavefunctions. The last picture (c) is a schematic representation of the mobility edges (E_c).*

diagonalize the Hamiltonian of a system 250 times smaller using standard diagonalization routines!

4.3.2. Anderson Localization

We shall give a precise definition for our utilization of the term *disordered* in the context of electronic systems. An electronic system is *ordered* whenever its characteristics can be explained departing from a long-range ordered, translationally invariant, description, including the effects of dynamic or static disturbances by perturbation theory. It is *disordered* when such an approximation is meaningless — and the DEM (4.33) at finite magnetization is one such case.

Disordered problems are interesting because localized states can therein occur. Again, we need an operational definition of localized state. In the crystalline case, the probability of finding a Bloch electron at a given lattice site, $\vec{R}_i$, is the same for all sites, and for all k-states[16] . Bloch states are cases of ideal *extended states* in that they spread uniformly over the entire system. When disorder is gradually added, the phase coherence length and mean free path of the states decrease, and $|\psi|$ starts to fluctuate markedly in space. Nevertheless, such states can still be extended if the wavefunctions spread indefinitely across the system. At some point, disorder and interference will be so intense that some wavefunctions will remain finite only within restricted regions of space, decaying exponentially to the outside. The extent of those regions is characterized in terms of a characteristic length — the *localization length.*

Anderson [1958] carried the first quantitative calculations on the problem of localization using a simple but relevant model of electronic disorder. He considered a three dimensional point lattice occupied with atoms having a single state of energy ϵ_i, and studied the effects of disorder by maintaining the lattice positions and taking ϵ_i as a stochastic variable, uniformly distributed within $[-W/2, W/2]$ (Fig. 4.6a). The Hamiltonian for such model is

$$\mathcal{H}_{AM} = t \sum_{ij} c_i^\dagger c_j + \sum_i \epsilon_i c_i^\dagger c_i \,. \tag{4.45}$$

Anderson places a single electron at some site $\vec{R}_i$ at $t = 0$, and, studying the time evolution of the wavefunction, inquires about the probability of finding the electron at that point again as $t \to \infty$. If there is no localization, the wavefunction amplitude will diffuse away to infinity, leading to a zero probability

[16]This probability is $N^{-1/2}$, and follows from the plane-wave normalization.

of return as $t \rightarrow \infty$. However, this probability will be nonzero if the starting site belongs to a region containing a localized state. This happens because in such case, the starting state has a finite overlap with the localized one(s), meaning that diffusion gets restricted to a finite volume. His important result was that the magnitude W/t decides between these two alternatives, and that there is a critical W_c above which the probability of return is zero for a state with $E = 0$. This threshold defines the so-called Anderson transition: the point at which all the states become localized.

Later Economou and Cohen [1972], studying the analytical properties and convergence of a suitably defined perturbation expansion of the electronic self energy, were able to establish that, for a given energy, there exists a $W_c(E)$ such that when $W > W_c(E)$ the states at that energy are localized. Stated differently, for a given strength of disorder, W, there will be regions of the spectrum consisting of only localized states, the remainder of the band corresponding to extended states (Fig. 4.6c). This is the sort of transition we are interested in. It follows from Economou's calculation that the transition between extended and localized regions is sharp, characterized by a specific energy, E_c, dubbed *mobility edge*[17] by Mott [1967]. The Anderson transition can therefore be interpreted as the merging of pairs of mobility edges as depicted in Fig. 4.6c, thus completely exhausting the extended states.

Two ingredients are crucial in Anderson's and Economu's treatment: the local point of view, and the considerations of statistical distributions imposed by the stochasticity of ϵ_i. Unfortunately, these are also the reasons why analytical approaches are so difficult and generally inaccurate. In a simplistic way, any analytical approach will need to employ some averaging procedure at some point to proceed and, as Economu already pointed out, there lies the very delicate point: either calculations are cumbersomely difficult, or the wrong assumptions simply wipe out the localization effects from the results.

Numerical calculations have been an essential tool in establishing the remarkable features of localization since the early years, and arguably the most reliable means in obtaining precise quantitative information [Kramer and MacKinnon, 1993]. The Anderson Hamiltonian (4.45) played an important role, being the most studied model in this context. As a consequence, much of the concepts, results and intuitions related to Anderson localization in disordered electronic systems, stem from the properties of this specific model. The DEM, on the other hand, has remained much unexplored in this context[18], and, as we will see below, there are some peculiarities not found in the results for the Anderson model. For comparison purposes, and clarity, we decided to accompany the results below for the DEM with the behavior of the Anderson model under the same circumstances. We therefore proceed to analyze the problem of disorder in the DEM versus the Anderson model under different perspectives[19] .

4.3.2.1. Full Diagonalization — Wavefunction Based

There are essentially two rigorous ways to ascertain exactly whether we have localization in a system or not. One of them is obviously through σ_{DC} at $(T = 0)$[20], and the other is by looking directly at the spacial distribution of wavefunctions of the disordered Hamiltonian. Both entail the full diagonalization

[17] Absence of diffusion for the localized states, results in a vanishing Kubo-Greenwood conductivity: hence the origin of the term *mobility edge*. See also Cohen et al. [1969].

[18] Essentially because of the DEM had been studied in the context of the manganites, where Anderson localization effects alone turned out to be rather inconsequent for such target compounds [Li et al., 1997; Millis et al., 1995; Varma, 1996].

[19] It goes without saying that we are only interested in the 3D case.

[20] $T = 0$ is important to suppress activated behavior.

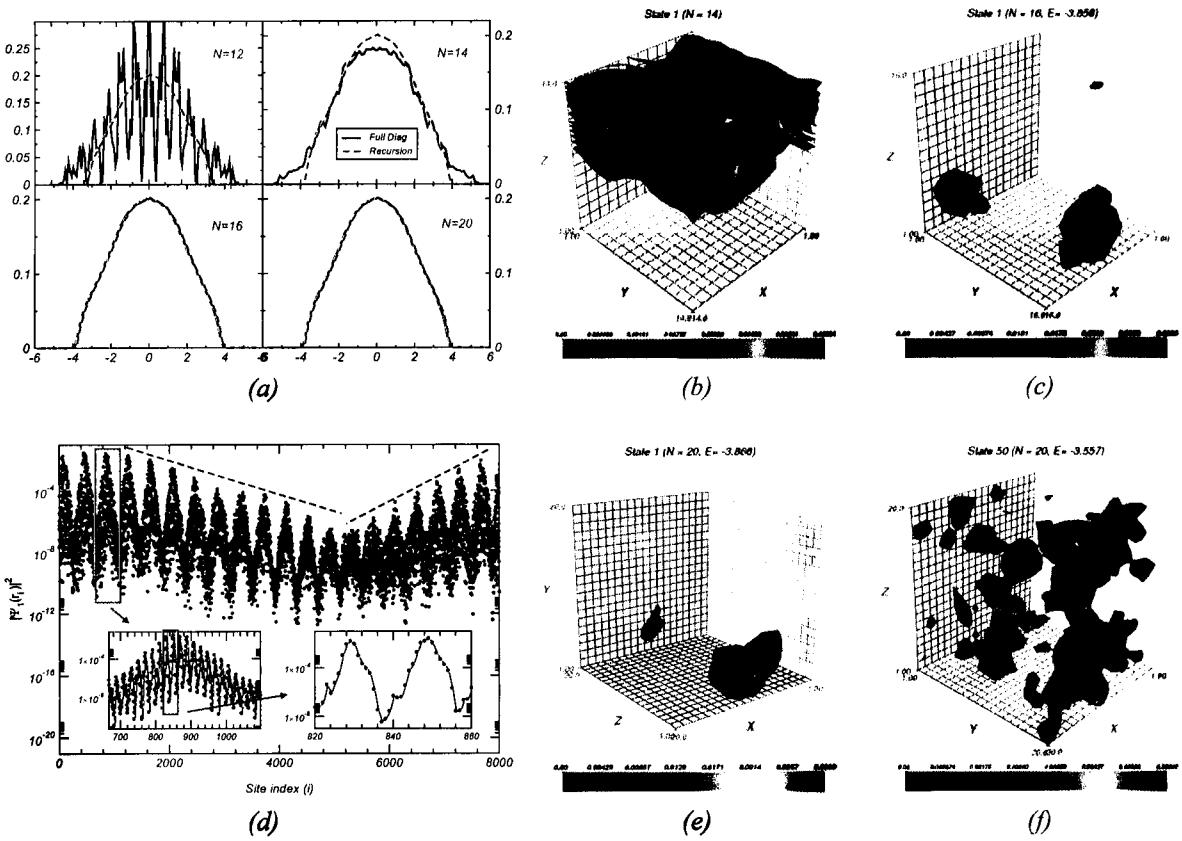

FIGURE 4.7 .: *(a) Paramagnetic DOS: Full diagonalization for $N = 14, 16, 18, 20$ vs. thermodynamic limit (recursion). Frames (b), (c), (e) and (f) show 3D contour plots of selected single particle wavefunctions obtained at $M = 0$ for selected system sizes and energies. The iso-surfaces represent the regions of constant $|\Psi_i(r|)^2$. In frame (d) we show the same ground-state wavefunction plotted in (e), but now using the unfolded lattice representation discussed in the text. Each inset of this frame represents different magnifications, as sketched.*

of the Hamiltonian and the recourse to numerical diagonalization techniques. This poses immediately two possible problems. The first is that, in order to trust that a result obtained for a single configuration of disorder will apply to a macroscopic system, we need a self-averaging quantity. But self-averaging requires rather large systems — a clear obstacle for a full diagonalization procedure[21].

The second difficulty is a consequence of this: for weak disorder one expects the typical localization lengths to span several unit cells, and thus small systems are again a problem. Notwithstanding, it is instructive to analyze directly some results coming from the full diagonalization of the Hamiltonian. The first thing one notices, by inspection of Fig. 4.7a, is that the spectrum and spectral density obtained from the full diagonalization of finite systems does not resemble the behavior expected for the thermodynamic limit but for $N > 16^3$. It is particularly important to notice that the bandwidth in smaller systems is essentially $\simeq 12t$ (the bandwidth in the FM limit) even for the highest disorder case ($M = 0$), which poses an important restriction upon the reasonable sizes to consider in the study of a DEM system with small carrier densities. Next, we look directly at the wavefunctions. For that, tridimensional contour plots of

[21]For instance, standard diagonalization routines requiring the complete storage of the matrix, demand $\sim$ 1, 1.7 and 3.4 GB of RAM to fully diagonalize the DE Hamiltonian in cubic systems of linear dimension 20, 22 and 24 respectively. The fact that the matrix is complex is not favorable either.

$|\Psi_n(r_i)|^2$ have been included in figs. 4.7b, 4.7c, 4.7e and 4.7f. These show the surfaces where the square modulus of the wavefunction is constant. To put all in perspective, 20 equidistant surfaces have been chosen for the different plots, the scale varying as depicted. So in Fig. 4.7b the lowest energy eigenstate for $N = 14^3$ is shown, being evident that such wavefunction spreads over the entire lattice, albeit only on a restricted region in the z direction. Higher energy states only spread more and more uniformly across the system and therefore no localized states exist in this smaller system, disorder notwithstanding. This is also the reason why the bandwidth is so different from its value as $N \to \infty$.

Turning our attention now to Figs. 4.7c and 4.7e that correspond to the lowest eigenstates for $N = 16^3$ and $N = 20^3$, we verify that they are indeed localized, because the wavefunction weight is mostly distributed within a quite restricted region of the lattice. To ascertain whether they are exponentially localized, we plotted one of them using an unfolded representation of the lattice[22]in Fig. 4.7d. The first thing to notice is the logarithmic scale in the vertical axes an that the wavefunction squared varies among 12 orders of magnitude! The main panel in this figure shows $|\Psi_n(r_i)|^2$ for the entire lattice. In the chosen representation, each lump of points represents a given z plane and so, if we follow the maxima at each of these lumps, we see that they decay linearly (the dashed lines are a guide for the eye in this comparison). We can do the same within a given z plane, as is shown in the first inset, or even look along a single x direction as is done in the second inset. In any case, the decay is clearly exponential. An estimate of the localization length based on the exponential decay for this specific state gives

$$\lambda \simeq 1.7\,, \tag{4.46}$$

in lattice units. At higher energies, the states shall become extended and that is seen in Fig. 4.7f where we see an eigenstate slightly above the mobility edge, already spreading throughout the entire lattice.

Unfortunately, this sort of analysis becomes unwieldy precisely in the most interesting region near E_c. According to the scaling theory of localization [Abrahams et al., 1979], the localization length diverges at E_c, posing obvious and serious finite size problems. Adding to this the known multifractal nature of the wavefunctions at E_c [Brndiar and Markos, 2006; Grussbach and Schreiber, 1995], then quantitative numerical conclusions based on an estimate of the localization length as above are essentially impossible in practice.

An interesting peculiarity of the nature of disorder and localization in the DEM is that, unlike the Anderson model, the localization length cannot get arbitrarily small. Indeed, in Anderson's case, for W large enough we expect the states at the bottom of the band (the more localized ones) to have amplitude only within a single lattice site (cfr. Fig. 4.6a). That corresponds to an electron being trapped by a large fluctuation in the local potential. By contrast, the DEM exhibits non-diagonal disorder. Furthermore, the only energy in the electronic system is kinetic, coming from the hopping. Now, the states for whom the localization length is the smallest are the ones at the extremes of the band. But being at the extremes means having the highest/lowest kinetic energies, which, in tight binding, implies delocalization! So there has to be a trade-off in this process. This is even more stringent in the case of DE because the

[22]To each lattice site we ascribe an index i defined as $i = x + yL + zL^2$, where (x, y, z) is the coordinate of the lattice point and L the linear size of the cubic lattice.

probability of having $t_{ij} = 0$ is exactly zero!, as shown in eq. (4.35)[23]. The states seen in figs. 4.7c and 4.7e are the more localized ones in the case of maximum disorder possible ($M = 0$).

Moving along, there is a quantity of great interest derived directly from the exact, normalized, wavefunctions: the moments of the wavefunction amplitude

$$I_q(E_n) = \sum_i |\Psi_n(r_i)|^{2q} \,. \tag{4.47}$$

In particular, $I_2(E)$ defines the so-called Inverse Participation Ratio (IPR),

$$\mathcal{P}(E_n) = \sum_i |\Psi_n(r_i)|^4 \,, \tag{4.48}$$

and is the parameter used in the earliest numerical investigations of localization [Edwards and Thouless, 1972]. The very definition of extended state entails that the wavefunction is spread rather uniformly across the entire system, wherefrom $\mathcal{P}(E)$ for such state should scale as $\sim N^{-1}$. On the contrary, localized wavefunctions will contribute significant amplitudes only from the R sites in which they lie, and $\mathcal{P}(E)$ will consequently scale as $\sim R^{-1}$, and should be size independent. This parameter essentially gives an account of the number of orbitals participating in a certain eigenstate. Since it permits this distinction (albeit rather coarsely near E_c), the IPR can be used as a sort of order parameter for the localization transition. The main advantage for us here is that using the IPR we can perform ensemble averages and study some of its statistics which are rather illuminating[24].

We calculated such quantity for different system sizes (N), and over many realizations of disorder. Afterwards, statistics are collected within a narrow energy window. Plots for the resulting average IPR along the band are shown in Fig. 4.8a. Two things are clear in these curves: the IPR is $\simeq N^{-1}$ for most of the band, rising several orders of magnitude as the band edges are approached. This rapid increase in the IPR is monotonous and correlates with the decreasing localization lengths. The inset shows that $\mathcal{P}(E) \times N$ is indeed N-independent far from the band edges. For a quick exercise, we pick the highest value of the IPR: $\mathcal{P}(E_1) \simeq 0.026$, and obtain that an estimate for the localization length of the lowest eigenstates is

$$2\lambda \sim \sqrt[3]{R} \simeq \sqrt[3]{1/0.026} = 3.38 \,. \tag{4.49}$$

This is fully consistent with the above estimate of λ from the decay of the wavefunction amplitude.

Although $\langle \mathcal{P}(E) \rangle$ is rather revealing, the fluctuations of this parameter are more interesting. In Fig. 4.9 the relative fluctuations of the IPR are plotted. These are the standard deviations of $\mathcal{P}(E)$ (designated $\sigma_{\mathcal{P}}$) divided by the respective mean $\langle \mathcal{P}(E) \rangle$. It's quite remarkable that the relative fluctuations increase markedly at the band edges. But most remarkable yet is the fact that there is a certain energy where the relative fluctuations are maximized. And this fact is independent on the system size or the energy window considered. We could conjecture, in view of this, that

The point of maximum fluctuation signals the mobility edge E_c.

[23] For a system with $\mathcal{P}(t_{ij} = 0) \neq 0$ it is statistically possible to have disconnected clusters and the problem acquires some flavors of quantum percolation. The small humps at $E = 0$ in figs. 4.8a and 4.9 to come are interpreted in this context.

[24] Just as an aside comment, a practical aspect of using the IPR is that one doesn't need to carry a data file containing the wavefunctions with some $\sim$ 2GB around!

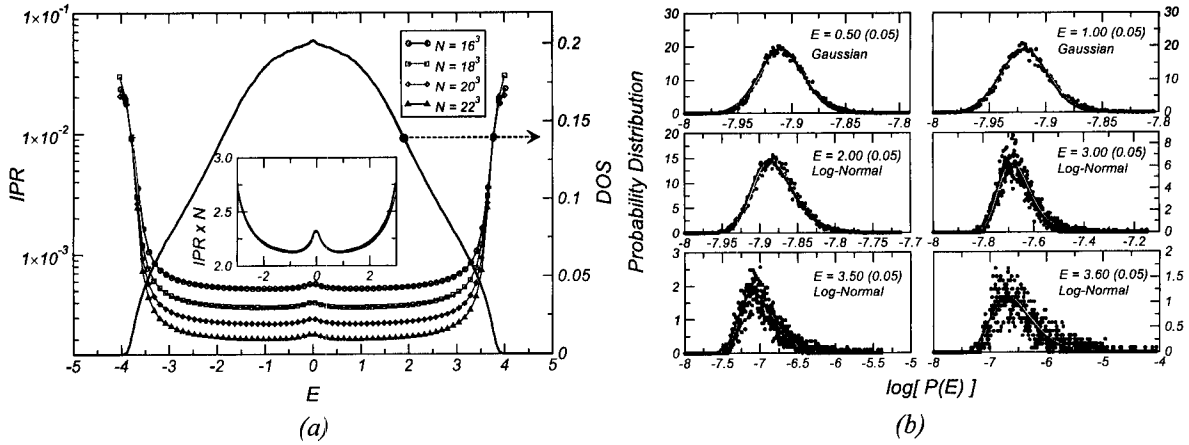

FIGURE 4.8 .: *IPR statistics for the DEM at* $M = 0$. *(a) Averaged IPR using an energy window of* $0.1t$ *for* $N = 16^3, 18^3, 20^3, 22^3$, *and averaging over* $240, 160, 40, 10$ *configurations, respectively. The thermodynamic DOS is also shown in the main panel for reference. The inset shows* $\mathcal{P}(E) \times N$ *outside the band edges. (b) In this panel, distributions of* $\log(\mathcal{P}(E))$ *for* $N = 18^3$ *are shown at different zones of the band. The continuous lines, are fitting results: to a Gaussian in the first 2 frames, and to log-normal distributions in the remainder.*

Thus, the prediction for the mobility edge at $M = 0$ would be

$$E_c = 3.65 \pm 0.05\,. \tag{4.50}$$

The mobility edge for the DEM at $M = 0$ has been calculated[25] by Li et al. [1997] who obtained $3.55 < E_c < 3.6$, in accord with the conjecture. This sort of behavior in the fluctuations of $\mathcal{P}$ has never been explored in this way before in the literature, and such diverging fluctuations surely bring the IPR closer to being a proper order parameter in the classical sense of critical phenomena. A closer look near E_C reveals yet another interesting aspect. To see what is involved here let us look at the inset of Fig. 4.9. The existence of a critical energy at which $\sigma_{\mathcal{P}}/\langle\mathcal{P}\rangle$ becomes size-invariant is apparent in a very compelling way, since the four curves seem to cross very close to each other. Unfortunately, unlike the maximum, this crossing point is rather sensitive to the energy window chosen to collect statistics. A finite size scaling was actually attempted but without any significant success. The reason lies in the impossibility of collecting more statistics at such *large* system sizes, which, in turn, forces us to consider a relatively large energy window, and a large distance between successive data points ensues. This renders the task of analyzing $\sigma_{\mathcal{P}}/\langle\mathcal{P}\rangle$ and its possible scaling behavior close to the crossing point very difficult at the current time.

For the reader who might care about the actual distributions for the IPR, their histograms have been plotted in Fig. 4.8b at different energies, using $N = 18^3$, and the same energy window of $0.1t$. It is more convenient to build the histograms of $\log(\mathcal{P})$ rather than $\mathcal{P}$ itself, these being the results actually shown. From those plots one sees that, at energies near the center of the band, the log of IPR has a Gaussian distribution, meaning that $\mathcal{P}$ itself is log-normally distributed[26]. However, the statistics of $\log(\mathcal{P})$ collected closer to the band edges start to behave like a log-normal distribution as the plotted fits

[25] Although the mobility edge at $M = 0$ has been known since 1997, its trajectory with M had not been calculated, to our knowledge, until this work. This will be shown in the subsequent pages.

[26] x is said to be log-normally distributed if its logarithm is normally distributed. Consequently, the probability distribution of

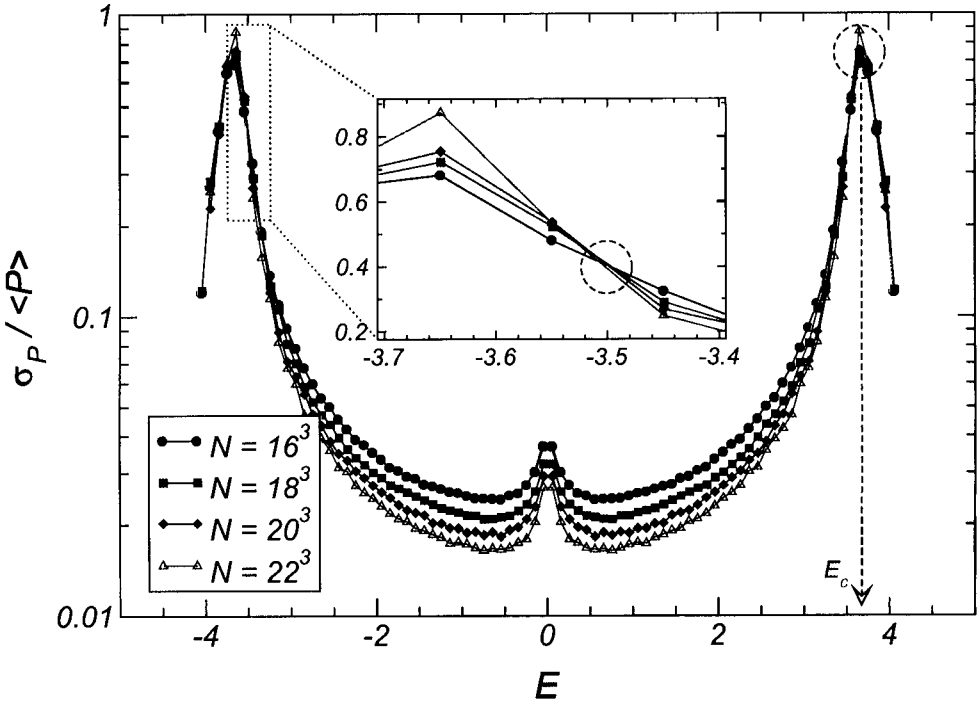

FIGURE 4.9.: *Ratio of the standard deviation to the average of the IPR using the same parameters as in Fig. 4.8. The inset is a magnification showing an apparent point of scale invariance.*

document. This means that $\mathcal{P}$ starts to behave log-log-normally!, in a clear indication of considerable *fat tail behavior* in the distribution, and the cause of the increasing fluctuations observed in Fig. 4.9[27].

Another interesting aspect following from Fig. 4.9 is the noticeable enhancement of the relative fluctuations near the center of the band. By extension, this behavior reveals a slight tendency for localization at those energies, and is completely understandable in terms of the DEM. Even though the probability distribution for the hopping modulus being exactly zero is itself zero (4.35), it is not hard to envisage the occurrence of very small hopping probabilities around some atom. When that happens, and adds to interference effects induced by the phase of the hopping, the electron will have an impaired diffusion and its energy will lie close to zero. Hence it is not very surprising that the relative fluctuations in the IPR, and the IPR itself, are enhanced near zero energy. Notwithstanding, the metallicity of the system should arguably be rather insensitive to this effects because of the high DOS at $E = 0$.

We are thus presenting a new method for the identifications of the mobility edge. Additional results demonstrating the reproducibility of the behavior of the IPR near the critical point are given in Appendix 4.E, both for the DE and Anderson models, lending more support as to the applicability of the above conjecture.

---

x is $p(x) = \exp\left[-(\log(x) - \mu)^2/(2\sigma^2)\right]/\sqrt{(2\pi\sigma^2 x^2)}$.

[27] The log-normal fits in some panels of Fig. 4.8b were performed doing a translation $x \longrightarrow x + c$ to circumvent the logarithms of negative quantities.

4.3.2.2. Local Environment — LDOS Fluctuations

Full diagonalization of the Hamiltonian matrix is always restricted to small lattice sizes, an imposition arising both from storage and execution time restrictions. Even more so when statistics are needed and we have seen that, in this particular problem, results start being meaningful for greater N's.

Perhaps the most challenging and enduring theoretical difficulty surrounding the Anderson transition has been the difficulty in defining a proper order parameter for the transition. The discovery that the Anderson problem can be mapped onto an effective field theory based on the non-linear, supersymmetric, σ model [Efetov, 1983], brought some hopes of an order parameter. However, these so derived order parameters are related to the DOS, and turned out to be analytical at the transition. Hence, the usual machinery of critical phenomena remains inapplicable at a precise quantitative level. Later on, Mirlin and Fyodorov [1993] reinterpreted some results of the supersymmetric formalism, conjecturing that a meaningful order parameter is in fact related to the distribution of local Green functions.

In this context we set about to study the distribution of LDOS which are directly related to the local Green functions. As a matter of fact, we can be easily convinced that the LDOS is indeed a quantity of interest, for if we recall its definition:

$$\rho_i(E) = \sum_n |\langle r_i|\Psi_n\rangle|^2 \, \delta(E - E_n)\,, \tag{4.51}$$

it says that $\rho_i(E)$ simply *measures* the total weight of the wavefunctions with energy $E \pm \delta E$ at the lattice site r_i. If E happens to be on the localized side, the corresponding eigenfunction will have considerable weight on very few sites and, consequently, the *typical* value of the LDOS has to be very close to zero. A precise definition of *typical* LDOS will be presented in a moment. The important point is that, for this reasoning to work, a considerable sampling of LDOS thoughout the lattice has to be made, and, again, the study of its distribution becomes crucial.

Aiming at the understanding of its statistics in disordered tight-binding systems in general — and our DEM in particular — the recursive method was employed to calculate LDOS in much larger lattices ($N = 100^3$) than the ones considered in the previous section. The process involves the random choice of a lattice site, the calculation of the LDOS there and the repetition of the process for different spin configurations and lattice points. In the end, statistics are collected within a narrow energy window[28]. The fact that the consideration of a finite energy window has no influence on the results can be confirmed with reference to Figs. 4.10a, 4.10b and 4.10c, that show a density plot of the probability distribution for the LDOS in the (E, ρ_i) plane. These are for the Anderson model (4.45), and, for comparison, we present the ordered case ($W = 0$) together with two small disorder strengths ($W = 1, 2$). As the pictures document, the features in the probability distributions are due entirely to disorder[29].

Fig. 4.10 shows the aspect of the LDOS histograms along the band for $M = 0$. The distribution of ρ_i is unimodal across the entire band. Near the band center, it is clearly log-normal, something

[28] This is not strictly necessary because the recursive method allows the consideration of arbitrarily small energy windows, zero in particular. However, we still chose to stick with the energy window because it allows a useful amplification of the statistics, with no influence on the results.

[29] For instance, the ordered case is sharply peaked, showing no broadening at all, other than the one due to the finite energy window. As a result the density plot is simply the profile of the global DOS for the tight-binding Hamiltonian in the cubic lattice, as we naturally expect.

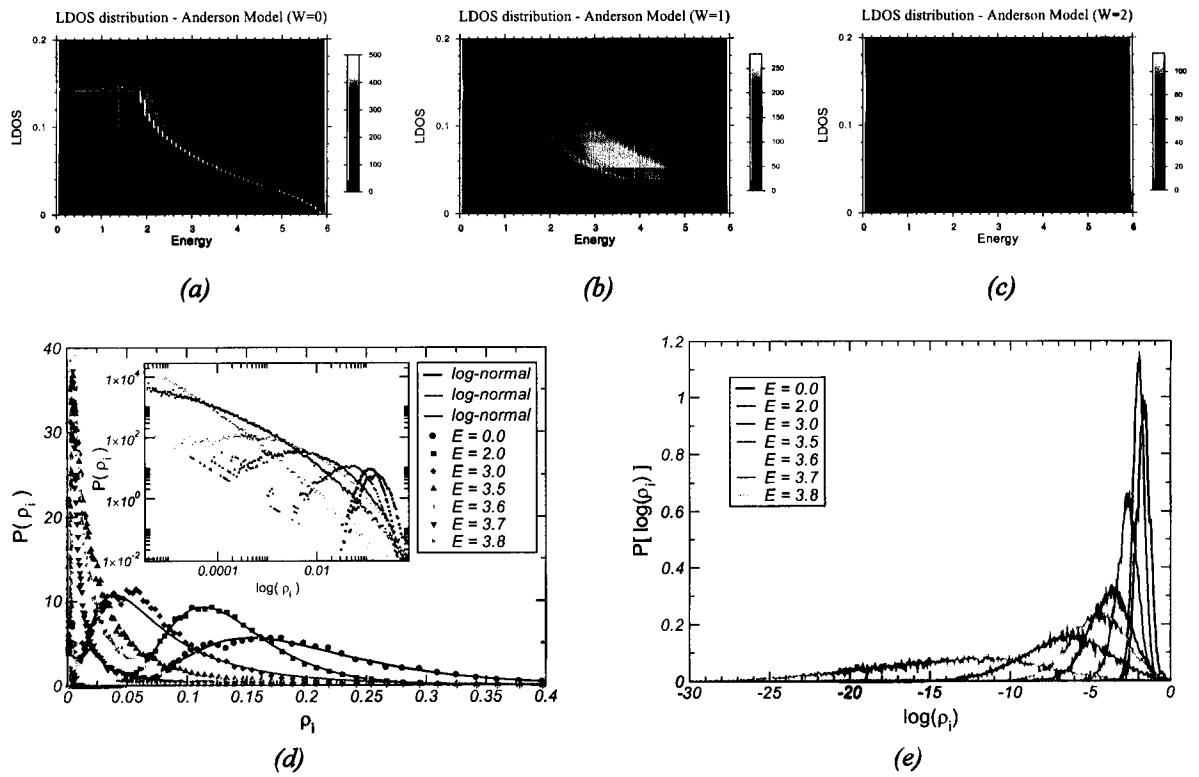

FIGURE 4.10 .: *LDOS distributions. Frames (a), (b) and (c) are density plots of the probability distribution of the LDOS, $P(E, \rho_i(E))$, for the Anderson model. (d) Histograms of $\rho_i(E)$ in the DEM at $M = 0$ for selected energies, using an energy window of $0.1t$. The solid lines are log-normal fits. The inset presents the same data in a log-log plot scale. Notice how a maximum is absent after a certain energy. (e) Histograms of $\log(\rho_i(E))$ showing how rapidly the distribution broadens after certain energies. All data were obtained with systems with $N = 100^3$ orbitals.*

confirmed by the excellent fits superimposed on the numerical data. Progressing towards the band edge the distribution consistently deviates from log-normality (the quality of the fit worsens visibly) and, past some threshold, its modal point ceases to rest at finite ρ_i, being actually zero. This is best appreciated in the log-log plot included as inset to this frame. There one clearly witnesses something changing between $E = 3.6$ and $E = 3.7$ that causes the maximum to disappear. In Fig. 4.10e we gain a deeper insight into what is really happening. The plots are now histograms of $\log(\rho_i(E))$, and is evident that, at the same threshold, the probability distributions begin to broaden quite abruptly, with their weight rapidly spreading across many orders of (negative) magnitude! This means that fluctuations are again playing a role near the Anderson transition. As it turns out, the fluctuations in $\log(\rho_i)$ are actually diverging at the Anderson transition. This is demonstrated by the curves in Fig. 4.11, where the relative fluctuations in $\log(\rho_i)$ (i.e. $\sigma_{\log(\rho_i)} / \langle \log(\rho_i) \rangle$) are plotted for the DEM and, to better appreciate the reproducibility of the phenomenon, for the Anderson model as well. As already happened with the fluctuations in the IPR, the LDOS also displays diverging fluctuations at some energy close to the band edges. A new conjecture is therefore introduced stating that

The LDOS has statistical fluctuations diverging at the mobility edge.

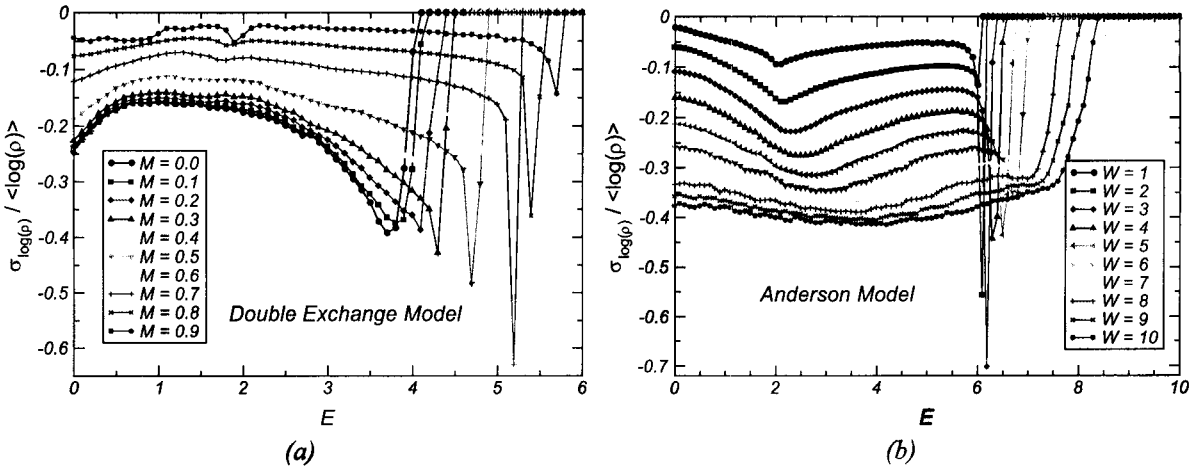

FIGURE 4.11 .: *LDOS fluctuations (a) Relative fluctuations of* $\log(\rho_i)$ *in the DEM at different magnetizations. Zero values signify that* $\langle \log(\rho_i) \rangle = 0$. *(b) Relative fluctuations of* $\log(\rho_i)$ *for the Anderson model at different disorder strengths,* W. *Both data have been sampled from* 40×40 *realizations of disorder.*

Faithful to this, the mobility edge can be easily extracted from the plots on the figure, and in particular, we obtain in the paramagnetic regime,

$$E_c = 3.70 \pm 0.05 \,. \tag{4.52}$$

This value is in complete accord with the one obtained previously in (4.50) through the statistics of the IPR.

We remark, however, that while the divergence is clearly pronounced in the DEM at all magnetizations (Fig. 4.11a), it is not so in the case of the Anderson model (Fig. 4.11b). It is indeed visible that above $W \simeq 8t$, the peak in the relative fluctuations is considerably softened for the case of diagonal disorder. But we should bear in mind that at this point, the disorder strength is already of the same magnitude as the bandwidth in the clean system. This means *strong* diagonal disorder, in which case our conjecture seems weaker. It is not clear at this time the reason for the softening of the divergence under strong disorder, but presumably it will have to do with poor statistics, and the possibility that for certain static configuration of disorder, the band starts to loose its connected support (gaps), posing problems to the accurate determination of the LDOS in those cases.

Such obviously diverging fluctuations certainly hint at the putative existence of an underlying order parameter. Given that the fluctuations are in the $\log(\rho_i)$, it has to be $\langle \log(\rho_i) \rangle$. A momentarily reflection will show us that

$$\langle \log(\rho_i) \rangle = \frac{1}{M} \sum_{p=1}^{M} \log\big((\rho_i)_p\big) = \log \left[\prod_{p=1}^{M} (\rho_i)_p \right]^{1/M} = \log(\varrho^t) \,, \tag{4.53}$$

where ϱ^t is the *geometrical average* of the LDOS. Thus, unlike the arithmetic average that simply yields the DOS in the thermodynamic limit and is featureless at the localization transition, the geometric average is quite interesting. We designate this geometric average by Typical Density of States (TDOS),

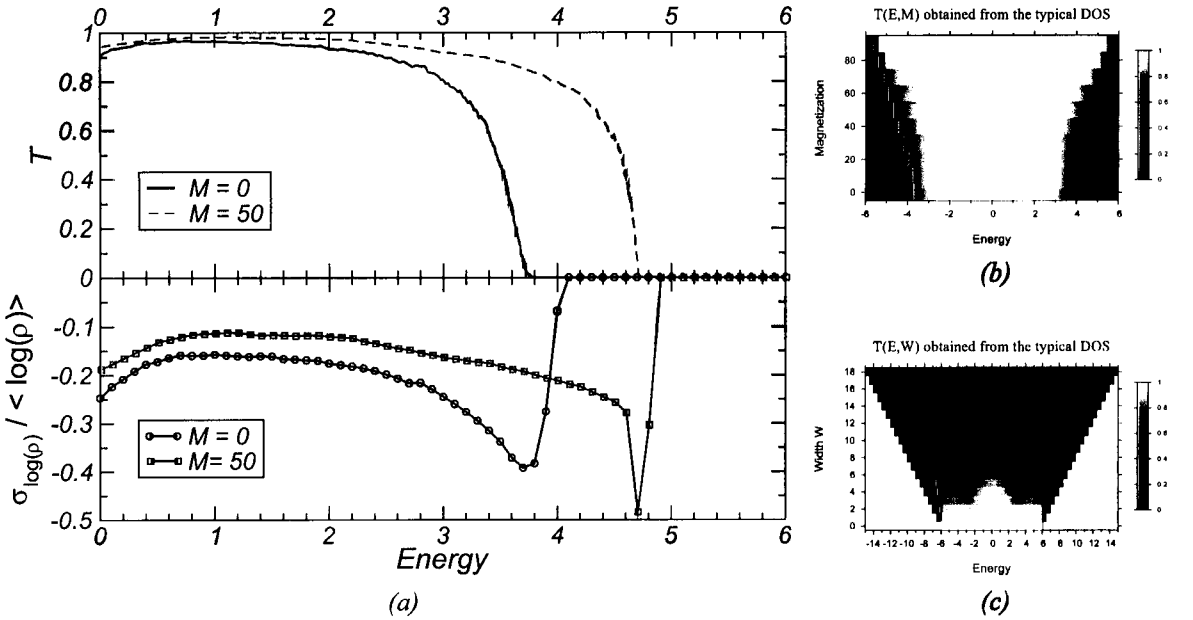

FIGURE 4.12 .: *Typical DOS in the (E, M) plane. (a) Joint plot of $\mathcal{T}$ and the relative fluctuations for selected magnetizations in the DEM. (b) Density plot of the parameter $\mathcal{T}$ in the DEM. (c) Density plot of the parameter $\mathcal{T}$ in the Anderson model. The black boundary marks the position of the Lifshitz band edges.*

and its ratio to the average DOS defines the order parameter $\mathcal{T}(E, M)$:

$$\mathcal{T}(E, M) = \frac{\varrho^t(E, M)}{\rho(E, M)} . \tag{4.54}$$

When this is plotted as a function of energy and magnetization, the results of Fig. 4.12 obtain. In the first panel we have the density plot of $\mathcal{T}(E, M)$, and is quite noticeable that $\mathcal{T}$ drops precipitously at the point where the fluctuations diverge (vis. panel 4.12a). Either this or Fig. 4.11 provide us with the trajectory of the mobility edge in the (E, M) plane. As for the results of $\mathcal{T}$ pertaining to the Anderson model (Fig. 4.12c), it is clear that the transition is not as sharp at higher disorder strengths, which is consistent with the weakening in the divergence of the relative fluctuations already mentioned and seen in Fig. 4.11b.

Treating the geometric average of the LDOS as an order parameter is actually quite reasonable from the physical point of view. The definition (4.51) can be understood as stating that the LDOS gives an account of the overall projection of the eigenstates onto the specific site r_i at which ρ_i is being calculated. In the localized regime, when the eigenstates correspond to energy levels with $E < E_c$, the wavefunctions are expected to be exponentially localized, with a real space distribution somehow similar to the illustration in Fig. 4.13. Evidently, on our sampling we are randomly selecting the sites r_i for each energy, E, and so, it is not surprising that at some point we will pick a site where there

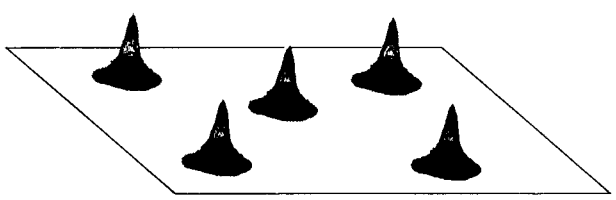

FIGURE 4.13 .: *Schematic wavefunctions when $E < E_c$.*

is no amplitude contribution from any of the eigenstates, provided that $E < E_c$ and that the sampling is statistically good enough. Hence $\rho_i = 0$ at such energy and at such site. Of course, the vast majority of the lattice sites will not have this property because we know that, on (arithmetic) average, we should be picking the *global* DOS, which is smooth across E_c and vanishes only at the band edge. The remarkable fact is that, if we are in the localized region, then there ought to be some sites for which ρ_i is zero in practice[30].

The typical DOS (4.53), being the geometric mean of our sample is most appropriate to pinpoint this threshold. Actually a single one would suffice to establish that we are beyond E_c onto the localized phase: given that it involves the product of all ρ_i, the presence of a single occurrence for which $\rho_i(E) = 0$ immediately kills the final result. That's why $\mathcal{T}$, as defined above, is a seemingly good order parameter for the localization transition.

That $\mathcal{T}$ might be a good candidate for order parameter in the Anderson transition has also been proposed quite recently by Schubert et al. [2003], using a related approach to the numerical calculation of the LDOS. However, these authors limit themselves to the study of the TDOS for the Anderson Hamiltonian, with a special emphasis on the Anderson transition at $E = 0$. They completely ignore the question of fluctuations, which are indeed the driving and implicit mechanism underlying this novel order parameter[31].

Our current results provide an extension to non-diagonally disordered electrons, and quite convincingly support the inference by Mirlin and Fyodorov [1993] in the context of supersymmetry that a proper order parameter for the Anderson transition is related to the local DOS.

This and the previous section prove that fluctuations play a vital role at the localization-delocalization transition. In particular, the physical meaning of the fluctuating parameters underlines the relevance of the local point of view in the problem of disordered electronic systems, just as Anderson and Economu envisaged in the early years.

4.3.2.3. Trajectory of the Mobility Edge

We culminate the discussion around the Anderson localization problem in the DEM, by presenting a map of the mobility edge both as a function of energy and magnetization. This result has been obtained for the first time in the context of this PhD program when trying to unveil the physics of EuB_6. The result is shown in Fig. 4.14a, whose purpose is mainly to compare the results calculated with different methods, and to show how reliably the study of LDOS fluctuations permits the determination of E_c. The results from the transfer matrix method [MacKinnon and Kramer, 1981; Pichard and Sarma, 1981] have been obtained by E. V. Castro and first published in **VITOR M. PEREIRA**et al. [2004a]. The results from the fluctuations in the LDOS have been obtained by inspecting the energies at which their distributions loose the finite modal point (cfr. inset of Fig. 4.10d), and the error bars are just the size of the energy window considered. Again we stress that, in principle, the energy window can be reduced, at the expense of more

[30] The states are exponentially localized, so we always expect some finite but arbitrarily small LDOS, as can be seen in the plots of Fig. 4.10e.

[31] Furthermore, a practical consequence of the direct observation of the diverging fluctuations is that it allows the introduction of appropriate error bars in the position of the mobility edge.

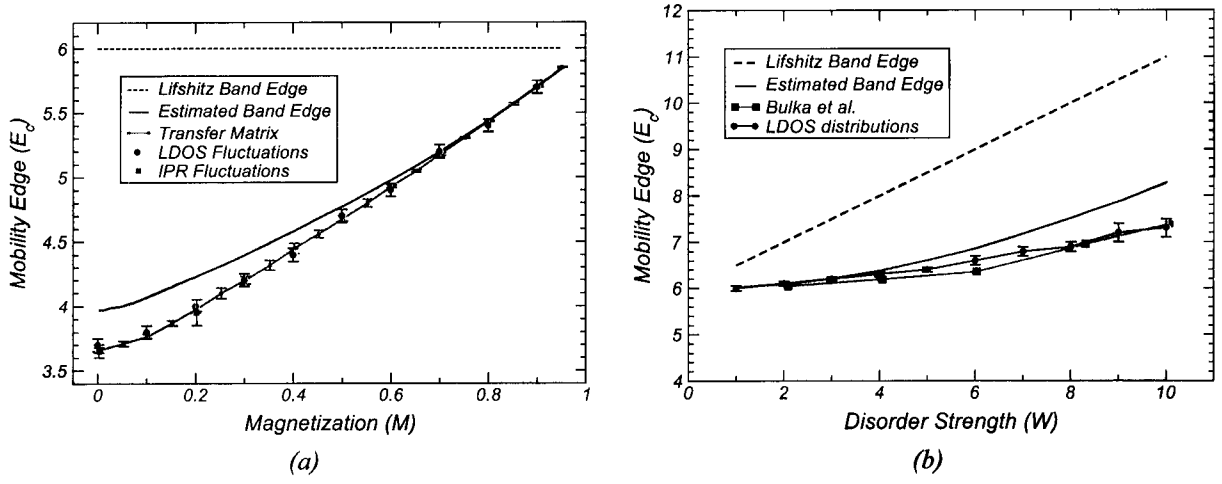

FIGURE 4.14.: *Trajectory of the mobility edge for the DEM in the (M, E) plane (a) and for the Anderson model in the (W, E) plane (b). For comparison, estimated band edges and Lifshitz band edges are also plotted.*

statistics being required[32] .

For comparison we add the corresponding result for the Anderson model in Fig. 4.14b. In this case, results from the transfer matrix were extracted from Bulka et al. [1985]. Overall the agreement between E_c from the LDOS and E_c from transfer matrix is not as perfect as in the case of the DEM, particularly at higher values of W, a circumstance stemming from the issues mentioned before with regards to the strong disorder regime.

The most relevant detail regarding E_c in the DEM for the physics of EuB_6 is related with the close proximity between the E_c and the band edge. This is obvious in Fig. 4.14a, where both the actual and Lifshitz band edges have been added[33]. The consequences are explored next.

4.3.3. Spectral and Transport Properties

4.3.3.1. Single Particle Spectral Function

A conventional way to begin to address the nature of the electronic transport in a system is to investigate, for instance, the momentum state lifetimes around E_F. The lifetime, $\tau(E)$ is an important quantity insofar as all theories of transport, from classical Drude, to semiclassical Boltzmann and up, resort to such concept for quantifying the electrical response of the material. For now we will be interested in the one-electron response to the disordered potential caused by the random spin orientations. The standard treatment begins with the unperturbed lattice ("free" electrons), for which k is a proper quantum number, and summarizes the effects of the disorder (and interactions, if present) in the electron self-energy, $\Sigma_k(\omega)$. The Green Function (GF) formalism is of great avail here. In particular, the Matsubara GF

$$\mathcal{G}_k(i\omega_n) = \frac{1}{i\omega_n - \varepsilon_k - \Sigma_k(i\omega_n)} \tag{4.55}$$

[32]Meaning longer times of execution and, preferably, greater system sizes.

[33]The term *"actual band edge"* designates the energy behind which the global DOS is effectively zero. It is the physically relevant band edge in the thermodynamic limit

can be used to calculate the *retarded* GFs via the usual analytical continuation

$$G_k^R(\omega) = \mathcal{G}_k(\omega + i\delta) = \frac{1}{\omega - \varepsilon_k - \Sigma_k^R(\omega) + i\delta}, \quad \text{where } \Sigma_k^R(\omega) = \Sigma_k(\omega + i\delta)\,. \tag{4.56}$$

An important derived quantity is the one-electron spectral function, relevant for its direct connection with spectroscopic experiments, and defined as the imaginary part of (4.56):

$$A(k,w) = -\frac{1}{\pi}\Im\left[G_k^R(\omega)\right]. \tag{4.57}$$

A moment's notice will bring about that, for the unperturbed lattice where $\Sigma_k = 0$, $A(k,w)$ is simply $\delta(\omega - \varepsilon_k)$, whereas for a perturbed system one has in general:

$$A(k,\omega) = -\frac{1}{\pi}\frac{\Im\left[\Sigma_k^R(\omega)\right]}{\left(\omega - \varepsilon_k - \Re\left[\Sigma_k^R(\omega)\right]\right)^2 + \Im\left[\Sigma_k^R(\omega)\right]^2} \equiv -\frac{1}{\pi}\frac{\Gamma_k(\omega)}{\left(\omega - \Omega_k(\omega)\right)^2 + \Gamma_k(\omega)^2}. \tag{4.58}$$

For ω-independent Γ and Ω, one has simply a lorentzian centered at some renormalized eigenenergies. This lorentzian corresponds to the broadening of the Dirac-deltas caused by the nonzero imaginary part of the self-energy. Therefore, $\Gamma_k \equiv \Im(\Sigma_k)$ is associated with damping, and physically translates into the inverse lifetime of a k state in the perturbed system.

It is important to notice that $A(k,\omega)$ is just another instance of a projected DOS. To appreciate that, consider the GF of a single electron in the spectral (Lehmann) representation[34] :

$$G_k^R(\omega) = \sum_\lambda \left|\left\langle \lambda \left| c_k^\dagger \right| 0 \right\rangle\right|^2 \frac{1}{\omega - E_\lambda + i\delta}, \tag{4.59}$$

and take its imaginary part:

$$A(k,\omega) = -\frac{1}{\pi}\Im\left(G_k^R(\omega)\right) = \sum_\lambda |\langle k|\lambda\rangle|^2\, \delta(\omega - E_\lambda)\,. \tag{4.60}$$

This means that $A(k,\omega)$ can be obtained via recursion method, using a Bloch state $|k\rangle$ as the starting vector. Hence, it is possible to numerically calculate the spectral function without any approximation. Such numerical results are presented in Fig. 4.15 for selected magnetizations in the DEM. These plots have been obtained by calculating $A(k,\omega)$ for selected k within the cubic BZ. Following convention, the k vectors were chosen along the symmetry directions of the BZ, as labeled in each panel. It is quite visible the remarkable broadening occurring at $M = 0$, particularly in the middle of the band. The linewidth diminishes consistently with increasing M as expected and, for a given magnetization, the sharpest lines always appear at the band edges. Another aspect, observable particularly well in the panels at the lower row, is that $A(k,\omega)$ fits well to a lorentzian distribution near the band center (high energies), but starts to deviate from this shape the closer the peak is to the band edges. This hints at stronger E-dependencies of the inverse lifetime $\Gamma_k(\omega)$ and renormalized energy $\Omega_k(\omega)$ near the band edges.

[34] Notice that we are considering a *single* electron, and hence, the absence of the second term in (4.59), that would correspond to states below the Fermi energy.

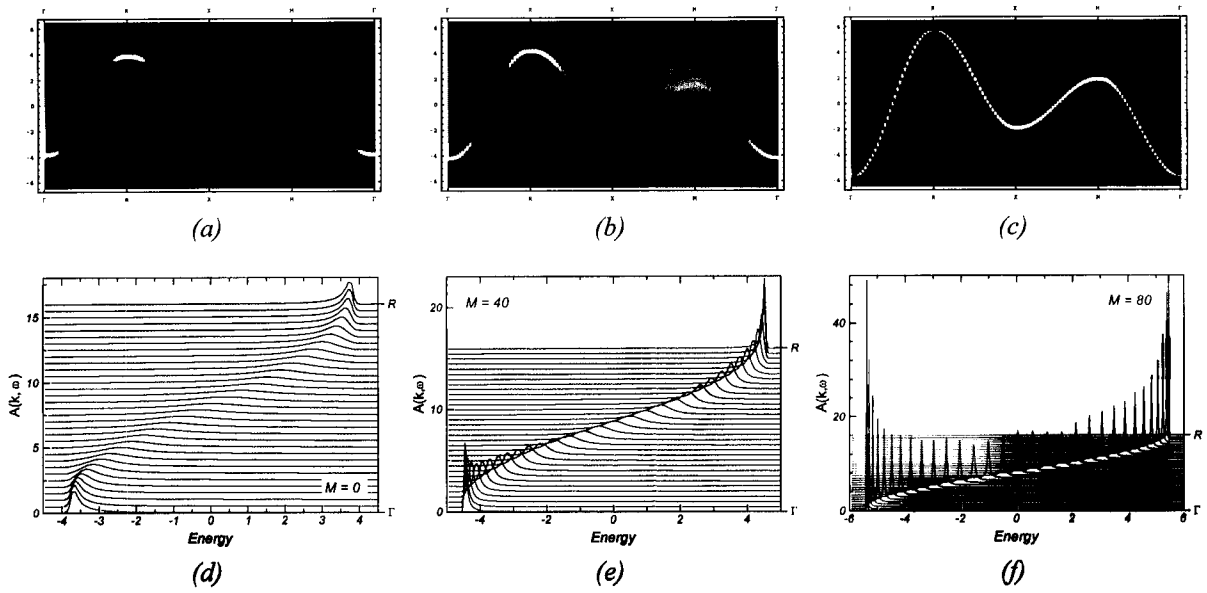

FIGURE 4.15.: *Single particle spectral function in the DEM along the symmetry directions of the cubic BZ. The top row are density plots of $A(k,\omega)$ along $\Gamma \to R \to X \to M \to \Gamma$ at $M = 0$ (a), $M = 40$ (b) and $M = 80$ (c). The second row, shows a detail of individual $A(k,\omega)$ along $\Gamma \to R$, for the same M as above. The density color scale is the same used in Fig. 4.12b.*

These two facts seem consistent with a perturbative calculation of $\Gamma_k(\omega)$ that yields a damping factor proportional to the DOS. In fact, it can be shown (Appendix 4.F for details) that, in the case of the Anderson model (4.45), first order perturbation theory prescribes

$$\Gamma_k(\omega) = 2\pi\rho^0(\varepsilon_k)\frac{W^2}{12}. \tag{4.61}$$

We can actually see this working in practice for this case of Anderson disorder. With that goal, we took the Anderson model and calculated the spectral functions $A(k,\omega)$, just as in the case of the DEM. The curves $A(k,\omega)$ were fitted to lorentzian distributions after which their centers and widths have been obtained. According to the result above, plotting the width against the center should yield a curve that reproduces the (unperturbed) DOS multiplied by a constant. Results gathered for disorder strengths $W = 1, 5, 10$ are presented in Fig. 4.16a. These three panels show the inverse lifetime as a function of energy throughout the band, with very interesting results. In particular, it is remarkable that

1. At low disorder ($W = 1$, first panel in Fig. 4.16a), the lifetimes that follow from the lorentzian fits to $A(k,\omega)$ are very well reproduced by the perturbative result (4.61).

2. At moderate disorder ($W = 5$, second panel in Fig. 4.16a) the perturbative result (dashed/blue) curve no longer follows the actual lifetimes extracted from the spectral function. However, if the unperturbed DOS, $\rho^{(0)}$, is replaced by the true, disorder averaged, DOS in (4.61), then the perturbative calculation still works, albeit not as perfectly as before.

In virtue of this, we conclude that the perturbative result is seemingly reliable considerably beyond the

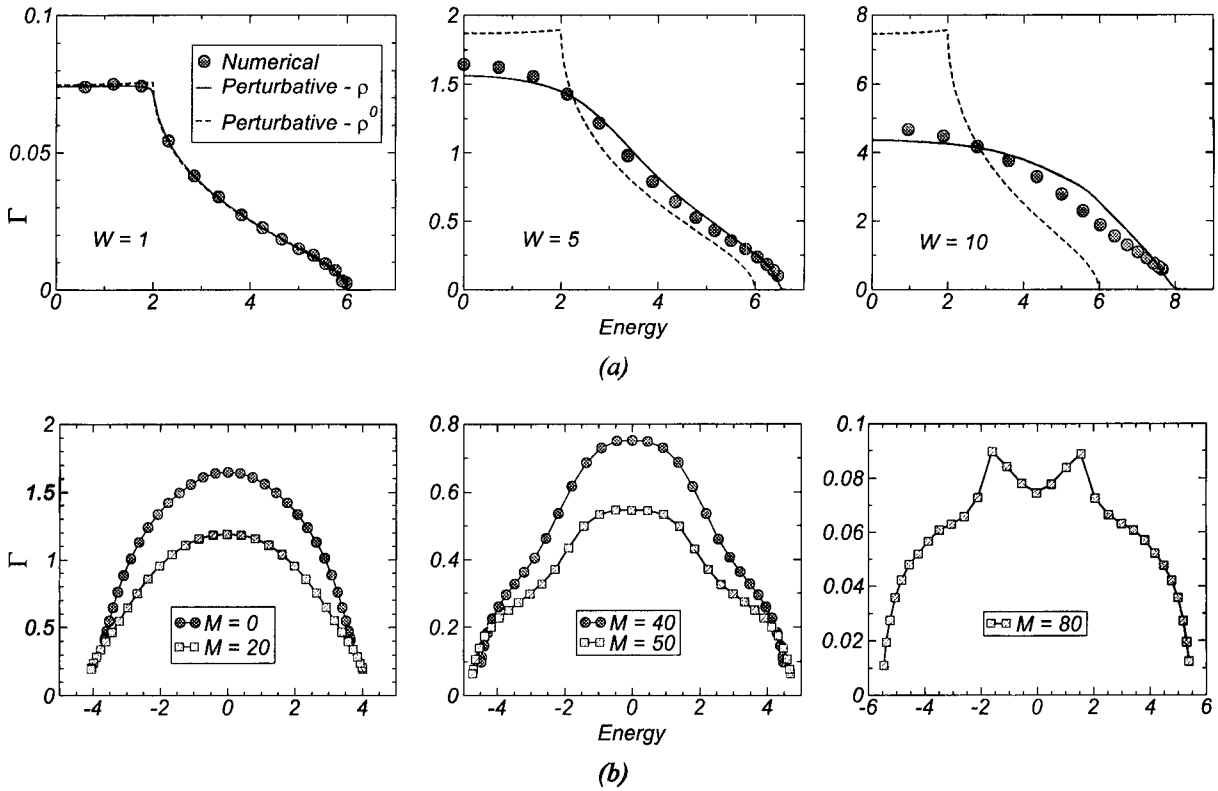

FIGURE 4.16..: *Inverse single-particle lifetimes. (a) The top row shows the inverse lifetimes* $\Gamma(E)$ *obtained from lorentzian fits to* $A(k,\omega)$ *in the Anderson model.* $A(k,\omega)$ *was calculated numerically with the recursive method (dots). The lines correspond to the perturbative result* (4.61) *for the corresponding* W*'s, using the actual numerical DOS (solid/red lines) or the unperturbed DOS (dashed/blue lines). (b) The lower row presents the inverse lifetimes* $\Gamma(E)$ *obtained from lorentzian fits to* $A(k,\omega)$ *in the DEM, for several magnetizations, as indicated.*

perturbative regime[35], provided that the unperturbed DOS is replaced by the actual DOS corresponding to such particular disorder strength. This in turn is a signature that the major corrections to (4.61) come essentially from the renormalization of the DOS when disorder is progressively *turned on*[36] .

Returning from our brief digression into the Anderson model, can we expect these findings to hold in the case of disorder caused by the DE? First of all, the only analogue of a perturbative parameter in the DEM is the average magnetization, M. Thus the DEM nature of disorder in this model is non-perturbative in the sense that, say in the PM regime, one cannot turn on an arbitrarily small potential. In second place, we can always re-write the Hamiltonian (4.19) as

$$\mathcal{H}_{DE} = -t\sum_{\langle ij\rangle} d_i^\dagger d_j + \text{h.c} + t\sum_{\langle ij\rangle}(1-a_{ij})d_i^\dagger d_j\,, \tag{4.62}$$

and treat the second terms as the perturbing part. But, unlike the Anderson model, the perturbing potential now happens to be non-local. An essential point in deriving the inverse lifetime given above (eq. (4.61)

[35]Notice that at $W = 5$, the disorder distribution has a width of half the bandwidth of the clean lattice, and therefore, the amplitude of the perturbing potential is quite high already.

[36]A comment is perhaps in order here. In effect, the fact that (4.61) has $\rho^0(\varepsilon_k)$ instead of the full $\rho(\varepsilon_k)$ follows from the fact that the calculation is based upon simple perturbation theory. In diagrammatic terms this is akin to a self energy containing $G_k^0(\omega)$. It is possible to show that, using a more detailed diagrammatic expansion of the self energy that includes self-consistency, the same result (4.61) is obtained with $\rho^0(\varepsilon_k)$ replaced by $\rho(\varepsilon_k)$.

and Appendix 4.F) was the local and uncorrelated nature of the perturbing potential that allows a simple calculation of averages of the type $\overline{\varepsilon_i \varepsilon_j}$. The same procedure applied to the Hamiltonian in the form (4.62) will bring about disorder averages of terms such as

$$\overline{(1-a_{ij})(1-a_{mn})^*}\,. \tag{4.63}$$

But, now, these terms are not completely uncorrelated, for the hopping from $i \rightarrow j$ is correlated with the hopping $j \rightarrow k$. Furthermore, the a_{ij} are complex entities and interference effects are expected to be significant in the averaging above. All this, added to the non-locality that introduces an extra momentum summation, renders the perturbative approach unwieldy for the case of DE. But, although, such analytical result might be important for comparison purposes as it was in Anderson's case above, it is actually immaterial, as far as the numerical calculations are concerned. Indeed, the recursive method is impervious to such intricacies of the problem, and results are readily obtained for the spectral function in that case. They are shown in Fig. 4.16b, where only the $\Gamma(\omega)$ extracted from lorentzian fits to $A(k,\omega)$ are shown. Two important observations are due: one is that the highest values of Γ obtained for M are of the same order of magnitude than the ones at $W \simeq 5$ in the Anderson model. The second observation is to the shape of curve $\Gamma(E)$ at $M = 80$: it does not resemble the unperturbed DOS at all, and, inclusively, displays a marked dip as E approaches the band center. This provides strong evidence for the peculiarities of the electronic disorder in the DEM discussed just above, and certainly deserves further investigation in the future. As far as we know, this numerical approach to the calculation of momentum lifetimes has not been reported before in the literature.

4.3.3.2. Mobility Gap, Extended and Localized Carriers

Given that the DEM displays a clearly defined mobility edge (Fig. 4.14a) it remains to understand how this can affect the physical response of DE based materials. Of course, the quantities most sensitive to the existence of this mobility edge, will be the ones related to electrical transport. Electrical transport is governed to a great extent by the nature of the states near the Fermi level, E_F, and by the number of carriers involved in the current carrying process. Therefore, it is more or less evident that the relative position of E_F with regards to E_c plays a role of paramount importance. To analyze that, a few definitions are introduced. The density of localized states, $n_{loc}(M)$, and of conducting (extended) states, $n_{cond}(M)$, are defined as

$$n_{loc}(M) = \int_{-\infty}^{E_c(M)} \rho(E,M)dE\,, \qquad n_{cond}(M) = \int_{E_c(M)}^{E_F(M)} \rho(E,M)dE\,. \tag{4.64}$$

The total density of electrons per unit cell is, of course,

$$n_e = \int_{-\infty}^{E_F(M)} \rho(E,M)dE\,, \tag{4.65}$$

and a completely filled band has $n_e = 1$. In the above, $\rho(E,M)$ is the numerical DOS, averaged over disorder configurations at a given magnetization M (as discussed in § 4.3.1). We also introduce the

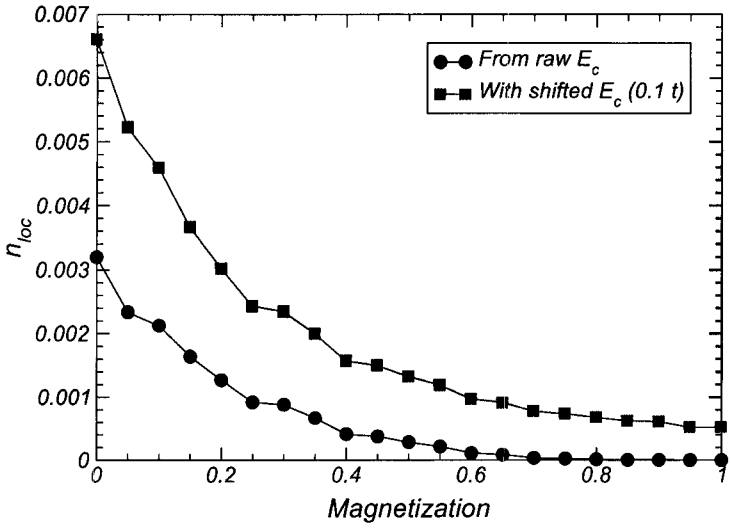

FIGURE 4.17 .: *Density of localized states in the DEM, obtained from integration of the DOS up to E_c. The difference between the two curves is that the red/squares curve uses $E_c' = E_c + 0.1t$, as discussed in the text.*

magnetization dependent mobility gap:

$$\Delta(M) = E_c(M) - E_F(M)\,, \tag{4.66}$$

that quantifies the relative position of the two energies. Unless otherwise mentioned, we work in the canonical ensemble where the total electronic density n_e is constant. Consequently, in virtue of the M dependence of the bandwidth and the overall shape of the DOS (Fig. 4.5), the Fermi level is necessarily M-dependent, and this dependence was explicitly shown in the above formulae.

The density of localized carriers is an intrinsic property of the model, just as E_c is. Their values are shown in Fig. 4.17 in two different circumstances. The first one (circles) is just n_{loc} obtained from the strict application of (4.64) using the numerically calculated $\rho(M)$ and $E_c(M)$. The magnetic disorder intrinsic to the DEM localizes 0.32 % of the electronic states in the PM phase[37]. As expected, the onset of ferromagnetism suppresses the disorder, causing a considerable reduction of n_{loc}, which eventually reaches zero in the fully polarized regime ($M = 1$). Now the figure $n_{loc} = 0.003$ might seem rather tiny ,insofar as it means that only a system having carrier densities of 0.003 electrons per unit cell, or less, can be a complete Anderson insulator[38]. However, this is the point at which the discussions in § 4.1 need to be recalled. Our target physical system is the FM metal EuB_6, which, as discussed before, has typical carrier densities in the PM phase of the order of precisely 0.003! [Paschen et al., 2000]. So, if EuB_6 is a DE system as we claim, this circumstance where localized and extended carrier densities are of the same order of magnitude, should imply a critical sensitivity of these hexaborides to Anderson localization effects!

Experimental evidence strongly points to the carriers in EuB_6 originating from the presence of B-related defects in the crystalline lattice (recall the experimental details mentioned in 3.1). Such defects

[37]Only the states localized at the bottom of the band are accounted for by this number. When the states localized at the opposite extreme of the band are considered, the figure doubles, obviously.

[38]The same applies for holes, of course. But, again, only the bottom of the band is considered in this discussion.

certainly introduce an additional source of disorder into the electronic system. At first sight this kind of substitutional disorder should be considerably small because, assuming that defects are actually B octahedra, whose absence promotes 2 bonding electrons to the conduction band, then their concentration would be of the order of half the carrier density, and thus very small. Under such assumption, and given that the source of carriers is not definitely established experimentally yet[39], we condense the effects of this disorder into a small, magnetization independent, renormalization of the mobility edge. In particular we take

$$E_c(M) \to E_c(M) + 0.1t., \tag{4.67}$$

which is a correction of $\sim$ 3 % to the value of $E_c(M = 0)$. This modification will naturally affect the E_c dependent quantities, n_{loc} being one example in particular. The $n_{loc}(M)$ obtained after (4.67) are shown in the same Fig. 4.17, in the data conveyed by the red (squares) line. As expected, the procedure in (4.67) leads to an overall enhancement of the localized carriers, and the existence of some residual localized states ($\sim 5 \times 10^{-4}$) even when the magnetic subsystem is fully polarized. This is totally acceptable physically inasmuch as not only the presumed B-related disorder, but also intrinsic lattice inhomogeneities tend to localize a few of the last states in the band.[40]

Localized states do not contribute to transport, and the interesting physics lies in the amount of extended states, and its dependence upon the magnetization of the sample. Hall effect measurements in EuB_6 reveal the presence of ~ 0.003 negative carriers per unit cell in the PM phase. If we add up the knowledge that the behavior of the electrical resistivity is undoubtedly metallic, then this implies that the density of conducting (extended) carriers is

$$n_{cond}(0) = 0.003 \tag{4.68}$$

in EuB_6, and, consequently, this is the value to be used in our model calculations. Knowing this and $n_{loc}(M)$, we can determine $E_F(M = 0)$, which in turn determines every other density at any finite magnetization[41]. Hence, the knowledge of the experimental carrier density completely constrains the other quantities within our model. In particular we have for the PM phase:

$$n_e = 0.0096\,, \qquad E_F(0) = -3.489t\,, \qquad \Delta(0) = -0.071t\,. \tag{4.69}$$

The complete dependence of the conducting carriers on M is plotted in Fig. 4.18, where is visible the marked enhancement of the carriers available for electrical transport with the onset of the FM long range order. Overall there is a threefold amplitude in the variation of n_{cond} between $M = 0$ and $M = 1$. But the most outstanding fact in this plot is that this enhancement of the carriers reproduces very well the experimental quantitative result, as can be confirmed by comparing this curve with the experimental one shown in Paschen et al. [2000, Fig. 10]. Again, we underline that the only tuning parameter is $n_{cond}(0)$, chosen to agree with the experimental one. After that, the variation with M shown in Fig. 4.18 is totally determined by the behavior of $E_c(M)$, which is a characteristic of the DEM. Thus

[39] ...and therefore no specific model of disorder to mimic the B-defects stands up as preferable.

[40] This is just a consequence of the fact that any arbitrarily small disorder always induces a mobility edge lying at a finite distance from the bottom of the band.

[41] Because $E_F(M = 0)$ determines the total carrier density (4.65), which is constant, irrespective of the value of M.

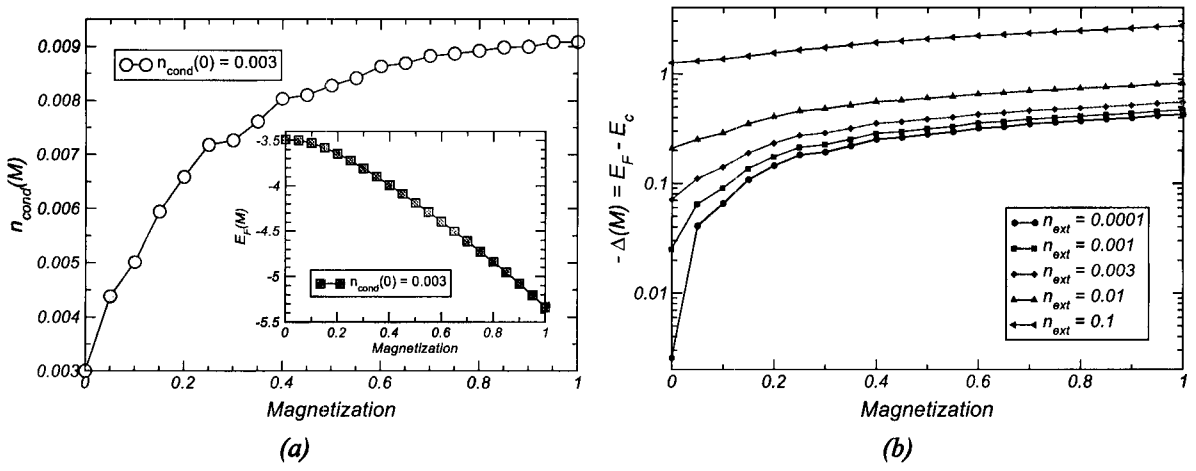

FIGURE 4.18 .: *(a) Variation of n_{cond} with M using $n_{cond}(0) = 0.003$ as discussed. The inset displays the corresponding evolution of the Fermi energy. (b) M-dependence of the (negative) mobility gap, $-\Delta(M)$, for different values of $n_{ext}(0)$.*

the DEM mechanism and its associated Anderson localization effects reproduce with very good quantitative and qualitative accord, the puzzling enhancement of the carrier density measured in the Hall response of EuB_6.

Within this DE-based perspective, such experimental behavior is no longer as puzzling as it first appeared: the appearance of FM progressively reduces the magnetic disorder, producing a concomitant sliding of the mobility edge towards the bottom of the band. During this process localized carriers are progressively *released* into the extended side, with more and more being detected in the Hall measurements as a result. Notice that it is not a trivial matter that the extended carrier density should increase in general, because such outcome depends upon the relative motion of both $E_c(M)$ and $E_F(M)$, together with the changes in the DOS at different magnetizations. This mechanism in the DEM not only gives the correct qualitative behavior found in EuB_6, but also exhibits an important numerical agreement. Furthermore, it might have been noticed that the hopping parameter t does not enter here at all: the reproduction of the experimental variation of $n_{cond}(M)$ within our DE picture, being in essence, a spectral property (counting of states), doesn't depend on the specific energy scale dictated by the hopping[42]. A more direct comparison with experiment can be obtained by plotting the density of conducting carriers against temperature. In order to map magnetizations into temperatures we use the zero-field curve $M(T)$ from [Henggeler et al., 1998], and plot the resulting curve of $n_{cond}(T)$ in Fig. 4.19a. In the same graph the experimental results from [Paschen et al., 2000] are superimposed for comparison. One can appreciate again how the amplitude of variation is well reproduced. The overall shape of the two curves seems to differ but it should be remarked that the experimental data, coming from the Hall effect, are taken at a constant external field (1 T in this case), and also that the $M(T)$ curve from [Henggeler et al., 1998] has been obtained with a different sample. In view of this, the agreement is still quite remarkable, in a confirmation of the extreme sensitivity of EuB_6 to Anderson localization effects.

[42] As remarked before, since $T_C \sim 15$ K, the temperature is effectively zero from the point of view of the electronic system.

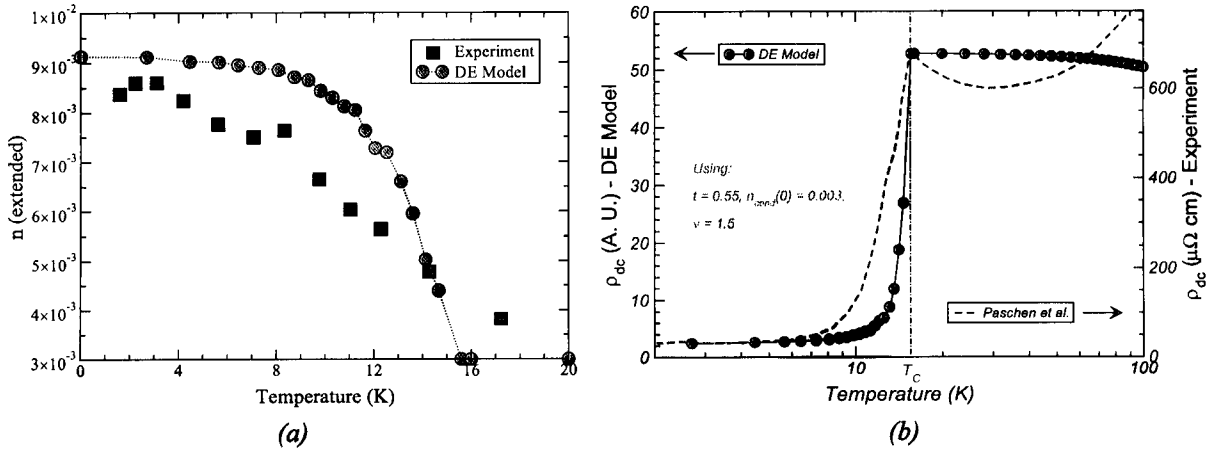

FIGURE 4.19 .: *(a) Comparison between the temperature dependence of n_{cond} obtained within the DE picture, and the experimental results by Paschen et al. [2000, Fig. 10]. (b) Temperature dependence of the resistivity calculated within the scaling prescription, and comparison with the experimental data extracted from Paschen et al. [2000, Fig. 6a] (also reproduced in our Fig. 3.5b).*

4.3.3.3. Electrical Resistivity

In the context of the scaling theory of localization it is known that, in order for a single parameter scaling to hold, the zero-temperature conductivity, $\sigma_{dc}(E)$, should be critical in the vicinity of the Anderson transition [Lee and Ramakrishnan, 1985], just like the localization length:

$$\sigma_0(E) \propto (E - E_c)^s , \qquad \xi(E) \propto (E - E_c)^{-\nu} . \tag{4.70}$$

If we take this result together with Mott's prescription for the behavior of the finite temperature conductivity [Mott and Davis, 1987]

$$\sigma(T) = \int_{E_c}^{+\infty} \frac{\sigma_0(E)}{T} \exp\left(\frac{E - E_F}{T}\right) f(E)^2 dE , \text{ with } f(E) = \frac{1}{e^{(E-E_F)/T} + 1} , \tag{4.71}$$

then we have a way to estimate the contribution of the localization effects to the conductivity. Although the scaling exponents ν, and s are still unknown for the localization transition in the DEM, we can employ the values ($s = \nu = 1.5$) known for the Anderson model [Kramer and MacKinnon, 1993] without great loss and calculate $\sigma(T)$ in the vicinity of the transition within this model. The resulting curve is plotted in Fig. 4.19a, where, instead of $\sigma(T)$ we show the experimentally accessible resistivity. Once again, to map temperatures into magnetizations the experimental data for $M(T)$ cited above has been used.

Let us analyze this curve in some detail. It is clear that the onset of ferromagnetism has a dramatic impact on the resistivity, which drops precipitously immediately below T_C. This steep suppression as the temperature is lowered is caused entirely by the variation occurring at the mobility gap. The role of temperature in (4.71) is mainly indirect, through $M(T)$ only. This is clearly seen by observing the region $T > T_C$ of the plot, where the variation of $\rho_{dc}(T)$, due solely to temperature activation effects, is manifestly small. The decisive mechanism is still the magnetization induced drift of the mobility

edge. For comparison purposes, the experimental curve of $\rho_{dc}(T)$ from Paschen et al. [2000, Fig. 6a], corresponding to the same sample used in the Hall measurements, has been superimposed on our graph. Clearly, a strict comparison of the two curves is beyond reasonableness, for the experimental curve encompasses all kinds of contributions, including phonons, spin scattering (presumably responsible for the cusp at T_C [Fisher and Langer, 1968]), etc. The main point in contrasting the model result with the experimental curve is to show that the amplitude of variation $\rho_{dc}(T_C)/\rho_{dc}(T \ll T_C)$ is well reproduced by the theory. This lends a strong support to the interpretation above of the underlying mechanism being caused by Anderson localization, through the release of localized carriers into the conducting region of the band.

Naturally this analysis based on eqs. (4.70) and (4.71) only addresses the localization-induced effects. We see that they are the most relevant near/below T_C , but in order to explain the overall profile of the resistivity from zero to room temperatures, the other intervening contributions need to be properly investigated. Given that our interest was upon the regions with $T \leq T_C$, and on the localization effects, we did not pursue the calculation of those contributions.

4.3.3.4. Optical Response: The Plasma Edge

As was discussed more or less extensively in § 3.6, the electrical resistivity is not the only property exhibiting unexpected features in EuB_6. Its optical response, registered mainly in reflectivity and magneto-optical Kerr effect experiments, also reveals surprising characteristics. The magnetization-induced blue-shift of the plasma edge is arguably the most remarkable [Degiorgi et al., 1997]. Recalling briefly the essence of this phenomenon, it is observed that the signal for the frequency dependent reflectivity in EuB_6 denounces a good metal with a completely defined plasma edge at $\omega = \omega_p$. As soon as the systems enters into the FM phase, the value of ω_p is considerably enhanced (blue-shift), increasing more than twice between T_C and $T \simeq 0$. A plot of ω_p obtained at different temperatures and magnetic fields, shows a remarkable scaling of the plasma edge with the magnetization [Broderick et al., 2002b]. This means that $\omega_p(T, H) = \omega_p\left(M(T, H)\right)$ and, consequently, the variation of ω_p can be ascribed entirely to the changes in the magnetization of the system.

Now that we know what happens to the carrier density when M varies, it might not seem that surprising, for in the context of this DE interpretation, the enhancement of n_{cond} has to be directly related with the changes in the plasma frequency. This statement follows from the consideration of the Drude classical definition of the plasma frequency:

$$\omega_p{}^2 = \frac{4\pi n e^2}{m^*}. \tag{4.72}$$

Since the classical theory hinges upon the dynamics of mobile carriers, then n above shall correspond to the density of extended states, n_{cond}. Given that n_{cond} increases below T_C , the concurrent increase in ω_p is not unexpected. But even the classical result (4.72) adds a slight complication: the optical effective mass, m^*, is not expected to be constant, and there is experimental evidence for considerable variations of m^* [Broderick et al., 2002b]. So additional care must be undertaken in the analysis of ω_p within this model.

Although disordered, and hence non-trivial for analytical approaches sensitive to the details of Anderson localization, our model is still modeled by a tight-binding Hamiltonian. For those cases, ω_p is related to the average kinetic energy of the system[43] via a sum rule. Given that this is a general result we will expound it hereupon. The emphasis is on the sum rule, but we sketch the main steps involved in the overall argument.

Interaction Hamiltonian Since we are interested in the linear response of the solid to external electromagnetic fields, the interaction (perturbing) Hamiltonian retains only the terms linear in the vector potential operator $\vec{A}(r,t)$:

$$H' = -\frac{1}{c}\int \vec{j}(\vec{r},t)\cdot\vec{A}(\vec{r},t)\,, \tag{4.73}$$

with the electric potential, $\phi(\vec{r},t)$ being zero in the chosen Coulomb gauge, and the current operator $\vec{j}(\vec{r},t)$ defined as

$$\vec{j}(\vec{r},t) = \frac{1}{2m}\sum_i e_i\left[\vec{p}_i\delta(\vec{r}-\vec{r}_i) + \delta(\vec{r}-\vec{r}_i)\vec{p}_i\right]. \tag{4.74}$$

Notice, however, that this current is not the one the experimentalist is interested in when magnetic fields are included. This happens because the measured current relates to the average carrier velocity, and, as well known, momentum and velocity are not the same in the presence of $\vec{B}(\vec{r},t)$:

$$m\vec{v} = \vec{p} - \frac{e}{c}\vec{A}(\vec{r},t)\,. \tag{4.75}$$

Consequently, the *truly* measured current is in fact

$$\vec{J} = \left\langle\vec{j}\right\rangle - \frac{e^2}{mc}\vec{A}(\vec{r},t)\rho(\vec{r})\,, \tag{4.76}$$

where ρ is the particle density. When an electric field (external+induced) $\vec{E}(\vec{r},t) = \vec{E}_0(\vec{r},t)e^{(i\vec{q}.\vec{r}-i\omega t)}$ is applied, this current should be, in linear response:

$$\vec{J}(\vec{r},t) = \sigma(\vec{q},\omega)\vec{E}(\vec{r},t) \quad\Leftrightarrow\quad J_\alpha = \sum_\beta \sigma_{\alpha\beta}(\vec{q},\omega)E_\beta(\vec{r},t)\,. \tag{4.77}$$

The above defines the microscopic optical conductivity. In the Coulomb gauge, $\vec{E} = -c^{-1}\partial_t\vec{A}$, which means that $\vec{E}(\vec{r},t) = i\omega/c\vec{A}(\vec{r},t)$. Plugging back in eq. (4.76) we get

$$\vec{J}(\vec{r},t) = \left\langle\vec{j}(\vec{r},t)\right\rangle + i\frac{e^2}{m\omega}\vec{E}(\vec{r},t)\rho(\vec{r})\,, \tag{4.78}$$

and hence the calculation of $\left\langle\vec{j}\right\rangle$ is all that is needed to get the optical conductivity from (4.77).

[43] Which should not come as a surprise since there is only one energy scale: the hopping t.

Kubo Formula for the Optical conductivity The microscopic details of $\langle \vec{j} \rangle$ involve the calculation of, formally and exactly,

$$\langle \vec{j}(\vec{r},t) \rangle = \langle \psi_0 \left| e^{i\mathcal{H}t} j_\alpha(\vec{r},t) e^{-i\mathcal{H}t} \right| \psi_0 \rangle \,, \tag{4.79}$$

plus a spacial averaging over the entire system that eliminates atomic fluctuations and connects the result with the macroscopic electromagnetism to which the experimental probes are sensitive. The Kubo formula corresponds to the perturbative calculation of the above up to $\mathcal{O}(H')$, yielding [Mahan]

$$\langle \vec{j}(\vec{r},t) \rangle = \frac{1}{\omega} \sum_\beta E_\beta(\vec{r},t) e^{-i\vec{q}\cdot\vec{r}} \int_{-\infty}^{t} e^{i\omega(t-t')} \Big\langle \big[j_\alpha(\vec{r},t), j_\beta(\vec{q},t') \big] \Big\rangle_{\psi_0} \,, \tag{4.80}$$

which is then spatially averaged, and substituted back in (4.78), providing the frequency and momentum dependent conductivity[44]

$$\sigma_{\alpha\beta}(\vec{q},\omega) = \frac{1}{\omega} \int_0^\infty dt e^{i\omega t} \Big\langle \big[j_\alpha^\dagger(\vec{q},t), j_\beta(\vec{q},t') \big] \Big\rangle_{\psi_0} + \frac{ine^2}{m\omega} \delta_{\alpha,\beta} \,. \tag{4.81}$$

It is useful to introduce the retarded correlation function

$$\chi_{\alpha\beta}(\vec{q},\omega) = i \int_{-\infty}^{\infty} dt \theta(t) e^{i\omega t} \Big\langle \big[j_\alpha^\dagger(\vec{q},t), j_\beta(\vec{q},0) \big] \Big\rangle_{\psi_0} \,, \tag{4.82}$$

in terms of which the conductivity reads

$$\sigma_{\alpha\beta}(\vec{q},\omega) = \frac{1}{i\omega} \Big\{ \chi_{\alpha\beta}(\vec{q},\omega) - \frac{ne^2}{m^*} \delta_{\alpha,\beta} \Big\} \,. \tag{4.83}$$

Sum Rules The above is still a formal and general result, which we are interested to particularize for a tight-binding Hamiltonian. In the following we assume homogeneous (or sufficiently long wavelength) fields and drop the $\vec{q}$ dependence. In addition, we will focus upon an isotropic medium where the non-diagonal $\chi_{\alpha\beta}$ vanish and $\chi_{11} = \chi_{22} = \chi_{33}$ (which is always the case for a cubic crystal).

In terms of the real and imaginary components, $\sigma = \sigma' + i\sigma''$, our goal is to get an expression for the complete integral $\int_0^\infty \sigma'(\omega) d\omega$. The correlation function χ can be spectrally decomposed as

$$\chi_{\alpha\alpha}(\omega) = \sum_n |\langle 0 \left| j_\alpha \right| n \rangle|^2 \left(\frac{1}{\omega + \epsilon_n - \epsilon_0 + i\eta} - \frac{1}{\omega - \epsilon_n + \epsilon_0 + i\eta} \right) \,, \tag{4.84}$$

and from (4.83) it follows that

$$\sigma'_{\alpha\beta}(\omega) = \frac{1}{\omega} \chi''_{\alpha\beta}(\omega) \,, \qquad \sigma'_{\alpha\alpha}(\omega) = \pi \sum_n \frac{|\langle 0 \left| j_\alpha \right| n \rangle|^2}{\epsilon_n - \epsilon_0} \delta(|\omega| + \epsilon_0 - \epsilon_n) \,. \tag{4.85}$$

In order to see how this form is useful consider the polarization operator, $\vec{P}$, and its representation in

[44] Here, the electron spacial density, $\rho(\vec{r})$, is replaced by its homogeneous ($q = 0$) component, or average density, n.

terms of Wannier orbitals

$$\vec{P} = \int \psi^\dagger(\vec{r})\vec{R}\psi(\vec{r})d\vec{r} = \sum_i \vec{r}_i c_i^\dagger c_i \,. \tag{4.86}$$

To obtain the current operator required for the calculation of Eq. (4.85) we simply notice that

$$\vec{j} = q\,\partial_t \vec{P} = iq[\mathcal{H}, \vec{P}] = -iq\sum_{\langle ij\rangle} t_{ij} c_i^\dagger c_j(\vec{r}_j - \vec{r}_i) \,. \tag{4.87}$$

Hence, we can take $\langle 0\,|j_\alpha|\,n\rangle = iq(\epsilon_0 - \epsilon_n)\,\langle 0\,|P_\alpha|\,n\rangle$ and substitute in (4.85) as follows:

$$\begin{aligned}\sigma'_{\alpha\beta}(\omega) &= \frac{\pi}{2}\sum_n \left(\frac{\langle 0\,|j_\alpha|\,n\rangle\,\langle n\,|j_\alpha|\,0\rangle}{\epsilon_n - \epsilon_0} + \frac{\langle 0\,|j_\alpha|\,n\rangle\,\langle n\,|j_\alpha|\,0\rangle}{\epsilon_n - \epsilon_0}\right)\delta(|\omega| + \epsilon_0 - \epsilon_n) \\ &= \frac{i\pi}{2}\sum_n \left(\langle 0\,|j_\alpha|\,n\rangle\,\langle n\,|P_\alpha|\,0\rangle - \langle 0\,|P_\alpha|\,n\rangle\,\langle n\,|j_\alpha|\,0\rangle\right)\delta(|\omega| + \epsilon_0 - \epsilon_n) \,. \end{aligned} \tag{4.88}$$

After integration:

$$\int_0^\infty \sigma'_{\alpha\beta}(\omega)d\omega = \frac{\pi}{2} iq\big\langle [j_\alpha, P_\alpha]\big\rangle \,. \tag{4.89}$$

So, it remains to calculate the current-polarization commutator, which is trivial for a tight-binding Hamiltonian:

$$[j_\alpha, P_\beta] = -iq\sum_{\langle ij\rangle} t_{ij}(x_j^\alpha - x_i^\alpha)(x_j^\beta - x_i^\beta)c_i^\dagger c_j \,, \tag{4.90}$$

and therefore

$$\frac{2}{\pi}\int_0^\infty \sigma'_{\alpha\alpha}(\omega)d\omega = q^2\left\langle \sum_{\langle ij\rangle} t_{ij}(x_j^\alpha - x_i^\alpha)^2 c_i^\dagger c_j \right\rangle \tag{4.91}$$

If we define $\sigma(\omega)$ as the average of the three components

$$\sigma(\omega) = \frac{1}{3}\sum_\alpha \sigma_{\alpha\alpha}(\omega) \,, \tag{4.92}$$

and take $(x_j^\alpha - x_i^\alpha) = a$ as the cubic lattice parameter, we finally obtain

$$\frac{2}{\pi}\int_0^\infty \sigma'(\omega)d\omega = -\frac{1}{3}q^2a^2\,\langle \mathcal{H}\rangle \tag{4.93}$$

This sum rule states that the frequency integrated σ' is simply the kinetic energy of the system, irrespective of the details of the microscopic hoppings t_{ij}.

Relation to the Optical Sum Rule There is an important sum rule for crystals that reads [Wooten, 1972]

$$\int_0^\infty \omega\varepsilon''(\omega)d\omega = \frac{\pi}{2}{\omega_p}^2 \,, \tag{4.94}$$

and, since $\varepsilon''(\omega)$ is associated with dissipation, it physically means that the total rate of energy absorption by the solid is determined by its plasma edge, ω_p. For a good metal as EuB_6, it generally happens that the optical response of the solid is quite well described within the Drude-Lorentz classical absorption

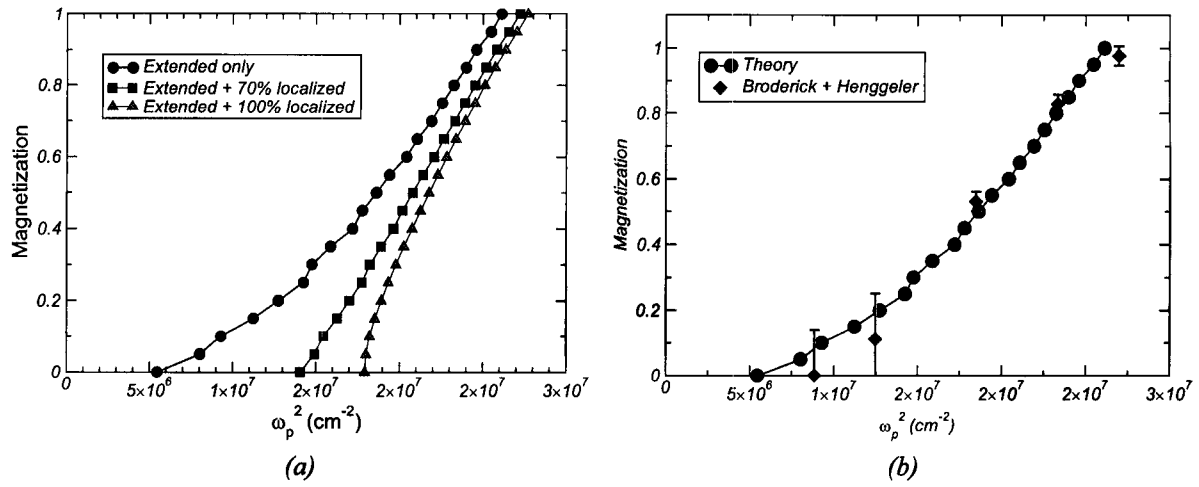

FIGURE 4.20 .: *Plasma frequency, ω_p, as function of the magnetization. (a) Comparison between the three scenarios discussed in the text for the calculation of ω_p. (b) Comparison of the model prediction for $\omega_p\,(M)$ with the experimental dependence. For the experimental points, $\omega_p(T)$ data from Broderick et al. [2002b] have been combined with $M(T)$ data from Henggeler et al. [1998]. All theoretical curves have been obtained with $t = 0.55$ eV and $n_{cond}(0) = 0.003$, as in the previous figure 4.19.*

theory. In practice, this means that the measured optical reflectivity (or, for that matter, other accessible optical property), and its frequency dependence can be fitted to $\sigma(\omega)$ and $\varepsilon(\omega)$ predicted by such classical model with great accuracy. In that case, when Drude-Lorentz holds, we have

$$\varepsilon(\omega) = 1 + \frac{4\pi i}{\omega}\sigma(\omega) \tag{4.95}$$

whence

$$\frac{2}{\pi}\int_0^\infty \sigma'(\omega)d\omega = \frac{1}{4\pi}{\omega_p}^2, \tag{4.96}$$

and the desired relation between ω_p and the kinetic energy ensues:

$${\omega_p}^2 = -\frac{4\pi}{3}q^2a^2\,\langle\mathcal{H}\rangle\ . \tag{4.97}$$

Comparison with the Experiment The last result provides us with means to address the optical response predicted by our theoretical model and compare the result with the measured values. For that, it is necessary to recollect how the experimental values of ω_p are calculated. In the experiments of concern to us, the procedure is to measure the frequency dependent reflectivity, $\mathcal{R}(\omega)$, [Broderick et al., 2002b; Degiorgi et al., 1997] or the optical Kerr rotation, $\theta_K(\omega)$, [Broderick et al., 2002a, 2003]. From $\mathcal{R}(\omega)$ all the optical functions (conductivity, refractive index, dielectric constant, etc.) are then straightforwardly extracted via Kramers-Kronig transformations and classical identities [Wooten, 1972]. Classical dispersion theory is subsequently used to fit the data, and fits of excellent quality are obtained [Degiorgi et al., 1997], which in turn implies that the optical response is well described within the Drude-Lorentz framework. There are two main techniques used by experimentalists to obtain ω_p. One of them is to extract the optical conductivity $\sigma(\omega)$, integrate over all the frequencies and use the optical sum-rule (4.96) to

get the value of ω_p [45]. The other method hinges upon the fact that ω_p is itself a fitting parameter of the classical Drude-Lorentz model [Fox, 2004], and can be extracted in that way from the fit results.

Anyhow, the signals being well described within Drude-Lorent, and Drude-Lorentz pertaining to the dynamical description of *free carriers*, strongly hints at the extended carriers being the main players in these optical processes. The argument is that, since the densities of localized and extended carriers is of the same order of magnitude, and since at $M = 0$ there are presumably more localized than extended states (roughly in the proportion 2:1, Fig. 4.19), the localized states should provide only a small contribution to the optical response. This is important because, in order to obtain the model results for ω_p using eq. (4.97), we need to calculate $\langle \mathcal{H}_{DEM} \rangle$ using the numerical DOS:

$$\langle \mathcal{H}_{DEM} \rangle_M = \int_?^{E_F(M)} \rho(E, M) E dE \,. \tag{4.98}$$

The question mark underlines the point we have been trying to introduce: that it is not trivial where the lower limit of integration should be. We have essentially three distinct possibilities:

(i) only extended states contribute and $? = E_c(M)$;

(ii) a fraction of the localized states also contributes and $-\infty < ? < E_c(M)$:

(iii) all the band states contribute and $? = -\infty$.

The outcome of each of these scenarios is shown in Fig. 4.20a for the magnetization dependence of the plasma frequency. The results have been calculated by setting $n_{cond}(M = 0) = 0.003$ as before, and taking for the hopping $t = 0.55$ eV. The first curve (○) has been calculated in the first scenario, where only states between $E_c(M)$ and $E_F(M)$ accounted. In the second case (□) 70% of the localized states closest to E_c are taken into account. This means that the integration is done in the domain $[E^*(M), E_F(M)]$, where $E^*(M)$ satisfies

$$(1 - 0.7)\, n_{loc}(M) = \int_{-\infty}^{E^*(M)} \rho(E, M) dE \,. \tag{4.99}$$

It has to be remarked, however, that this case, and the choice of the figure 70% in particular, is rather arbitrary. The physical idea is that one might envisage some of the localized states with largest localization lengths contributing to the optical processes, and hence needing to be accounted for in the calculation of the kinetic energy. Even if this were the case, the condition above would be a considerable simplification because it takes a *rigid* fraction of carriers at all magnetizations, whereas we would expect this fraction to be a function of M as well, determined by some definite criterion. This curve is shown here mainly for illustration purposes since it interpolates between scenario (i) and (iii). As to the latter, represented by the triangles in the figure, it is the situation more difficult to reconcile conceptualy with the great success of the Drude-Lorentz fits to the experiments, as discussed above. In this scenario, $\omega_p(M)^2$ basically follows the variation of the bandwidth with magnetization, as can be see by comparison with the M-dependence of the bandwidth (cfr. blue curve in Fig. 4.14a, or 4.23), while the situation in the other two cases is quite different. An important point in common between all three scenarios is the linear

[45] Actually, due to the finite frequency range scanned experimentally, in practice the frequency integration is done up to some high energy cut-off.

dependence $\omega_p(M)^2 \sim A + BM$ at high magnetizations, in accord with the experimental scaling of the plasma edge with M [Broderick et al., 2002b].

In Fig. 4.20b we set the results obtained under (i) face to face with the experimental data for ω_p at different magnetizations. The quantitative agreement is quite striking, especially at higher magnetizations. Once again, this agreement demonstrates how important the consideration of localized states is to the physics of this hexaboride, in the sense that the theoretical curve plotted there corresponds to the calculation of

$$\omega_p^2 = -\frac{4\pi}{3} q^2 a^2 \int_{E_c(M)}^{E_F(M)} \rho(E, M) E dE \,, \tag{4.100}$$

where the contribution from the localized states is explicitly taken out. This theoretical result adds to the ones shown previously in Fig. 4.19, in support of our DE-based interpretation of the interesting physics in EuB_6. As the results document, this theoretical picture does seem to capture the essence of the most intriguing experimental features of these compounds. This has been published in the letter [**VITOR M. PEREIRA**et al., 2004a].

Before closing this section, a point is worth mentioning. To obtain the variation of $n_{cond}(M)$ and resistivity (Fig. 4.19) we had to adjust a single parameter: the carrier density. In reality, this is not quite a free parameter in the sense that $n_{cond}(0)$ was tied to the experimentally measured values. Notwithstanding, the curve calculated for $n_{cond}(M)$ accords to the extent visible in the figure with the measured one. The hopping doesn't enter at this stage, because the calculation involves just counting states. But, of course, the hopping is essential to determine ω_p. Having fixed $n_{cond}(0)$, we determined the hopping, t, that best reproduces the experimental plasma frequency, having obtained $t = 0.55$ eV. This value is completely within the range indicated in (4.2), which is based on several experiments and electronic structure calculations. This shows consistency of the model predictions among the two independent experiments.

4.4. The DE interpretation of $Eu_{1-x}Ca_xB_6$

In the previous pages, a series of theoretical results were derived for the DEM in the regime of low carrier densities. By substituting the hopping and density parameters adequate in the context of EuB_6, a good agreement between theory and experiment followed. It is appropriate at this point to summarize the overall understanding that this DE-based picture provides regarding the microscopic details of these hexaborides, and how several distinctive experimental signatures can be consistently understood within this framework.

The series $R_{1-x}A_xB_6$, where A is an alkaline-earth metal such as Ca or Sr, and R a rare-earth magnetic ion, constitutes a family of cubic compounds where a divalent lanthanoid occupies the central position on a cube, surrounded by eight B_6 octahedra at each vertex. Boron atoms make up a rigid cage, held together by covalent bonds between neighboring B atoms. EuB_6 is a ferromagnetic metal, ordering at $T_C \approx 15$ K, and characterized by a quite small effective carrier density, of order of 10^{-3} per unit cell, at high temperatures. Magnetism is found to arise from the half-filled $4f$ shell of Eu, whose localized electrons account for the measured magnetic moment of $7\,\mu_B$ per formula unit. The FM transition temperature is reported to decrease with increasing Ca content and the totally substituted compound CaB_6 exhibits no magnetism.

In the previous sections we have proposed a simple model that describes quantitatively the following properties revealed by the experiments done in EuB_6:

(i) A precipitous drop in the dc resistivity just below T_C, with a change by a factor as high as 50 between T_C and the lowest temperatures;

(ii) The large negative magnetoresistance observed near T_C;

(iii) An increase in the number of carriers, by a factor of $2-3$, upon entering the ordered phase, as evidenced by Hall effect;

(iv) A large blue shift of the plasma edge, seen also for $T \leq T_C$, both in reflectivity, $R(\omega)$, and polar Kerr rotation;

(v) A scaling of the plasma frequency with the magnetization.

The enumerated features constitute a definite case of strong coupling of the magnetization to the transport properties. As will be clear below, the effects of chemical doping with non-magnetic Ca are also considered, and the theory explains qualitatively the following experimental findings:

1. With doping, x, the metallic regime, found in EuB_6 ($x = 0$), evolves to a semiconducting behavior above T_C;

2. Just below T_C the carrier density increases by at least two orders of magnitude;

3. The plasma edge is visibly smeared while the corresponding resonance in the polar Kerr rotation is greatly attenuated;

4. $\rho(T, H)$ and ω_p display an exponential dependence in the magnetization;

5. There remains a significant and rapid decrease of $\rho(T)$ just below T_C, albeit by a smaller factor than in the undoped case.

To understand how this comes about in the doped case consider the following. Band structure calculations seem to agree that the conduction band has a strong $5d$ Eu component. Ca doping not only dilutes the magnetic system but also the conducting lattice. In order to model this effect, the hoping parameter $t_{i,j}$ should then be replaced by $t_{i,j}p_ip_j$, where $p_i = 1$ if the site i is occupied by a Eu atom and $p_i = 0$, otherwise. The microscopic problem thus becomes a DE problem in a percolating lattice which, at $T = 0\,\mathrm{K}$, reduces to a quantum percolation problem [Shapir et al., 1982].

Since Ca and Eu are isovalent in hexaborides one does not expect the number of carriers to depend on x. Nevertheless, since carriers are presumed to arise from defects it is difficult to be specific on this issue. The mobility edge, on the other hand, is very sensitive to the $\mathrm{Eu} \rightarrow \mathrm{Ca}$ substitution, and should drift toward the band center reflecting the increased disorder. Therefore, the effects should be much more pronounced in E_c than in E_F. In the paramagnetic regime ($T > T_C$), and as more Ca is introduced, E_c should move past the Fermi energy at some critical doping x_{MI}^P, after which the mobility gap (4.66) becomes positive (Fig. 4.21). Naturally, this determines a crossover from the metallic regime

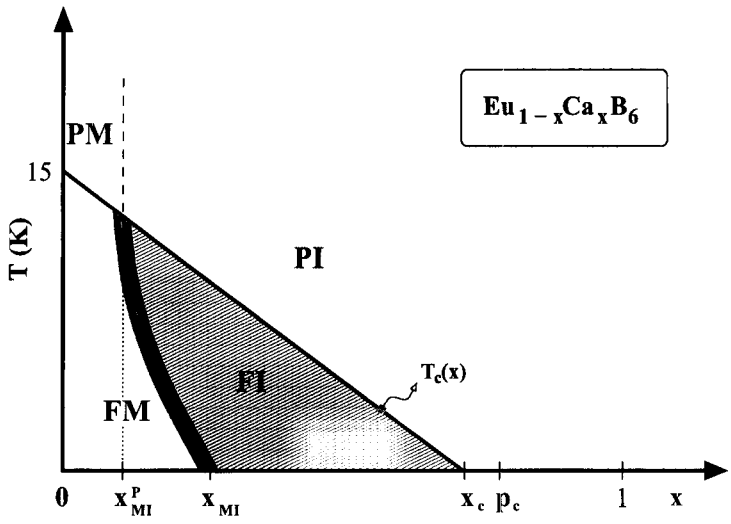

FIGURE 4.21 .: *Schematic phase diagram for $Eu_{1-x}Ca_xB_6$ in the $T-x$ plane in standard notation: PM stands for paramagnetic metal, PI for paramagnetic insulator, FM means ferromagnetic metal and FI ferromagnetic insulator.*

to an insulating behavior for $T > T_C$, exactly as seen in the doped compounds [Paschen et al., 2000; Wigger et al., 2002a]. At finite T the mobile carriers arise from thermal activation across the mobility gap. The resistivity should display a semiconducting behavior with T and its dependence on M should be dominated by an exponential factor $\rho(M) \sim \exp(\Delta(M)/T)$ [Mott and Davis, 1971]. In fact, using $\Delta(M) \approx \Delta_0(1 - \alpha M)$, as happens in the non-diluted case for either of the $\Delta(M) \lessgtr 0$ situations, we find that $\rho(M) \sim \exp(-\zeta M)$ (ζ is a constant), as seen in the experiments [Wigger et al., 2002a].

As T is lowered below T_C and M increases on the percolating cluster, one expects the crossover from metallic to semiconducting behavior to occur at larger values of x; this is illustrated in Fig. 4.21 by the curved/dashed line separating the FM and FI regions. In the vicinity of this line, a sharp metal–semiconducting distinction is not possible on account of thermal effects, resulting possibly in a *bad–metal* behavior. At $T = 0$, there is a metal–insulator transition occurring at a concentration $x_{MI} \geq x_{MI}^P$, which corresponds to the quantum percolation transition for a small number of carriers[46]. Even though we expect x_{MI} to be close to x_{MI}^P, the possibility of a semiconducting behavior crossing over to metallic at low T (for some $x_{MI}^P < x < x_{MI}$) cannot be excluded[47].

Ferromagnetism induced by the DE mechanism is expected to persist past x_{MI} as long as the localization length is greater than the lattice spacing. Naturally, the critical concentration, x_c, where $T_C \to 0$, should not be higher than $p_c \approx 0.69$, the classical site–percolation threshold for the simple cubic lattice [Stauffer and Aharony, 1994]. The values of x_{MI}^P and x_{MI} in Fig. 4.21 vary with carrier density and are expected to be sample dependent, since carriers seemingly arise from defects. Actually, annealing experiments can be quite important for the study of the phase diagram.

[46]This is different from the usual quantum percolation point $p_Q < p_c$, which is defined by the localization of all states in the band [I. Chang *et al.*, 1994].

[47]According to this picture, the mobility edge still changes with magnetization, even with doping. Therefore, if we have a system with x closely above x_{MI}^P, (which, in turn, means that $E_F(M = 0) \simeq E_c(M = 0)$) then, upon entering the FM phase E_c should move towards the band edge just as in pure EuB_6, causing E_c to stay behind E_F and yielding a metal at lower temperatures.

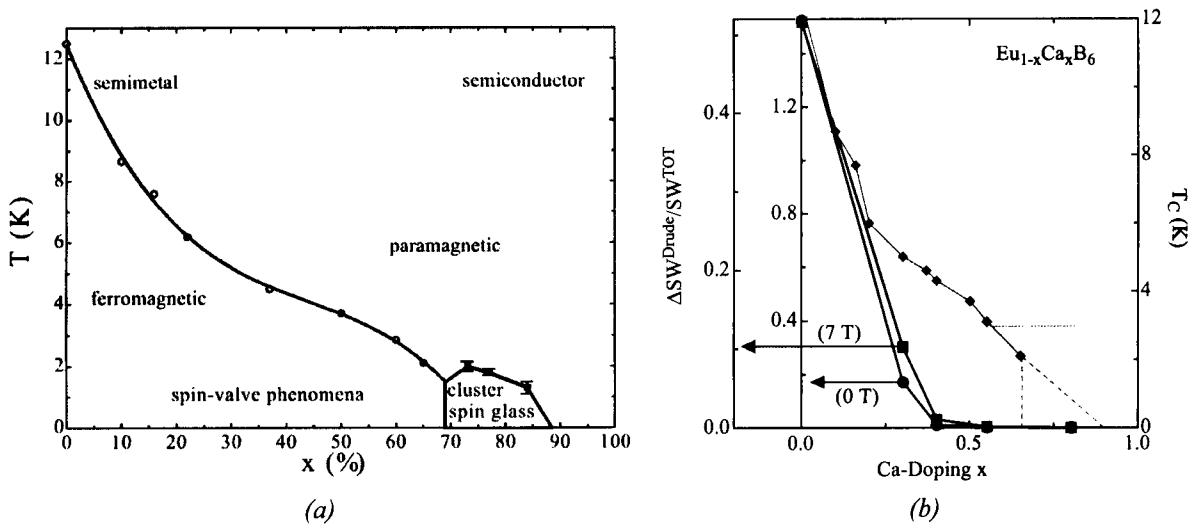

FIGURE 4.22 .: *Recent developments in the experimental data available for* $Eu_{1-x}Ca_xB_6$. *(a) Magnetic phase diagram obtained from specific heat, resistivity and magnetization measurements in* $Eu_{1-x}Ca_xB_6$. *The small dome in the range* $70 \lesssim x \lesssim 90$ *corresponds to a region where glassy-like correlations are found [Wigger et al., 2005]. (b) Dependence of* T_C *on the Ca doping level, compared with the change of spectral weight of the Drude component in* $\sigma'(\omega)$. *Notice that, irrespective of the external magnetic field, the magneto-optical response drops to zero much earlier than the magnetism [Caimi et al., 2006].*

Another consequence of the DE picture is that within this model T_C scales with $\langle \mathcal{H} \rangle$ [de Gennes, 1960; Kubo and Ohata, 1972]. Since ω_p^2 follows the same scaling, we expect that in the series $Eu_{1-x}Ca_xB_6$ the squared plasma frequency should scale approximately with T_C.

This interpretation is summarized in the phase diagram presented in Fig. 4.21. At the time of original publication [**VITOR M. PEREIRA**et al., 2004b], this phase diagram was still a prediction since only two experimental studies for $x = 0.2$ and $x = 0.4$ were known. Next we reproduce some subsequent developments that seemingly confirm this phase diagram for the family $Eu_{1-x}Ca_xB_6$.

4.4.1. Recent Experimental Developments

The first relevant set of results came from a relatively comprehensive study of the magneto-transport thoughout the Ca-doped series by Wigger et al. [2004]. These experiments revealed that the Eu→Ca substitution leads to strong percolation-related effects in the characteristics of both the magnetic order and electrical transport. They made possible the construction of the experimental phase diagram shown in Fig. 4.22a, which clearly resembles the theoretically proposed one in Fig. 4.21.

Another set of experiments undertook the analysis of the optical response in the $Eu_{1-x}Ca_xB_6$ series, and provides a most interesting and revealing study complementary to the magneto-transport results [Caimi et al., 2006]. The practical procedure consisted in collecting reflectivity spectra, $\mathcal{R}(\omega)$, for differently doped samples, and analyzing them within Kramers-Kronig and Drude-Lorentz theory, just as described in § 4.3.3.4.

The primary target was the evaluation of the change of Spectral Weight (SW) of the metallic component of $\sigma'(\omega)$ at $\overline{T} > T_C$, between 0 and 7 T. This difference is calculated on the basis of the Drude-

Lorentz results and is defined as:

$$\Delta SW^{\text{Drude}} = SW^{\text{Drude}}(\overline{T}, 7\text{ T}) - SW^{\text{Drude}}(\overline{T}, 0\text{ T}) \tag{4.101}$$

The magnetic field of 7 T is high enough to drive the system into magnetic saturation for all values of x, such that $\sigma'(\omega)$ at 7 T reflects the maximum metallicity reached by increasing the magnetic field.

Fig. 4.22b reproduces the variation of the normalized Drude spectral weight (i.e., $\Delta SW^{\text{Drude}}/SW^{\text{Total}}$) as a function of x, in comparison with the variation of T_C across the series [Caimi et al., 2006]. The ranges on the vertical axes were chosen such that $T_C(x = 0)$ coincides with the renormalized changes of the Drude spectral weight. ΔSW^{Drude} decreases sharply between $x = 0$ and 0.3, reaching zero at approximately 50 % Ca content.

The x dependence of ΔSW^{Drude} reveals the reduction of the itinerant charge carriers with increasing doping. The field-induced enhancement of ΔSW^{Drude} as a function of x and its correlation with the evolution of T_C is fully consistent with the microscopic mechanisms that are considered in the low-density DE model applied to a percolating lattice. Fig. 4.22b shows that the spectral weight of the Drude contribution to $\sigma'(\omega)$ is enhanced when the system is driven from a PM metallic state into full polarization, up to $x \simeq 0.4$. The progressive reduction of this enhancement with x reflects the drift of E_C and the consequently weakened metallic conduction. For higher Ca concentrations, the Drude spectral weight is insensitive to the spin polarization, a signal that the mobility edge went past the Fermi energy and thus the polarization no longer releases any of the localized states. The decay to zero in the curves for $\Delta SW^{\text{Drude}}/SW^{\text{Total}}$ is equivalent to the T-dependent crossover line in the theoretical phase diagram (dashed line in Fig. 4.21). The tail-like behavior of $\Delta SW^{\text{Drude}}/SW^{\text{Total}}$ for $x \gtrsim 0.4$ can be understood as originating from the nonzero temperature excitations of carriers across the mobility gap. It is also significant that the results do not depend on the magnetic field used for the normalization of ΔSW^{Drude}, as evidenced by the two curves, where ΔSW^{Drude} is normalized by SW^{Total} at either 0 or 7 T.

With respect to magnetic order, Fig. 4.22b shows that the Curie temperature decreases with x, as expected if site percolation is important. Unlike the Drude spectral weight, long-range magnetic order survives until the Ca concentration coincides with the threshold of site percolation. This is in accord with the DE scenario in which the effective magnetic coupling is the result of the electron itinerancy among sites with localized moments. From the optical point of view, the results in Fig. 4.22b perfectly reflect the phase diagram predicted in Fig. 4.21: up to $x_{MI} \simeq 0.4$ one has a metallic ferromagnet; for higher Ca content the system remains a ferromagnetic Anderson insulator until it reaches the percolation threshold. Near and above the percolation threshold the number of disconnected Eu-rich magnetic clusters becomes significant. Even though the tendency should be towards ferromagnetism, it is not surprising that the regime above $x \simeq 0.7$ (beyond percolation, and at very low temperatures) seems to be characterized by glassy magnetism [Wigger et al., 2005], on account of the possible presence of superparamagnetic clusters and competing dipolar interactions at such extreme dilutions of the magnetic moments.

The fact that this optical phase diagram strongly resembles the phase diagram coming from our DE picture, underlines the significance of localization effects in the description of these compounds.

Appendices for this chapter

Appendix 4.A Bilinear Fermionic Commutators

Consider the $\hat{A}$ and $\hat{B}$ operators, bilinear in the fermionic creation and annihilation operators:

$$\hat{A} = \Psi^\dagger A \Psi \equiv \sum_{i,j} A_{i,j} c_i^\dagger c_j \quad \text{and} \quad \hat{B} = \Psi^\dagger B \Psi \equiv \sum_{i,j} B_{i,j} c_i^\dagger c_j \quad \text{, with} \quad \Psi = \begin{pmatrix} c_1 \\ \vdots \\ c_N \end{pmatrix} . \tag{4.102}$$

The commutator $[\hat{A}, \hat{B}]$ evaluates as follows:

$$\begin{aligned} [\hat{A}, \hat{B}] &= \sum_{ijkl} A_{ij} B_{kl} [c_i^\dagger c_j, c_k^\dagger c_l] = \sum_{ijkl} A_{ij} B_{kl} (\delta_{jk} c_i^\dagger c_l - \delta_{il} c_k^\dagger c_j) = \sum_{ijk} c_i^\dagger c_j (A_{ik} B_{kj} - B_{ik} A_{kj}) \\ &= \Psi^\dagger [A, B] \Psi . \end{aligned} \tag{4.103}$$

This is not surprising at all. Now, suppose that the basis of the Hilbert space for which the c_i are defined, is actually a tensorial product of two vectorial spaces, say $h_1 \otimes s$, that suits electrons in some single particle Hilbert space h_1. Rather than using the extended spinor notation spanning the full Hilbert space, as in (4.102), second quantized operators for single particle processes are customarily presented as

$$\hat{A} = \sum_{ij} \Psi_i^\dagger a_{ij} \Psi_j \equiv \sum_{\substack{i,j \\ \alpha\beta}} a_{i,j}^{\alpha\beta} c_{i\alpha}^\dagger c_{j\beta} . \tag{4.104}$$

If we commute two operators in this representation the result will be[48]

$$\begin{aligned} [\hat{A}, \hat{B}] &= \sum_{ijkl} \sum_{\alpha\beta\gamma\delta} a_{ij}^{\alpha\beta} b_{kl}^{\gamma\delta} [c_{i\alpha}^\dagger c_{j\beta}, c_{k\gamma}^\dagger c_{l\delta}] \\ &= \sum_{ijkl} \sum_{\alpha\beta\gamma\delta} a_{ij}^{\alpha\beta} b_{kl}^{\gamma\delta} (\delta_{jk} \delta_{\beta\gamma} c_{i\alpha}^\dagger c_{l,\delta} - \delta_{il} \delta_{\alpha\delta} c_{k,\gamma}^\dagger c_{j\beta}) \\ &= \sum_{ijk} \sum_{\alpha\beta\gamma} (a_{ik}^{\alpha\gamma} b_{kj}^{\gamma\beta} - b_{ik}^{\alpha\gamma} a_{kj}^{\gamma\beta}) c_{i\alpha}^\dagger c_{j\beta} \\ &= \sum_{ijk} \Psi_i^\dagger \left(a_{ik} b_{kj} - b_{ik} a_{kj} \right) \Psi_j . \end{aligned} \tag{4.105}$$

[48] Notice that now the a_{ij} are 2×2 matrices and $a_{ij}^{\alpha\beta}$ its matrix elements.

One notices that the last term is not the commutator of the two 2×2 matrices a_{ij} and b_{ij}. It is just an explicit form of the result that, for matrices in $h_1 \otimes s$, we have

$$[h_1^a \otimes s^a, h_1^b \otimes s^b] = h_1^a h_1^b \otimes s^a s^b - h_1^b h_1^a \otimes s^b s^a \,. \tag{4.106}$$

Appendix 4.B DEM: Projecting out the high energy scales

Recall the KLM hamiltonian written in the local quantization basis presented in eq. (4.11), that we decompose here, for simplicity, as

$$\mathcal{H}_{KLM} = \sum_{i,j} \tilde{\Psi}_i^\dagger \Big(\mathcal{T}_{ij} + \mathcal{J}_{ij} \Big) \tilde{\Psi}_j = \mathsf{T} + \mathsf{J} \,. \tag{4.107}$$

One then starts from the formal identity

$$\hat{H}' = e^{\hat{S}} \hat{H} \, e^{-\hat{S}} = \hat{H} + [\hat{S}, \hat{H}] + \frac{1}{2}[[\hat{S}, [\hat{S}, \hat{H}]] + \frac{1}{3!}\Big[\hat{S}, [[\hat{S}, [\hat{S}, \hat{H}]]\Big] + \dots \,, \tag{4.108}$$

applied to $\mathcal{H}_{KLM}$. We will have then

$$\hat{H}' = \mathsf{J} + \mathsf{T} + [S, \mathsf{T}] + [S, \mathsf{J}] + \frac{1}{2}[[S, [S, \mathsf{T}]] + \frac{1}{2}[[S, [S, \mathsf{J}]] + \dots \,. \tag{4.109}$$

The objective is to project out the off-diagonal terms in spin space. For that one would usually separate the Hamiltonian into diagonal and an off-diagonal parts, and follow a straightforward process to determine the S that accomplishes that. Here we chose the separation above because it simplifies some sums in real space that will arise below. What is needed to project out the off-diagonal spin components to lowest order in perturbation theory is an operator S that is $S \sim \mathcal{O}(t/J)$ and such that

$$\mathsf{T} + [S, \mathsf{J}] \equiv \mathsf{P} = \sum_{i,j} \tilde{\Psi}_i^\dagger \, p_{ij} \tilde{\Psi}_j \tag{4.110}$$

is diagonal. Now from Appendix 4.A one knows that

$$p_{ij} = \mathcal{T}_{ij} + J \sum_k (s_{ik} \, \tau_3 \, \delta_{kj} - \tau_3 \, \delta_{ik} \, s_{kj}) = \mathcal{T}_{ij} + J(s_{ij} \, \tau_3 - \tau_3 \, s_{ij}) \tag{4.111}$$

$$= t_{ij} \begin{pmatrix} a_{ij} & b_{ij} \\ -b_{ij}^* & a_{ij}^* \end{pmatrix} + J \begin{pmatrix} 0 & -2s_{ij}^{12} \\ 2s_{ij}^{21} & 0 \end{pmatrix} \tag{4.112}$$

A valid choice for s_{ij} is

$$s_{ij} = \frac{t_{ij}}{2J} \begin{pmatrix} 0 & b_{ij} \\ b_{ij}^* & 0 \end{pmatrix} . \tag{4.113}$$

Defining $\mathsf{Q} = [S, \mathsf{J}]$ and using the definition of P above, the transformed Hamiltonian is at this stage

$$\hat{H}' = \mathsf{J} + \mathsf{P} + [S, \mathsf{P}] - \frac{1}{2}[S, \mathsf{Q}] + \mathcal{O}\left(\frac{t^3}{J^2}\right) . \tag{4.114}$$

We thus still need to evaluate these two commutators.

$$[S,\mathsf{P}] = \sum_{ijk} \tilde{\Psi}_i^\dagger \, (s_{ik}p_{kj} - p_{ik}s_{kj})\tilde{\Psi}_j$$

$$[S,\mathsf{P}]_{ij} = \sum_k \frac{t_{ik}t_{kj}}{2J} \begin{pmatrix} 0 & b_{ik}a_{kj}^* - a_{ik}b_{kj} \\ b_{ik}^*a_{kj} - a_{ik}^*b_{kj}^* & 0 \end{pmatrix}, \tag{4.115}$$

$$[S,\mathsf{Q}] = \sum_{ijk} \tilde{\Psi}_i^\dagger \, (s_{ik}q_{kj} - q_{ik}s_{kj})\tilde{\Psi}_j$$

$$[S,\mathsf{Q}]_{ij} = \sum_k \frac{t_{ik}t_{kj}}{2J} \begin{pmatrix} 2b_{ik}b_{kj}^* & 0 \\ 0 & -2b_{ik}^*b_{kj} \end{pmatrix}. \tag{4.116}$$

Interestingly, these two terms allow for three site hopping processes as we expect in second order of perturbation in t/J. Replacing the last results back in eq. (4.114), one obtains the transformed Hamiltonian below:

$$\hat{H}' = \sum_{i,j} \tilde{\Psi}_i^\dagger \, h'_{ij} \tilde{\Psi}_j \tag{4.117}$$

in which

$$h'_{ij} = J\delta_{ij} \begin{pmatrix} 1 & 0 \\ 0 & -1 \end{pmatrix} + t_{ij} \begin{pmatrix} a_{ij} & 0 \\ 0 & a_{ij}^* \end{pmatrix} + \sum_k \frac{t_{ik}t_{kj}}{2J} \begin{pmatrix} b_{ik}b_{kj}^* & 0 \\ 0 & -b_{ik}^*b_{kj} \end{pmatrix}$$

$$+ \sum_k \frac{t_{ik}t_{kj}}{2J} \begin{pmatrix} 0 & b_{ik}a_{kj}^* - a_{ik}b_{kj} \\ b_{ik}^*a_{kj} - a_{ik}^*b_{kj}^* & 0 \end{pmatrix} + \mathcal{O}\left(\frac{t^3}{J^2}\right). \tag{4.118}$$

Unluckily, there remains a non-diagonal term in second order. This isn't a surprise and is the trade-off for having chosen the separation (4.107) instead of a full diagonal-off diagonal one[49] . This poses no problem at all inasmuch as a second unitary transformation can now be applied, yielding another Hamiltonian diagonal up to $\mathcal{O}(t/J^2)$. We separate $\hat{H}'$ exactly in the same way as in eq. (4.107), upon which our newly transformed Hamiltonian finally reads

$$h''_{ij} = J\delta_{ij} \begin{pmatrix} 1 & 0 \\ 0 & -1 \end{pmatrix} + t_{ij} \begin{pmatrix} a_{ij} & 0 \\ 0 & a_{ij}^* \end{pmatrix} + \sum_k \frac{t_{ik}t_{kj}}{2J} \begin{pmatrix} b_{ik}b_{kj}^* & 0 \\ 0 & -b_{ik}^*b_{kj} \end{pmatrix} + \mathcal{O}\left(\frac{t^3}{J^2}\right). \tag{4.119}$$

At this point, given that transitions between the states $\{|R_i,+\rangle\}$ and $\{|R_j,-\rangle\}$ have been suppressed up to second order, the high energy subspace can be projected out in the strong coupling limit and, if only

[49] This is just a reminiscence of the fact that there is an arbitrariness in the second and higher order terms in perturbation theory, depending on the choice at 1st order. And the requirement that (4.110) be diagonal just takes care of the lowest order. This is analogous to the arbitrariness in the formal quantum mechanical perturbation expansions that interpolate between the Rayleigh–Schrodinger and Brillouin–Wigner schemes.

two site terms are considered, the following effective Hamiltonian is generated[50] :

$$H''_{eff} = \sum_{ij} t_{ij} a_{ij} d_i^\dagger d_j - \sum_{ik} \frac{|t_{ik}|^2}{2J} (\vec{n}_i.\vec{n}_k) d_i^\dagger d_i \,. \tag{4.120}$$

The constants have been dropped in the above result and the last term uses the fact that, according to (4.13b),

$$|b_{ik}|^2 = \frac{1 - \vec{n}_i.\vec{n}_k}{2} = \sin\left(\frac{\Theta_{ij}}{2}\right)^2 . \tag{4.121}$$

A final comment to this result is the fact that an effective magnetic coupling between the local spins and results from this effective Hamiltonian. There is an implicit coupling embedded int the first term, which is ferromagnetic insofar as the FM state for the local spins minimizes the energy of the electronic system in first order. But there is in addition an explicit Antiferromagnetic or Antiferromagnetism (AFM) coupling in the second term that couples to the electronic density.

The Hamiltonian (4.120) with only its first term retained is known as the Double Exchange (DE) Hamiltonian [Anderson and Hasegawa, 1955; de Gennes, 1960], and describes effective spinless fermions with a hopping integral $t_{ij}a_{ij}$ that depends explicitly on the spacial orientation of the local spins at $\vec{R}_i$ and $\vec{R}_j$:

$$a_{ij} = \cos\left(\frac{\theta_i}{2}\right)\cos\left(\frac{\theta_j}{2}\right) + \sin\left(\frac{\theta_i}{2}\right)\sin\left(\frac{\theta_j}{2}\right) e^{i(\varphi_j - \varphi_i)} \,. \tag{4.122}$$

Appendix 4.C KLM within a Virtual Crystal Approximation

The starting point is the KLM Hamiltonian in the basis that diagonalizes $\vec{S}_i.\tau$ at each site (4.11), and the results of (4.11), (4.13b) and (4.14b) for the different matrix elements. It is clear that, at any non-zero temperature, there will be no translation invariance as a consequence of fluctuations in the local spins, and hence, in the magnetic background landscape within which the electrons move.

In its essence, the VCA aims at, to some extent, restore this broken symmetry by introducing an *effective medium* that somehow summarizes the macroscopic consequences of the local fluctuations. In the present case, the variation of the hopping integrals a_{ij} and b_{ij} from site to site is substituted by global (constant) parameters a and b, as defined along the main text in (4.21).

$$a_{ij} \to |a_{ij}| \to \langle |a_{ij}| \rangle \equiv a = \cos\left(\frac{\Theta}{2}\right), \quad b_{ij} \to |b_{ij}| \to \langle |a_{ij}| \rangle \equiv b = \sin\left(\frac{\Theta}{2}\right) . \tag{4.123}$$

A further simplification consists in avoiding the complex phases, resulting in a generalized de Gennes-like approach to the KLM:

$$\mathcal{H}_{KLM} = t \sum_{ij} \tilde{\Psi}_i^\dagger \begin{pmatrix} a & b \\ b & a \end{pmatrix} \tilde{\Psi}_j + J \sum_i \tilde{\Psi}_i^\dagger \, \tau_3 \tilde{\Psi}_i \,. \tag{4.124}$$

[50] For definiteness $J < 0$ is assumed, although the result for $J > 0$ is trivially related to this one.

Introducing the Fourier transformed spinor operators

$$\tilde{\Psi}_k = \frac{1}{\sqrt{N}} \sum_k e^{i\vec{k}.\vec{R}_i} \tilde{\Psi}_i \,, \tag{4.125}$$

is immediate to obtain

$$\mathcal{H}_{KLM} = \sum_{\boldsymbol{k}} \tilde{\Psi}_k^\dagger h_k \tilde{\Psi}_k = \tilde{\Psi}_k^\dagger \begin{pmatrix} \epsilon_a(k) + J & \epsilon_b(k) \\ \epsilon_b(k) & \epsilon_a(k) - J \end{pmatrix} \tilde{\Psi}_k \,, \tag{4.126}$$

where the matrix elements read

$$\epsilon_a(k) = -2at \sum_{\mu=1}^{3} \cos(k_\mu) = -2t \cos\left(\frac{\Theta}{2}\right) \sum_{\mu=1}^{3} \cos(k_\mu) \tag{4.127a}$$

$$\epsilon_b(k) = -2bt \sum_{\mu=1}^{3} \cos(k_\mu) = -2t \sin\left(\frac{\Theta}{2}\right) \sum_{\mu=1}^{3} \cos(k_\mu) \tag{4.127b}$$

As usual, a $SU(2)$ matrix, V, that diagonalizes h_k is introduced so that

$$\mathcal{H}_{KLM} = \sum_k \tilde{\Psi}_k^\dagger V^\dagger V h_k V^\dagger V \tilde{\Psi}_k = \sum_k \bar{\Psi}_k^\dagger \bar{h}_k \bar{\Psi}_k = \sum_k \bar{\Psi}_k^\dagger \begin{pmatrix} E_+(k) & 0 \\ 0 & E_-(k) \end{pmatrix} \bar{\Psi}_k \tag{4.128}$$

is diagonal in the transformed operators. The eigenvalues $E_\pm(k)$ are trivial:

$$E_\pm(k) = \epsilon_a(k) \pm \sqrt{J^2 + \epsilon_b(k)^2} \,, \tag{4.129}$$

and the transformation matrix V is also computed straightforwardly reading

$$V = \begin{pmatrix} \sin(\xi_+) & \cos(\xi_+) \\ \sin(\xi_-) & \cos(\xi_-) \end{pmatrix} \tag{4.130}$$

where the parametrization hides the explicit values

$$\begin{aligned} \sin(\xi_\lambda) &= \sigma_\lambda \sqrt{\frac{1}{2}\left[1 + \frac{J}{E_\lambda - \epsilon_a(k)}\right]} \\ \cos(\xi_\lambda) &= \sqrt{\frac{1}{2}\left[1 - \frac{J}{E_\lambda - \epsilon_a(k)}\right]} \end{aligned} \quad \text{and} \quad \sigma_\lambda = \begin{cases} +1 & \text{if } \lambda = \text{“+”}, \\ -1 & \text{if } \lambda = \text{“-”} \end{cases} \tag{4.131}$$

It is now a matter of algebra to calculate the expectation value of any operator. Of particular interest is

the local spin polarization, introduced in eq (4.20). One has

$$m = \frac{1}{N_e}\sum_k \left\langle \tilde{\Psi}_k \tau_3 \tilde{\Psi}_k^\dagger \right\rangle = \frac{1}{N_e}\sum_k \left\langle \bar{\Psi}_k (V\tau_3 V^\dagger) \bar{\Psi}_k^\dagger \right\rangle$$
$$= \frac{1}{N_e}\sum_k \left(\cos^2(\xi_-) - \sin^2(\xi_-)\right) \left\langle c_{k+}^\dagger c_{k+} - c_{k-}^\dagger c_{k-} \right\rangle , \tag{4.132}$$

whence, using the above expressions for ξ_λ, we get

$$m = \frac{1}{N_e}\sum_k \frac{J}{\sqrt{J^2 + \epsilon_b(k)^2}}(n_{k+} - n_{k-}) \tag{4.133}$$

Since the two bands $(+,-)$ in (4.129) never overlap, for systems less than half-filled ($N_e < N$) only the lowest bands needs to be accounted for and thus

$$m = -\frac{1}{N_e}\sum_{k<k_F} \frac{J}{\sqrt{J^2 + \epsilon_b(k)^2}} . \tag{4.134}$$

For small densities, near the bottom of the band, it is legitimate to introduce the parabolic approximation for the dispersion $\epsilon_b(k)$:

$$\frac{\epsilon_b(k)}{J} \simeq -2\frac{tb}{J}(3 - \frac{k^2}{2}) = -g(3 - \frac{k^2}{2}) , \tag{4.135}$$

after which the calculation of m can be carried out analytically:

$$m\, n_e \simeq -\operatorname{sign}(J)\int_0^{k_F} k^2(1 + 9g^2 - 3g^2k^2)^{-1/2}\frac{dk}{2\pi^2}$$
$$\simeq -\frac{\operatorname{sign}(J)}{2\pi^2\sqrt{1+9g^2}}\int_0^{k_F}\left(1 + \frac{3}{2}\frac{g^2k^2}{1+9g^2}\right)k^2 dk = -\frac{\operatorname{sign}(J)}{\sqrt{1+9g^2}}\left(\frac{k_F^3}{6\pi^2} + \frac{3}{20\pi^2}\frac{g^2k_F^5}{1+9g^2}\right)$$
$$m \simeq -\frac{\operatorname{sign}(J)}{\sqrt{1+9g^2}}\left[1 + \frac{9}{10}\frac{g^2}{1+9g^2}(6\pi^2 n_e)^{2/3}\right] \tag{4.136}$$

We see at once that in the limit $n_e \to 0$ there is a residual local spin polarization per electron equal to $-\operatorname{sign}(J)[1 + (6tb/J)^2]^{-1/2}$.

Appendix 4.D Average hoppings within mean field

The mean angle between any two local spins arises when the KLM is projected onto the DE limit, and has been introduced in eqs. (4.13b) and (4.14b). Within mean field we can easily compute

$$\left\langle \cos\left(\frac{\Theta_{ij}}{2}\right)\right\rangle_M , \text{ and } \left\langle \sin\left(\frac{\Theta_{ij}}{2}\right)\right\rangle_M , \tag{4.137}$$

where the average is over configurations of disorder compatible with a given magnetization, M. These averages are defined as

$$\Big\langle F\big(\{\vec{S}_i\}\big)\Big\rangle_M = \frac{1}{Z_N}\int d\vec{S}_1 \cdots \int d\vec{S}_N\, F\big(\{\vec{S}_i\}\big)\, e^{h(M)\sum_i \cos(\theta_i)} \tag{4.138}$$

implying uncorrelated moments, and where the magnetization enters implicitly through the *mean field*, $h(M)$ (that absorbs the temperature of the Boltzmann factor):

$$M(h) = \mathcal{L}(h) \equiv \coth(h) - \frac{1}{h} \tag{4.139}$$

Clearly, the probability distribution for a single spin is simply

$$\mathcal{P}_M(\theta_i,\varphi_i) = \frac{1}{Z_1(M)} e^{h(M)\cos(\theta_i)} \quad \text{with} \quad Z_1(M) = \frac{4\pi}{h}\sinh(h) \tag{4.140}$$

To start we decompose the co-sine of the mean angle into Legendre polynomials:

$$\cos\left(\frac{\Theta_{ij}}{2}\right) = \sqrt{\frac{1+\cos(\Theta_{ij})}{2}} = \sum_{l=0}^{\infty} A_l P_l(x) \quad \big(x \equiv \cos(\Theta_{ij})\big) \tag{4.141}$$

$$A_l = \frac{2l+1}{2}\int_{-1}^{1} dx \sqrt{\frac{1+x}{2}} P_l(x) = (-1)^{l+1}\frac{2}{(2l-1)(2l+3)} \tag{4.142}$$

We see at once from the above and the parity of the $P_l(x)$ that the expansion coefficients for $\sin\left(\frac{\Theta_{ij}}{2}\right)$ are simply $A'_l = (-1)^l A_l$, and thus we need to care only about the average $\langle P_l(x)\rangle_M$:

$$\left\langle \cos\left(\frac{\Theta_{ij}}{2}\right)\right\rangle_M = \sum_{l=0}^{\infty} A_l \langle P_l(x)\rangle_M \tag{4.143}$$

We now recall that Θ_{ij} is the angle between two unit vectors $\vec{n}_i = \big(\sin(\theta_i)\cos(\varphi_i), \sin(\theta_i)\sin(\varphi_i), \cos(\theta_i)\big)$ and $\vec{n}_j = \big(\sin(\theta_j)\cos(\varphi_j), \sin(\theta_j)\sin(\varphi_j), \cos(\theta_j)\big)$. Hence, the addition theorem for the spherical harmonics comes to great avail here insomuch as it states that [Arfken, 1970]

$$P_n\big(\cos(\Theta_{ij})\big) = \frac{4\pi}{2n+1}\sum_{m=-n}^{n} Y_n^m(\theta_i,\varphi_i) Y_n^m(\theta_j,\varphi_j)^*\,, \tag{4.144}$$

the spherical harmonics $Y_n^m(\theta_i,\varphi_i)$ relating to the associated Legendre functions through the standard definitions [Arfken, 1970]:

$$Y_n^m(\theta,\varphi) = (-1)^m \sqrt{\frac{2n+1}{4\pi}}\sqrt{\frac{(n-m)!}{(n+m)!}} P_n^m(\cos(\theta))\, e^{im\varphi} \tag{4.145}$$

$$P_n^m(x) = (1-x^2)^{m/2}\frac{d^m}{dx^m}P_n(x)\,. \tag{4.146}$$

This is good because the averaging in $\langle P_l\big(\cos(\Theta_{ij})\big)\rangle_M$ is over uncorrelated spins with uniform distribution in the variable φ. Therefore, the angular integrals over φ_i integrate the components with $m \neq 0$

out to zero and hence:

$$\left\langle P_l\big(\cos(\Theta_{ij})\big)\right\rangle_M = \frac{4\pi}{2n+1}\langle Y_n^0(\theta_i,\varphi_i)\rangle\langle Y_n^0(\theta_j,\varphi_j)\rangle = \left\langle P_l\big(\cos(\theta_i)\big)\right\rangle_M \tag{4.147}$$

This is easier to handle because [Arfken, 1970]

$$\left\langle P_l\big(\cos(\theta_i)\big)\right\rangle_M = \frac{2\pi}{Z_1(M)}\int_{-1}^{1} P_n(x)e^{-hx} = \frac{2\pi}{Z_1(M)}2i^n j_n(ih)\,, \tag{4.148}$$

the $j_n(x)$ being the spherical Bessel functions. Finally, rearranging everything, and using the fact that

$$j_n(z) = (-1)^n z^n \left(\frac{d}{zdz}\right)^n \frac{\sin(z)}{z} \tag{4.149}$$

one gets

$$\left\langle \cos\left(\frac{\Theta_{ij}}{2}\right)\right\rangle_M = -\frac{2}{j_0(-ih)^2}\sum_{l=0}^{\infty}\frac{1}{(2l-1)(2l+3)}j_l(ih)^2 \tag{4.150a}$$

$$\left\langle \sin\left(\frac{\Theta_{ij}}{2}\right)\right\rangle_M = -\frac{2}{j_0(-ih)^2}\sum_{l=0}^{\infty}\frac{(-1)^l}{(2l-1)(2l+3)}j_l(ih)^2\,. \tag{4.150b}$$

In this last result, the magnetization enters still implicitly through h and (4.139). We can pursue a series expansion of the above result in terms of M, that might be useful for mean-field, de-Gennes-like approaches to the DE problem. The first few terms of such expansion are as follows

$$\left\langle \cos\left(\frac{\Theta_{ij}}{2}\right)\right\rangle_M = \frac{2}{3} + \frac{2}{5}M^2 - \frac{6}{175}M^4 - \frac{18}{875}M^6 - \frac{918}{67375}M^8 + \mathcal{O}(M^{10}) \tag{4.151a}$$

$$\left\langle \sin\left(\frac{\Theta_{ij}}{2}\right)\right\rangle_M = \frac{2}{3} - \frac{2}{5}M^2 - \frac{6}{175}M^4 - \frac{162}{6125}M^6 - \frac{7758}{336875}M^8 + \mathcal{O}(M^{10})\,. \tag{4.151b}$$

Closing this discussion, it is interesting to remark that, notwithstanding the rather cumbersome aspect of the exact results in eqs. (4.150), an extremely simple algebraic form can be obtained for an approximation that interpolates incredibly well those results at all magnetizations:

$$\left\langle \cos\left(\frac{\Theta_{ij}}{2}\right)\right\rangle_M \simeq \frac{2}{3}\sqrt{1+\frac{5}{4}M^2}\,, \qquad \left\langle \sin\left(\frac{\Theta_{ij}}{2}\right)\right\rangle_M \simeq \frac{2}{3}\sqrt{1-M^2}\,. \tag{4.152}$$

That this is so can be seen in Fig. 4.23 where the above interpolations are compared with the actual exact results of (4.150). Of course, a little inspection reveals that the above doesn't reproduce the series expansion in eqs. (4.151), starting at $\mathcal{O}(M^2)$[51]. In case an interpolation that respects the analyticity of

[51] Notice, however, that in the case of $\cos(\Theta_{ij}/2)$, the second order coefficient is exactly $25/24$ of the exact expansion coefficient, and thus, still a good approximation for Landau-type expansions of the Free energy.

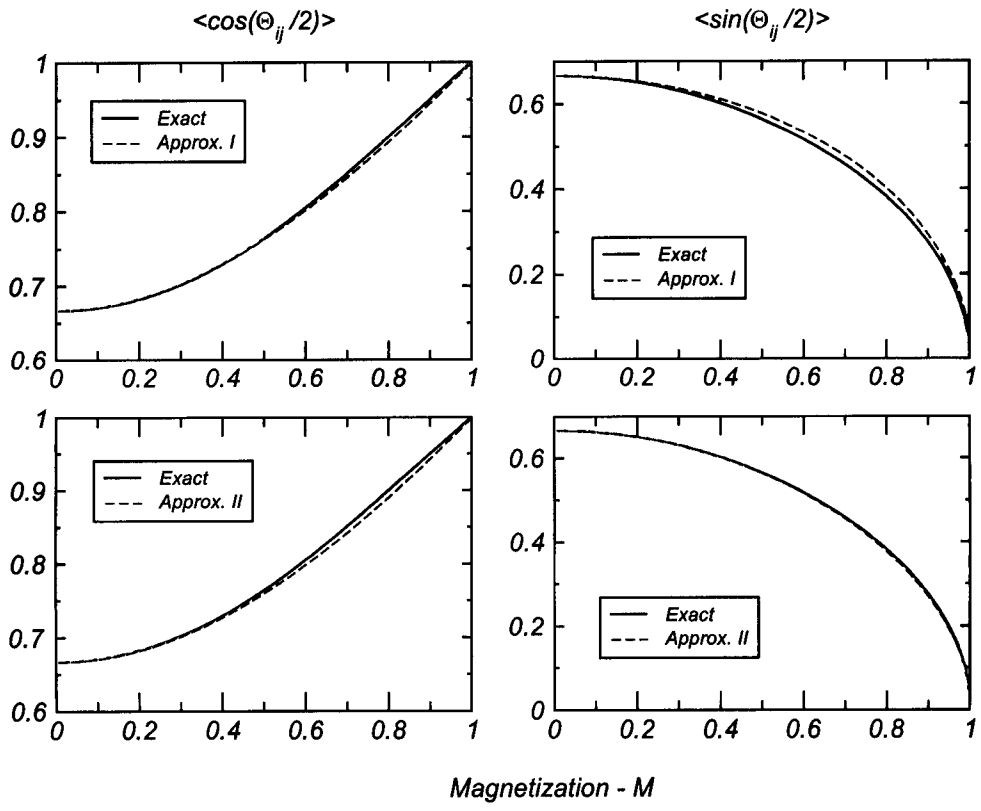

FIGURE 4.23 .: *Comparison of the two interpolations for the average cosine and sine of the half-angle between pairs of spins. The left column pertains to the results for* $\langle \cos(\Theta_{ij}/2) \rangle$, *and the one on the right to* $\langle \sin(\Theta_{ij}/2) \rangle$. *The top row compares the exact results with the approximations in eq.* (4.152), *whereas in the bottom are the interpolations of eq.* (4.153).

the exact series is wanted, one can use

$$\left\langle \cos\left(\frac{\Theta_{ij}}{2}\right)\right\rangle_M \simeq \frac{2}{3}\sqrt{1+\frac{5}{4}M^2-\frac{1}{20}M^2(1-M^2)} \tag{4.153a}$$

$$\left\langle \sin\left(\frac{\Theta_{ij}}{2}\right)\right\rangle_M \simeq \frac{2}{3}\sqrt{1-M^2-\frac{1}{5}M^2(1-M^2)}\,, \tag{4.153b}$$

which are also comparatively shown in Fig. 4.23.

Appendix 4.E IPR Statistics – Additional Results

In § 4.3.2.1, and Fig. 4.9 in particular, we have shown the relative fluctuations of the IPR for the DEM at $M = 0$. It was advanced that the behavior of this quantity might work as an indicator of the localization transition. Here we reinforce this statement with additional results for $\sigma_{\mathcal{P}}/\langle \mathcal{P} \rangle$. The first data pertain to the DEM, but now for an average magnetization of 20%, and are presented in Fig. 4.24. The overal behavior is exactly the same found in Fig. 4.9, with the relative fluctuations being significantly enhanced at a given energy. Unlike the case with $M = 0$, the inset does not show such a good crossing as could be seen before, and gives an example of how more extensive numerical calculations are needed to ascertain with definiteness the existence of scale invariance or not. The same sort of analysis has been undertaken

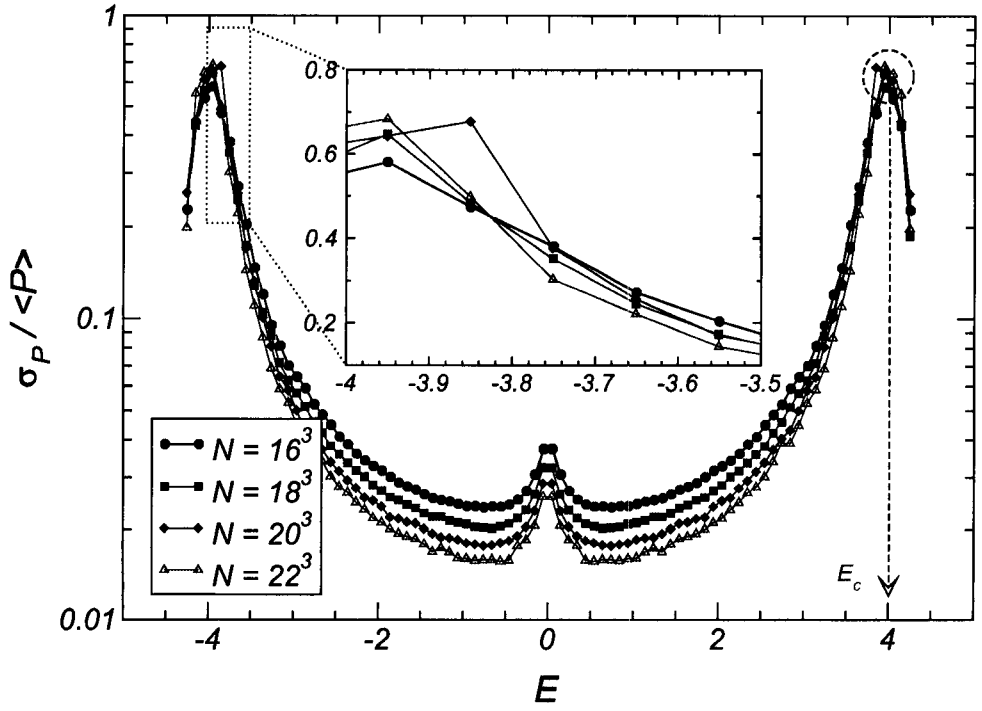

FIGURE 4.24.: *Ratio of the standard deviation to the average of the IPR for the DEM at* $M = 0.2$. *The inset is a magnification, and statistics have been collected with an energy window of* $\Delta E = 0.1$.

for the Anderson model, with the outcome shown in Fig. 4.25. Again, the qualitative behavior of the relative fluctuations of the IPR consists of a marked enhancement at the band edges, and the existence of a maximum at a given energy. Two cases, $W = 3$ and $W = 5$ are presented in panels 4.25a and 4.25b, respectively. In the latter we introduced two insets that put in evidence the fact that the existence of a well defined crossing point is rather sensitive to the energy window considered. This, again, is evidence that more statistics are needed.

Finally, it is worth underlying that the behavior of the relative fluctuations at $E \simeq 0$ is clearly distinct in the DEM and the Anderson model, having to do with the details and nature of disorder in these two cases, as discussed in the main text.

Appendix 4.F Lifetime within perturbation theory for the Anderson model

We start from the Anderson Hamiltonian

$$\mathcal{H}_{AM} = t \sum_{ij} c_i^\dagger c_j + \sum_i \epsilon_i \, c_i^\dagger c_i \,, \tag{4.154}$$

and treat the first term as the interaction with a local perturbing potential, calling it V. Assume that we have an electron in an eigenstate, $|k\rangle$, of the unperturbed lattice. The probability amplitude for a

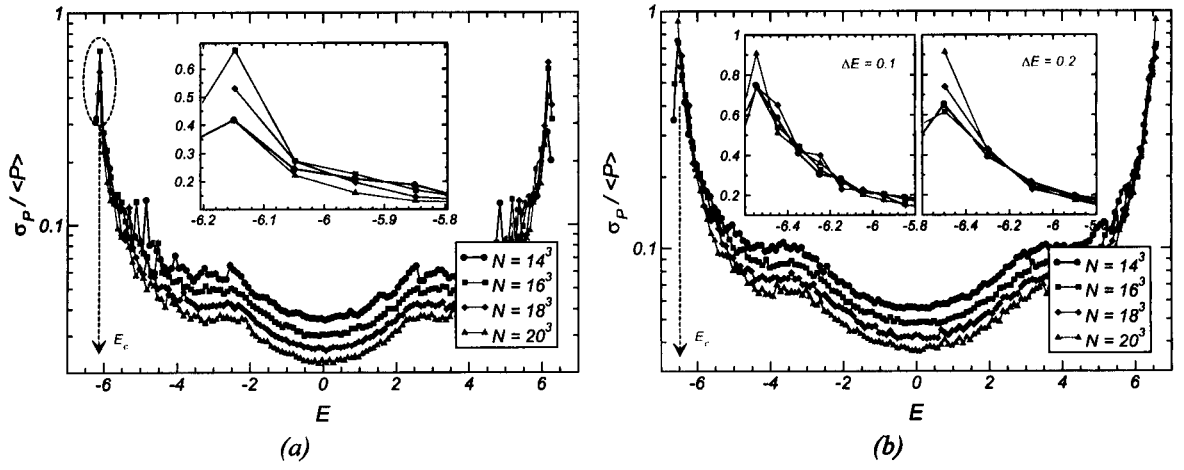

FIGURE 4.25 .: *Ratio of the standard deviation to the average of the IPR for the Anderson model at $W = 3$ (a) and $W = 5$ (b). Statistics collected within energy windows of $\Delta E = 0.1$. In (b) there are two insets: the one on the left is just the magnification of the main panel; the one on the right shows the same region but using $\Delta E = 0.2$.*

transition into some other state is, to first order in V,

$$\tau_k^{-1} = 2\pi \sum_{k'} \left|\langle k'|V|k\rangle\right|^2 \delta(E_{k'} - E_k)\,. \tag{4.155}$$

Now we know that,

$$\begin{aligned}\langle k'|V|k\rangle &= \sum_i \varepsilon_i \left\langle k' \left| c_k^\dagger c_{k'}^\dagger \right| k \right\rangle \\ &= \frac{1}{N}\sum_i \varepsilon_i \exp\big(i(\vec{k}' - \vec{k}).\vec{r}_i\big) \qquad (4.156)\\ \left|\langle k'|V|k\rangle\right|^2 &= \frac{1}{N^2}\sum_{ij} \varepsilon_i\varepsilon_j \exp\big(i(\vec{k}' - \vec{k}).(\vec{r}_i - \vec{r}_j)\big),. \qquad (4.157)\end{aligned}$$

When the average over disorder is performed, we get averages of $\overline{\varepsilon_i\varepsilon_j}$. Since in the Anderson model the ε_i are uncorrelated and have a uniform probability distribution

$$p(\varepsilon_i) = \frac{1}{W}\theta(W/2 - |\varepsilon_i|)\,, \tag{4.158}$$

it follows that $\overline{\varepsilon_i\varepsilon_j} = \overline{\varepsilon_i^2}\delta_{ij}$, and hence,

$$\left|\langle k'|V|k\rangle\right|^2 = \frac{1}{N}\overline{\varepsilon_i^2}\,. \tag{4.159}$$

The average of ε_i^2 follows trivially from (4.158), and putting everything back together we attain

$$\tau_k^{-1} = \frac{2\pi}{N}\sum_{k'} \delta(E_{k'} - E_k)\frac{W^2}{12} = 2\pi\rho^0(E_k)\frac{W^2}{12}\,, \tag{4.160}$$

where ρ^0 is the unperturbed DOS.

5. Magnetic Polarons and Phase Separation

5.1. Magnetic Polarons in the DEM

5.1.1. Magnetic Polarons in Perspective

The earlier descriptions of the concept of magnetic polaron appear with the considerations by de Gennes on the relevance of the Double Exchange (DE) mechanism to the mixed valent manganites [de Gennes, 1960], and then with Nagaev's studies of antiferromagnetic semiconductors, who coined the term *ferron* also often used in the context[1]. Some of the first theories based upon the presence of magnetic polarons were developed later in the context of the ferromagnetic semiconductor EuO, to explain the spectacular metal-insulator transition found at the onset of ferromagnetism for the Eu-rich samples of this compound [Oliver et al., 1972; Torrance et al., 1972]. Further developments on this concept permitted the explanation of the spin-flip Raman scattering characteristic of certain Diluted Magnetic Semiconductors (DMS) [Dietl and Spalek, 1982, 1983; Heiman et al., 1983; Torrance et al., 1972] and, more recently, their presence was also claimed to be present in the EuB_6 hexaborides, as we saw in § 3.6 [Nyhus et al., 1997; Snow et al., 2001].

Just as in the analogous case of the electrostatic polaron, one can devise a pictorial description of a magnetic polaron in real space as consisting of a charge carrier surrounded by a cloud of polarized local spins in an unpolarized magnetic background — a state that arises from the exchange interaction between the carrier spin and the lattice spins. A distinction is usually made between the so-called Bound Magnetic Polaron (BMP) and the Free Magnetic Polaron (FMP). The BMP is invoked when the charge carrier is bound via Coulomb interaction to an impurity center, and is typical in the magnetic semiconductors. In this case the trapped carrier polarizes the lattice spins within its effective Bohr radius as a consequence of the *s–d*-like interaction between electron and lattice spins. The FMP, by contrast, results from the fact that a free carrier interacting with lattice spins via an *s–d* coupling, can minimize its kinetic energy by polarizing its vicinity. Under certain conditions this carrier can then become self-trapped in the resulting potential well created by the effect of the local ferromagnetism.

The presence of such type of entities is believed to play an important role in the emergence of many interesting properties of several important magnetic materials: many peculiarities of the manganites, such as the CMR effect and other anomalies in its transport and magnetism, have been attributed in part to the development of magnetic polarons near the ferromagnetic transition [2][Amaral et al., 1998; Teresa et al., 1997, 2000]; an interpretation for the CMR in the Mn pyrochlores was also proposed on the basis of magnetic polarons Majumdar and Littlewood [1998]; besides their relevance for the already

[1] See, for instance, Nagaev [2001, 2002] and references therein.

[2] Although in this case the influence of orbital and lattice degrees of freedom are equally important.

mentioned Eu-chalcogenides and II-VI semiconductors, in the III-V DMS like $Ga_{1-x}Mn_xAs$, the ferromagnetic transition can be interpreted within a BMP percolating scenario [Kaminski and Sarma, 2002]; in EuB_6, our target magnetic metal exhibiting CMR, their presence in signaled in the optical response [Nyhus et al., 1997; Snow et al., 2001], although the theoretical interpretation of these results is still subject to questioning [Calderon et al., 2004].

Given that these different classes of magnetic materials have attracted considerable attention in recent years because of their potential for the development of new magnetoelectronic devices, and since magnetic polarons have an apparently ubiquitous presence among them, a number of theoretical approaches to the problem have been developed through the years. In particular, extensive work has been done with emphasis in the physics of magnetic semiconductors [Dietl and Spalek, 1982; Heiman et al., 1983; Kasuya et al., 1970; Mauger, 1983; Nagaev, 2002] and CMR manganites [Batista et al., 2000; Garcia et al., 2002; Meskine et al., 2004; Varma, 1996].

In the ensuing paragraphs we will focus our attention on the stability conditions for the free magnetic polaron in the DEM. Studies devoted to the polaronic stability in this particular model and its variations have been performed by several authors both analytically and numerically, although under different assumptions [Daghofer et al., 2004a,b; Garcia et al., 2002; Koller et al., 2003; Neuber et al., 2004; Pathak and Satpathy, 2001; Wang and J.Freeman, 1997; Yi et al., 2000].

5.1.2. The Independent Polaron Model

For the present discussion, we consider the DEM Hamiltonian (4.19) that reads

$$\mathcal{H}_{DE} = t \sum_{\langle ij \rangle} a_{ij} d_i^\dagger d_j \,. \tag{5.1}$$

where $a_{ij} = \cos(\theta_i/2)\cos(\theta_j/2) + \sin(\theta_i/2)\sin(\theta_j/2)\, e^{-i(\phi_i - \phi_j)}$.

Within the simple DEM, where no other polaron-favoring interactions are included[3], the only possibility for the stabilization of magnetic polarons is at low electronic densities. This happens because the local spins of several neighboring unit cells are expected to participate in the magnetization cloud of each electron. Were it otherwise (i.e. at high electronic densities), the electronic wave functions would overlap considerably destroying this polaron picture.

In order to investigate these questions we will first discuss the thermodynamic stability of magnetic polarons within the DEM. We can write a free energy for the system including an electronic contribution consisting of the ground state energy for the electrons in a given magnetic configuration [4], the local spins contributing only with an entropic term. To tackle the first part, one can calculate numerically the exact electronic DOS for a given spin configuration as usual. Averaging over disorder, we can write the electronic contribution as

$$E_{el}(M, n_e) = \int \Theta\left(E_F(M, n_e) - \epsilon\right) E\rho(E, M) dE \,, \tag{5.2}$$

[3]For instance, many of the existing approaches include an AFM exchange term between the local spins.
[4]The relevant temperature ranges satisfy $k_B T \ll t$.

When $n_e \ll 1$, and for the purposes of the current calculation, eq. (5.2) can be approximated simply by

$$E_{el}(M, n_e) \approx E_b(M) n_e \,, \tag{5.3}$$

with E_b representing the bottom of the band – it becomes just a single electron problem. Indeed, given the nature of the calculation and approximations involved here, the consideration of the finite band filling introduces only minor corrections and thus we proceed with the above approximation to the electronic energy (Appendix 5.A). Now, for a disordered system, the concept of *"bottom of the band"* has to be taken carefully as the DOS will always exhibit Lifshitz exponential tails. In this case, from the calculations of the averaged DOS, the *bottom* of the band is found to lie at $-4t$ for the PM ($\mathcal{M} = 0$) case[5] (cfr. Figs. 4.14a and 4.5). We intend to construct the polaronic phase having the paramagnetic, uniform, phase as reference. Within a virtual-crystal approximation, the electron at the bottom of the band has an energy of $-4t$, and will be extended throughout the system. If a region of ferromagnetism develops locally, its reference energy in this region will be lowered to $-6t$, but there is an extra energy that has to be paid if the electron is to become confined to this region. For simplicity let us assume that the polaron so formed consists of a region inside a cube of side R (in units of the lattice parameter, a), inside which $M = 1$. Obviously, given that in the DEM the magnetic interaction is mediated by electron itinerancy, one expects that, once the electron localizes inside this cube, there will be no magnetism outside, at any temperature. The variation of free energy per lattice site when going from the PM homogeneous phase to this polaronic one will be written as

$$\Delta F_{\text{Pol}}(R, T) = 4tn_e - 6tn_e \cos\left(\frac{\pi}{R+1}\right) + Tn_e R^3 \log(2S+1) - T\mathcal{S}_{\text{Cfg}}(n_e, R) \,, \tag{5.4}$$

and reflects the two competing effects at play: the first is the electron's preference for a ferromagnetic background accompanied by an energy cost for the localization; the second is the reduction of entropy caused by the appearance of the (fully polarized) magnetic polarons. The last contribution, $\mathcal{S}_{\text{Cfg}}$, expresses a configurational entropy, related to the spacial distribution of the polarons inside the system. It can be approximated by

$$\mathcal{S}_{\text{Cfg}} \simeq \frac{1}{R^3} \log\left(\frac{1}{1 - n_e R^3}\right) - n_e \log\left(\frac{n_e R^3}{1 - n_e R^3}\right) , \tag{5.5}$$

but, since we are working with $n_e \ll 1$ and the polaronic system is below the percolation threshold, it happens to be the smallest contribution to ΔS, allowing us to neglect it without important quantitative consequences.

In writing eq. (5.4) some important assumptions were made regarding the wave function of the electron. Reasoning in terms of the original band state of the electron, it is clear that when the magnetic background polarizes, the electron energy is lowered by $2t$. Thus, the potential well is, at most, $2t$ deep and any bound state will always exhibit exponential leaking of the wave function to the outside, whereas the energy of the bound state in (5.4) was chosen as the energy of an electron inside an infinite poten-

[5] Interestingly, this result is actually the one we would obtain following the mean-field procedure carried by de Gennes [1960]. See also Appendix 4.D.

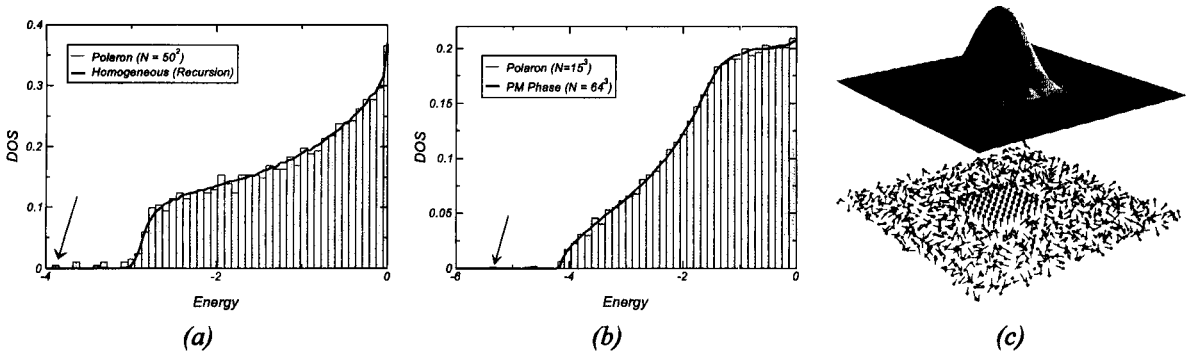

FIGURE 5.2 .: *Comparison of the disorder-averaged electronic DOS for the homogeneous PM phase (line) with the exact spectrum obtained for the same configuration with a polaronic region or size R (histogram). Arrows highlight the lowest bound state. The results are for 2-D (a) and 3-D (b) lattices, neglecting the Berry phase in the hopping (i.e.: using $a_{ij} \rightarrow |a_{ij}|$). Panel (b) shows one of those spin configurations together with the wavefunction of the lowest bound state.*

tial well. On the other hand, since one can think of an effective magnetic coupling as proportional to $|\psi_e(\vec{r})|^2$, the magnetization profile of the polaron should also display a smooth variation, whereas in eq. (5.4) $M = 0$ outside and $M = 1$ inside the polaron. These statements amount to say that the exact treatment of the problem requires a self-consistent calculation of the bound state starting from the DEM or perhaps from the full Hamiltonian [Kasuya et al., 1970; Pathak and Satpathy, 2001]. In this sense, eq. (5.4) is to be understood in the spirit of a variational approach, R being the variational parameter.

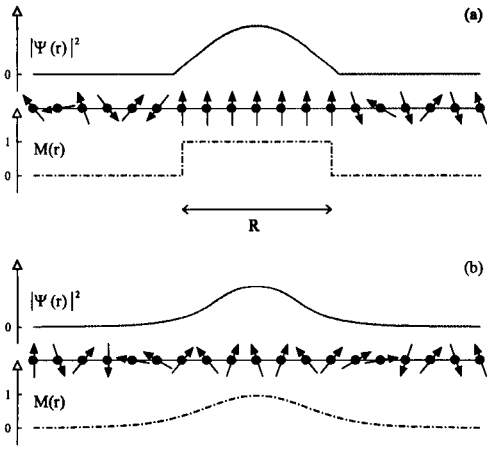

FIGURE 5.1 .: *Contrasting the variational approach considered in eq.* (5.4) *(a) to the more realistic, self-consistent, situation (b). Represented are the wave function of the self-localized electron, a possible spin configuration and the magnetization profile.*

There are several reasons to expect it to be a good approximation: (i) the electron density is very small, meaning that the overlap of the wave functions of self-trapped electrons (and thus the polarons) should be negligible; (ii) even if one could devise a full, self-consistent, solution to the problem, the exact energy of the bound state is expected to differ from the one used in this approximation only by numerical factors of $\mathcal{O}(1)$[6]; (iii) numerical calculations strongly favor this approach. To dwell a while on this last point, we studied the effect of a region of full polarization embedded in a PM background on the electronic spectrum. Performing exact diagonalizations of the DEM using spin configurations like the one depicted in Figs. 5.1 and 5.2c, one finds, as a result, the appearance of well defined bound states below the continuum band. This is clearly seen in Figs. 5.2a and 5.2b, where the bound states appear with energies and degeneracy coinciding with the value expected for a finite box in d-dimensions: $-2dt\sum_{\mu=1}^{d}\cos\left(\frac{\pi}{R+1}n_\mu\right)$. At the same time, inspecting particular realizations of disor-

[6]Specific confirmation for this can be found, for instance, in the 1-D calculations of Pathak and Satpathy [2001], who find that the two energies (calculated using the same kind of variational wave function used in the current work and the exact energy obtained numerically) differ by less than 3 % in the limit relevant to our discussion.

der as the one in Fig. 5.2c, one concludes that the wave function is clearly localized within the polarized region, thus supporting our trial function selection for the evaluation of the electronic energy.

The stability of the magnetic polaron is determined by the condition $\Delta\mathcal{F}\left(R_{\text{eq}}, T\right) < 0$, R_{eq} being the value that minimizes the free energy (5.4). Important insights can be extracted from the direct analytic results obtainable in its continuum version. In this case, it's trivial to see that the equilibrium radius is

$$R_{\text{eq}}\left(T\right) \simeq \left[\frac{2t\pi^2}{T\log\left(2S+1\right)}\right]^{1/5}, \tag{5.6}$$

increasing at low temperatures as $T^{-1/5}$. Using this result in the stability condition, one finds the stability temperature, T_m, below which the polaronic phase appears:

$$T_m = \frac{8}{25\pi^3\log\left(2S+1\right)}\sqrt{\frac{2}{5}}t. \tag{5.7}$$

These two results convey the essential information for the physical situation as one reduces the temperature of our system. The high-temperature phase is characterized by PM order until T decreases below T_m, at which point, the *"entropic pressure"* is not enough to counteract the energy gain and the polaronic phase is stabilized. The transition is sharp as a consequence of the one-particle nature of the free energy (5.4), and the polarons set in with a finite radius $R_{\text{eq}}\left(T_m\right)$. Continuing the decrease in temperature, the polaron radius increases until the overlapping probability can no longer be ignored, therefrom arising an instability towards an homogeneous FM phase. An estimate of the Curie temperature, T_C , can thus be extracted from a percolation criterion

$$n_e R_{\text{eq}}\left(T_C\right)^3 \simeq p_c\,, \tag{5.8}$$

yielding

$$T_C^P \simeq \frac{2\pi^2 t}{\log(2S+1)}\left(\frac{n_e}{p_c}\right)^{5/3}, \tag{5.9}$$

where p_c is the percolation threshold ($\mathcal{O}\left(1\right)$). For $T_C < T < T_m$, an anomaly in the paramagnetic susceptibility is expected to signal the presence of the polarons through an enhanced effective moment.

A natural question can surface at this point regarding the fact that, since de Gennes [1960], we know that, using the virtual crystal and the one-particle approach used above, a transition between uniform PM and FM phases should occur. It is therefore of natural interest to investigate how this magnetic transition is altered by the stabilization of the polaronic phase. In order to do that we follow the same approach as the one carried by de Gennes in evaluating the electronic energy as a function of the magnetization, obtaining a description in terms of the free energy $\Delta F_{FM}(T, M)$. Combining this with eq. (5.4) we can calculate the regions of relative stability of the three phases, and draw the phase diagram shown in Fig. 5.3. In this plot, T_C^{MF} represents the line that would be obtained ignoring the possibility of polaron formation, as de Gennes did; T_C^P is just the curve from eq. (5.9) corresponding to the percolation criterion; T_C and T_m are the actual transition lines calculated by minimizing (5.4) with respect to the polaron radius and $\Delta F_{FM}(T, M)$ with respect to M. Even in such simple phase diagram we observe important physical consequences of the presence of the polaronic phase, namely: (a) the polaronic phase

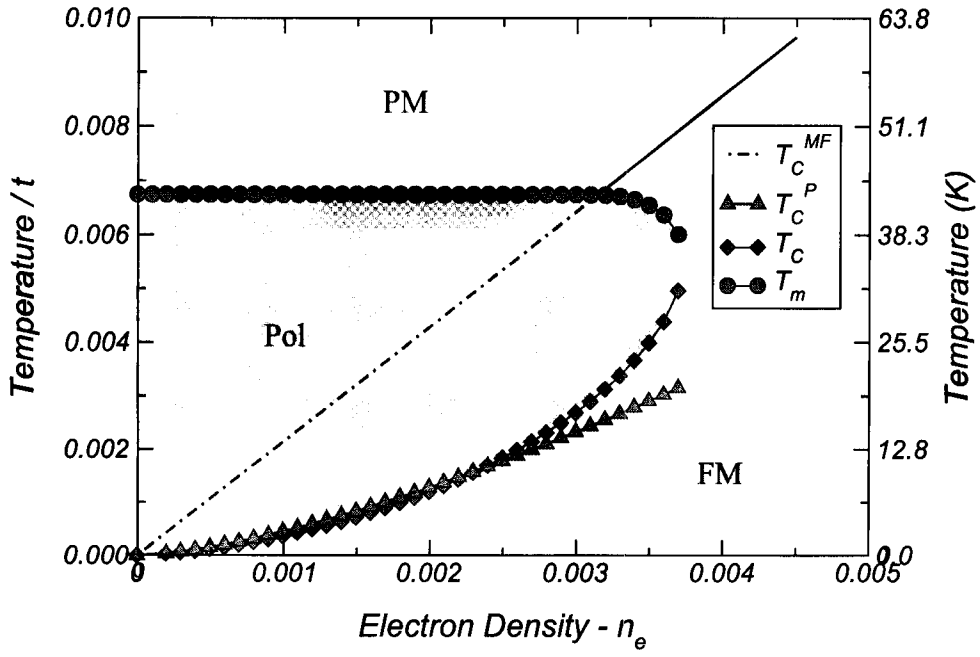

FIGURE 5.3 .: *Phase boundaries obtained within the IPM. The polaronic phase (Pol) appears as a precursor to the ferromagnetism (FM) at low densities (dashed region). The dotted-line curve represents T_C obtained in mean field. See the text for other notations. The left vertical scale is in units of t, and the one on the right in Kelvin, using $t = 0.55$ eV.*

mediates the transition from an homogeneous PM to an homogeneous FM phase, as expected; (b) the transition temperature calculated in the mean-field approach T_C^{MF} is notably reduced at low densities by the onset of the polarons; (c) the Curie temperature obtained with the percolation criterion, T_C^P, gives a very good estimate of T_C (as follows from the superposition of the two curves in almost the entire region), supporting the interpretation of the ferromagnetic transition arising from polaron percolation.

Of course that, as discussed above, in the present framework the PM $\rightarrow$ Pol transition in this diagram is of first order and, strictly speaking, the same occurs at the Pol $\rightarrow$ FM transition, because the phase boundaries are calculated from the relative stability of the two phases. At first sight this would mean that, during the Pol $\rightarrow$ FM transition, the magnetization has a discontinuity at T_C. However, from the interpretation of the FM transition in terms of polaron percolation, one expects a continuous transition, in the sense that the magnetization of the system should be weighted by the *mass* of the *infinite percolating cluster*, which evolves continuously from the percolation threshold. Finally, it is interesting to notice the order of magnitude of the relevant temperatures and densities for this phase. If, for definiteness, one assumes that $t \sim 1$ eV, eqs. (5.7) and (5.9) reveal that the stability condition is realized for densities of $\mathcal{O}\left(10^{-3}\right)$, and temperatures typically in the dozens of Kelvin. As is shown in Appendix 5.A, a more realistic approximation for the electronic energy doesn't appear to modify these ranges significantly, which somehow restrict the range of materials where the effect might be realizable.

5.1.3. The Polaronic Evidence in EuB_6

As mentioned in the chapter dedicated to the experimental features of EuB_6, this magnetic metal with extremely reduced electron density, exhibits all the characteristic signatures of a polaronic phase in Ra-

man scattering measurements [Nyhus et al., 1997; Snow et al., 2001]. Such experiments reveal that the FM transition at $T_C \simeq 15$ K is preceded by an interval of temperatures where the response of the system is dominated by the presence of magnetic polarons.

Our theoretical proposal suggests that EuB_6 is very likely a DEM material in the low density regime [VITOR M. PEREIRAet al., 2004a], characterized by a hopping integral of $t = 0.55$ eV, and a carrier density per unit cell $n_e \sim 10^{-3}$. If we incorporate such hopping (found in § 4.3.3.4 to reproduce the variation in ω_p for EuB_6) in the phase diagram for the IPM, the result is the one in Fig. 5.3, where the absolute temperatures should be read in the rightmost vertical axis.

It is interesting to compare this phase diagram for $n_e \simeq 0.003$ with the experimental results in Fig .3.7. They reveal a polaronic region being stabilized essentially in the same temperature range as the one in Fig. 5.3 for the appropriate densities. This seems to show that our simple description of the polaronic phase captures the essential details of the polaron physics in EuB_6. In particular, we emphasize that, the calculation of the Curie temperature based on the de Gennes approach (the dotted portion of the straight line), clearly overestimates the actual T_C by a factor of 3 or more inside the polaron stability range. As a matter of fact, placing ourselves at a density $n_e = 0.003$ in the diagram of Fig. 5.3, we find $T_C \simeq 17$ K. This lies noticeably close to the experimental T_C , without adjusting parameters.

5.2. The Problem of Phase Separation

5.2.1. Canonical Free Energy and Phase Diagram

The independent polaron model discussed before, is based on various approximations that stem from the low electronic density of the systems we aim to describe. In particular, the same assumption for the electronic energies used by de Gennes was employed. One of the implications of approximating eq. (5.2) by $E_{el}(\mathcal{M}, n_e) \approx E_b(\mathcal{M})n_e$ is that the Curie temperature calculated in mean-field for homogeneous PM and FM phases is simply proportional to the electronic density.

But a more serious question regarding the double exchange in the low density limit is the problem of Phase Separation (PS). It is know that the DEM is unstable towards phase separation at low carrier densities, even without additional AFM (superexchange) couplings between the lattice spins [Alonso et al., 2001a,b; Arovas et al., 1999; Kagan et al., 1999; Nagaev, 1998; Yunoki et al., 1998]. In order to study this aspect of the model in more detail, we abandon the previous approximation for the electronic energy and calculate this quantity exactly within the Hybrid Thermodynamic Approach (HTA) discussed in § 4.3.1. Unless whenever stated otherwise, throughout this section we will be concerned only with the homogeneous phases (PM and FM) of the DEM. In the HTA one tries to trace the electrons out of the problem and obtain an effective Hamiltonian for the lattice spins, in such a way that the partition function becomes simply (4.37):

$$\Xi = \int \mathcal{D}\vec{S}_i \, \exp\left(-\beta H_{eff}(\vec{S}_i)\right) .$$

This effective Hamiltonian contributes to the total free energy through eqs. (4.39), (4.42) and (4.43), and

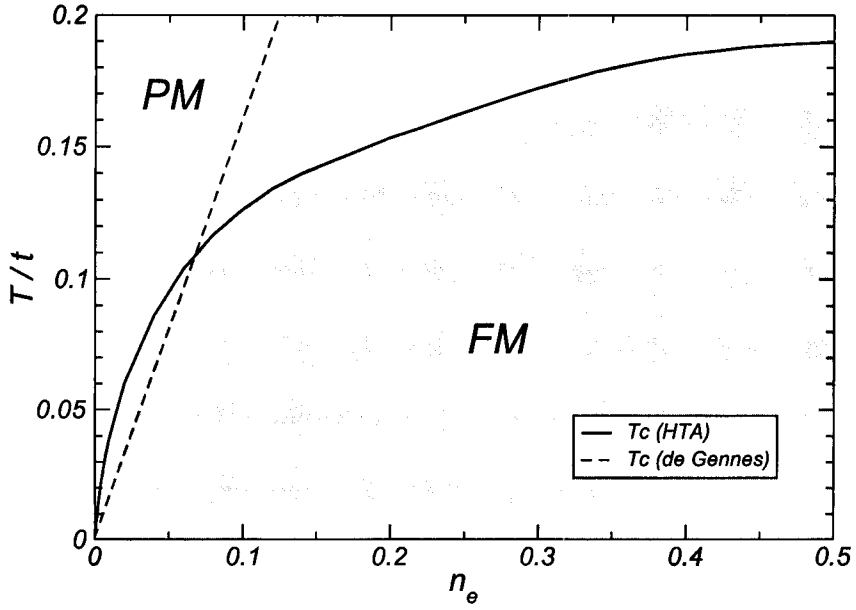

FIGURE 5.4.: *Phase diagram of the DEM obtained within the HTA. For comparison, the result for T_C obtained by de Gennes is also plotted (dashed line).*

we have, at the end:

$$\mathcal{F}(M, n_e) = \int^{E_F(n_e,M)} \epsilon\rho(\epsilon, M)d\epsilon - T\mathcal{S}(M)\,. \tag{5.10}$$

The free energy in eq. (5.10) should be minimized with regards to M to obtain the equilibrium free energy $\mathcal{F}_{eq}(n_e)$. We work at constant electron density and our focus in the cases where $T \ll t$ is implicitly assumed in the omission of the electronic entropy. The phase diagram that emerges from the minimization of (5.10) is drawn in Fig. 5.4 and reproduces the results obtained by Alonso et al. [2001b][7]. The PM–FM transition happens to be continuous for all densities and the deviations from the result obtained with the *bottom of the band*, de Gennes-like, approximation are quite evident. It turns out, however, that this phase diagram is incomplete.

5.2.2. The Essence of the Problem

Reflecting the relative stability of the two homogeneous phases, the plot in Fig. 5.4 says nothing regarding density fluctuations. To determine whether the system is unstable in relation to density fluctuations, we need to look at the behavior of the equilibrium free energy, $\mathcal{F}_{eq}(n_e)$, with the electronic density.

Thermodynamic stability requires $\mathcal{F}_{eq}(n_e)$ to be a globally upward convex function, so that the compressibility, $\kappa = n^{-1}\partial n/\partial\mu$, is never negative. Whenever this condition is violated and the density of the total system is kept constant, it will naturally segregate into two distinct phases in such a way that guarantees the restoration of convexity in the resulting free energy. The equilibrium state in this phase-separated region can be obtained by the so-called Maxwell construction, which, geometrically, is tantamount to substitute the underlying $\mathcal{F}_{eq}(n_e)$ by the envelope of all inferior tangents [Callen, 1985]. A sketch of the situation is presented in Fig. 5.5.

[7]Not strictly since in [Alonso et al., 2001b] the authors used the full fermionic free energy (4.43), instead of the zero temperature approximation used here. But the differences are barely visible.

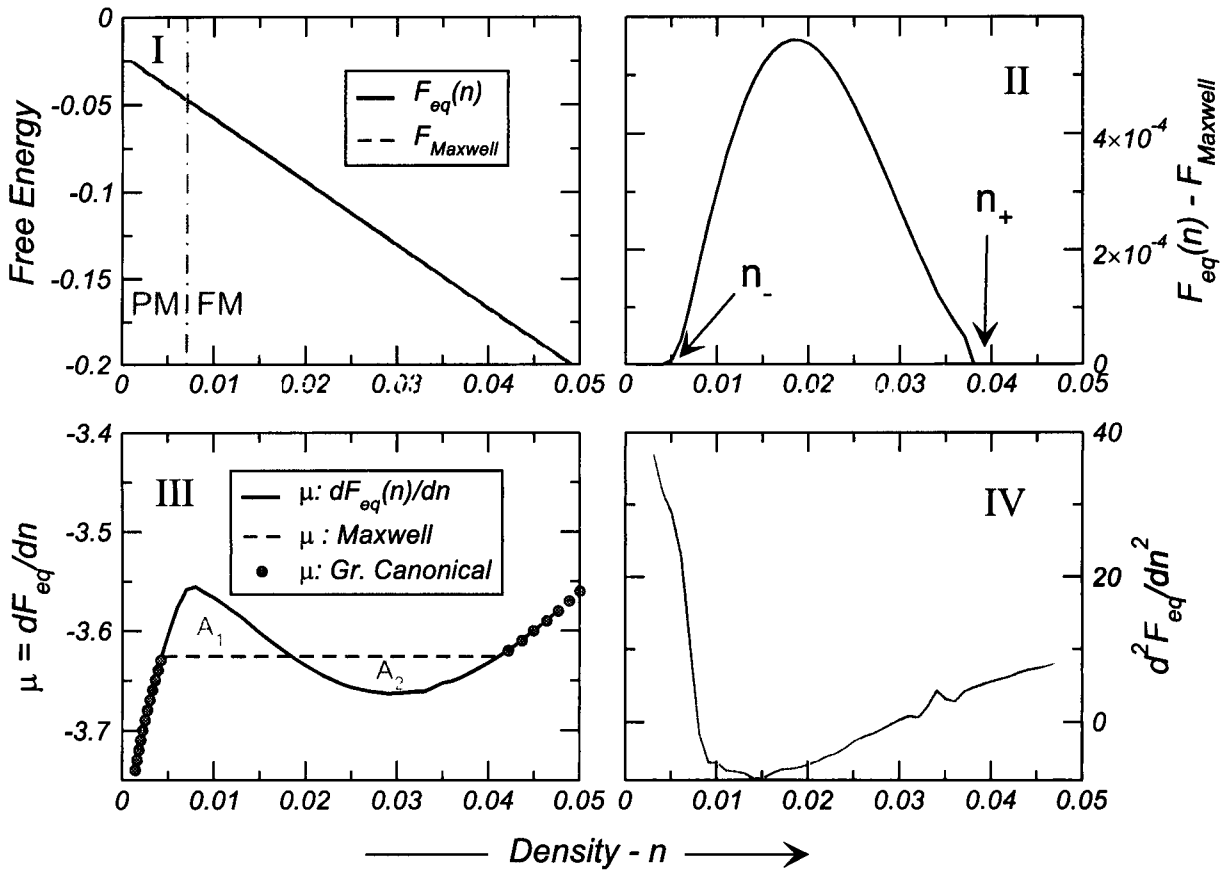

FIGURE 5.6 .: *Details of the Maxwell construction for the DEM at* $T = 0.03t$. *The result of the construction is barely discernible from the underlying* $\mathcal{F}_{eq}(n_e)$ *(I) and, for clarity their difference is plotted on panel II. For comparison, the chemical potential extracted from the results in I is shown together with calculations in the grand canonical ensemble (III). Panel IV shows* $\partial^2\mathcal{F}_{eq}/\partial n_e^2$.

It so happens that, when the behavior of the isothermals of $\mathcal{F}_{eq}(n_e)$ for the DEM calculated using eq. (5.10) is analyzed, the signature of this instability emerges at low densities by the violation of the global convexity. A typical result is shown in detail in Fig. 5.6. Since there is a considerable amount of information in this figure let us go through it in detail (everything is calculated at a constant temperature, $T = 0.03t$).

In the first panel (I) we show the equilibrium free energy $\mathcal{F}_{eq}(n_e)$ as a function of the electronic density n_e (continuous/black line). Despite looking like a straight line, it does have a slight upwards curvature at the lowest densities, downwards at intermediate densities, and upwards again at higher densities. This can be seen in the curve $\partial^2\mathcal{F}_{eq}/\partial n_e^2$ plotted in panel (IV). Thus, we have an instability and a Maxwell construction has to be done in order to find the *true* equilibrium free energy of the system. The Maxwell construction is the dashed/red line in panel (I). Since the effect is rather subtle, we plot the difference between $\mathcal{F}_{eq}(n_e)$ and the free energy after the Maxwell construction in panel (II). In panel (I) we also show the density corresponding to the PM–FM transition at this temperature, signaled by the dot-dashed vertical line (cfr. Fig. 5.4). If we call this particular density $n_e(T_C = 0.03)$, then it is clear that $n_- < n_e(T_C = 0.03) < n_+$. Then, although the relative difference between the free energies is

only $\sim 1\%$, it is qualitatively significant because the system exibiths cohexistence of PM and FM, each of the cohexisting thermodynamic phases having its own electron density.

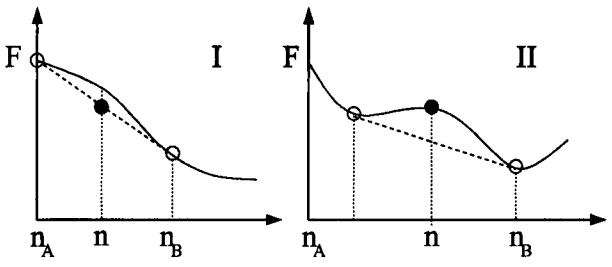

FIGURE 5.5 .: *Free energy for a system unstable towards density fluctuations. The system is unstable for $n_A < n < n_B$ and segregates between regions of density n_A and n_B. The Maxwell construction restoring the curvature of $\mathcal{F}_{eq}(n_e)$ is represented by the dashed lines.*

In panel (III) we present the chemical potential calculated in three different ways. The first one (black/continuous) is simply the curve corresponding to $\partial F_{eq}(n)/\partial n$, and the instability is also clearly seen here since $\mu(n)$ should be monotonously increasing. The dashed (red) curve is the chemical potential resulting from the free energy after the Maxwell construction. Below n_- and above n_+ the result is the same, but in between it is simply an horizontal line. Altough not shown in the figure, the position of this horizontal part is such that the areas A_1 and A_2 are exactly equal, as it should happen[8]. The third curve (circles) shows the chemical potential obtained my minimizing the free energy in the grand canonical ensemble. In this case, since not n but μ is kept constant, the phase separation instability arises naturally through a discontinuity in the $\mu(n)$ curve. The discontinuity appears precisely in the region of densities where the Maxwell construction is in effect, and is just another way to observe this phenomenon.

Actually it is quite instructive to pursue in some more detail this complementarity between the canonical and grand canonical treatments for this particular case. Our scenario is completely analogous to the well known behavior of the van der Waals isothermals for the liquid–gas transition [Callen, 1985]. This is best understood with reference to the plots of $\mu(n_e)$ in Fig. 5.7a at several temperatures. Just as in the $P - v$ phase diagram of the gas, the $\mu(n_e)$ curve is monotonous for temperatures above some critical value. Below this point, the compressibility of the system ($dn_e/d\mu$) becomes negative in some density interval implying an instability. The coexistence curve is then defined by n_- and n_+ obtained from the Maxwell construction and, naturally, coincides with the jump in the density obtained in the grand canonical calculation. Despite the analogy and resemblance of the coexistence curve for the DEM and the van der Waals gas, there is an important qualitative detail not present in the latter case: the coexistence curve for the DEM is re-entrant.

The stability analysis was performed for all the temperatures and densities shown in the phase diagram of Fig. 5.4. The system is unstable towards phase separation at low densities, and the qualitative behavior of the thermodynamic functions is always the one discussed above. As a consequence, one obtains the updated phase diagram presented in Fig. 5.7b.

The information conveyed by this diagram can be translated as follows: for densities above $n_e \sim 0.04$, the system is homogeneous and exhibits a magnetic transition at $T_C(n_e)$. If the density is lower than $n_e \sim 0.01$ the system is homogeneous and PM at high temperatures until $n_-(T)$ is reached. At that point the homogeneous phase is no longer sustainable and two phases start to coexist: one with density $n_-(T)$ and PM together with another of density $n_+(T)$ and FM. Below a temperature signaled as $T_{\text{PS-1}}$,

[8] In fact, we can do the Maxwell construction in both the $\mathcal{F}_{eq}(n)$ or the $\mu(n)$ diagram. In the latter, the Maxwell construction corresponds to finding the horizontal line that yields exactly $A_1 = A_2$ [Callen, 1985].

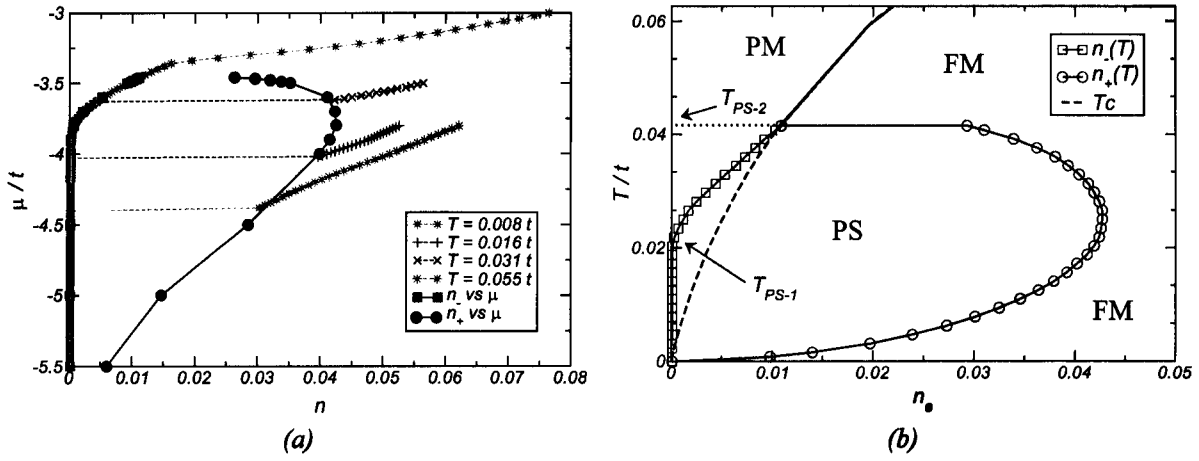

FIGURE 5.7.: *(a) Isothermals in the $\mu - n_e$ plane for selected temperatures. The coexistence curves n_- (squares) and n_+ (circles) were obtained from the Maxwell construction, whereas the $\mu(n_e)$ curves are calculated in the grand canonical ensemble, for comparison. (b) Detail of the low density region of the updated $T - n_e$ phase diagram. The phase separated region (PS) is bounded by the curves $n_-(T)$ and $n_+(T)$ obtained from the Maxwell construction.*

$n_-(T) = 0$ and thus the PM portion of the system is devoid of electrons[9]. If $0.01 \lesssim n_e \lesssim 0.04$, the re-entrant nature of the coexistence curve means that the system can become an homogeneous ferromagnet below $T_C(n_e)$ but still segregate at lower temperatures whenever the condition $n_e = n_+(T)$ is met. In any case, the magnetization of the system is always continuous – a simple consequence of the relation between the densities and volume fractions of each phase:

$$n_e = n_- \frac{V_-}{V} + n_+ \frac{V_+}{V} \,. \tag{5.11}$$

This constraint introduces some peculiarities regarding the nature of the phase separated state. To understand that, in Fig. 5.8 we draw a sketch of the phase separated region in the phase diagram of Fig. 5.7b.

Using this sketch as reference, assume that our system is initially at some high temperature $T > T_1$ and has a given density n. Under these circumstances, the phase diagram states that the equilibrium corresponds to an homogeneous PM phase. We can lower the temperature until T_1 is reached, at which point an instability arises. Exactly at $T = T_1$ there will be a segregation between a PM phase with density $n_{1-} = n$ and another, FM, with density n_{1+}. In order to satisfy the constraint (5.11), the volume fraction of the FM phase will be $V_{1+} = 0$, at $T = T_1$. A slight decrease in the temperature from T_1 to T_2 will reorganize the system so that the PM phase with density n_{2-} now coexists

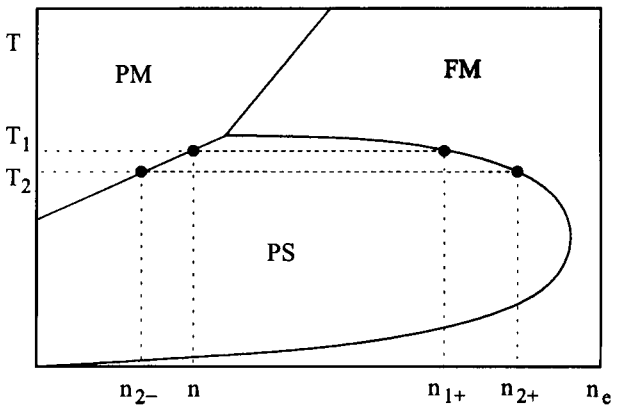

FIGURE 5.8.: *Schematic representation of Fig. 5.7b.*

[9]The fact that $n_-(T)$ goes exactly to zero at $T_{PS\text{-}1}$ has to do with the *zero temperature* approximation used in (5.10) for the electronic energy. Had we included the Fermi-Dirac distribution in (5.10) the curve of $n_-(T)$ would go to zero in a seemingly singular way, the result being barely distinguishable from the one plotted in Fig. 5.7b.

with a FM phase of density n_{2+}. For T_2 very close to T_1, the density of the PM phase is just slightly different from the global density:

$$n_{2-} = n - \varepsilon\,, \tag{5.12}$$

where ε is a small quantity. This determines the volume fractions to be

$$V_{2+} \approx \frac{\varepsilon}{n_{2+} - n}\,. \tag{5.13}$$

Evidently, this means that most of the electrons still remain in the PM phase, and just a few populate the FM regions. But this poses a problem. The Coulomb interaction will certainly prevent the accumulation of charges in a very small volume and the system must remain neutral.

5.2.3. Electrostatic Suppression of Phase Separation

The Maxwell construction is inexpressive with regards to the spatial organization of the phase separated state. This follows from the fact that the Maxwell construction for two coexisting phases of densities n_+ and n_- amounts to saying that,

$$\mathcal{F}_{Maxwell}(n) = \mathcal{F}(n_+)\frac{V+}{V} + \mathcal{F}(n_-)\frac{V-}{V} = \mathcal{F}(n_+)x + \mathcal{F}(n_-)(1-x)\,, \tag{5.14}$$

where $x = V_+/V$ and V_-/V represents the volume fraction of the two coexisting phases. This is simply a linear interpolation between the two values $F(n_+)$ and $F(n_-)$, as illustrated in Fig. 5.5. Therefore, the resulting free energy, $\mathcal{F}_{Maxwell}$, corresponds to the situation where we have a system made of two independent thermodynamic components. In particular, the Maxwell prescription above says nothing about the way the system reorganizes when it phase-separates. This can only come from additional interaction terms that should be added to the right hand side of eq. (5.14), in order to include surface, boundary and other effects. In our case the two phases have different electronic densities, both different from the homogeneous density, the latter satisfying

$$n = n_+x + n_-(1-x)\,. \tag{5.15}$$

Obviously, with mobile negative charges, the system can indeed adjust itself by accumulating electrons in some regions, and depleting them from others. But since the background of positive atomic charges stays essentially immutable and homogeneous, this means that the *total* charge of each phase is not zero. Coulomb interactions are therefore crucial. Under this assumption we now investigate two important corrections for the free energy in the phase separated regime.

5.2.3.1. Electrostatic Correction

Given that we are not assuming any sort of anisotropy, the electrostatic constraint will most certainly favor the development of bubbles of the FM, high density phase, dispersed in the PM, low density phase. Such scenario is schematically depicted in Fig. 5.9.

The charge density is assumed uniform and continuous inside each FM bubble and across the PM background. To calculate the electrostatic energy associated with this charge distribution we take notice to the fact that, on the grounds of overall charge neutrality, it should be possible to find an appropriate neighborhood around each FM bubble such that the total charge on the bubble plus PM neighborhood adds to zero. In Fig. 5.9 this is represented by the wavy lines that, in this way, define cells of charge neutrality. Following Wigner [Pines, 1963], these cells are replaced by the equivalent Wigner-Seitz (WS) spherical cell containing the same volume fractions of FM and PM phases (as shown on the right-hand side of the diagram), which means that

$$R_+^3 = xR_-^3 \tag{5.16}$$

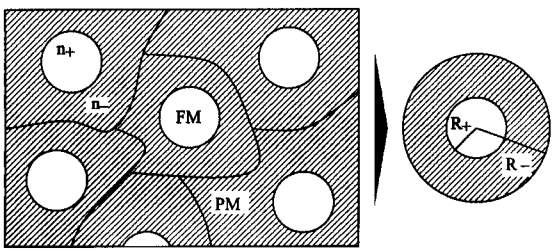

FIGURE 5.9 .: *Depiction of the Wigner-Seitz construction discussed in the text.*

For each WS cell, the total electrostatic energy is calculated considering three terms

$$E_C = U_{++} + U_{--} + U{+-}, \tag{5.17}$$

with the first accounting for the electrostatic self-energy of the "+" region, the second the self-energy of the "-" region, and the last the mutual electrostatic interaction between the two. All of them are calculated within classical electrostatic theory assuming uniform charge distributions in the two regions. Hence

$$U_{++} = \frac{3}{5}\frac{Q_+^2}{R_+}, \tag{5.18}$$

and represents the electrostatic energy of the inner sphere containing the "+" region;

$$U_{--} = \frac{3Q_-^2}{R_-^3 - R_+^3}\left(\frac{R_-^5 - R_+^5}{5} - R_+^3\frac{R_-^2 - R_+^2}{2}\right) \tag{5.19}$$

stands for the energy of the outer shell of the "-" region, and

$$U_{+-} = \frac{3}{2}Q_+Q_-\frac{R_-^2 - R_+^2}{R_-^3 - R_+^3} \tag{5.20}$$

is the electrostatic interaction between the inner sphere and outer shell. In the above $Q_\pm$ are the total charges (positive background + electrons) inside the two regions, and $R_\pm$ the respective radii, as depicted in Fig. 5.9. For reasons regarding numerical stability, in the following we will take always $n_- = 0$. Looking at Fig. 5.7b, this comes as a natural approximation because $n_+ \gg n_-$ for $T_{PS1} < T < T_{PS2}$, and becomes exact for $T < T_{PS1}$. Hence, using the identities

$$\begin{aligned} Q_+ &= e(n - n_+)V_+ = en(x-1)V & \qquad V_+ &= \frac{4\pi}{3}R_+^3 \\ Q_- &= e(n - n_-)V_- = en(1-x)V & \qquad V_- &= \frac{4\pi}{3}(R_-^3 - R_+^3) \end{aligned} \tag{5.21}$$

the Coulomb term can be cast as

$$E_C = \frac{8}{15} e^2 \pi^2 n^2 R_+^5 \frac{2 - 3x^{1/3} + x}{x^2}, \tag{5.22}$$

which yields an energy per unit of volume of

$$\epsilon_C = \frac{E_C}{V} = \frac{2}{5} e^2 n^2 \pi R^2 \frac{2 - 3x^{1/3} + x}{x}. \tag{5.23}$$

For simplicity we replaced R_+ by R and keep this lighter notation below. The bubble radius, R, is a variational parameter. The result (5.23) implies that, for a given volume fraction of the two phases, say x, the electrostatically favorable situation is to shrink the FM bubbles to an arbitrarily small size, meaning that $R \to 0$[10]. But this treatment is yet incomplete, inasmuch as the consideration of finite-sized bubbles of electrons requires another correction, of different nature, to the ground-state energy.

5.2.3.2. Phase Space Correction

The electronic contribution to the free energy (5.10) is calculated in the thermodynamic limit. In the phase separated regime, the electron rich bubbles are expected to be of relatively small size. Therefore, one cannot rely on the electronic energy calculated in the thermodynamic limit and the need to introduce finite size corrections arises.

The leading correction to the energy of an electron gas confined to a finite sized volume comes through the correction to the electronic DOS of the free electron gas which, as discussed in Appendix 5.B, leads to a correction to the ground state energy per electron reading

$$\frac{E(R, n_+)}{N_e} = \frac{E(\infty, n_+)}{N_e} \left[1 + \frac{15}{16} \left(\frac{\pi}{6n_+} \right)^{1/3} \frac{1}{R} \right]. \tag{5.24}$$

The term in R^{-1} is the correction for each bubble. To obtain the total correction we just multiply by the number of WS cells, obtaining the total energy per unit volume

$$\frac{E(R, n_+, x)}{V} = \frac{E(\infty, n_+)}{V} \left[1 + \frac{15}{16} \left(\frac{\pi}{6n} \right)^{1/3} \frac{x^{1/3}}{R} \right] x. \tag{5.25}$$

As expected, the phase space correction acts to the effect of rising the ground state energy of the electron gas. This induces a tendency opposed to the one embodied in the electrostatic term (5.23), and the two should balance at some optimum value of R.

The free energy in the phase separated regime (5.14) needs to be updated for these two corrections that go beyond the Maxwell construction. The result is

$$\begin{aligned} \mathcal{F}_{Maxwell}(n) =& \mathcal{F}(n_+)x + \mathcal{F}(n_-)(1 - x) + \frac{2}{5} e^2 n^2 \pi R^2 \frac{2 - 3x^{1/3} + x}{x} \\ & \frac{E_{el}(n_+)}{V} \frac{15}{16} \left(\frac{\pi}{6n} \right)^{1/3} \frac{x^{4/3}}{R}. \end{aligned} \tag{5.26}$$

[10] At first sight it might seem that the electrons are disappearing! In reality it just means that, according to the WS picture, more and more WS cells appear in the system, as R diminishes, because the total number of electrons and the total volume are fixed.

Since the FM radius is entering only in the correcting terms, the minimization with respect to R can be performed at once, and the final result is

$$\mathcal{F}_{Maxwell}(n) = \mathcal{F}(n_+)x + \mathcal{F}(n_-)(1-x) + \frac{3}{2^{2/3}}\left(\frac{2}{5}\frac{e^2}{a}\pi n_e^2\right)^{1/3}\left[\frac{3}{5}\,t\,n_e(6\pi^2 n_e)^{2/3}\frac{15}{16}\left(\frac{\pi}{6n_e}\right)^{1/3}\right]^{2/3}\left[\frac{2+x-3x^{1/3}}{x^{5/3}}\right]^{1/3}. \tag{5.27}$$

This last expression is the free energy per site of the original lattice when phase separation is in effect. a is the lattice parameter, n_e the electron density per unit cell of the crystal, and t is the hopping integral. Naturally, when there is no PS instability, $x = 1$ by definition and the above reduces to $\mathcal{F}(n_e)$ as one certainly expects. In the PS regime, the equilibrium radius of the electron rich FM bubbles satisfies

$$\frac{4}{3}\pi\, n_+ R^3 = \frac{15}{16}\frac{at}{e^2}\left(\frac{6\pi^5 n_e}{x}\right)^{1/3}\frac{1}{2+x-3x^{1/3}}, \tag{5.28}$$

and this relation can be used, for instance, to inspect the typical number of electrons inside each FM bubble.

5.2.4. Consequences to the Phase Diagram

The natural question is now: what happens when the equilibrium free energy is recalculated with these corrections? Namely, we want to know wheather the PS instability persists when the Maxwell construction is updated according to (5.27). It is useful to have a tuning parameter that interpolates between the case in (5.27) and the previous calculation where localization effects were disregarded. With that purpose, we introduce the dielectric constant, ε_r, that renormalizes the electron charge as $e^2 \to e^2/\varepsilon_r$ in the expressions above. By varying ε_r between 1 and 1000 the curves in Fig. 5.10 were obtained. In this plot, we are focusing on the low density region of the phase diagram where PS occurs. The red (circles) curve pertains to the case $\varepsilon_r \to \infty$ (or, equivalently, zero electronic charge) and is again the result shown before in the phase diagram of Fig. 5.7b[11]. The figure is transparent as to what happens when the Coulomb interaction is *turned on*: the PS region is progressively reduced! Not only that but it is clear that an overwhelming shrinking of the PS region takes place when $\varepsilon = 1$, which is a reasonable value for a good metal.

Thus, the consideration of the free energy (5.27), corrected for the effects arising as a consequence of charge accumulation, leads to the suppression of the PS instability. The electrostatic payoff involved in the segregation leads the system to phase-separate only at much lower densities and/or temperatures. Just how low these are is controlled by the effective electronic charge.

[11] In order to compare directly with the polaronic stability region, the Langevin entropy was replaced by the Brillouin entropy in the magnetic contribution to the free energy, for consistency. The behavior is the same irrespective of which case is considered, up to global numerical factors.

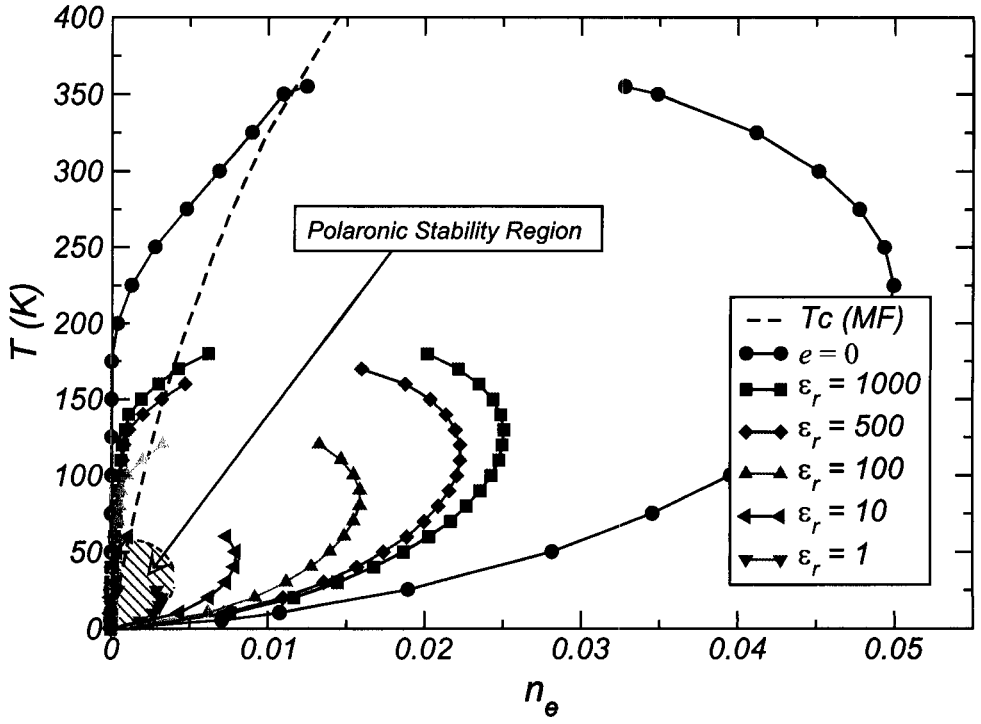

FIGURE 5.10 .: *Phase diagram calculated within the HTA with a corrected Maxwell construction according to eq.* (5.26). *The arrow marks the polaronic stability region, represented by the dashed area at low density and temperature. Notice how the region of phase separation lies inside the polaronic bubble for dielectric constants of* $\varepsilon_r \sim 1$.

5.2.4.1. Phase Separation and Magnetic Polarons

There is a question of relevance that we have been postponing since the beginning of this section on the problem of PS. In § 5.1 (pp. 119) we developed a set of calculations leading to the phase diagram of Fig. 5.3 (or Fig. 5.13a) describing the stability conditions for free magnetic polarons in the DEM. From the polaronic phase diagram follows that magnetic polarons are only stable at considerably low temperatures and densities. In fact much lower than the temperatures and densities at which the PS instability sets in. The reader might have noticed since Fig. 5.8 that the density and temperature scales for the PS bubble are much higher than the scales for the polaronic bubble. More precisely, the polaronic phase lies well inside the PS region when the corrections to the Maxwell construction are ignored. These two regions can be seen in perspective in Fig. 5.10, where the polaronic stability region is highlighted by the dashed region in the lower left corner, and completely inside the PS region for $\varepsilon \to \infty$.

This is clearly a problem to our arguments concerning the polaronic phase. The polaronic stability has been determined by studying its relative stability with regards to an *homogeneous* FM phase. The diagram above is saying that, at such low densities, there are no homogeneous phases — the system phase separates! So the study of polaronic stability has a problem.

But this is only if the electrostatic effects are ignored. With their inclusion, the PS region retreats to lower and lower densities and, as the figure documents, for $\varepsilon_r \sim 1$, it rests already completely inside the polaronic region. So, it seems that the problems above with the polaronic phase have just diminished.

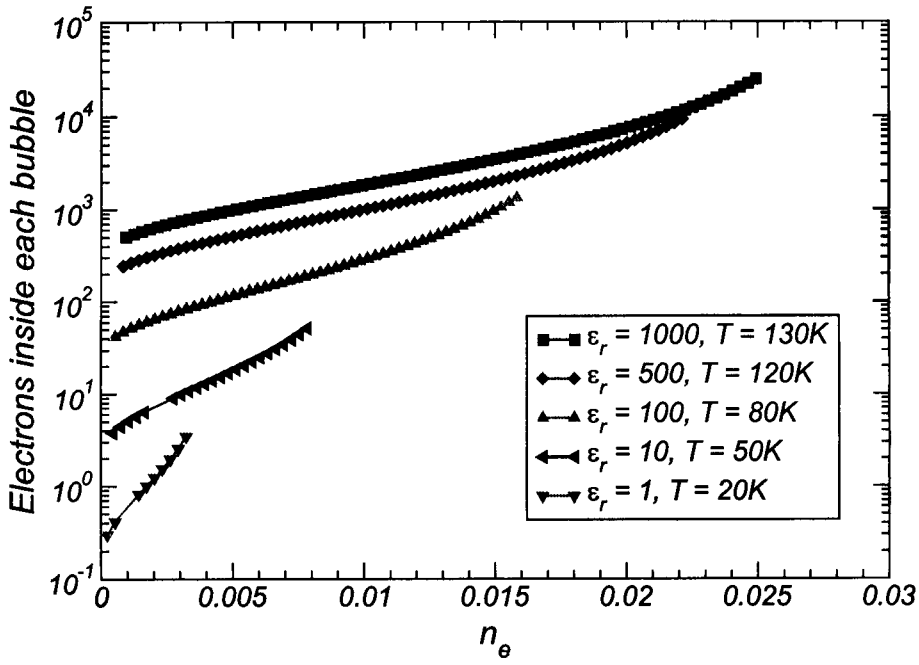

FIGURE 5.11 .: *The number of carriers inside each FM bubble calculated according to* (5.28) *for selected temperatures and dielectric constants.*

The connection between PS and magnetic polarons is indeed remarkably close. The ferromagnetic droplets, associated with a localization energy for the electrons in a restricted volume, are nothing more than our description of the magnetic polaron. So, in this sense, the PS regime studied here and the magnetic polarons are different perspectives of the same physical concept. One of the differences is that, while the magnetic polaron is defined as a FM droplet with a single electron, the PS regime allows for droplets with many electrons.

To explore this further, it is interesting to know the number of electrons inside each FM bubble in the PS regime. Some typical results are plotted in Fig. 5.11 for the same ε_r used before. The most remarkable fact about these curves is that the one pertaining to $\varepsilon_r = 1$ is of the order of unity. Therefore, there is essentially one electron per FM droplet. In addition, the temperatures at which PS occurs for this value of ε_r are so low that the FM droplets are very nearly full polarization. But, a fully polarized FM droplet with one electron inside is just our definition of magnetic polaron! Thus, the peculiarities of the phase segregation in this system are completely consistent with the magnetic polaron picture and, with that respect, the similarity between the shape of the two phase diagrams (Figs. 5.7b and 5.13a) seems hardly coincidental.

5.2.5. General Argument Regarding Phase Separation

Although we have been focusing so far on the specificities of the phase separation instability in the DEM, phase separation is quite a general phenomenon in thermodynamics. To conclude our discussion, we put forward an argument showing that

> *phase separation is ubiquitous in electronic systems whose bandwidth is magnetization dependent.*

To see how this happens, recall that the free energy (5.10) is given by only two contributions: the electronic ground state energy plus an entropic term attributed uniquely to the local moments. For reasons that will be clear in a moment, this argument unfolds more clearly if we work in the grand canonical ensemble, where the electronic chemical potential, μ, is held constant. In this case the free energy (5.10) is simply replaced by the grand canonical potential, and is akin to replacing $E_F \rightarrow \mu$ and $\varepsilon \rightarrow \varepsilon - \mu$ there.

Consider now the following facts, regarding the relevant thermodynamic quantities seen as functions of the magnetization:

1. The magnetic entropy (4.42) is monotonous and downward convex, for all the domain of M;
2. For a given chemical potential, μ, the electronic energy is monotonous and downward convex throughout the entire domain of variation of M;
3. The electronic density is monotonous and upward convex.

Item 1 follows from the fact that $S(M)$ is a proper thermodynamic entropy for a magnetic system, having all the required analytical properties.

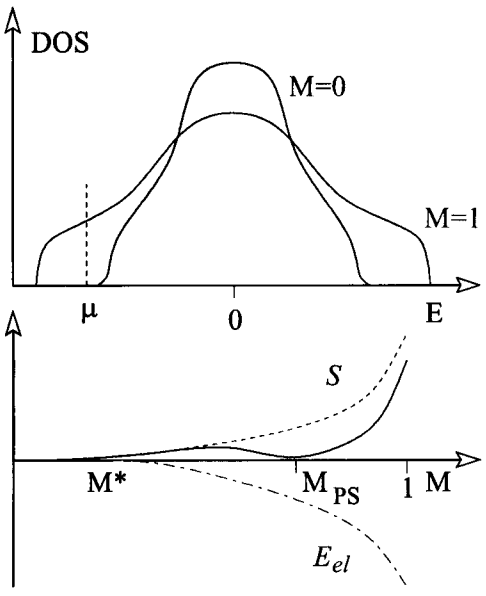

FIGURE 5.12 .: *Schematic variation of DOS, entropy and electronic energy with M at constant μ.*

Point 3 is a trivial consequence of the electronic density being the integrated DOS. Point 2 can be understood from the fact that the electronic bandwidth is monotonous with M (cfr. Figs 4.5 or 4.14a). There is a subtlety however in that, if μ happens to be below the band edge at $M = 0$, then, the electronic energy will be identically zero until some critical magnetization, say M^*, is reached for which the band edge coincides with μ. For higher magnetizations, the energy decreases and the overall shape is as depicted in Fig. 5.12. Since the same plateau is present in the electronic density, for exactly the same reasons, the result for the grand canonical potential will be something like the solid curve drawn schematically in the bottom frame panel of Fig. 5.12. Evidently, there will be a temperature at which the minimum of this curve exactly touches the horizontal axis (as depicted), thus precipitating a first order transition. At the precise temperature, T, at which this happens, the system stays undecided as to which state it should have because the thermodynamic potentials at $M = 0$ and $M = M_{PS}$ are degenerate. Since μ is kept constant, $M = 0$ and $M = M_{PS}$ correspond to different electronic densities. This is but our phase separation instability seen from the grand canonical perspective.

The important thing here is that nothing in this argument mentions the details of the specific model under consideration, and therefore is valid as long as the basic assumptions remain valid. In particular, the magnetization is as good as any other suitable thermodynamic parameter, and, thus, the arguments extends to any appropriate classical variable coupled to the electronic energy as the magnetization is in our specific case.

That phase separation has to emerge always follows from the fact that one can always place μ in between the band edges at $M = 0$ and $M = 1$. So, if temperatures are so low that the fermionic entropy can be disregarded, this kind of treatment should always yield a phase separated regime at low densities.

Appendices for this chapter

Appendix 5.A Effects of Finite Band Filling on Polaron Stability

In the main discussion of the polaronic physics in the DEM, the simplification is made of considering that the electronic energy is simply accounted by the energy at the bottom of the band, multiplied by the electron density (5.3).

In order to account for the finite electronic density, we rely on a *rigid band* approximation for the DOS. This means that we calculate the electronic energy for a given density of polarons, n_p, assuming the DOS in the conduction band doesn't change significantly[12]. The free energy per lattice site then becomes

$$\begin{aligned} F_{\rm Pol}(R, M, n_p) &= -6tn_p \cos\left(\frac{\pi}{R+1}\right) + \int_{E_b(M)}^{E_F(n_e-n_p,M)} \rho(\epsilon, M)\epsilon d\epsilon \\ &+ (1 - n_p R^3) TS(M, S)\,. \end{aligned} \tag{5.29}$$

In this approximation, the electronic energy is counted essentially by transferring electrons from the conduction band to the bound states. The Fermi energy satisfies $E_F(n_e - n_p, M) > E_b(M)$, reflecting the existence of $n_e - n_p$ electrons in the band. An important difference relative to the case of the empty band considered in §. 5.1.2 follows: since we are allowing the existence of $n_e - n_p$ states extended throughout the system, the non-polaronic part can still be ferromagnetic below some temperature. So, in principle, the magnetic polarons could be embedded in a background with finite spin polarization, and, therefore, we have to introduce the magnetization of the background, M, as a third variational parameter, together with R and n_p. The minimization of 5.29 with respect to these parameters, and the comparison of the resulting equilibrium free energy with the homogeneous case (5.10), produces the phase diagram displayed in Fig. 5.13a. The overall qualitative features obtained previously in Fig. 5.3 remain basically the same, the important differences now being: (i) The PM–FM transition curve (dashed line) now places T_C for homogeneous phases at higher temperatures than the ones obtained with the de Gennes treatment; (ii) The polaron stability temperature, T_m, is seen to increase with density if $n_e \lesssim 0.001$, just as expected because, the higher the density, the higher the Fermi energy and the more favorable it becomes to create a polaron for the same price in entropy; (iii) The reentrance of the polaronic phase is now very pronounced, being a consequence of (i). It is nonetheless interesting to observe that the critical density for the stabilization of the polaronic phase ($n_e \simeq 0.004$) and the typical stabilization temperature, T_m, are almost exactly the same as the ones encountered in § 5.1.2.

The nature of the transitions as the temperature is lowered is as follows (see Fig. 5.13b for reference).

[12] We are actually allowed to do that since only a few bound states appear beyond the band edge, as can be seen in Fig. 5.2.

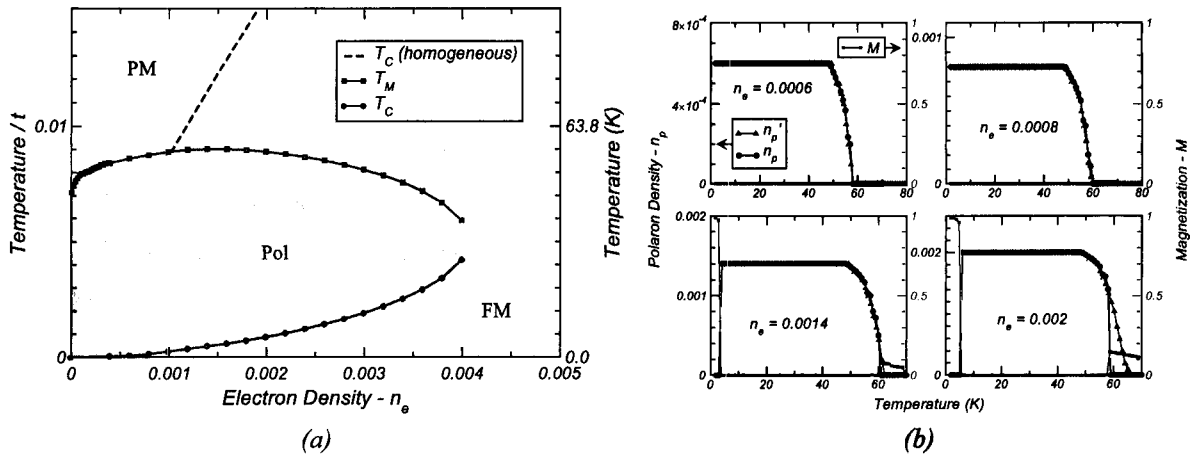

FIGURE 5.13 .: *Polaronic stability relative to homogeneous PM/FM phases when a finite band filling is considered. (a) Phase diagram. (b) Each frame shows the equilibrium values of n_p and M (order parameters) for total electronic concentrations of $n_e = 0.0006, 0.0008, 0.0014, 0.0016$. The blue (triangles) curve shows the equilibrium n_p that is obtained when only paramagnetism is allowed (i.e. constraining $M = 0$).*

Below $n_e \simeq 0.001$ the PM–Pol transition is continuous; $n_p(T)$ varies continuously from 0 to the saturation value $n_p = n_e$, and no FM is stabilized except at very low temperatures, below the Pol phase. For $n_e \gtrsim 0.001$, FM is stabilized with a continuous PM–FM transition; FM persists only until $T_m(n_e)$ is reached, at which point the polarons set in; the FM–Pol transition is discontinuous because the magnetization drops to zero and n_p jumps from 0 to quasi-saturation upon crossing T_m[13]. At lower temperatures, when the T_C line (red/circles) is crossed, the magnetization jumps to the value found in an homogeneous FM phase, concurrently with a discontinuous drop of n_p from n_e to zero. Notice that the T_C line is barely changed by the consideration of a finite band filling. This is related to the fact that, when T_C is reached, the polaron density has long since saturated at n_e, thus emptying the band from carriers.

Appendix 5.B Finite Size Corrections to the Electronic DOS

To estimate the $1/L$ corrections to the ground state energy of an electron gas consider free electrons inside a box of dimensions L_x, L_y and L_z. The electronic spectrum is

$$E_k = \frac{\hbar^2}{2m}k^2, \qquad \text{with} \quad \vec{k} = \pi\left(\frac{n_x}{L_x}, \frac{n_y}{L_y}, \frac{n_z}{L_z}\right), \quad (n_i \geq 1). \tag{5.30}$$

The integrated DOS will clearly be

$$\Omega(E) = \sum_{n_x,n_y,n_z \geq 1} \Theta\left(\kappa^2 - k(n_x, n_y, n_z)^2\right), \tag{5.31}$$

[13]This can be seen clearly in the bottom frames of Fig. 5.13b: above $n_e \gtrsim 0.001$ the curve T_m jumps discontinuously at $T_m(n_e)$ to meet n_p'.

which corresponds, geometrically, to the set of integers (n_x, n_y, n_z) bounded by the ellipsoid

$$\frac{\kappa^2}{\pi^2} \geq \frac{n_x^2}{L_x^2} + \frac{n_y^2}{L_y^2} + \frac{n_z^2}{L_z^2} \,. \tag{5.32}$$

In the thermodynamic limit, $L_{x,y,z} \to \infty$ and the usual procedure consists in replacing the discrete number of states satisfying (5.32) by the volume of the ellipsoid in the first octant, divided by the elementary phase space volume. It is obvious that, by doing this, one is either neglecting or overcounting some of the points in phase space that rightfully satisfy (5.32). This happens mainly at the *boundaries*, and is all right when $L_{x,y,z} \to \infty$ because the errors are of the order of $1/L$ or $1/L^2$ (Fig. 5.14). However, when L is finite, such corrections are clearly relevant. A particularly important one arises from the fact that, when we calculate the volume of the ellipsoid, the points lying at the coordinate axes are automatically included, whereas from (5.30) they should not be. So let

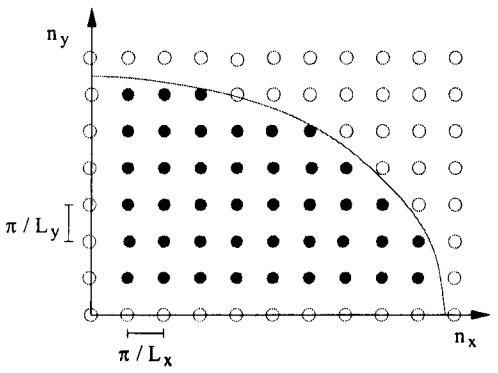

FIGURE 5.14 .: *Discrete Phase Space.*

$$\Omega'(E) = \sum_{n_x,n_y,n_z} \Theta\left(\kappa^2 - k(n_x,n_y,n_z)^2\right) \,, \qquad \text{with} \quad n_i \in \mathbb{Z} \,, \tag{5.33}$$

which relates to $\Omega(E)$ defined in (5.31) by

$$\begin{aligned}
\Omega'(E) = 8\,\Omega(E) &+ \sum_{n_x,n_y} \Theta\left(\kappa^2 - k(n_x,n_y,0)^2\right) \\
&+ \sum_{n_x,n_z} \Theta\left(\kappa^2 - k(n_x,0,n_z)^2\right) + \sum_{n_y,n_z} \Theta\left(\kappa^2 - k(0,n_y,n_z)^2\right) \\
&- \sum_{n_x} \Theta\left(\kappa^2 - k(n_x,0,0)^2\right) - \sum_{n_y} \Theta\left(\kappa^2 - k(0,n_y,0)^2\right) \\
&- \sum_{n_z} \Theta\left(\kappa^2 - k(0,0,n_z)^2\right) + 1 \,.
\end{aligned} \tag{5.34}$$

The above result reflects the fact that, when calculating the continuum volume enclosed by the ellipsoid, one is adding an *extra* portion of phase space near the coordinate axes that should not be included, as in Fig. 5.14. Assuming that κ^2/π^2 is still reasonably greater than L_x^{-1}, L_z^{-1} or L_z^{-1}, these terms correspond to

$$\begin{aligned}
\Omega'(E) &\simeq \text{Volume of ellipsoid with axes } L_x, L_y, L_z \,; \\
\sum_{n_i,n_j} \Theta\left(\kappa^2 - k(n_i,n_j,0)^2\right) &\simeq \text{Area of ellipse of axes } L_i, L_j \,; \\
\sum_{n_i} \Theta\left(\kappa^2 - k(n_i,0,0)^2\right) &\simeq \text{Length of the axis } L_i \,.
\end{aligned} \tag{5.35}$$

Therefore, we have that

$$\frac{4}{3}\pi\left(\frac{k}{\pi}\right)^3 L_xL_yL_z = 8\Omega(E) + \pi\left(\frac{k}{\pi}\right)^2 (L_xL_y + L_yL_z + L_zL_x) - 2\frac{2}{\pi}(L_x + L_y + L_z) + 1\,, \quad (5.36)$$

implying that the corrected phase space volume is actually

$$\Omega(E) = \frac{\kappa^3}{6\pi^2}L_xL_yL_z - \frac{\kappa^2}{8\pi}(L_xL_y + L_yL_z + L_zL_x) + \frac{\kappa}{4\pi}(L_x + L_y + L_z) - \frac{1}{8}\,. \quad (5.37)$$

There is still the error associated with the under/over estimates of the volume near the surface of the ellipsoid. This gives an additional contribution of the order $\mathcal{O}(\kappa)$[14]. But since the precise numerical factors are impossible to extract analytically, we do not include this correction. Consequently, the expression above is meaningful only down to $\mathcal{O}(\kappa^2)$. Given that the volume and surface area of the volume enclosing the electron gas are related to the L's by $L_xL_yL_z = V$ and $L_xLy + L_yL_z + L_zL_x = S/2$, the above can be summarized as

$$\Omega(\kappa) \simeq \frac{\kappa^3}{6\pi^2}V - \frac{\kappa^2}{16\pi}S\,, \quad (5.38)$$

from which the corrected DOS follows:

$$g(\kappa) = \frac{\partial\Omega(\kappa)}{\partial\kappa} = \frac{k^2}{2\pi}V - \frac{k}{8\pi}S = g_\infty(\kappa)\left(1 - \frac{\pi}{4\kappa}\frac{S}{V}\right)\,. \quad (5.39)$$

For instance, taking the leading correction for electrons inside a cubic box ($L_i = L$), implies a correction to the ground state energy per electron reading

$$\frac{E}{N_e} = \frac{E_\infty}{N_e}\left[1 + \frac{15}{8}\frac{\pi}{L}\left(\frac{1}{6\pi^2 n}\right)^{1/3}\right]\,, \qquad \text{with} \quad \frac{E_\infty}{N_e} = \frac{3}{5}\frac{\hbar^2}{2m}\kappa_{F_\infty}^2\,. \quad (5.40)$$

In the main text, we are interested in the corrections to the energy of an electron gas confined to finite sized spherical bubbles. We notice that for a cube of side L,

$$\left(\frac{S}{V}\right|_{\text{cube}} = \left(\frac{S}{V}\right|_{\text{inscribed sphere}}\,, \quad (5.41)$$

the surface to volume ratio, equals the same ratio for the inscribed sphere with $R = L/2$. Hence we take the result (5.40) and simply substitute L by $2R$, obtaining

$$\frac{E}{N_e} = \frac{E_\infty}{N_e}\left[1 + \frac{15}{16}\left(\frac{\pi}{6n}\right)^{1/3}\frac{1}{R}\right]\,, \quad (5.42)$$

which provides an estimate of the leading corrections to the ground state (and $T = 0$) energy of the confined electron gas.

[14] This can be inspected numerically by plotting the difference between (5.37) and (5.31) against κ. For $L_x = L_y = L_z = L$ the difference appears majored by a term linear in κ.

6. Two Dimensional Carbon

"It is surprising that a low-energy experiment can produce an effect thought to occur only with particles going close to the speed of light."

— **Norman Dombey**, Quoted by *Science NOW* Daily News (23 Aug. 2006).

6.1. A Two Dimensional Solid Made Reality

Carbon is arguably the most important element in the periodic table: certainly so if the inquirer happens to be a earthly living form. Carbon defines the class of organic compounds which are present in virtually all cellular structures, and therefore leads ultimately to life. But the ubiquity and relevance of carbon is not restricted to the biological domains. Indeed, being the key element behind the great energetic yield of hydrocarbons, carbon is at the very foundation of our modern economies and, by extension, our societies.

For the physicist, carbon is a very interesting element in itself, on account of its chemical versatility: carbon can form more compounds than any other element [Chang, 1991]. Its valence orbitals are known to hybridize in many different forms like sp^1, sp^2, sp^3, and others. As a consequence, carbon can exist in many stable allotropic forms, characterized by the different relative orientions of the carbon atoms, with diamond and graphite being the ones more widely known[1]. Carbon binds through covalence, and leads to the strongest chemical bonds found in nature. This translates, for instance, into fusion points as high as $\sim$ 4000 K for graphite and diamond[2].

These and other feats led to the quest and ultimate synthesis of new allotropes of carbon [3]. One of them are the now well known carbon nanotubes, consisting of a rolled two dimensional sheet of sp^2 carbon. Nanotubes can be made of a single sheet or multi-walled, and can even come with caps of different shapes which determine some of their electronic properties. One of the remarkable peculiarities of the electronic structure of nanotubes is that, depending on the way in which they are rolled (the chiral vector) they can be metallic or insulating. This follows directly from the theoretical electronic structure associated with different chiral vectors [Hamada et al., 1992; Saito et al., 1992] and STM experiments reveal an impressive accord with the theoretical result [Odom et al., 1998] (Fig. 6.1). Since the nanotube diameter is of the order of a few lattice spacings, and much smaller than its length, nanotubes have one dimensional character because the allowed electronic wavevectors rest on a finite set of lines in the BZ.

[1] Strictly speaking, graphite is the stable allotrope, diamond being actually unstable towards it. But, in practice and to reassure diamond owners, the rate of spontaneous transmutation is of the order of millions of years.

[2] Graphite does not even have a liquid state at normal pressures. It undergoes direct sublimation.

[3] As an aside note, there is, inclusively, a journal entirely dedicated to carbonaceous solids and structures, sponsored by the American Carbon Society, and published by Elsevier. It's name is, well, *Carbon*.

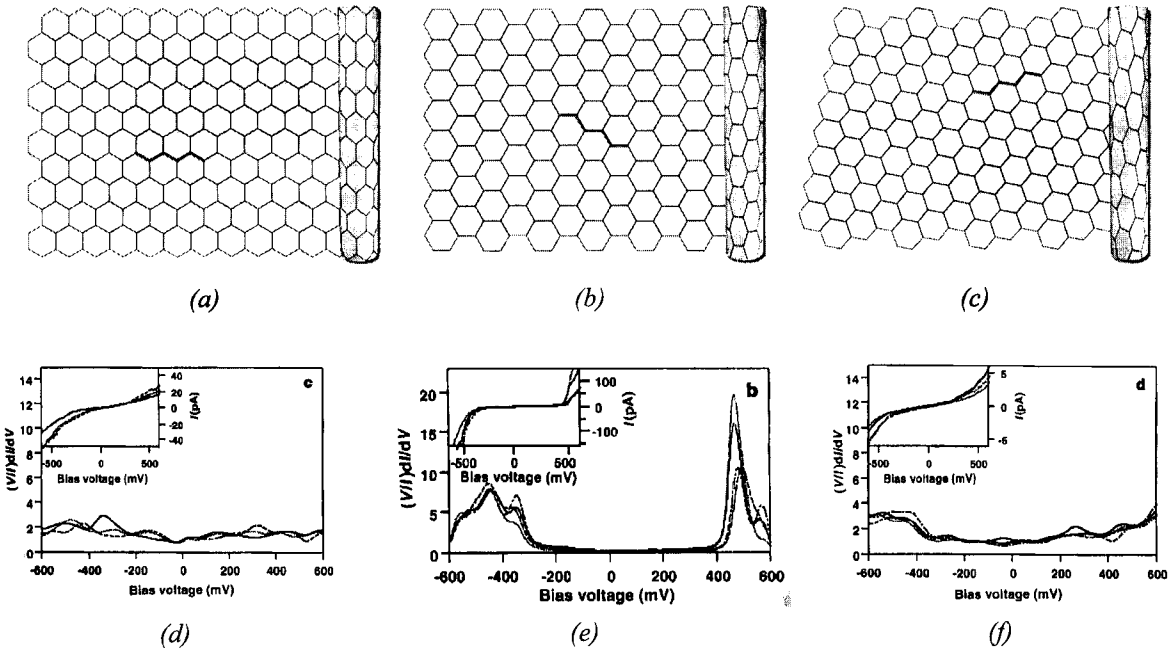

FIGURE 6.1 .: *Different rollings of nanotubes and consequences on transport. (a) Zig-zag* $(n,0)$ *nanotube, (b) armchair* (n,n) *nanotube and (c) general chiral* (n,m) *nanotube. In the bottom row, we present experimental measurements of the normalized conductance and I-V curves corresponding to nanotubes with chiral vectors* $(11,2)$, $(14,-3)$ *and* $(12,3)$ *respectively [Odom et al., 1998].*

Fullerenes are another *synthetic* carbon allotrope, consisting of *balls* of carbon atoms held together by a combination of hexagonal and pentagonal structures. From the electronic point of view they have a zero-dimensional character. C_{60} is a representative example, consisting of a truncated icosahedron, exactly as in a soccer ball. Other known allotropes of carbon are represented in Fig. 6.2.

Common to these forms of carbon is the so-called graphene sheet. Graphene is a single sheet of sp^2 carbon organized in an honeycomb lattice (Fig. 6.2b). Graphite, for instance, is made of stackings of graphene planes and nanotubes from rolled graphene sheets. Yet, for many years, it was believed that graphene itself would be thermodynamically unstable. This presumption has been put to rest by a series of remarkable experiments in which truly bidimensional (one atom thick) sheets of graphene have been synthesized and characterized [Novoselov et al., 2004]. So far this is the first known stable bidimensional crystal that can exist free standing, and with no need for some substrate, as reported[4] [Novoselov et al., 2005b]. Since this discovery, graphene has sprung into the spotlight on account of the unconventional physics it exhibits. Among other no less interesting aspects, graphene displays a strong electric field effect in the sense that the nature of the electronic carriers can be changed continuously and smoothly from electron-like to hole-like under the application of appropriate gate voltages, and can support much higher density currents that conventional metals [Novoselov et al., 2004]. This arises because graphene is a degenerate semimetal, with conduction and valence bands touching exactly at the Fermi level, at which point the DOS vanishes. Its low energy electronic structure is described by the 2D Dirac equation, having a characteristic linear dispersion near the Fermi energy. This aspect is clearly catpured in STM

[4]This means that studies of the 2D electron gas can now be performed on a truly 2D crystal, as opposed to the traditional measurements made at interfaces as in Metal-Oxide-Semiconductor Field Effect Transistors (MOSFETs) and other structures.

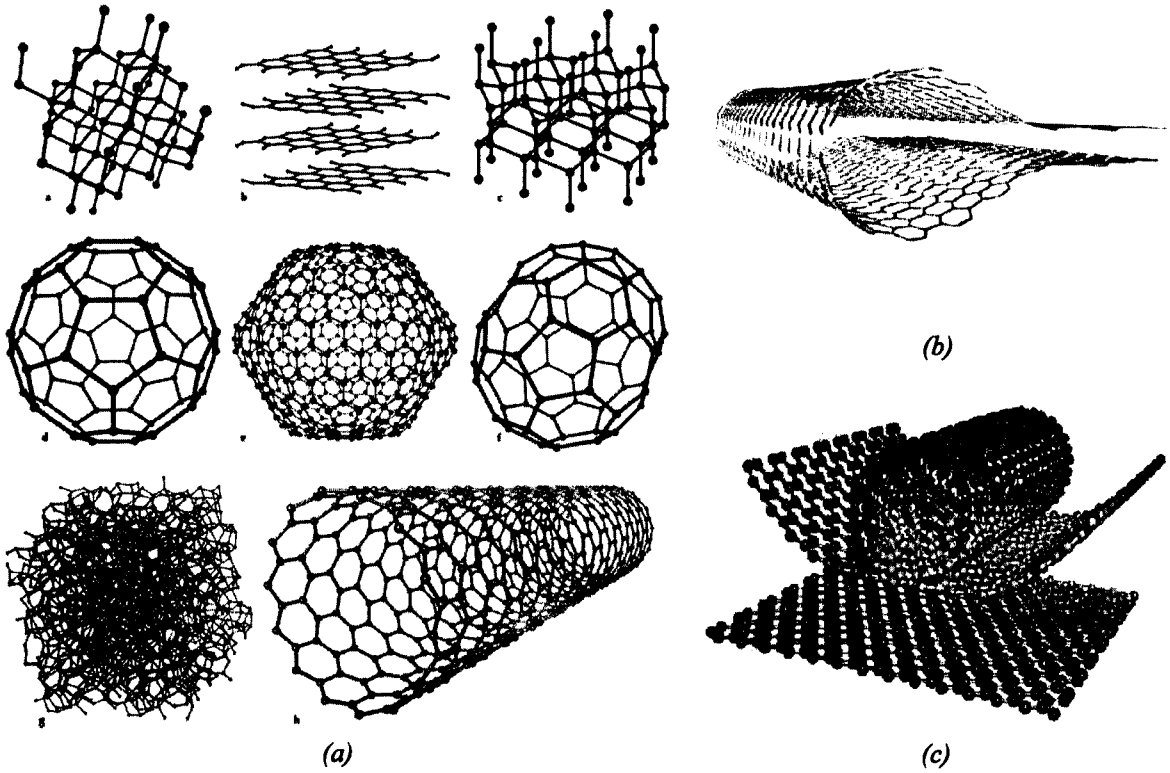

FIGURE 6.2 .: *In panel (a) the different allotropic forms of carbon are represented: a–Diamond, b–Graphite, c–Lonsdaleite, d–Buckminsterfullerene (C_{60}), e–C_{540}, f–C_{70}, g–amorphous carbon, h–single-walled carbon nanotube. In panel (b) a folded graphene sheet is drawn and in (c) we show a depiction of how graphene can be thought of as an unrolled nanotube.*

and conductance measurements, that show results in complete accord with the theoretical DOS derived for graphene. In addition, this new material has seized people's attention because of the appearance of a minimum metallic conductivity and the *exotic* Quantum Hall Effect (QHE), characterized by an anomalous quantization of the Landau levels [Novoselov et al., 2005a; Peres et al., 2005, 2006; Zhang et al., 2005].

6.2. Electrons in a Honeycomb Lattice

The purpose of this section is to review some properties of the electronic spectrum in graphene. It is no exhaustive analysis as the goal is just to introduce the basic properties and details relevant for the subsequent discussions.

Graphene consists of carbon atoms organized into a honeycomb lattice, bonded through covalence between two sp^2 orbitals of neighboring atoms (Fig. 6.3a). The graphene plane is defined by the plane of the sp^2 orbitals. The saturation of the resulting σ bonding orbitals, leaves an extra electron at the remaining $2p_z$ orbital per carbon atom. Ideal graphene has therefore a half-filled electronic ground state. The Bravais lattice that underlies the translation symmetries of the honeycomb lattice is the triangular lattice, whose primitive vectors $\vec{a}_1$ and $\vec{a}_2$ are depicted in Fig. 6.3a. One of the consequences is the

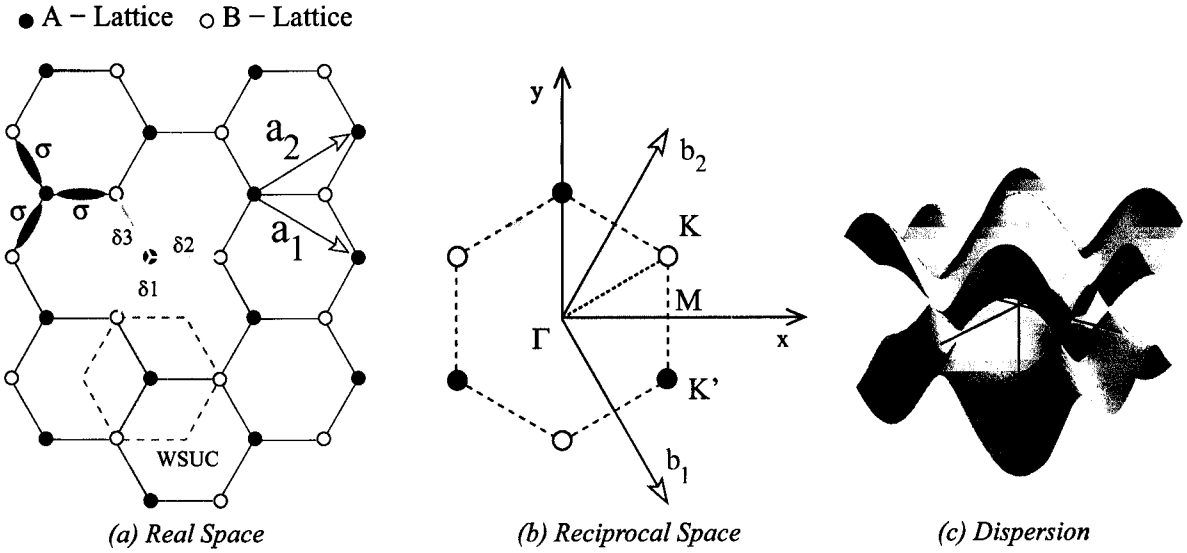

(a) Real Space *(b) Reciprocal Space* *(c) Dispersion*

FIGURE 6.3 .: *Honeycomb lattice. In (a) $\vec{a}_1$ and $\vec{a}_2$ are the primitive vectors that define the WS unit cell highlighted as the dashed hexagon. The lattice parameter, a, is 1.4 Å. The first BZ of the associated reciprocal lattice is shown in (b), together with the points of high symmetry Γ, M and the nonequivalent K and K'. Panel (c) presents the band structure of graphene ($t' = 0$) with the two bands touching at the K and K' points of the BZ.*

existence of two atoms per unit cell, that define two sublattices (A and B in the figure): indeed, the honeycomb lattice can be thought as two interpenetrating triangular lattices. This bipartite nature of the crystal lattice, added to the half-filled band, imposes an important particle-hole symmetry as will be discussed hereafter.

The electronic structure of graphene can be captured within a tight-binding approach, in which the electrons are allowed to hop between immediate neighbors with hopping integral $t \simeq 2.7$ eV, and also between next-nearest neighbors:

$$H = -t \sum_{\langle i,j \rangle} c_i^\dagger c_j - t' \sum_{\langle\langle i,j \rangle\rangle} c_i^\dagger c_j + \text{h.c.} \ . \tag{6.1}$$

The presence of the second term is motivated by some STM measurements that display a slight asymmetry in the I-V curves [Matsui et al., 2005; Niimi et al., 2004; Peres et al., 2005], which is captured by the term in t', and violates particle-hole symmetry. To underline the two sublattice structure of the honeycomb, we can write the Hamiltonian as

$$H = -t \sum_{i \in A, \delta} a_i^\dagger b_{i+\delta} - t \sum_{i \in B, \delta} b_i^\dagger a_{i+\delta} - t' \sum_{i \in A, \Delta} a_i^\dagger a_{i+\Delta} - t' \sum_{i \in B, \Delta} b_i^\dagger b_{i+\Delta} \, , \tag{6.2}$$

with operators a_i and b_i pertaining to sublattices A and B respectively. The vectors $\vec{\delta}$ connect the unit cells of atom i and its immediate neighbors, and, similarly, the $\vec{\Delta}$ connect the unit cells of atom i and its six second neighbors.

Fourier transforming eq. (6.2) leads to

$$H = \sum_k \Psi_k^\dagger \begin{pmatrix} \epsilon_2(k) & \epsilon_1(k) \\ \epsilon_1(k)^* & \epsilon_2(k) \end{pmatrix} \Psi_k \,, \qquad \text{with } \Psi_k = \begin{pmatrix} a_k \\ b_k \end{pmatrix} . \tag{6.3}$$

In all the above equations, the index associated with the electronic spin has been omitted for simplicity, but is always implicitly included. The functions $\epsilon_1(k)$ and $\epsilon_2(k)$ are[5]

$$\epsilon_1(k) = -t \sum_{\vec{\delta}} e^{-i\vec{\delta}.\vec{k}} \,, \qquad \epsilon_2(k) = -t' \sum_{\vec{\Delta}} e^{-i\vec{\Delta}.\vec{k}} \tag{6.4}$$

$$\epsilon_2(k) = -2t' \cos(\sqrt{3}k_y a) - 4t' \cos\left(\frac{\sqrt{3}}{2}k_y a\right) \cos\left(\frac{3}{2}k_x a\right) \tag{6.5}$$

$$|\epsilon_1(k)|^2 = 3t^2 + 2t^2 \cos(\sqrt{3}k_y a) + 4t^2 \cos\left(\frac{\sqrt{3}}{2}k_y a\right) \cos\left(\frac{3}{2}k_x a\right) , \tag{6.6}$$

and yield, after diagonalization of (6.3), the dispersion relations for graphene:

$$E_\pm(k) = \epsilon_2(k) \pm |t| \sqrt{3 - \frac{\epsilon_2(k)}{t'}} \,. \tag{6.7}$$

The two bands $E_\pm(k)$ are represented in Fig. 6.3c in the domain $k_{x,y} \in [-\pi, \pi]$. The outstanding feature of this bandstructure is that, being half filled, graphene is a very peculiar semimetal. A semimetal because the valence and conduction band touch at the Fermi energy, peculiar because the bands meet at a set of measure zero constituted by the points K and K' of the BZ. Peculiar also because the low energy physics is dictated by the dispersion around those two nonequivalent points[6], which turns out to be linear in k. In fact, expanding (6.6) around either

$$K = \frac{4\pi}{3\sqrt{3}a}\left(\frac{\sqrt{3}}{2}, \frac{1}{2}\right) \qquad \text{or} \qquad K' = \frac{4\pi}{3\sqrt{3}a}\left(\frac{\sqrt{3}}{2}, -\frac{1}{2}\right) \tag{6.8}$$

one gets the so-called $\vec{K}.\vec{p}$ *effective* bandstructure:

$$E(\vec{K} + \vec{p}) = -3t' \pm v_F\, |\vec{p}| + \frac{9t'a^2}{4}\vec{p}^{\,2} \,, \tag{6.9}$$

with a Fermi velocity, $v_F = 3/2ta$. When $t' = 0$ the dispersion is purely conical, as in a relativistic electron in 2D. For this reason, the two cones tipped at K and K' are known as Dirac cones. Indeed, the low-energy, continuum limit of (6.2) is given by

$$H = v_F \int d^2\boldsymbol{r}\, \psi^\dagger(\boldsymbol{r})\, \vec{\sigma} \cdot \vec{p}\, \psi(\boldsymbol{r}) \,, \tag{6.10}$$

where $\psi(\boldsymbol{r})$ is a two dimensional spinor obeying the Dirac equation in 2D [González et al., 1992, 1996].

Some quantitative aspects of graphene's band structure are plotted in Fig. 6.4. In panel (a) the band

[5]For obvious reasons, $\epsilon_2(k)$ alone is the dispersion relation of a triangular lattice.

[6]Naturally, only one K and one K' point lie within the first BZ.

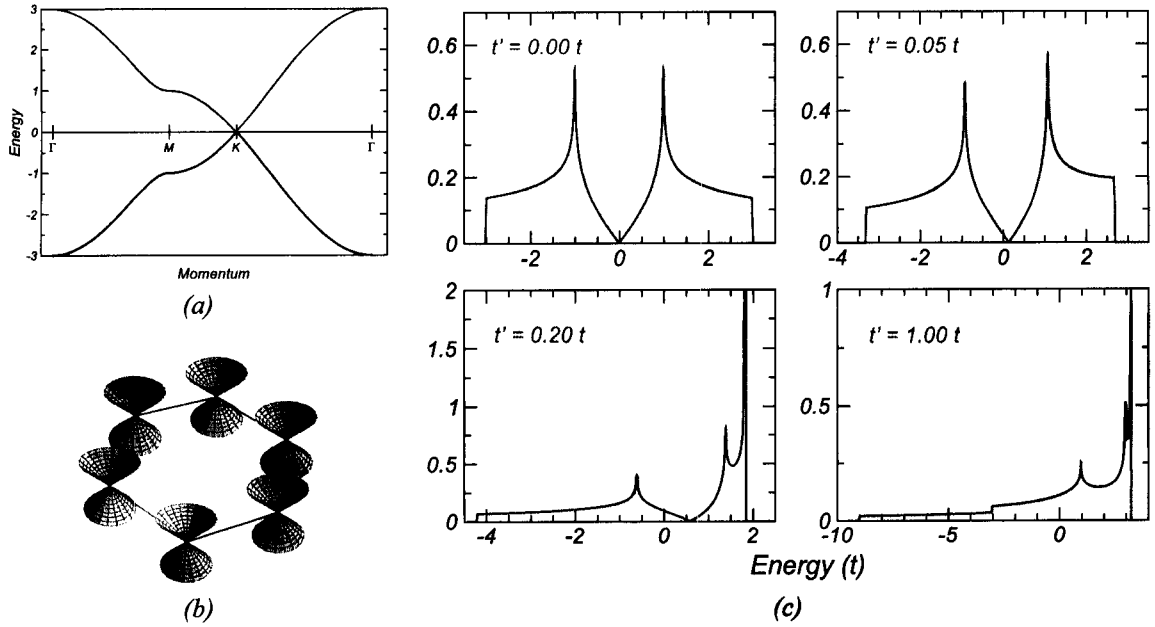

FIGURE 6.4 .: *(a) Band structure along the symmetry directions of the reciprocal BZ of the honeycomb. (b) The band structure near the K points consists of the so-called Dirac cones. (c) DOS associated with eq. 6.7 for different values of t'.*

dispersion is plotted along the symmetry directions of the BZ indicated in Fig. 6.3b, and in panel (c) the DOS for different values of the nearest-neighbor hopping, t', are plotted. Focusing on the particle-hole symmetric case ($t = 0$), it is clear that, besides the marked van Hove singularities at $E = \pm t$, the most important feature is the linear vanishing of the DOS at the Fermi level, a fact that is at the origin of many transport anomalies in this material [Peres et al., 2005].

Particle-hole symmetry in this problem arises from the bipartite nature of the honeycomb lattice, and is a general property of systems whose underlying crystal lattice has this sort of symmetry. To see how it comes about, when we have a bipartite lattice, the basis vectors of the Hilbert space can always be ordered so that, for any ket, $|\varphi\rangle$, the amplitudes in sublattice A come first. For example, if $\{\phi_A^1, \phi_A^2, \ldots, \phi_A^N\}$ are the Wannier functions for the orbitals in sublattice A, and $\{\phi_B^1, \phi_B^2, \ldots, \phi_B^N\}$ the ones in sublattice B, then our ordered basis could be $\{\phi_A^1, \ldots, \phi_A^N, \phi_B^1, \ldots, \phi_B^N\}$. If the Hamiltonian includes hopping only between nearest neighbors, this means that it will only promote itinerancy between different sublattices. The stationary Schrödinger equation then reads, in matrix block form,

$$\begin{pmatrix} 0 & h_{AB} \\ h_{AB}^\dagger & 0 \end{pmatrix} \begin{pmatrix} \varphi_A \\ \varphi_B \end{pmatrix} = E \begin{pmatrix} \varphi_A \\ \varphi_B \end{pmatrix} . \tag{6.11}$$

Expanding we get

$$\begin{cases} h_{AB}\, \varphi_B = E\varphi_A \\ h_{AB}^\dagger\, \varphi_A = E\varphi_B \end{cases} \quad \Rightarrow \quad (h_{AB}^\dagger h_{AB})\, \varphi_B = E^2 \varphi_B \,, \tag{6.12}$$

and therefore, if E is an eigenstate, so is $-E$. For a half-filled system, the elementary excitations around

the Fermi sea can be thought, as usual, as particle-hole pairs. Since in that case $E_F = 0$, particles and holes have symmetric dispersions. This is completely analogous to the situation found in simple semiconductors or semimetals, although matters are slightly more complicated here because there are two degenerate points, K and K' in the BZ. Thus there will be two families of particle and hole excitations: one associated with the Dirac cone at K, and the other with the cone at K'.

6.3. Disorder and Localization in Graphene

6.3.1. Relevance of Disorder in Graphene

Disorder is omnipresent in any real solid state material, graphene being no exception. In graphene this statement is even more insurmountable inasmuch as it is a bidimensional crystal. True long-range order in 2D implies a broken continuous symmetry (translation), which violates the Hohenberg-Mermin-Wagner theorem [Hohenberg, 1967; Mermin and Wagner, 1966]. So, defects must be present in graphene and, in a sense, as paradoxical as it might sound, are presumably at the basis of its thermodynamic stability.

But the study of disorder effects on graphene is motivated by more extraordinary experimental results. One of them is the study undertaken by Esquinazi et al. [2003] in which Highly Oriented Pyrolytic Graphite (HOPG) samples were irradiated via high energy proton beams. As a result, the experiments revealed that the samples acquired a magnetic moment, displaying long range FM order up to temperatures much above 300 K. This triggered enormous interest, since the technological possibilities arising from organic magnets are many and varied. Furthermore, carbon, being the most covalent of the elements, has a strong tendency to saturate its shell in its allotropes, and is somehow the antithesis of magnetism. More than the moment formation, it was found that the magnitude of the saturation moment registered in hysteresis curves was progressively increased with successive irradiations. This is strong evidence that the defects induced by the proton beam are playing a major role in this magnetism. In this context the study of defects and disorder in graphene gains a significant pertinence.

In the following paragraphs we will unveil some details and peculiarities that emerge from different models of disorder applied to free electrons in the honeycomb lattice.

6.3.2. Vacancies

Vacancies are the defects more likely to be induced in the graphene structure by proton irradiation. A vacancy is simply the absence of an atom at a given site. Now, when an atom is removed two scenarios are possible: either the disrupted bonds remain as dangling bonds, or the structure undergoes a bond reconstruction in the vicinity of the vacancy, with several possible outcomes [Ding, 2005]. In either case, a slight local distortion of the lattice is expected. In the following discussion, however, it is assumed that, as first approximation, the creation of a vacancy has the sole effect of removing the π_z orbital at a lattice point, together with its conduction band electron. In this sense, the physics of the conduction band electrons is still described by the Hamiltonian (6.1), where now the hopping to the vacancy sites is *forbidden*.

6.3.2.1. Vacancies and a theorem

An interesting thing happens with vacancies when $t' = 0$. If the distribution of vacant sites is uneven between the two sublattices, then we can be sure that zero energy modes will appear. This follows from a theorem in linear algebra and can be seen as follows. Assume, very generally, that we have a bipartite lattice, with sublattices A and B[7], and that the number of orbitals/sites in A (B) is N_A (N_B). Just as we did before, the basis vectors of the Hilbert space can always be ordered so that any ket, $|\Psi\rangle$, has the amplitudes on sublattice A appearing first, followed by the amplitudes on sublattice B:

$$|\Psi\rangle = (\varphi_A, \varphi_B) = (\phi_A^1, \phi_A^2, \ldots, \phi_A^{N_A}; \phi_B^1, \phi_B^2, \ldots, \phi_B^{N_B}) . \tag{6.13}$$

We now consider an Hamiltonian containing only nearest-neighbor hopping, plus some local energy (ϵ_A, ϵ_B) on each sublattice. The corresponding stationary Schrödinger equation will then be (in matrix block form that respects the ordering of the basis)

$$\mathcal{H}|\Psi\rangle = E|\Psi\rangle \mapsto \begin{pmatrix} \epsilon_A \mathbf{1}_{N_A} & h_{AB} \\ h_{AB}^\dagger & \epsilon_B \mathbf{1}_{N_A} \end{pmatrix} \begin{pmatrix} \varphi_A \\ \varphi_B \end{pmatrix} = E \begin{pmatrix} \varphi_A \\ \varphi_B \end{pmatrix} , \tag{6.14}$$

where $\mathbf{1}_M$ is the $M \times M$ identity matrix, h_{AB} a $N_A \times N_B$ matrix, and φ_A (φ_B) a vector in a subspace of dimension N_A (N_B).

The spectrum To analyze the spectrum we note that

$$\begin{cases} h\,\varphi_B = (E - \varepsilon_A)\varphi_A \\ h^\dagger\,\varphi_A = (E - \varepsilon_B)\varphi_B \end{cases} , \tag{6.15}$$

which, from cross-substitution, certainly implies that

$$h^\dagger h \varphi_B = (E - \varepsilon_A)(E - \varepsilon_B)\varphi_B . \tag{6.16}$$

If we call λ^2 to the (non-negative) eigenvalues of $h^\dagger h$, the spectrum of $\mathcal{H}$ is then

$$E = \frac{\varepsilon_A + \varepsilon_B}{2} \pm \sqrt{\frac{\varepsilon_A - \varepsilon_B}{2} + \lambda^2} . \tag{6.17}$$

The symmetry about $(\varepsilon_A + \varepsilon_B)/2$ simply reflects the particle-hole symmetry already discussed.

Uncompensated lattices and "localized" modes States of a *peculiar* nature should appear when the number of sites in each sublattice is different. Without any loss of generality we take $N_A > N_B$. Since the block h_{AB} in (6.14) is a linear application from a vector space having $\dim(A) = N_A$, onto a vector space B with $\dim(B) = N_B$, it follows from basic linear algebra that

- $\mathrm{rank}(h_{AB}) = \mathrm{rank}(h_{AB}^\dagger) = N_B$;

[7] It can be any bipartite lattice like the square or honeycomb lattices in 2D, etc.

- $h_{AB}\,\varphi_B = 0$ has no solutions other than the trivial one;
- $h_{AB}^\dagger\,\varphi_A = 0$ has non-trivial solutions that we call φ_A^0. From the rank-nullity theorem,

$$\text{rank}(h_{AB}^\dagger) + \text{nullity}(h_{AB}^\dagger) = N_A\,, \tag{6.18}$$

and hence the null space of $h_{AB}^\dagger$ has dimension: $\text{nullity}(h_{AB}^\dagger) = N_A - N_B$.

Consequently, there are states of the form $|\Psi^0\rangle = (\varphi_A^0, 0)$, in which φ_A^0 satisfies $h_{AB}^\dagger\,\varphi_A^0 = 0$, that are eigenstates of $\mathcal{H}$ with eigenvalue ε_A:

$$\mathcal{H}|\Psi^0\rangle = E|\Psi\rangle \mapsto \begin{cases} h\,0 = (\varepsilon_A - \varepsilon_A)\varphi_A \\ h^\dagger\,\varphi_A^0 = (\varepsilon_A - \varepsilon_B)0 \end{cases}\,. \tag{6.19}$$

Furthermore, since $\text{nullity}(h_{AB}^\dagger) = N_A - N_B$ implies the existence of $N_A - N_B$ linearly independent φ_A^0, this eigenstate has a degeneracy of $N_A - N_B$. It should be noticed that a state of the form $(\varphi_A, 0)$ has only amplitude in the A sublattice. Therefore, we conclude that, whenever the two sublattices are not balanced with respect to their number of atoms, there will appear $N_A - N_B$ states with energy E_A, all linearly independent and localized only on the *majority* sublattice. In addition, we can do whatever we fancy to the sublattice B (remove more sites, for instance) that these topologically localized states will remain totally undisturbed.

It is important to notice that in the above the details of the hopping matrix h_{AB} where not specified and need not be. The result holds in general, provided that the hopping induces transitions between different sublattice only, and that the diagonal energies are constant (diagonal disorder is excluded).

Zero modes The case with $\varepsilon_A = \varepsilon_B = 0$ is of obvious relevance for us, since our model for pristine graphene does not include any local potentials. In this situation, the above results imply that introducing a vacancy in an otherwise perfect lattice, immediately creates a zero energy mode. Now this is important because those states are created precisely at the Fermi level, and have this peculiar topological localization determining that they should live in just one of the lattices.

Even more interestingly, it is possible to obtain the exact analytical wavefunction associated with the zero mode induced by a single vacancy in a honeycomb lattice. This was done by the author and collaborators in [**VITOR M. PEREIRA**et al., 2006], and will not be developed here. We only mention that the wavefunction can be constructed by an appropriate matching of the zero modes of two semi-infinite and complementary ribbons of graphene[8], and that, in the continuum limit the wavefunction has the form [**VITOR M. PEREIRA**et al., 2006]

$$\begin{aligned} \Psi^{(L)}(x,y) &\sim \int_{2\pi/3}^{4\pi/3} dk\,(-2\cos(k/2))^{2x/3}\,e^{iky/\sqrt{3}} \\ &\approx \frac{e^{(4\pi iy)/(3\sqrt{3})}}{x+iy} + \frac{e^{2\pi i(x+y/\sqrt{3})/3}}{x-iy}\,. \end{aligned} \tag{6.20}$$

[8]It is known that graphene ribbons with zig-zag edges (like a zig-zag nanotube, Fig. 6.1a, but with a macroscopic radius) also support edge states with zero energy. See [**VITOR M. PEREIRA**et al., 2006] and references therein.

The important point is that the amplitude of this state decays with the distance to the vacancy as $\sim 1/r$, and thus has a quasi-localized character, although not-normalizable. Once again, we underline that this localized state appears at the Fermi level.

If another vacancy is introduced in the same sublattice, we already know that another zero mode will appear. However, the nature of the two zero modes will depend whether the vacancies are close or distant. In the latter case, the hybridization between the two modes should be small on account of the $1/r$ decay, and we can expect two states of the form (6.20) about each vacancy site. Of course significant effects in the thermodynamic limit can only arise with a finite concentration of vacancies, and for such analysis we undertook the numerical calculations described next.

6.3.2.2. Numerical Results

Single Vacancy The first calculation coming to mind is the numerical verification of the exact analytical result for the localized state in (6.20). For that, we consider the tight-binding Hamiltonian (6.1) and calculate numerically the exact spectrum and eigenstates in the presence of a single vacancy. For some typical results we turn our attention to Fig. 6.5. There we are plotting a real-space representation of some selected wavefunctions. This has been done by drawing a circle at each lattice site, whose radius is proportional to the wavefunction amplitude at that site, and whose color (red/blue) reflects the sign (+/-) of the amplitude at each site. Thus bigger circles mean higher amplitudes. In the first panel, (a), we are showing the eigenstate with lowest, yet non-zero, absolute energy. It is visible that the wavefunction associated with such state spreads uniformly across the totality of the system. In the second panel, (b), we draw the wavefunction of the state $E = 0$, that corresponds to (6.20). The state is clearly decaying as the distance to the central vacancy increases. In addition, the state exhibits the full C_3 point symmetry about the vacant site, just as expected. This picture provides a snapshot of the lattice version of (6.20). Since only one vacancy was introduced, the state shown in 6.5b is the only zero mode present.

When particle-hole symmetry is disturbed by a non-zero t', we still find states having this quasi-localized nature, although the wavefunction amplitude is not so concentrated about the vacancy. Two examples are shown in panels (b) and (c). They are two eigenstates with neighboring energy calculated for the same system. An important difference occurs here, in that, unlike the case $t' = 0$ where only one localized state appears, the particle-hole asymmetric case opens the possibility for more than one of such states.

This fact can be seen perhaps more transparently through the Inverse Participation Ratio (IPR) of the eigenstates. With such purpose in mind, the IPR (4.48)

$$\mathcal{P}(E_n) = \sum_i |\Psi_n(r_i)|^4$$

was calculated across the band in both the $t' = 0$ and $t' \neq 0$ cases, with a single central vacancy. Typical results are shown in Fig. 6.6. From 6.6a we do confirm that, when $t' = 0$, the presence of a vacancy introduces a localized state at $E = 0$, which is reflected both by the enhanced IPR there, and by the sharply peaked LDOS calculated at the vicinity of the vacancy site. Although not shown in this figure, the amplitude of the peak in the LDOS at $E = 0$, $\rho_i(0)$, decays as the distance between $\vec{R}_i$ and the

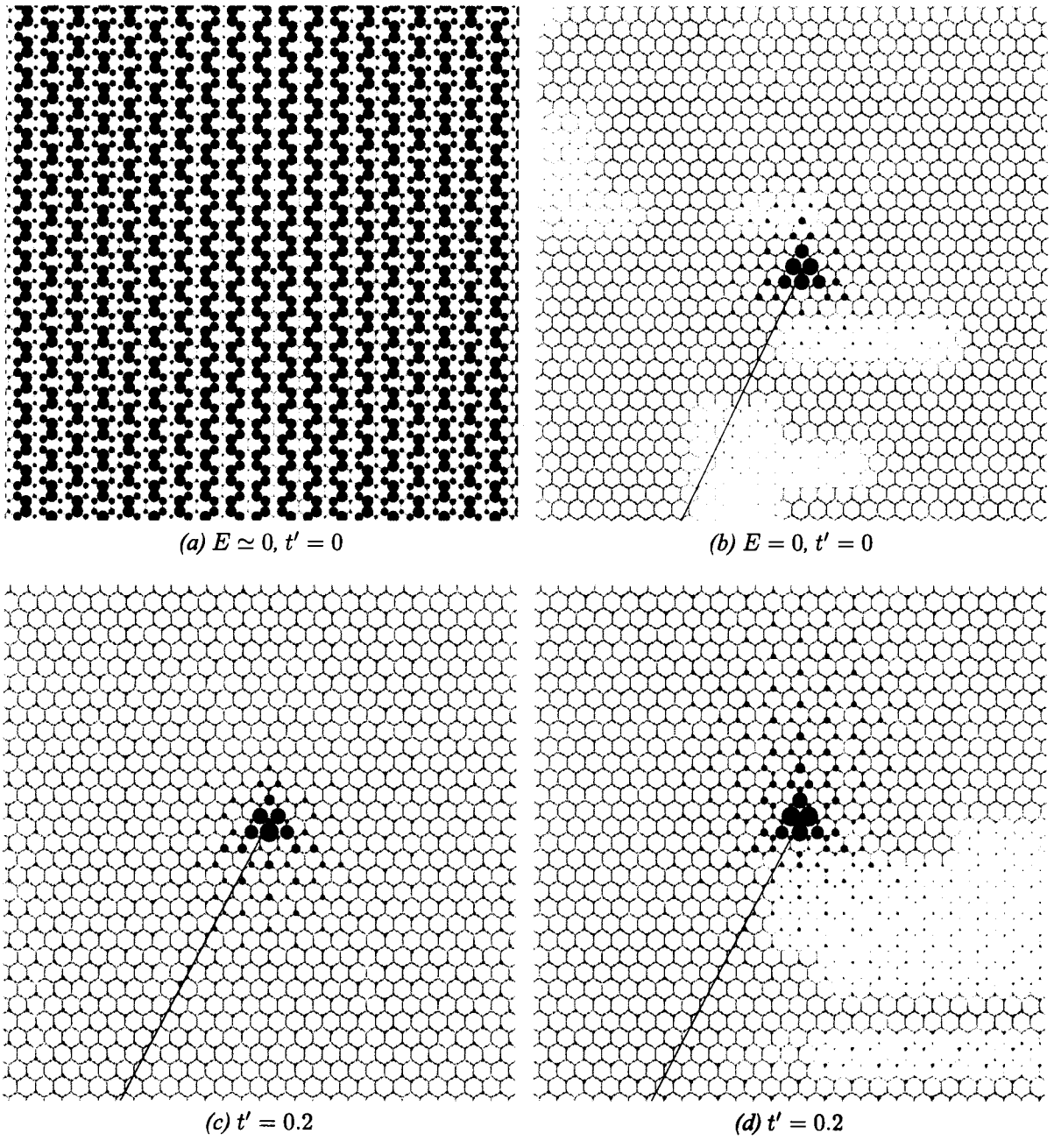

FIGURE 6.5.: *Selected eigenstates in a graphene sheet with* 80^2 *atoms containing a single impurity at the center (black dot). Only the region near the vacancy is shown. (a) The eigenstate with energy closest, but different, to zero.. (b) The eigenstate with* $E = 0$. *(c) and (d) show the presence of two quasi-localized eigenstates even with* $t' \neq 0$.

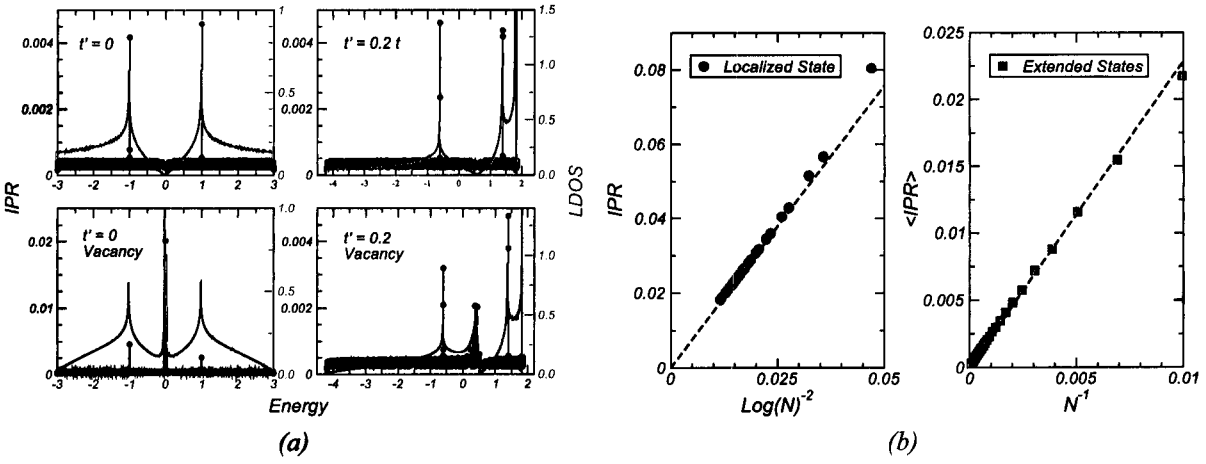

FIGURE 6.6 .: *IPR and LDOS calculated at one site closest to the vacancy. In panel (a), we have results for the IPR with $t' = 0$ and $t' \neq 0$ without any vacancy (top row), and with a single vacancy (bottom) for comparison. In panel (b) we show the dependence of the IPR of the zero mode, $\mathcal{P}(E = 0)$, with the system size N (left), and also $\langle \mathcal{P}(E) \rangle$ versus N for the remainder states (right). Dashed lines are simply guides for the eye.*

vacancy increases, in total consistence with the analytical picture. When next-nearest neighbor hopping is included, we also confirm the appearance of states with a considerably enhanced IPR. Not only that, but, instead of one, we do observe a couple of states with IPR much larger than the average for the remainder of the band. The LDOS is also enhanced near these energies, although now the effect appears more like a resonance in contrast with the sharp peak in the previous, particle-hole symmetric, case.

A more definite and quantitative analysis is provided by the results in the subsequent panel (Fig. 6.6b). Here we present the dependence of $\mathcal{P}(E)$ on the system size, N. As discussed in previous sections, the IPR for extended states should scale as

$$\mathcal{P}(E) \sim \frac{1}{N} . \tag{6.21}$$

But, for the zero mode, we face an interesting circumstance[9]. Remember that the wavefunction (6.20) is not normalizable. So, strictly speaking, the state is not localized, and hence the designation *quasi-localized* that we have adopted above. The consequence of this is that the normalization constant for $\Psi(x, y)$ depends on the system size:

$$\sum_{i}^{N} |\Psi(x, y)|^2 \sim \log(\sqrt{N}) \sim \log(N) . \tag{6.22}$$

This, in turn has an effect on the IPR because $\mathcal{P}(E)$ is defined in terms of normalized wavefunctions:

$$\mathcal{P}(0) = \frac{1}{\log(N)^2} \sum_{i}^{N} |\Psi(x, y)|^4 \sim \frac{1}{\log(N)^2} . \tag{6.23}$$

This scaling of the IPR with N is precisely the one obtained numerically in Fig. 6.6b (left) for the zero mode, and is just another way of confirming the $1/r$ decay of this wavefunction.

[9]It should be obvious that when the term *zero mode* is employed, we are referring to the case with $t' = 0$.

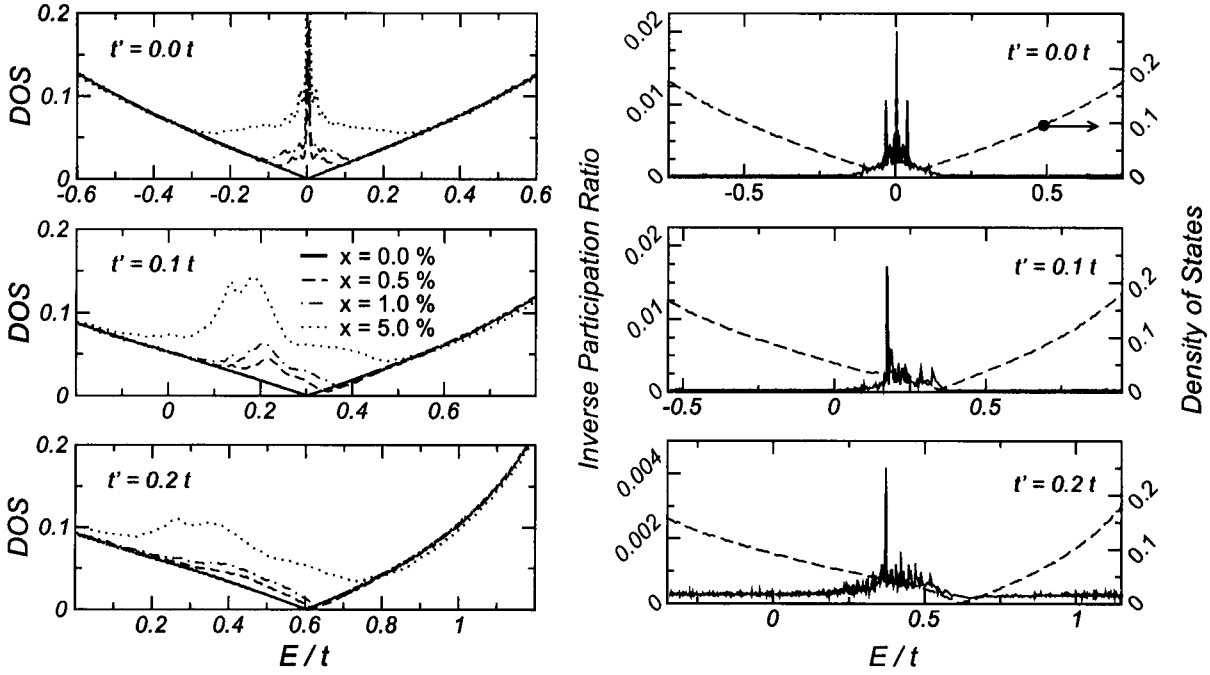

(a) DOS (b) IPR with $x = 0.5\,\%$

FIGURE 6.7.: *IPR and DOS for the diluted honeycomb lattice. The concentration of vacancies is x, and only the vicinity of the Fermi level is shown. (a) DOS for selected concentrations, x, and different values of t'. (b) IPR for selected values of t' using a concentration $x = 0.5\,\%$. For comparison, the corresponding DOS is also plotted in each case.*

Finite Concentration of Vacancies Unlike the single vacancy case, the dilution of the honeycomb via the introduction of a finite concentration of vacancies is not solvable using the analytical expedients employed in [VITOR M. PEREIRAet al., 2006], and numerical calculations become essential in this case. Our procedure consists in diluting the honeycomb lattice with a constant concentration of vacancies, which we call x. The diluted sites are chosen at random and the global DOS, averaged over several vacancy configurations, is calculated afterwards. This is clearly a disordered problem, and we employ the recursive method allowing us to obtain the DOS for systems with 2000^2 sites[10]. Some results are summarized in Fig. 6.7.

One of the effects of this disorder is, as always occurs, the softening of the van-Hove singularities (not shown). But the most significant changes occur in the vicinity of the Fermi level (Fig. 6.7a). In the presence of electron-hole symmetry ($t' = 0$), the inclusion of vacancies brings an increase of spectral weight to the surroundings of the Dirac point, leading to a DOS whose behavior for $E \approx 0$ mostly resembles the results obtained elsewhere within Coherent Potential Approximation (CPA) [Peres et al., 2005]. Indeed, for higher dilutions, there is a flattening of the DOS around the center of the band just as in CPA. The most important feature, however, is the emergence of a sharp peak at the Fermi level, superimposed upon the flat portion of the DOS (apart from the peak, the DOS flattens out in this neighborhood as x is increased past the 5 % shown here). The breaking of the particle-hole symmetry by a finite t' results in the broadening of the peak at the Fermi energy, and the displacement of its position by

[10]We remark that such number of atoms is already of the same order of magnitude of the number of atoms in real nanoscopic samples of graphene studied experimentally.

an amount of the order of t'. All these effects take place close to the the Fermi energy. At higher energies, the only deviations from the DOS of a clean system are the softening of the van Hove singularities and the development of Lifshitz tails (not shown either) at the band edge, both induced by the increasing disorder caused by the random dilution. The onset of this high energy regime, where the profile of the DOS is essentially unperturbed by the presence of vacancies, is determined by $\epsilon \approx v_F/l$, $l \sim n_{\rm imp}^{-1/2}$ being essentially the average distance between impurities.

To address the degree of localization for the states near the Fermi level, the IPR was calculated again, via exact diagonalization on smaller systems. Results for different values of t' are shown in Fig. 6.7b for random dilution at 0.5 %. One observes, first, that $\mathcal{P}_m \sim 3/N$ for all energies but the Fermi level neighborhood, as expected for states extended up to the length scale of the system sizes used in the numerics. Secondly, the IPR becomes significant exactly in the same energy range where the DOS exhibits the vacancy-induced anomalies discussed above. Clearly, the farther the system is driven from the particle-hole symmetric case, the weaker the localization effect, as illustrated by the results obtained with $t' = 0.2\,t$. To this respect, it is worth mentioning that the magnitude of the strongest peaks in $\mathcal{P}_m$ at $t' = 0$ and $t' = 0.1\,t$ is equal to the magnitude of the IPR calculated above for a single impurity problem. Such behavior indicates the existence of quasi-localized states at the center of the resonance, induced by the presence of the vacancies. For higher doping strengths, the enhancement of $\mathcal{P}_m$ is weaker in the regions where the DOS becomes flat. This explains the qualitative agreement between our results and the ones obtained within CPA in that region, since CPA does not account for localization effects.

In summary, before we abandon this section, we saw that a single vacancy introduces a quasi-localized zero mode. Its presence is ensured by the uncompensation between the number of orbitals in the two sublattices, and a theorem from linear algebra. The presence of this mode translates in the appearance of a peak in the LDOS near the vacancy, and in an enhanced IPR for this state. When we go from one to a macroscopic number of vacancies, we saw that both the peak and the enhancement of the IPR persists at E_F.

6.3.3. Selective Dilution

It is important to recall that the results of the previous section pertain to lattices that were randomly diluted. During such process, we expect that the number of vacancies in sublattice A will be equal to the number of vacancies in sublattice B, on average. Strictly speaking, since our original lattices are always chosen with $N_A = N_B$, the fluctuations on the degree of uncompensation, $N_A - N_B$, should scale as $1/\sqrt{N}$ thus vanishing in the thermodynamic limit. Because of this, in principle, we would expect the lattices used above to be reasonably compensated. But the theorem in (§ 6.3.2.1) only guarantees the presence of zero modes when the lattice is uncompensated. It turns out that, notwithstanding our utilization of rather large system sizes, such $\sqrt{N}$ fluctuations are still significant and the lattices were indeed slightly uncompensated.

This clearly begs the clarification of the origin of the zero modes in the cases with finite densities of vacancies. Do they appear only through these fluctuations in the degree of sublattice compensation, or can we have zero modes even with full compensation? To try to elucidate this we developed a controlled approach to this issue, as follows. From now on we consider only the particle-hole symmetric situation

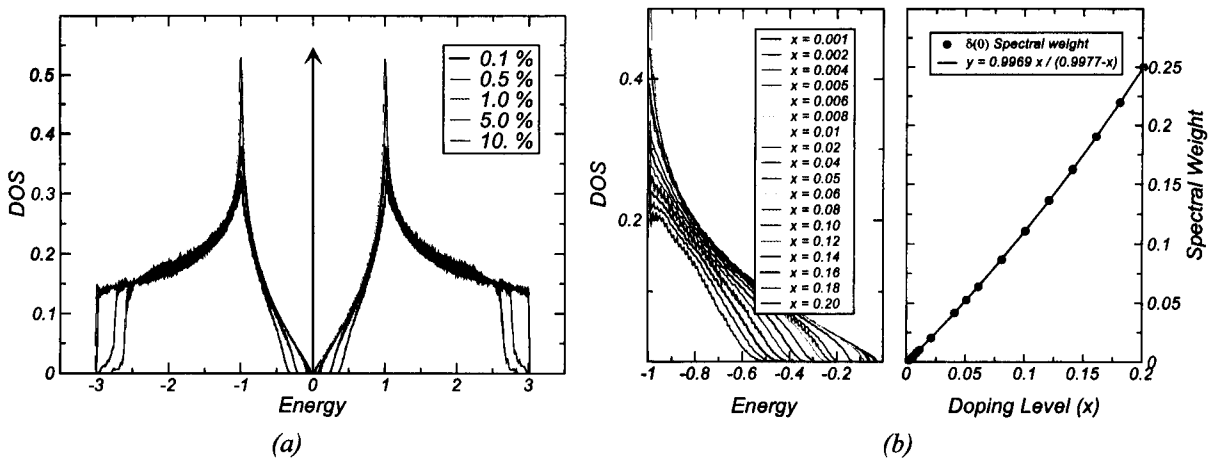

FIGURE 6.8.: *Dilution of just one sublattice of the honeycomb. (a) DOS for different dilution strengths, diluting only sublattice A. (b) On the left we show a detail of the DOS and the evolution of the gap with vacancy concentrations. On the right we plot the dependence of the missing spectral weight ($= 1 - w_\delta$) with x (circles). The continuous line is a least squares fit using $f(x) = ax/(b - x)$ to the data represented by the circles.*

($t' = 0$).

Complete uncompensation The first thing to do is to dilute selectively just one of the sublattices (sublattice B for definiteness). Accordingly, we have studied the DOS for systems in which one of the sublattices was randomly diluted, with a finite concentration of vacancies. In this case there is no other chance for the system than having precisely a number of zero modes that equals the number of vacancies. Starting from a clean lattice with $N = N_A + N_B$ sites, the latter corresponds to $N_v = Nx$. We should thus expect a $\delta(0)$ peak contributing to the global DOS, with an associated spectral weight, w_δ that coincides with the fraction of zero modes:

$$w_\delta = \frac{Nx}{N(1-x)} = \frac{x}{1-x}\,. \tag{6.24}$$

Since the total spectral weight is normalized to 1, the spectral weight at $E = 0$ has to come from somewhere else in the band. In Fig. 6.8 we expose what is happening. In panel (a) the results for the DOS are rather explicit. The selective dilution promotes the appearance of a gap in the DOS, whose magnitude increases with the amount of dilution. At the center of the gap we can only see an enormous peak (not visible in the range used) staying precisely at $E = 0$, corroborating our expectations regarding the Dirac-delta in the DOS. But since it appears exactly at $E = 0$, we cannot resolve numerically its associated spectral weight. To obtain such spectral weight we calculated the spectral weight loss in the remainder of the band. In other words, since, by definition, our recursive method always yields a DOS normalized to unity, we calculated the spectral weight of the band shown in the picture, and subtracted it from unity. The result and its variation with x is displayed in the right-most frame of Fig. 6.8b. A non-linear fit to the data reveals that the dependence expected from (6.24) is indeed verified.

In the context of the selective dilution, the surprise comes certainly not from this, but from the areas involved in the transfer of spectral weight. As Fig. 6.8 documents, the spectral weight is transferred

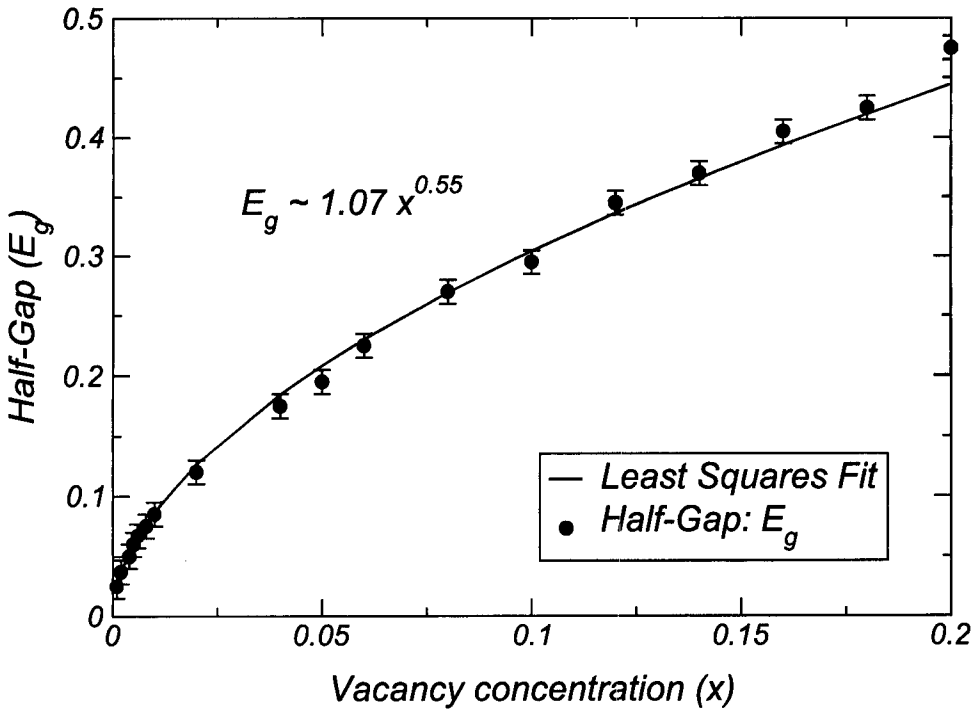

FIGURE 6.9.: *The gap estimated from the numerical curves in Fig. 6.8 is plotted against the vacancy concentration, x. The continuous line is a least squares fit to $f(x) = ax^b$.*

almost entirely from the low energy region near E_F and from the high energy regions at the band edges. This depletion near $E = 0$ introduces the gap, $2E_g$. A gap implies the existence of a new energy scale in the problem. Since the hopping t is the only energy scale in the Hamiltonian, such new scale has to come from the concentration of vacancies. By dimensional analysis, such scale is dictated essentially by the average distance between vacancies (l)

$$\epsilon \sim \frac{v_F}{l} \sim n_{\text{vacancies}}^{1/2} \sim \sqrt{x} \qquad (\hbar = 1)\,. \tag{6.25}$$

When the the magnitude of the gap found numerically is plotted against x we arrive at the curve of Fig. 6.9. The least squares fit shown superimposed onto the numerical circles leaves little doubt as to the validity of the above assumption regarding the energy scale associated with the gap. With this we arrive at a quite interesting situation, of having a half-filled, particle-hole symmetric and gapped system, with a finite concentration of (presumably quasi-localized) zero modes at the mid-gap point.

Controlled uncompensation Instead of this extreme selective dilution, we now turn to a more controlled approach to the dilution and uncompensation. For that we need to introduce an additional parameter, η that will measure the degree of uncompensation. As before, we want to study finite concentrations of vacancies. This is determined by x in such a way that the number of vacancies in a lattice

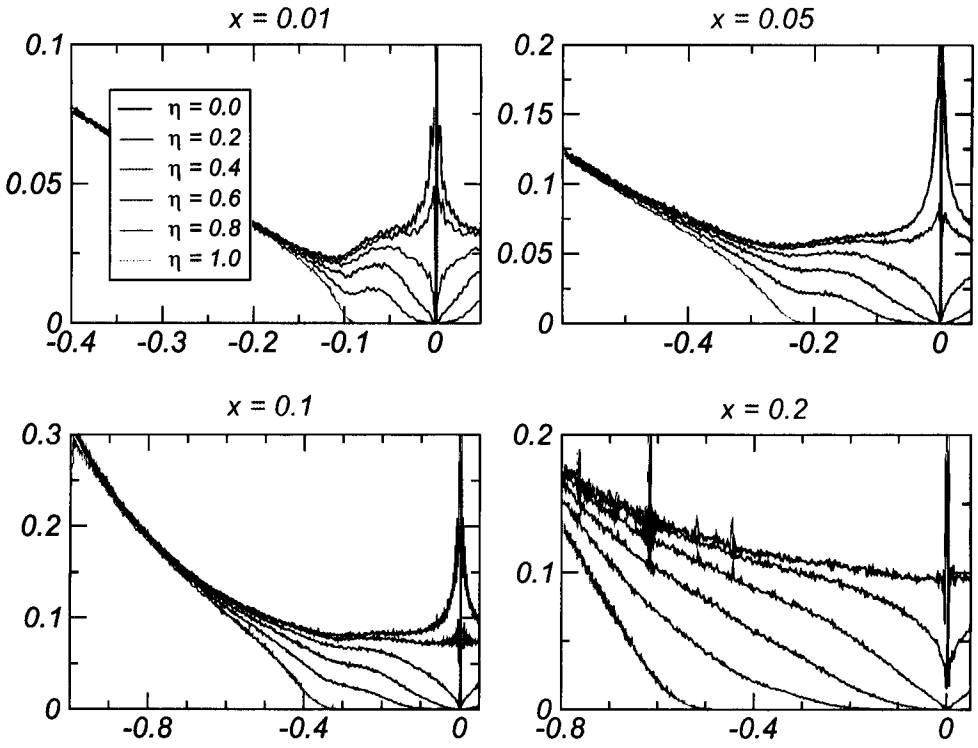

FIGURE 6.10 .: *DOS for the honeycomb lattice using the controlled selective dilution discussed in the text, calculated for different concentrations of vacancies, x, and several degrees of uncompensation, η. Only the low energy region id shown.*

with N sites will be $N_v = Nx$. But now, the number of vacancies in each sublattice is determined by

$$N_v^A = \frac{1}{2}Nx(1+\eta)$$
$$N_v^B = \frac{1}{2}Nx(1-\eta)\,, \tag{6.26}$$

with $0 \leq \eta \leq 1$. Therefore, the parameter η permits an interpolation between completely uncompensated dilution ($\eta = 1$), and totally compensated dilution ($\eta = 0$). Let us look directly at the results for the DOS, calculated at different x and η, and plotted in Fig. 6.10. At any concentration x the following sequence of events unfolds as η decreases from 1 to 0: (i) There is a perfectly defined gap in the limit $\eta = 1.0$ discussed above; (ii) for $\eta \lesssim 1$ a small hump develops at the same energy scale of the previous gap; (iii) although the gap seems to disappear, it is clearly visible that when $\eta \lesssim 1$, the DOS decays to zero after the hump and is zero at $E = 0$; (iv) decreasing further η towards complete compensation (say, for $\eta = 0.6,\ 0.4$), this behavior persists, being visible that the DOS drops to zero at $E = 0$; (v) closer to full compensation ($\eta = 0.1$) the DOS seems to display an upward inflection near $E = 0$, and apparently does not drop to zero. Unfortunately, we are unable to resolve this region numerically with the desired accuracy. For instance, at higher dilutions $x = 0.2$ we can still see the curve of $\eta = 0.2$ dropping to zero near $E = 0$.

Naturally that, for all the cases with $\eta \neq 0$, the existence of $N_v^A - N_v^B$ zero modes is guaranteed. As before, we inspected this by calculating the missing spectral weight in the bands, and confirmed that it does agree with the fraction of uncompensated vacancies. Hence, the picture emerging from these results

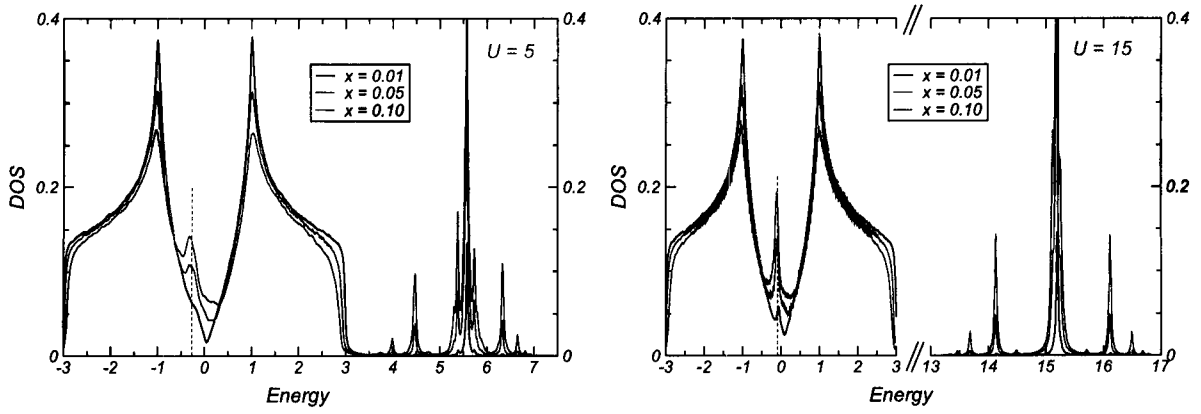

FIGURE 6.11 .: *DOS of the honeycomb lattice with local impurities modeled by the Hamiltonian* (6.27)*, using* $U = 5t$ *(a) and* $U = 15t$ *(b). In both cases, impurity concentrations of* $x = 0.01$, 0.05 *and* 0.1 *where used. Notice that in panel (b) the horizontal axis has been truncated.*

seems to suggest that, although the gap disappears for $\eta < 1$, the DOS still drops to zero at $E = 0$, and might drop in a singular way as η approaches zero. If we separate the contributions of the zero modes to the global DOS from the contribution of the other states, the consequence of this would be that, in a compensated lattice ($\eta = 0$), the DOS associated with the other states would seem to diverge as $E \to 0$, but would be zero precisely at $E = 0$. Stated in another way, coming from high energies, we would see a decreasing DOS up to some typical energy $\epsilon \sim \sqrt{x}$, at which point it would turn upwards. At very small energies the DOS would seem to be diverging but, at some point arbitrarily close to $E = 0$, it would drop precipitously down to zero.

Unfortunately the numerical calculations are not so accurate as to allow the confirmation or dismissal of such possibility. In fact, the peaks for $\eta = 0.0$ are of the same magnitude of the ones found when the dilution is completely random across the two sublattices (Fig. 6.7a). So, although the evidence is compelling towards the affirmative, these results are still inconclusive as to whether the zero modes disappear in a perfectly compensated diluted lattice or not.

6.3.4. Local Impurities

Vacancies are local scatterers in the unitary limit. A vacancy can be thought as an extreme case of a local potential, U, when $U \to \infty$. In this context we investigated the intermediate case characterized by a finite local potential. The Hamiltonian in this case changes from (6.1) to

$$H = U \sum_p c_p^\dagger c_p - t \sum_{\langle i,j \rangle} c_i^\dagger c_j - t' \sum_{\langle\langle i,j \rangle\rangle} c_i^\dagger c_j + \text{h.c.} \ , \tag{6.27}$$

where U is the local potential at the impurity sites p. The concentration of impurities, x, is kept constant, and their positions, p, are selected at random. The influence of the potential term in (6.27) on the electronic structure can be inspected through the changes it induces upon the DOS. Numerical results are plotted in Fig. 6.11. The presence of the local term clearly destroys the particle-hole symmetry, leading

to the asymmetric curves in the figure. We only analyzed moderate to high potentials ($5t < U < 30t$), and in the domain considered, we always witness the development of a narrow impurity band beyond the original band edge, and centered at $E \sim U$. The impurity band has an interesting splitted structure as can be seen in both panels of Fig. 6.11. Sure enough, the existence of this band is totally expected, and not particularly remarkable.

What is remarkable in these results is the emergence of a low energy resonance induced by the presence of the local impurities. Such resonances are signaled by the considerable enhancement in the DOS near the Dirac point. A couple of interesting details characterizes these resonances:

- At the strongest U's' a clearly defined peak develops on the top of the finite background;
- The resonances are sensitive to both U and x;
- For a given concentration x, the energy corresponding to the maximum of the resonance, ϵ_{res}, shifts towards the Dirac point as U is increased. Additionally, it follows from the numerical data on the range of U studied that $\epsilon_{\text{res}} \sim 1/U$, although a systematic analysis was not actually carried on.
- U and ϵ_{res} have opposite signs. The resonance thus appears at negative energies whereas the impurity band is at high and positive energies.
- The two plots clearly show how the vacancy case can be obtained as a limiting procedure of taking U to infinity.
- When U is kept constant and the concentration is changed, the maximum of the resonance seems to be slightly displaced away from the Dirac point.

Physically the model summarized in the Hamiltonian of eq. (6.27) could describe the situation in which some of the carbon atoms are substituted by a different species. Another realistic circumstance has to do with the fact that a real graphene sheet is expected to have some molecules from the environment adsorbed onto its surface. Consequently, even if the honeycomb lattice of the carbon atoms is not disrupted with foreign atoms, the presence of adsorbed particles can certainly induce a local potential at the sites where they touch the carbon lattice.

As a final remark, we mention that the experimental $I - V$ curves measured by Matsui et al. [2005] in HOPG, namely Fig. 5 of the cited reference, have a striking resemblance with the resonances seen in our numerical curves.

6.3.5. Non-Diagonal Impurities

Another effect expected with the inclusion of a substitutional impurity in the graphene lattice is the modification of the hoppings between the new atom and the neighboring carbons. This happens because the host and substituting atoms have different radii, because the nature of the orbitals involved in the conduction band is different, or, most likely, a combination of both. Customary impurities in carbon allotropes are nitrogen, working as a donor, and boron, working as an acceptor [Kaiser and Bond, 1959]. In fact, the selective inclusion of nitrogen and/or boron impurities in carbon nanotubes is a current practice in the hope to tune the nanotubes' electronic response [Nevidomskyy et al., 2003; Stephan et al., 1994].

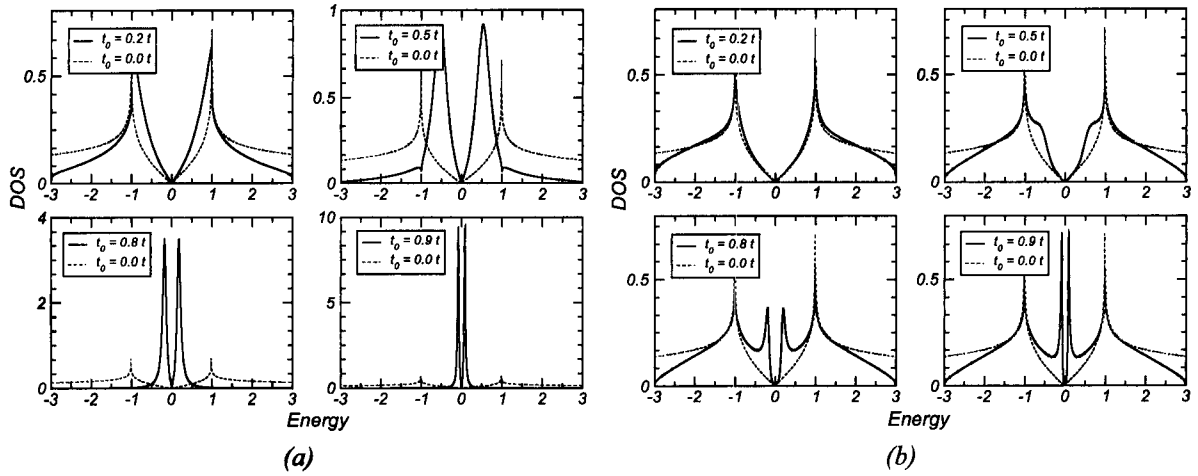

FIGURE 6.12 .: *Effect of a single substitutional impurity in the LDOS. In panel (a) we plot the LDOS calculated at the site of the impurity for the four different values of* t_0 *indicated in each frame. In (b) the situation is identical but the LDOS is calculated at the nearest neighboring site of the impurity.*

In general the study of a perturbation in the hopping is much less studied in problems with impurities than the case of diagonal, on-site, perturbations. In the context of our investigations, the perturbation in the hopping can, again, be interpreted as an interpolation between a vacancy and an impurity. To be more precise, let us introduce the relevant Hamiltonian:

$$H = -t \sum_{i,\delta} c_i^\dagger c_{i+\delta} + t_0 \sum_{p,\delta}{}' c_p^\dagger c_{p+\delta} + \text{h.c.}\,. \tag{6.28}$$

In this case, only nearest neighbor hopping is considered. Without the second term, H above is the Hamiltonian for pure graphene. The last sum is restricted to the impurity sites, p, and t_0 represents a perturbation in the hopping amplitude to its neighbors. Is plain to see that, when $t_0 = t$, all the impurity sites turn into vacancies since the hopping thereto is zero. As a result of that, this model provides another type of interpolation between pure graphene and diluted graphene. An important difference is that this model can be disordered when the impurities are placed at random, without breaking particle-hole symmetry, and, in this sense, is qualitatively much different from the case of local disorder discussed in the preceding section.

Figure 6.12 contains some typical results for the local DOS near the impurity, and at the impurity site itself. Irrespective of whether the LDOS is calculated at or near the impurity, the resulting curves display a strong resonance close to the Dirac point. As t_0 increases from zero, two simultaneous modifications in these resonances take place. The first is that they are clearly enhanced as t_0 approaches t. The second is its shift in the direction of the Dirac point, in such a way that, when $t_0 = 0.9t$, the peak is already very close to $E = 0$. With regard to this last point, we systematically investigated the variation of the peak position in the LDOS at the impurity site with the value of t_0. This dependence, which can be seen in Fig. 6.13, is approximately linear and, for $t_0 \gtrsim 0.6$, is reasonably well approximated by the linear function $\epsilon_{\max} \simeq t - t_0$.

When we go from one impurity to a finite density of impurities, x, we obtain a measurable influence in

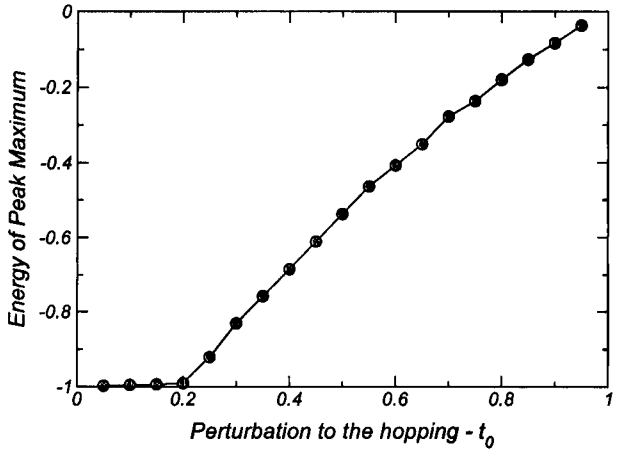

FIGURE 6.13 .: *Variation of the energy corresponding to the peak in the LDOS with the magnitude of* t_0. *The LDOS in question is the LDOS calculated at the impurity site.*

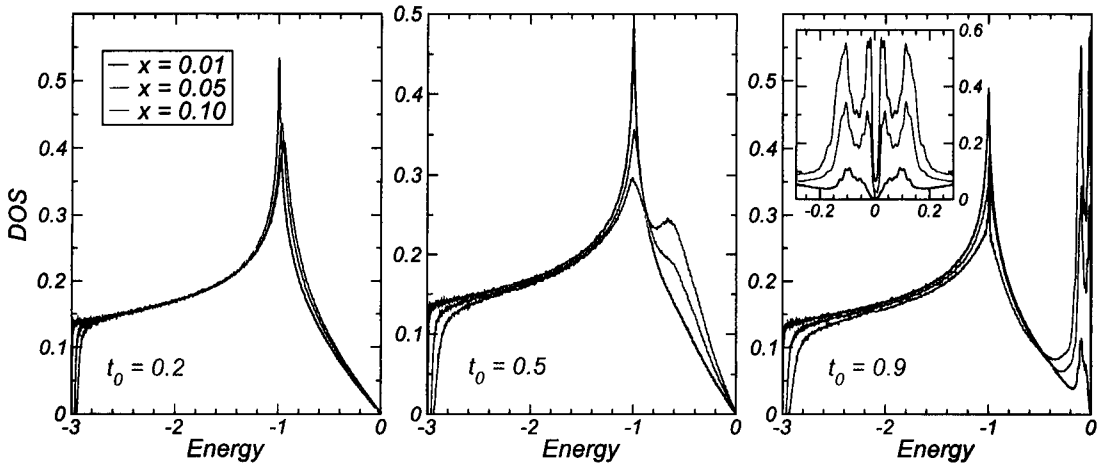

FIGURE 6.14 .: *The DOS corresponding to the model Hamiltonian* (6.28), *with a finite density of impurities. The three panels correspond to different values of the perturbing hopping* ($t_0 = 0.2$, 0.5 *and* 0.9), *and within each panel the three curves were obtained at different concentrations* ($x = 0.01$, 0.05 *and* 0.1). *The inset of the last panel is a magnification of the region near* $E = 0$.

the thermodynamic limit. Our method in this case, consists in placing impurities at random positions in the lattice, keeping their concentration constant. The global DOS, averaged over several realizations of disorder, is presented in Fig. 6.14. For intermediate values of t_0, the perturbation in the hopping induces a resonance appearing at roughly the same energies as the ones found in Fig. 6.13. The resonance is enhanced at higher concentrations of impurities, and becomes more sharply defined as $t_0 \rightarrow t$.

Before closing, just a comment on the physical origin of this perturbation. In effect, the presence of a substitutional impurity like N or B will introduce, simultaneously, a perturbation in the hopping, and in the local energy. However, it is more or less clear from the discussions in the previous section that the resonances near E_F occur when the local potential, U, is moderate or high, which is not the case for boron or nitrogen substituents. Hence, the perturbation in the hopping could perhaps be more significant in dictating the changes in the low-energy electronic structure.

6.4. Implications for real systems

The field of graphene is still in its childhood. Although the experimental progress obtained so far is remarkable, much is hoped for the future. The disorder effects considered and analyzed in this chapter, can have a direct influence in many important properties seeked in novel magneto-electronic devices based on graphene.

In particular, we have confirmed that the presence of vacancies introduces striking changes in the DOS at the Fermi level. The sharp peak developing at $E = 0$ can have decisive consequences for the magnetism found in proton irradiated HOPG, since the moment formation can be associated with the development of this feature in the DOS. In fact, in the context of the Random Phase Approximation (RPA) for itinerant magnetism, the magnetic susceptibility of the electron gas has the form

$$\chi(\vec{q},\omega) = \frac{\chi_0(\vec{q},\omega)}{1 - I\chi_0(\vec{q},\omega)}\,, \tag{6.29}$$

where $\chi_0(\vec{q},\omega)$ is the unperturbed particle-hole propagator giving the free electron spin susceptibility, and I is the intra-atomic (Hubbard) Coulomb integral. An instability in $\chi(\vec{q},0)$ reflects an instability in the paramagnetic ground state [Doniach and Sondheimer, 1999] and, from the above, the condition for such instability is simply $I\chi_0(\vec{q},\omega) = 1$. For the case of ferromagnetism we are interested in the $\vec{q} \to 0$ limit of this condition. It can be shown that $\chi_0(\vec{q},\omega)$ (the Pauli spin susceptibility) is simply the density of states at the Fermi energy. Thus the condition for the FM instability translates into

$$I\rho(E_F) = 1\,. \tag{6.30}$$

This provides the well known Stoner criterion for ferromagnetism: if $I\rho(E_F) > 1$ the ground state is ferromagnetic, and paramagnetic otherwise [Yosida, 1996]. Our results clearly show, either a Dirac-delta or a sharp peak in the DOS at E_F. Therefore, the condition $I\rho(E_F) > 1$ can be met even for an arbitrarily small I, which in turn implies an instability towards ferromagnetism in diluted graphene.

Although the problem of moment formation and its relation with the vacancy-induced localized states needs further investigation, this is a compelling and physically reasonable explanation for the vacancy induced ferromagnetism found in the experiments.

7. Conclusions

"There is a theory which states that if ever anyone discovers exactly what the Universe is for and why it is here, it will instantly disappear and be replaced by something even more bizarre and inexplicable.
There is another theory which states that this has already happened."

— **Douglas Adams**. The Restaurant at the End of the Universe [Adams, 1995].

Physics aims at no less than the understanding of nature. This is not a modest undertaking, especially when one considers the tortuous and continual nature of scientific inquiry, which Douglas Adams' quotation perfectly embodies. This act of understanding, for the physicist, means much more than observe, collect, classify and relate facts about nature. It means delving deep into the recesses of physical phenomena, in order to grab their essence, their irreducible elements, comprehend their workings and use such understanding to predict new phenomena. For the theoretically oriented physicist, nothing can be more rewarding than witnessing first hand a theory that describes a set of experiments related to his subject, a model that describes nature under a given set of circumstances.

For its physical significance, the core of this thesis is our DEM model for EuB_6 related hexaborides, which has already been summarized in § 4.4 (page 102). The DEM at extremely low densities provides a quite acceptable interpretation of the set of experimental peculiarities described in chapter 3, which include the electrical, magnetic and optical response of the hexaborides. When first published in late 2004 [**Vitor M. Pereira**et al., 2004a], this theory was received with some initial skepticism [Wigger et al., 2005], for it was an approach very different from the existing theoretical proposals. Under the DEM perspective, the physics of EuB_6 is essentially determined by the direct interplay between the electronic kinetic energy and magnetic disorder, with Anderson localization effects requiring consideration from the outset. Within roughly six months of publication, the magneto-optical measurements carried by L. Degiorgi and his collaborators for the Ca-doped family came to our knowledge. It was then clear that such data lent stronger support to our interpretation, and this ultimately led to the joint publication of those results in [Caimi et al., 2006].

From a purely theoretical point of view, this thesis hinges upon the DEM at low electronic densities. In such context, we were able to obtain important and insightful results into issues like the long standing problem of phase separation, the stability of free magnetic polarons, the details of the transition from the DE to the RKKY limit and, of course, the problem of Anderson localization and its influence in magneto-transport. Inevitably, the results obtained here introduced new questions. In the problem of phase separation, for instance, it would be rather interesting to see to which extent the suppression

of the phase separation bubble that we obtained is influenced by the geometry of the phase separated state. Likewise, the relation between the polaronic phase and the phase separated state when $\varepsilon_r \to 1$ would require a more careful analysis inasmuch as the classical, continuous approximation used for the electrostatic corrections in eq. (5.27) starts already to break down. This is certainly a hard problem, as is the possibility advanced in [**VITOR M. PEREIRA**et al., 2005] for the existence of a Wigner crystal of magnetic polarons at even more reduced densities, which we did not discuss herein.

With regards to the problem of Anderson localization, it would be most interesting to have the trajectory of the mobility edge when dilution disorder is added to the magnetic, non-diagonal, one. This is of direct relevance for quantitative results in the Ca-doped hexaborides. But things here are not so easy for the numerical methods currently used. The difficulty is related with the fact that, upon dilution, the problem turns essentially into quantum percolation, which, besides being the strongest type of electronic disorder, has its own peculiarities as far as localization is concerned [Kirkpatrick and Eggarter, 1972].

Our explorations in the context of the localization processes in the DEM, brought us to important results that seemingly apply to Anderson localization in general. They are the behavior of fluctuations in the LDOS and IPR, which indicate that an important quantitative role is played by the local electronic environment at the onset of the localization transition. As discussed, this deserves further attention, not only for the obvious relevance to such a long standing problem in condensed matter theory, but chiefly because more extensive numerical results are needed. One of the important things is certainly to discriminate whether those relative fluctuations exhibit scale invariance in a universal way at the transition or not[1].

In the last chapter we explored the role of disorder, in its several guises, upon the electronic structure of graphene. Our results could perhaps be seen as introductory to this problem, in the sense that so much is yet to be known about graphene and its physics. Notwithstanding, there are important aspects of some of our results that can have relevance for Dirac fermions in general, which applies, for instance, to some models of HTSC, and other correlated systems. Indeed, the discovery of the sharp peak associated with quasi-localized states at E_F (or the corresponding resonance in the particle-hole asymmetric case), is utterly meaningful and complementary to the seminal and influential studies carried by Peres et al. [2005] in disordered graphene. Another issue is the study of how disordered graphene behaves under magnetic fields, and what consequences it can bring to the QHE.

Finally, it is perhaps pertinent to mention the strong numerical component that pervades all these chapters, and the majority of the results therein. This has allowed the development of fairly reasonable programming skills by the author, especially at the level of optimization, and brought, as a consequent by-product, the mastery of different programming and scripting languages, among many other tools of the trade.

The paragraphs of this concluding chapter seem to stress more of what we would like to know, than what has been achieved. But this is a simple reflex of, arguably, the most important piece of knowledge that one might earn as a training physicist, or scientist in general: the most significant conclusion of a piece of work always comes in the form

"Humm... that's interesting. What if..."

[1] Unfortunately, this implies machines with considerably higher RAM capacity than the ones available during our work.

A. Relevant Publications by the Author

Below is the list of the publications by the author relevant in the context of this thesis, with the respective abstract.

G. Caimi, A. Perucchi, L. Degiorgi, H.R. Ott, V.M. Pereira, A.H. Castro-Neto, A.D. Bianchi, Z. Fisk.
MAGNETO-OPTICAL EVIDENCE OF DOUBLE EXCHANGE IN A PERCOLATING LATTICE.
Phys. Rev. Lett. 96, 016403 (2006).

> Substituting Eu by Ca in ferromagnetic EuB_6 leads to a percolation limited magnetic ordering. We present and discuss magneto-optical data of the $Eu_{1-x}Ca_xB_6$ series, based on measurements of the reflectivity $R(\omega)$ from the far infrared up to the ultraviolet, as a function of temperature and magnetic field. Via the Kramers-Kronig transformation of $R(\omega)$ we extract the complete absorption spectra of samples with different values of x. The change of the spectral weight in the Drude component by increasing the magnetic field agrees with a scenario based on the double-exchange model, and suggests a crossover from a ferromagnetic metal to a ferromagnetic Anderson insulator upon increasing Ca content at low temperatures.

Vitor M. Pereira, F. Guinea, J. M. B. Lopes dos Santos, N. M. R. Peres, A. H. Castro Neto.
DISORDER INDUCED LOCALIZED STATES IN GRAPHENE.
Phys. Rev. Lett. 96, 036801 (2006).

> We consider the electronic structure near vacancies in the half-filled honeycomb lattice. It is shown that vacancies induce the formation of localized states. When particle-hole symmetry is broken, localized states become resonances close to the Fermi level. We also study the problem of a finite density of vacancies, obtaining the electronic density of states, and discussing the issue of electronic localization in these systems. Our results have also relevance for the problem of disorder in d-wave superconductors.

Vitor M. Pereira, J. M. B. Lopes dos Santos, Eduardo V. Castro, A. H. Castro Neto.
DOUBLE EXCHANGE MODEL FOR MAGNETIC HEXABORIDES.
Phys. Rev. Lett. 93, 147202 (2004).

> A microscopic theory for rare-earth ferromagnetic hexaborides, such as $Eu_{1-x}Ca_xB_6$, is proposed on the basis of the double-exchange Hamiltonian In these systems, the reduced carrier concentrations place the Fermi level near the mobility edge, introduced in the spectral density by the disordered spin background. We show that the transport properties such as the Hall effect, magnetoresistance, frequency dependent conductivity, and dc resistivity can be quantitatively described within the model. We also make specific predictions for the behavior of the Curie temperature T_C as a function of the plasma frequency ω_p.

Vitor M. Pereira, J. M. B. Lopes dos Santos, A. H. Castro Neto.

THE DOUBLE EXCHANGE MODEL AT LOW DENSITIES.

Preprint: cond-mat/0505741 (2005)

We obtain the phase diagram of the double-exchange model at low electronic densities in the presence of electron-electron interactions. The single particle problem and its extension to low electronic densities, when a Wigner crystal of magnetic polarons is generated due to unscreened Coulomb interactions, is studied. It is argued that the Wigner crystal is the natural alternative to phase separation when this interaction is taken into account. We discuss the thermal and quantum stability of the crystalline phase towards a polaronic Fermi liquid and a homogeneous, metallic, ferromagnetic phase. The relevance and application of our results to EuB_6 is also considered.

S. Gu, Vitor M. Pereira, N. M. R. Peres.

SCALING STUDY OF THE METAL-INSULATOR TRANSITION IN ONE-DIMENSIONAL FERMION SYSTEMS.

Phys. Rev. B 66, 235108 (2002).

We consider the Ising phase of the antiferromagnetic XXZ Heisenberg chain on a finite-size lattice with N sites. We compute the large-N behavior of the spin stiffness, obtaining the correlation length ξ. We use our results to discuss the scaling behavior of the metal-insulator transitions in one-dimensional systems, taking into account the mapping between the XXZ Heisenberg chain and the spinless fermion model, and known results for the Hubbard model. We study the scaling properties of both the Hubbard model and the XXZ Heisenberg chain by solving numerically the Bethe ansatz equations. We find that for some range of values of ξ/N, the scaling behavior may be observed for the Hubbard model but not for the XXZ Heisenberg chain. We show how ξ can be obtained from the scaling properties of the spin stiffness for small system sizes. This method can be applied to models having not an exact solution, illuminating their transport properties.

Bibliography

E. Abrahams, P. W. Anderson, D. C. Licciardello, and T. V. Ramakrishnan. Scaling Theory of Localization: Absence of Quantum Diffusion in Two Dimensions. *Phys. Rev. Lett.*, 42:673, 1979.

Douglas Adams. *The Restaurant at the End of the Universe*. Hitchhiker's Guide Series. Random House Publishing Group, 1995.

Markus Aichhorn, Maria Daghofer, Hans Gerd Evertz, and Wolfgang von der Linden. Low temperature lanczos method. *Phys. Rev. B*, 67:161103R, 2003.

J. L. Alonso, L. A. Fernández, F. Guinea, V. Laliena, and V. Martín-Mayor. Discontinuous Transitions in Double-Exchange Materials. *Phys. Rev. B*, 63(64416), 2001a.

J. L. Alonso, L. A. Fernández, F. Guinea, V. Laliena, and V. Martín-Mayor. Variational Mean-Field Approach to the Double-Exchange Model. *Phys. Rev. B*, 63:54411, 2001b.

V. S. Amaral, J. P. Araújo, Yu. G. Pogorelov, J. B. Sousa, P. B Tavares, J. M. Vieira, J. M. B. Lopes dos Santos, A. A. C. S. Lourenço, and P. A. Algarabel. Anomalous Low-Field Magnetization in $La_{2/3}Ca_{1/3}MnO_3$ near critical Point: Stable Clusters? *J. Appl. Phys.*, 83(11):7154, 1998.

P. W. Anderson. Absence of Diffusion in Certain Random Lattices. *Phys. Rev.*, 109:1492, 1958.

P. W. Anderson and H. Hasegawa. Considerations on double exchange. *Phys. Rev.*, 100(2):675, 1955.

George Arfken. *Mathematical Methods for Physicists*. Academic Press, London, 2 edition, 1970.

M. C. Aronson, J. L. Sarrao, Z. Fisk, M. Whitton, and B. L. Brandt. Fermi surface of the ferromagnetic semimetal, EuB_6. *Phys. Rev. B*, 59:4720, 1999.

Daniel P. Arovas, Guillermo Gómez-Santos, and Francisco Guinea. Phase separation in double-exchange systems. *Phys. Rev. B*, 59:13569, 1999.

Francis Bacon. *Novum Organum – The Interpretation of Nature and the Kingdom of Man*. 1620. URL `http://www.constitution.org/bacon/nov_org.htm`.

George A. Baker. *Essentials of Padé Approximants*. Academic Press, New York, 1975.

C. D. Batista, J. Eroles, M. Avignon, and B. Alascio. Ferromagnetic Polarons in Manganites. *Phys. Rev. B*, 62:15047, 2000.

M. C. Bennett, J. van Lierop, E. M. Berkeley, J. F. Mansfield, C. Henderson, M. C. Aronson, D. P. Young, A. Bianchi, Z. Fisk, F. Balakirev, and A. Lacerda. Weak ferromagnetism in CaB_6. *Phys. Rev. B*, 69: 132407, 2004.

N. Beskin. *Fracções Contínuas* – Tradução de P. Lima, volume 11 of *Iniciação à matemática*. Editora Mir, Moscovo, 1987.

M. K. Blomberg, M. J. Merisalo, M. M. Korsukova, and V. N. Gurin. Single-crystal X-ray diffraction study of NdB_6, EuB_6 and YbB_6. *J. Alloys and Compounds*, 217:123, 1995.

J. Brndiar and P. Markos. Universality of the metal-insulator transition in three-dimensional disordered systems. *cond-mat/0606056*, 2006.

S. Broderick, L. Degiorgi, H. R. Ott, J. L. Sarrao, and Z. Fisk. Giant magneto-optical response of ferromagnetic EuB_6. *Eur. Phys. J. B*, 27:3–6, 2002a.

S. Broderick, B. Ruzicka, L. Degiorgi, H. R. Ott, J. L. Sarrao, and Z. Fisk. Scaling between magnetization and Drude weight in EuB_6. *Phys. Rev. B*, 65:121102(R), 2002b.

S. Broderick, L. Degiorgi, H.R. Ott, J.L. Sarrao, and Z. Fisk. Polar Kerr rotation of the ferromagnet EuB_6. *Eur. Phys. J. B*, 33(1):47–54, 2003.

B. R. Bulka, B. Kramer, and A. MacKinnon. Mobility edge in the three dimensional Anderson model. *Z. Phys. B - Cond. Mat.*, 60:13, 1985.

G. Caimi, A. Perucchi, L. Degiorgi, H.R. Ott, **VITOR M. PEREIRA**, A.H. Castro-Neto, A.D. Bianchi, and Z. Fisk. **Magneto-optical evidence of double exchange in a percolating lattice**. *Phys. Rev. Lett.*, 96:016403, 2006.

M.J. Calderon, L.G.L. Wegener, and P.B. Littlewood. Evaluation of evidence for magnetic polarons in EuB_6. *Phys. Rev. B*, 70:92408, 2004.

M. J. Calderón and L. Brey. Monte Carlo Simulations for the Magnetic Phase Diagram of the Double-Exchange Hamiltonian. *Phys. Rev. B*, 58:3286, 1998.

Herbert B. Callen. *Thermodynamics and an Introduction to Thermostatistics*. John Wiley & Sons, 1985.

D. Ceperley. Condensed-matter physics: Return of the itinerant electron. *Nature*, 397:386, 1999.

Raymond Chang. *Chemistry*. McGraw Hill, Inc., fourth edition, 1991.

J. A. Clack, J. D. Denlinger, J. W. Allen, D. M. Poirier, C. G. Olson, Z. Fisk, D. Young, and P.C. Canfield. Resonant, Core Level and Angle Resolved Photoemission Studies of Rare Earth Hexaborides. *Unpublished.*

Morrel H. Cohen, H. Fritzsche, and S. R. Ovshinsky. Simple Band Model for Amorphous Semiconducting Alloys. *Phys. Rev. Lett.*, 22:1065, 1969.

J. C. Cooley, M. C. Aronson, J. L. Sarrao, and Z. Fisk. High pressures and ferromagnetic order in EuB_6. *Phys. Rev. B*, 56:14541–14546, 1997.

F. Cyrot-Lackmann. On the electronic structure of liquid transitional metals. *Adv. Phys.*, 16:393, 1967.

F. Cyrot-Lackmann. Sur le calcul de la cohésion et de la tension superficielle des métaux de transition par une méthode de liaisons fortes. *J. Phys. Chem. Solids*, 29(7):1235, 1968.

F. Cyrot-Lackmann. On the calculation of surface tension in transition metals. *Surf. Sci.*, 15(3):535–548, 1969.

M. Daghofer, W. Koller, H. G. Evertz, and W. von der Linden. Ferromagnetic Polarons, Phase Separation, Stripes and Polaron Lattice: The two- and three-dimensional ferromagnetic Kondo Model. *cond-mat/0410274*, 2004a.

M. Daghofer, W. Koller, H. G. Evertz, and W. von der Linden. Polaronic aspects of the two-dimensional ferromagnetic Kondo model. *J. Phys. C: Solid State Physics*, 16:5469, 2004b.

Elbio Dagotto. *Nanoscale Phase Separation and Colossal Magnetoresistance*. Springer Verlag, Berlin, New York, 2003.

P.-G. de Gennes. Effects of Double Exhange in Magnetic Crystals. *Phys. Rev.*, 118(1):141, 1960.

L. Degiorgi, E. Felder, H. R. Ott, J. L. Sarrao, and Z. Fisk. Low-Temperature Anomalies and Ferromagnetism of EuB_6. *Phys. Rev. Lett.*, 79:5134, 1997.

J. D. Denlinger, J. A. Clack, J. W. Allen, G.-H. Gweon, D. M. Poirier, and C. G. Olson. Bulk Band Gaps in Divalent Hexaborides. *Phys. Rev. Lett.*, 89:157601, 2002.

T. Dietl and J. Spalek. Effect of Fluctuations of Magnetization on the Bound Magnetic Polaron: Comparison with Experiment. *Phys. Rev. Lett.*, 48:355, 1982.

T. Dietl and J. Spalek. Effect of thermodynamic fluctuations of magnetization on the bound magnetic polaron in dilute magnetic semiconductors. *Phys. Rev. B*, 28:1548, 1983.

Feng Ding. Theoretical study of the stability of defects in single-walled carbon nanotubes as a function of their distance from the nanotube end. *Phys. Rev. B*, 72:245409, 2005.

D. P. DiVincenzo and E. J. Mele. Self-consistent effective-mass theory for intralayer screening in graphite intercalation compounds. *Phys. Rev. B*, 29:1685, 1984.

S. Doniach. The Kondo Lattice and weak antiferromagnetism. *Physica*, 91B:231, 1977.

S. Doniach and E. H. Sondheimer. *Green's Functions for Solid State Physicists*. Imperial College Press, 1999.

E. N. Economou and Morrel H. Cohen. Existence of Mobility Edges in Anderson's Model for Random Lattices. *Phys. Rev. B*, 5:2931, 1972.

J. T. Edwards and D. J. Thouless. Numerical studies of localization in disordered systems. *J. Phys. C: Solid State Physics*, 5:807, 1972.

K. B. Efetov. Supersymmetry and theory of disordered metals. *Adv. Phys.*, 32:53, 1983.

Albert Einstein. Theoretische bemerkungen zur supraleitung der metalle. In *Gedenkboek aangeb. aan H. Kamerlingh Onnes (proceedings of the symposium honoring Kamerlingh Onnes)*, page 435. University of Leiden, 1922. URL `http://arxiv.org/abs/physics/0510251`.

P. Esquinazi, D. Spemann, R. Höhne, A. Setzer, K.-H. Han, and T. Butz. Induced Magnetic Ordering by Proton Irradiation in Graphite. *Phys. Rev. Lett.*, 91:227201, 2003.

J. Etourneau and P. Hagenmuller. Structure and physical features of the rare-earth borides. *Philos. Mag. B*, 52:589, 1985.

H. Feil and C. Haas. Magneto-Optical Kerr Effect, Enhanced by the Plasma Resonance of Charge Carriers. *Phys. Rev. Lett.*, 58:65–68, 1986.

Alexander L. Fetter and John Dirk Walecka. *Quantum Theory of Many-Particle systems*. International Series in Pure and Applied Physics. McGraw-Hill Book Company, 1971.

Michael E. Fisher and J. S. Langer. Resistive Anomalies at Magnetic Critical Points. *Phys. Rev. Lett.*, 20:665, 1968.

Z. Fisk, D. C. Johnston, B. Cornut, S. von Molnar, S. Oseroff, and R. Calvo. Magnetic, transport, and thermal properties of ferromagnetic EuB_6. *J. Appl. Phys.*, 50(B3):1911, 1979.

Mark Fox. *Optical Properties of Solids*. Oxford Master Series in Condensed Matter Physics. Oxford University Press, New York, 2004.

J. Friedel. Electronic Structure of Primary Solid Solutions in Metals. *Adv. Phys.*, 3:446, 1954.

D. J. Garcia, K. Hallberg, C. D. Batista, S. Capponi, D. Poilblanc, M. Avignon, and B. Alascio. Charge and spin inhomogeneous phases in the ferromagnetic kondo lattice model. *Phys. Rev. B*, 65:134444, 2002.

J. P. Gaspard and F. Cyrot-Lackmann. Density of states from moments. Applications to the impurity band. *J. Phys. C: Solid State Physics*, 6:3077–3096, 1973.

J. L. Gavilano, B. Ambrosini, P. Vonlanthen, H. R. Ott, D. P. Young, and Z. Fisk. Low-Temperature Nuclear Magnetic Resonance Studies of EuB_6. *Phys. Rev. Lett.*, 81:5648, 1998.

T. H. Geballe, B. T. Matthias, K. Andres, J. P. Maita, A. S. Cooper, and E. Corenzwit. Magnetic Ordering in the Rare-Earth Hexaborides. *Science*, 160(3835):1443–1444, 1968.

K Giannò, A V Sologubenko, H R Ott, A D Bianchi, and Z Fisk. Low-temperature thermoelectric power of CaB_6. *J. Phys.: Condens. Matter*, 14(5):1035, 2002.

J. González, F. Guinea, and M. A. H. Vozmediano. Continuum approximation to fullerene molecules. *Phys. Rev. Lett.*, 69:172, 1992.

J. González, F. Guinea, and M. A. H. Vozmediano. Unconventional Quasiparticle Lifetime in Graphite. *Phys. Rev. Lett.*, 77:3589, 1996.

R. G. Goodrich, N. Harrison, J. J. Vuillemin, A. Teklu, D. W. Hall, Z. Fisk, D. Young, and J. Sarrao. Fermi surface of ferromagnetic EuB_6. *Phys. Rev. B*, 58:14896, 1998.

H. Grussbach and M. Schreiber. Determination of the mobility edge in the Anderson model of localization in three dimensions by multifractal analysis. *Phys. Rev. B*, 51:663, 1995.

S. Gu, **VITOR M. PEREIRA**, and N. M. R. Peres. **Scaling Study of the Metal-Insulator Transition in one-Dimensional Fermion Systems**. *Phys. Rev. B*, 66(23):235108, 2002.

C. N. Guy, S. von Molnar, J. Etourneau, and Z. Fisk. Charge transport and pressure dependence of T_C of Single Crystal Ferromagnetic EuB_6. *Solid State Commun.*, 33:1055–1058, 1980.

Noriaki Hamada, Shin ichi Sawada, and Atsushi Oshiyama. New one-dimensional conductors: Graphitic microtubules. *Phys. Rev. Lett.*, 68:1579, 1992.

A Hasegawa and A Yanase. Electronic structure of CaB_6. *J. Phys. C: Solid State Physics*, 12:5431–5440, 1979.

R. Haydock. The Recursive solution of Schrödinger Equation. In *Solid State Physics*, volume 35, pages 216–294. Academic Press, New York, 1980.

R. Haydock and M. J. Kelly. Electronic structure from non-hermitian representations of the Hamiltonian. *J. Phys. C: Solid State Physics*, 8:L290–L293, 1975.

R. Haydock and C. M. M. Nex. Comparison of quadrature and termination for estimating the density of states within the recursion method. *J. Phys. C: Solid State Physics*, 17:4783–4789, 1984.

R. Haydock and C. M. M. Nex. A general terminator for the recursion method. *J. Phys. C: Solid State Physics*, 18:2235–2248, 1985.

R. Haydock, V. Heine, and M. J. Kelly. Electronic structure based on the local atomic environment for tight-binding bands. *J. Phys. C: Solid State Physics*, 5:2845–2858, 1972.

R. Haydock, V. Heine, and M. J. Kelly. Electronic structure based on the local atomic environment for tight-binding bands. II. *J. Phys. C: Solid State Physics*, 8:2591–2605, 1975.

Roger Haydock and Ronald L. Te. Accuracy of the recursion method. *Phys. Rev. B*, 49:10845, 1994.

D. Heiman, P. A. Wolff, and J. Warnock. Spin-flip Raman scattering, bound magnetic polaron, and fluctuations in (Cd,Mn)Se. *Phys. Rev. B*, 27:4848, 1983.

Volker Heine. Electronic Structure from the Point of View of the Local Atomic Environment. In *Solid State Physics*, volume 35, pages 1–128. Academic Press, New York, 1980.

W. Henggeler, H.-R. Ott, D. P. Young, and Z. Fisk. Magnetic ordering in EuB_6, investigated by neutron diffraction. *Solid State Commun.*, 108:929–932, 1998.

C. H. Hodges. Van Hove Singularities and Continued Fraction Coefficients. *J. Phys. Lett*, 38(1):L187, 1977.

P. C. Hohenberg. Existence of long-range order in one and two dimensions. *Phys. Rev.*, 158:383, 1967.

I. Chang *et al.* Localization Length Exponent in Quantum Percolation. *Phys. Rev. Lett.*, 74:2094, 1994.

J. Jaklic and P. Prelovsek. Lanczos method for the calculation of finite-temperature quantities in correlated systems. *Phys. Rev. B*, 49:5065, 1994.

M. D. Jones and D. M. Ceperley. Crystallization of the one-component plasma at finite temperature. *Phys. Rev. Lett.*, 76:4572, 1996.

M. Yu. Kagan, D. I. Khomskii, and M. V. Mostovoy. Double-exchange model: phase separation versus canted spins. *Eur. Phys. J. B*, 12, 1999.

W. Kaiser and W. L. Bond. Nitrogen, A Major Impurity in Common Type I Diamond. *Phys. Rev.*, 115: 857, 1959.

A. Kaminski and S. Das Sarma. Polaron Percolation in Diluted Magnetic Semiconductors. *Phys. Rev. Lett.*, 88:247202, 2002.

T. Kasuya, A. Yanase, and T. Takeda. Stability condition for the paramagnetic polaron in a magnetic semiconductor. *Solid State Commun.*, 8:1543, 1970.

M. J. Kelly. Applications of the Recursion Method to the Electronic Structure from an Atomic Point of View. In *Solid State Physics*, volume 35, pages 296–383. Academic Press, New York, 1980.

H. Kino, F. Aryasetiawan, K. Terakura, and T. Miyake. Abnormal quasiparticle shifts in CaB_6. *Phys. Rev. Lett.*, 66:121103R, 2002.

Scott Kirkpatrick and Thomas P. Eggarter. Localized States of a Binary Alloy. *Phys. Rev. Lett.*, 6:3598, 1972.

W. Kohn. Density Functional and Density Matrix Method Scaling Linearly with the Number of Atoms. *Phys. Rev. Lett.*, 76:3168, 1996.

Winfried Koller, Alexander Prüll, Hans Gerd Evertz, and Wolfgang von der Linden. Magnetic polarons in the one-dimensional ferromagnetic Kondo model. *Phys. Rev. B*, 67:174418, 2003.

B Kramer and A MacKinnon. Localization: theory and experiment. *Rep. Prog. Phys.*, 56:1469, 1993.

Kenn Kubo and Nagao Ohata. A Quantum Theory of Double Exchange I. *J. Phys. Soc. Jpn.*, 33(2):21, 1972.

J. Kunes and W. E. Pickett. Kondo and anti-Kondo coupling to local moments in EuB_6. *Phys. Rev. B*, 69:165111, 2004.

Patrick A. Lee and T. V. Ramakrishnan. Disordered electronic systems. *Rev. Mod. Phys.*, 57:287–337, 1985.

Li-Ping Li, Guang-She Li, Wen-Hui Su, Xu-Dong Zhao, and Xiaoyang Liu. A Mössbauer study of $La_{1-x}Eu_xB_6$ compounds synthesized at high pressure and temperature. *Hyperfine Interactions*, 128: 409, 2000.

Q. Li, J. Zang, A. R. Bishop, and C. M. Soukoulis. Charge Localization in Disordered Colossal-Magnetoresistance Manganites. *Phys. Rev. B*, 56:4541, 1997.

Chungwei Lin and Andrew.J.Millis. Dynamical Mean Field Theory of Temperature and Field Dependent Band Shifts in Magnetically Coupled Semimetals: Application to EuB_6. *Phys. Rev. B*, 71:75111, 2004.

W. Lipscomb. Structures of the Boron Hydrides. *J. Chem. Phys*, 22:985, 1954.

William N. Lipscomb and Doyle Britton. Valence Structure of the Higher Borides. *J. Chem. Phys.*, 33: 275, 1960.

M U Luchini and C M M Nex. A new procedure for appending terminators in the recursion method. *J. Phys. C: Solid State Physics*, 20:3125, 1987.

A. MacKinnon and B. Kramer. One-Parameter Scaling of Localization Length and Conductance in Disordered Systems. *Phys. Rev. Lett.*, 47:1546, 1981.

A. Magnus. Assymptotic behavior of continued fraction coefficients related to singularities of the weight function. In D. G. Pettifor and D. L. Wearie, editors, *The Recursion Method and its Applications*, volume 58 of *Springer Series in solid State Sciences*, page 22, Imperial College, London, September 13-14 1984. Springer-Verlag.

G. Mahan. The classical references for GF are: G. Mahan, *Many Particle Physics*, Springer (1990); S. Doniach and E. H. Sondheimer, *Green's Functions for Solid State Physicists*, Imperial College Press (1999); A. L. Fetter and J. D. Walecka, *Quantum Theory of Many-Particle systems*, McGraw-Hill Book Company (1971). Any modern solid-state textbook is also likely to include the subject and applications of the GF formalism .

Pinaki Majumdar and Peter Littlewood. Magnetoresistance in Mn Pyrochlore: Electrical Transport in a Low Carrier Density Ferromagnet. *Phys. Rev. Lett.*, 81:1314, 1998.

D. Mandrus, B. C. Sales, and R. Jin. Localized vibrational mode analysis of the resistivity and specific heat of LaB_6. *Phys. Rev. B*, 64:12302, 2001.

H. Martinho, C. Rettori, Z. Fisk, and S. B. Oseroff. Evidence for local structural symmetry-breaking in $Ca_{1-x}Eu_xB_6$. *cond-mat/0503294*, 2005.

S. Massidda, A. Continenza, T. M. de Pascale, and R. Monnier. Electronic structure of divalent hexaborides. *Z. Phys. B.*, 102(1):83–89, 1996.

K. Matsubayashi, M. Maki, T. Tsuzuki, T. Nishioka, and N. K. Sato. Magnetic properties (Communication arising): Parasitic ferromagnetism in a hexaboride? *Nature*, 430, 2002.

K. Matsubayashi, M. Maki, T. Moriwaka, T. Tsuzuki, T. Nishioka, C. H. Lee, A. Yamamoto, T. Ohta, and N. K. Sato. Extrinsic Origin of High-Temperature Ferromagnetism in CaB_6. *J. Phys. Soc. Jpn.*, 72:2097, 2003.

T. Matsui, H. Kambara, Y. Niimi, K. Tagami, M. Tsukada, and Hiroshi Fukuyama. STS Observations of Landau Levels at Graphite Surfaces. *Phys. Rev. Lett.*, 94:226403, 2005.

A. Mauger. Magnetic polaron: Theory and experiment. *Phys. Rev. B*, 27:2308, 1983.

Alan D. McNaught and Andrew Wilkinson. *IUPAC Compendium of Chemical Terminology (The* "Gold Book"*)*. IUPAC - International Union of Pure and Applied Chemistry, online version edition, 2005. URL `http://www.iupac.org/publications/compendium/index.html`.

N. D. Mermin and H. Wagner. Absence of ferromagnetism or antiferromagnetism in one- or two-dimensional isotropic heisenberg models. *Phys. Rev. Lett.*, 17:1133, 1966.

H. Meskine, T. Saha-Dasgupta, and S. Satpathy. Does the Self-Trapped Magnetic Polaron Exist in Electron-Doped Manganites? *Phys. Rev. Lett.*, 92:56401, 2004.

A. J. Millis, P. B. Littlewood, and B. I. Shraiman. Double Exchange Alone does not Explain the Resistivity of $La_{1-x}Sr_xMnO_3$. *Phys. Rev. Lett.*, 74(25):5144, 1995.

Alexander D. Mirlin and Yan V. Fyodorov. Distribution of local densities of states, order parameter function, and critical behavior near the Anderson transition. *Phys. Rev. Lett.*, 72:526, 1993.

R. Monnier and B. Delley. Point Defects, Ferromagnetism, and Transport in Calcium Hexaboride. *Phys. Rev. Lett.*, 87:157204, 2001.

A Mookerjee. A new formalism for the study of configuration-averaged properties of disordered systems. *J. Phys. C: Solid State Physics*, 6:L205, 1973.

Takao Mori and Shigeki Otani. Ferromagnetism in lanthanum doped CaB_6: is it intrinsic? *Solid State Commun.*, 123:287, 2003.

N. F. Mott. Electrons in disordered structures. *Adv. Phys.*, 16:49, 1967.

Nevil F. Mott and E. A. Davis. *Electronic processes in non-crystalline materials.* Clarendon Press, Oxford, 1971.

Nevil F. Mott and E. A. Davis. *Conduction in Non-Crystalline Materials.* Clarendon Press, Oxford, 1987.

Shuichi Murakami, Ryuichi Shindou, Naoto Nagaosa, and Andrei S. Mishchenko. Theory of excitonic states in CaB_6. *Phys. Rev. B*, 66:184405, 2002.

E. L. Nagaev. Instability of the double-exchange-induced canted antiferromagnetic ordering. *Phys. Rev. B*, 58:2415, 1998.

E. L. Nagaev. Colossal-magnetoresistance materials: manganites and conventional ferromagnetic semiconductors. *Phys. Rep.*, 346:387, 2001.

E. L. Nagaev. *Colossal Magnetoresistance and Phase Separation in Magnetic Semiconductors*. Imperial College Press, 2002.

D. R. Neuber, M. Daghofer, R. M. Noack, H. G. Evertz, and W. von der Linden. Ferromagnetic polarons in the one-dimensional ferromagnetic Kondo model with quantum mechanical S=3/2 core spins. *cond-mat/0501251*, 2004.

Andriy H. Nevidomskyy, Gábor Csányi, and Michael C. Payne. Chemically active substitutional nitrogen impurity in carbon nanotubes. *Phys. Rev. Lett.*, 91:105502, 2003.

C. M. M Nex. Estimation of integrals with respect to a density of states. *J. Phys. A: Math. Gen.*, 11:653, 1978.

Y. Niimi, T. Matsui, H. Kambara, K. Tagami, M. Tsukada, and Hiroshi Fukuyama. Scanning tunneling microscopy and spectroscopy studies of graphite edges. *physics/0404069*, 2004.

K. S. Novoselov, A. K. Geim, S. V. Morozov, D. Jiang, Y. Zhang, S. V. Dubonos, I. V. Grigorieva, and A. A. Firsov. Electric Field Effect in Atomically Thin Carbon Films. *Science*, 306:666, 2004.

K. S. Novoselov, A. K. Geim, S. V. Morozov, D. Jiang, M. I. Katsnelson, I. V. Grigorieva, S. V. Dubonos, and A. A. Firsov. Two-dimensional gas of massless Dirac fermions in graphene. *Nature*, 438:197, 2005a.

K. S. Novoselov, D. Jiang, F. Schedin, T. J. Booth, V. V. Khotkevich, S. V. Morozov, and A. K. Geim. Two-dimensional atomic crystals. *Proc. Natl. Acad. Sci. USA*, 102:10453, 2005b.

P. Nyhus, S. Yoon, M. Kauffman, S. L. Cooper, Z. Fisk, and J. Sarrao. Spectroscopic study of bound magnetic polaron formation and the metal-semiconductor transition in EuB_6. *Phys. Rev. B*, 56:2717–2721, 1997.

Teri Wang Odom, Jin-Lin Huang, Philip Kim, and Charles M. Lieber. Atomic structure and electronic properties of single-walled carbon nanotubes. *Nature*, 391:62, 1998.

M. R. Oliver, J. O. Dimmock, A. L. McWhorter, and T. B. Reed. Conductivity Studies in Europium Oxide. *Phys. Rev. B*, 5:1078, 1972.

Shigeki Otani and Takao Mori. Flux Growth and Magnetic Properties of CaB_6 Crystals. *J. Phys. Soc. Jpn.*, 71:1791, 2002.

G. A. Parker, W. Zhu, Y. Huang, D. K. Hoffman, and D. J. Kouria. Matrix pseudo-spectroscopy: iterative calculation of matrix eigenvalues and eigenvectors of large matrices using a polynomial expansion of the Dirac delta function. *Computer Phys. Comm.*, 96:27, 1996.

S. Paschen, D. Pushin, M. Schlatter, P. Vonlanthen, H. R. Ott, D. P. Young, and Z. Fisk. Electronic transport in $Eu_{1-x}Ca_xB_6$. *Phys. Rev. B*, 61:4174, 2000.

S. Pathak and S. Satpathy. Self-trapped magnetic polaron: Exact solution of a continuum model in one dimension. *Phys. Rev. B*, 63:214413, 2001.

Linus Pauling. The Nature of the Chemical Bond. II. The One-Electron Bond and the Three-Electron Bond. *J. Am. Chem. Soc.*, 53:3225, 1931.

VITOR M. PEREIRA, J. M. B. Lopes dos Santos, Eduardo V. Castro, and A. H. Castro Neto. **Double Exchange Model for Magnetic Hexaborides** . *Phys. Rev. Lett.*, 93(14):147202, 2004a.

VITOR M. PEREIRA, J. M. B. Lopes dos Santos, Eduardo V. Castro, and A. H. Castro Neto. **Double Exchange Model for Magnetic Hexaborides** . *cond-mat/0402671*, 2004b.

VITOR M. PEREIRA, J. M. B. Lopes dos Santos, and A. H. Castro Neto. **The Double Exchange Model at Low Densities**. *Preprint: cond-mat/0505741*, 2005.

VITOR M. PEREIRA, F. Guinea, J. M. B. Lopes dos Santos, N. M. R. Peres, and A. H. Castro Neto. **Disorder Induced Localized States in Graphene**. *Phys. Rev. Lett.*, 96(3):036801, 2006.

N. M. R. Peres, F. Guinea, and A. H. Castro Neto. Electronic Properties of Two-Dimensional Carbon. *Phys. Rev. B*, 73:125411, 2005.

N. M. R. Peres, A. H. Castro Neto, and F. Guinea. Conductance quantization in mesoscopic graphene. *Phys. Rev. B*, 73:195411, 2006.

A. Perucchi, G. Caimi, H.R. Ott, L. Degiorgi, A.D. Bianchi, and Z. Fisk. Optical evidence for a spin-filter effect in the charge transport of $Eu_{0.6}Ca_{0.4}B_6$. *Phys. Rev. Lett.*, 92:67401, 2003.

D. L. Peterson, D. U. Bartholomew, U. Debska, A. K. Ramdas, and S. Rodriguez. Spin-flip Raman scattering in n-type diluted magnetic semiconductors. *Phys. Rev. B*, 32:323, 1985.

J. L. Pichard and G. Sarma. Finite size scaling approach to Anderson localisation. *J. Phys. C: Solid State Physics*, 14(6):L127–L132, 1981.

David Pines. *Elementary Excitations in Solids*. Addison-Wesley Publishing Companay, 1963.

William H. Press, Saul A. Teukolsky, William T. Vetterling, and Brian P. Flannery. *Numerical Recipes - The Art of Scientific Computing*. Cambridge Cniversity Press, 1992.

F. C. Pu, Y. J. Wang, and C. H. Shang. *Aspects of Modern Magnetism: Lecture Notes on the 8th Chinese International Summer School of Physics*. World Scientific Publishing Co, 1995.

Emerson M. Pugh and Norman Rostoker. Hall Effect in Ferromagnetic Materials. *Rev. Mod. Phys.*, 25: 151, 1953.

G. T. Rado and H. Suhl, editors. *Magnetism*, volume IIa, page 105. Academic Press, New York, 1965.

Jong-Soo Rhyee, B. K. Cho, and H.-C. Ri. Electrical transport properties and small polarons in $Eu_{1-x}Ca_xB_6$. *Phys. Rev. B*, 67:125102, 2003a.

Jong-Soo Rhyee, B. H. Oh, B. K. Cho, M. H. Jung, H. C. Kim, Y. K. Yoon, Jae Hoon Kim, and T. Ekino. Formation of mid-gap states and ferromagnetism in semiconducting CaB_6. *cond-mat/0310068*, 2003b.

Jong-Soo Rhyee, B. H. Oh, B. K. Cho, H. C. Kim, and M. H. Jung. Magnetic properties in Ca-doped Eu hexaborides. *Phys. Rev. B*, 67:212407, 2003c.

C. O. Rodriguez, Ruben Weht, and W. E. Pickett. Electronic Fine Structure in the Electron-Hole Plasma in SrB_6. *Phys. Rev. Lett.*, 84:3903, 2000.

Riichiro Saito, Mitsutaka Fujita, G. Dresselhaus, and M. S. Dresselhaus. Electronic structure of graphene tubules based on C_{60}. *Phys. Rev. B*, 46:1804, 1992.

M. B. Salamon and M. Jaime. The Physics of Manganites: Structure and Transport. *Reviews of Modern Physics*, 77:583, 2001.

F. Salghetti-Drioli, P. Wachter, and L. Degiorgi. Magneto-optical Kerr effect in LaX (X=S, Se and Te): evidence for interplay between 4f-states and plasma resonance. *Solid State Commun.*, 109:773, 1999.

Gerald Schubert, Alexander Weisse, and Holger Fehske. Comparative numerical study of localization in disordered electron systems. *cond-mat/0309015*, 2003.

Yonathan Shapir, Amnon Aharony, and A. Brooks Harris. Localization and Quantum Percolation. *Phys. Rev. Lett.*, 49:486, 1982.

R. N. Silver and H. Röder. Calculation of densities of states and spectral functions by Chebyshev recursion and maximum entropy. *Phys. Rev. E*, 56:4822, 1997.

R. N. Silver, H. Roeder, A. F. Voter, and J. D. Kress. Kernel Polynomial Approximations for Densities of States and Spectral Functions. *J. Comput. Phys.*, 124:115, 1996.

C. S. Snow, S. L. Cooper, D. P. Young, and Z. Fisk. Magnetic polarons and the metal-semiconductor transitions in $(Eu,La)B_6$ and EuO: Raman scattering studies. *Phys. Rev. B*, 64:174412, 2001.

S. Souma, H. Komatsu, T. Takahashi, R. Kaji, T. Sasaki, Y. Yokoo, and J. Akimitsu. Electronic Band Structure and Fermi Surface of CaB_6 Studied by Angle-Resolved Photoemission Spectroscopy. *Phys. Rev. Lett.*, 90:27202, 2003.

Dietrich Stauffer and Amnon Aharony. *Introduction to Percolation Theory*. Taylor & Francis, London, 2nd (revised) edition, 1994.

O. Stephan, P. M. Ajayan, C. Colliex, Ph. Redlich, J. M. Lambert, P. Bernier, and P. Lefin. Doping Graphitic and Carbon Nanotube Structures with Boron and Nitrogen. *Science*, 266:5191, 1994.

S. Süllow, I. Prasad, M. C. Aronson, J. L. Sarrao, Z. Fisk, D. Hristova A. H. Lacerda, M. F. Hundley, A. Vigliante, and D. Gibbs. Structure and magnetic order of EuB_6. *Phys. Rev. B*, 57:5860–5869, 1998.

S. Süllow, I. Prasad, M. C. Aronson, S. Bogdanovich, J. L. Sarrao, and Z. Fisk. Metallization and magnetic order in EuB_6. *Phys. Rev. B*, 62:11626, 2000.

K. Taniguchi, T. Katsufuji, F. Sakai, H. Ueda, K. Kitazawa, and H. Takagi. Charge dynamics and possibility of ferromagnetism in $A_{1-x}La_xB_6$ (A = Ca and Sr). *Phys. Rev. B*, 66:64407, 2002.

J. M. De Teresa, M. R. Ibarra, P. A. Algarabel, C. Ritter, C. Marquina, J. Blasco, J. García, A. Del Moral, and Z. Arnold. Evidence for magnetic polarons in the magnetoresistive perovskites. *Nature*, 386:256, 1997.

J. M. De Teresa, M. R. Ibarra, P. Algarabel, L. Morellon, B. García-Landa, C. Marquina, C. Ritter, A. Maignan, C. Martin, B. Raveau, A. Kurbakov, and V. Trounov. Magnetic versus orbital polarons in colossal magnetoresistance manganites. *Phys. Rev. B*, 65:100403, 2000.

J. B. Torrance, M. W. Shafer, and T. R. McGuire. Bound Magnetic Polarons and the Insulator-Metal Transition in EuO. *Phys. Rev. Lett.*, 29:1168, 1972.

H. J. Tromp, P. van Gelderen, P. J. Kelly, G. Brocks, and P. A. Bobbert. CaB_6: A New Semiconducting Material for Spin Electronics. *Phys. Rev. Lett.*, 87:16401, 2001.

Hirokazu Tsunetsugu, Manfred Sigrist, and Kazuo Ueda. The ground-state phase diagram of the one-dimensional Kondo lattice model. *Rev. Mod. Phys.*, 69:809, 1997.

P Turchi, F. Ducastelle, and G. Tréglia. Band gaps and asymptotic behaviour of continued fraction coefficients. *J. Phys. C: Solid State Physics*, 15:2891–2924, 1982.

R. R. Urbano, P. G. Pagliuso, C. Rettori, S. B. Oseroff, J. L. Sarrao, P. Schlottmann, and Z. Fisk. Magnetic polaron and Fermi surface effects in the spin-flip scattering of EuB_6. *Phys. Rev. B*, 70, 2004.

C. M. Varma. Electronic and Magnetic States in the Giant Magnetoresistive Compounds. *Phys. Rev. B*, 54:7328, 1996.

P. Vonlanthen, S. Paschen, D. Pushin, A. D. Bianchi, and H. R. Ott. Thermal conductivity of EuB_6. *Phys. Rev. B*, 62:3246, 2000.

P. Wachter, F. Bommeli, L. Degiorgi, P. Burlet, F. Bourdarot, and E. Kaldis. The blue shift of the plasma edge of a ferromagnetic semimetal. *Solid State Commun.*, 105:675, 1998.

Xindong Wang and A. J.Freeman. Spin polarons in the double-exchange model. *J. Magn. Magn. Mater.*, 171:103, 1997.

Alexander Weisse, Gerhard Wellein, Andreas Alvermann, and Holger Fehske. The Kernel Polynomial Method. *cond-mat/0504627*, 2005.

G. A. Wigger, Ch. Wälti, , H. R. Ott, A. D. Bianchi, and Z. Fisk. Magnetization-dependent electronic transport in Eu-based hexaborides. *Phys. Rev. B*, 66:212410, 2002a.

G. A. Wigger, Ch. Wälti, , H. R. Ott, A. D. Bianchi, and Z. Fisk. Magnetization-dependent electronic transport in Eu-based hexaborides. *Phys. Rev. B*, 66:212410, 2002b.

G.A. Wigger, R. Monnier, H. R. Ott, D.P. Young, and Z. Fisk. Electronic transport in EuB_6. *Phys. Rev. B*, 69:125118, 2004.

G.A. Wigger, E. Felder, M. Weller, S. Streule, H.R. Ott, A.D. Bianchi, and Z. Fisk. Percolation limited magnetic order in $Eu_{1-x}Ca_xB_6$. *Eur. Phys. J. B*, 46:231, 2005.

F. Wooten. *Optical Properties of Solids*. Academic Press, New York, 1972.

Z. Wu, D.J. Singh, and R.E. Cohen. Electronic Structure of Calcium Hexaboride within the Weighted Density Approximation. *Phys. Rev. B*, 69:193105, 2004.

Masatoshi Yamazaki. Group-Theoretical Treatment of the Energy Bands in Metal Borides MeB6. *J. Phys. Soc. Jpn.*, 12:1, 1956.

Hongsuk Yi, N. H. Hur, and Jaejun Yu. Anomalous spin susceptibility and magnetic polaron formation in the double-exchange systems. *Phys. Rev. B*, 61:9501, 2000.

Kei Yosida. *Theory of Magnetism*, volume 122 of *Springer series in Solid-State Sciences*. Springer-Verlag, 1996.

D. P. Young, D. Hall, M. E. Torelli, Z. Fisk, J. L. Sarrao, J. D. Thompson, H.-R. Ott, S. B. Oseroff, R. G. Goodrich, and R. Zysler. High-temperature weak ferromagnetism in a low-density free-electron gas. *Nature*, 397:412–414, 1999.

S. Yunoki, J. Hu, A. L. Malavezzi, A. Moreo, N. Furukawa, and E. Dagotto. Phase Separation in Electronic Models for Manganites. *Phys. Rev. Lett.*, 80(4):845, 1998.

Yuanbo Zhang, Yan-Wen Tan, Horst L. Stormer, and Philip Kim. Experimental observation of the quantum Hall effect and Berry's phase in graphene. *Nature*, 438:201, 2005.

S. Zherlitsyn, B. Wolf, B. Lüthi, M. Lang, P. Hinze, E. Uhrig, W. Assmus, H.R. Ott, D.P. Young, and Z. Fisk. Elastic properties of ferromagnetic EuB_6. *Eur. Phys. J. B*, 22:327, 2001.

F. H. Zong, C. Lin, and D. M. Ceperley. Spin polarization of the low-density three-dimensional electron gas. *Phys. Rev. E*, 66:036703, 2002.